Phenomenological and Astroparticle analysis of Light Dark Matter particles

Daniel Albornoz Vásquez

UNIVERSITÉ DE GRENOBLE

THÈSE

Pour obtenir le grade de

DOCTEUR DE L'UNIVERSITÉ DE GRENOBLE

Spécialité : **Physique Théorique**

Arrêté ministérial : 7 août 2006

Présentée par

Daniel Albornoz Vásquez

Thèse dirigée par **Céline Bœhm**
et codirigée par **Pierre Salati**

préparée au sein **Laboratoire de Physique Théorique d'Annecy-le-Vieux**
et de **Ecole Doctorale de Physique, Grenoble**

Phenomenological and Astroparticle analysis of Light Dark Matter particles

Thèse soutenue publiquement le **19 septembre 2011**,
devant le jury composé de :

Monsieur Paolo Gondolo
Professeur, University of UTAH, Président

Monsieur Marco Cirelli
Docteur, CERN, Rapporteur

Monsieur Cyril Hugonie
Docteur, Université de Montpellier 2, Rapporteur

Monsieur Daniel Santos
Directeur de Recherche, LPSC Grenoble, Examinateur

Monsieur Aurélien Barrau
Professeur, Université Joseph Fourier Grenoble 1, Examinateur

Monsieur Julien Lavalle
Docteur, Universidad Autónoma de Madrid, Examinateur

Mademoiselle Céline Bœhm
Docteur, Durham University, Directeur de thèse

Monsieur Pierre Salati
Professeur, Université de Savoie, Co-Directeur de thèse

Al Pim y a la Mim,
en su búsqueda por trascender a través de la formación de sus hijos

Abstract

The Dark Matter problem is one of the most relevant quests for the understanding of the elementary constituents of the Universe: the nature of the Dark Matter is still unveiled. Experimental efforts aiming to detect the Dark Matter have shown a great progress in the last decade. This work is devoted to the phenomenological and astroparticle studies of Dark Matter candidates of supersymmetric nature –the neutralino– and beyond –scalar particles. The former, in the $(1-100)$ GeV mass range, is currently being tested by the Large Hadron Collider, direct detection and indirect detection experiments; this work shows that the interplay between experimental techniques is a decisive tool to thoroughly search for theoretical predictions. The latter is a non-standard candidate as light as 1 MeV which could be copiously produced at the Large Hadron Collider and, at the same time, it could explain other phenomena such as neutrino masses and/or the 511 keV line from the galactic center of the Milky Way.

Résumé

La Matière Sombre représente une des quêtes les plus importantes pour la compréhension des constituants élémentaires de l'Univers : la nature de la Matière Sombre reste un mystère. La dernière décennie a connu des développements expérimentaux remarquables dans la recherche de la Matière Sombre. Le but de ce travail est l'étude de candidats de Matière Sombre de nature supersymétrique (le neutralino) et au-delà (les particules scalaires) dans leurs aspects phénoménologiques et d'astroparticules. Le neutralino, dans l'intervalle de masses $(1 - 100)$ GeV, est testé par les expériences du Grand Collisionneur de Hadrons, et à travers des techniques de détection directe et de détection indirecte ; ce travail montre que la combinaison de ces techniques expérimentales est un outil décisif pour une recherche minutieuse des prédictions théoriques. Les particules scalaires sont des candidats non-standards ayant de masses aussi légères que 1 MeV qui pourraient être produits abondamment dans le Grand Collisionneur de Hadrons et, au même temps, expliquer d'autres phénomènes tels que la masse des neutrinos et/ou le signal à 511 keV provenant du centre galactique de la Voie Lactée.

Acknowledgements - Remerciements - Agradecimientos

Je remercie Céline Boehm pour ses directions, ses conseils, le partage de son savoir et son amitié pendant ces trois années. Tu avais raison, la thèse est un chemin de rencontre de soi-même.
Je remercie le laboratoire, le LAPTH, de m'avoir accuielli et pour tout son support. En particulier l'équipe administrative (Dominique, Véronique, Virginie et Nathalie), très aimable et toujours prête à venir en aide, et les directeurs (Patrick Aurenche quand je suis arrivé, Fawzy Boudjema ces jours-ci).
I would like to thank the Oxford Astrophysics and Theoretical Physics departments for receiving me during six months, and in particular Joe Silk and Subir Sarkar, to whom I owe the privilege of visiting Oxford. Je remercie la région Rhone-Alpes pour sa bourse ExploraDOC lors de ce séjour.
I would like to thank the UniverseNet Cosmology network for its support and excellent summer schools.
Je remercie particulièrement Geneviève Bélanger, ma principale collaboratrice et une guide dans la recherche. Je remercie mes autres collaborateurs: John Idárraga, Sacha Pukhov, Joe Silk, Frédéric Mayet, Julien Billard, Stephen West, Andrew Williams et Mads Frandsen.
I would like to thank Richard Taillet, Fawzi Boudjema, Pierre Salati, Pasquale Serpico and Subir Sarkar for their scientific advice, discussions and help.
I thank the members of my jury: Marco Cirelli and Cyril Hugonie who refereed this manuscript and gave me many useful corrections and comments, Paolo Gondolo, Julien Lavalle, Aurélien Barrau (who actually recommended the LAPTH and Céline Boehm to me), Daniel Santos, and my advisor and co-advisors Céline Boehm and Pierre Salati. You were all very kind to me in the constructive evaluation of this manuscript and the presentation for the viva.
I thank the proof readers of my thesis: Céline, Geneviève, Seba and Rod. I had plenty of mistakes, you had plenty of patience.
Je remercie mes amis dans cette étape de ma vie, Gata Ligueros, Samuel Belliard, Wessel Valkenburg, Julien Maes, Féti, Guillaume Drieu, Sandra Benotti, Sébastien Benotti, Sebastián Pérez, Camilo Vial, Vicente Neira, Rodrigo Guzman et Carine Nambala pour leur

présence, leur temps et leur aide. C'est toujours bon de savoir qu'on n'est pas seul.
Evidemment j'oublie beaucoup de personnes, mais je tiens à remercier tous celles et ceux qui m'ont accompagné dans ce chemin sur Annecy, sur Oxford, pendant le doctorat.
Gracias a mi familia. Soy un privilegiado de haber nacido y crecido entorno a ustedes, todos.

Contents

ETUDES PHÉNOMÉNOLOGIQUES ET ASTROPHYSIQUES DE LA MATIÈRE SOMBRE LÉGÈRE (RÉSUMÉ)

Introduction (Résumé)

Le contexte actuel des recherches en physique, que ce soit en physique des particules ou en cosmologie, est très prometteur. C'est l'ère des expériences remarquables, telles que le Grand Collisioneur de Hadrons (LHC) ou les satellites Fermi et Planck qui observent l'univers proche et lointain. C'est aussi un carrefour stimulant du côté théorique, puisque le modèle standard de la physique des particules (SM) et le modèle standard de la cosmologie (ΛCDM) soulèvent des questions auxquelles ils n'apportent pas de solution. Notamment, l'existence de la Matière Noire (ou Matière Sombre) (DM). Ce concept fut introduit en 1933 par l'astronome Fritz Zwicky pour expliquer la différence entre la masse dynamique et la masse lumineuse dans les amas de galaxies. Toutes les preuves expérimentales de l'existence de la DM sont, pour l'instant, issues d'effets gravitationnels. Bien qu'une modification de la théorie de la gravitation, de Newton et d'Einstein, peut expliquer ces observations, l'hypothèse la plus performante est celle de l'existence d'une nouvelle particule, massive et neutre. Des théories allant au-delà du SM proposent des candidats qui peuvent être testés par des expériences telles que le LHC et ses détecteurs, les expériences de détection directe (DD) et celles de détection indirecte (ID).

Les travaux ici présentés ont donné lieu à quatre articles scientifiques, dont deux déjà publiés [1, 2] et deux autres en cours de révision [3, 4]. En particulier, la possibilité de signaux correspondants à des particules de DM de masses dans le rang $(6-12)$ *GeV* au sein d'expériences de DD a motivé la recherche de neutralinos (candidats de DM supersymétrique) légers dans deux modèles différents [2, 3, 4]. Dans [1] sont montrées les potentielles signatures au LHC issues d'un modèle de DM scalaire avec de nouveaux fermions ayant des interactions fortes.

Dans ce mémoire, une première partie introduit des preuves de l'existence de la DM, sa place dans la cosmologie standard et sa distribution locale sous forme de halos. Ensuite, une deuxième partie traite les contraintes que doivent satisfaire les modèles de DM, puis présente des modèles supersymétriques contenant des neutralinos comme candidats de DM ainsi qu'un modèle de DM scalaire. Une troisième partie présente une méthode d'exploration de l'espace de paramètres supersymétriques, les résultats des recherches de modèles avec des neutralinos légers ainsi que les prédictions qui en découlent, et finalement une étude sur les possibilités de production de DM scalaire dans les collisionneurs hadroniques.

Première Partie : La problématique de la Matière Sombre (Résumé)

Chapitre 1 : Introduction à la Matière Sombre (Résumé)

Il y a une grande quantité d'indices qui justifient l'hypothèse de l'existence de DM. Par exemple, la densité de l'univers a été mesurée grâce aux anisotropies du fond diffus cosmologique (CMB). L'univers est plat : sa dynamique est mesurée par l'observation de supernovas lointaines. Ainsi, la composante de matière doit représenter plus d'un cinquième du contenu de l'univers. Les mesures de précision du CMB par le satellite WMAP montrent que la fraction de DM dans l'univers est de $(22.8 \pm 2.7)\%$.
Le modèle ΛCDM est une construction basée sur les équations de Friedman appliquant la relativité générale à un univers en expansion. L'éloignement apparent des objets lointains et la découverte du CMB ont motivé ce modèle qui décrit un univers contenant du rayonnement de contribution énergétique négligeable, de la matière dominée par la DM froide (CDM) et d'une constante cosmologique ou de l'Energie Noire. Ce modèle remporte un grand succès dans l'explication des étapes successives de l'histoire de l'univers, incluant la formation primordiale des éléments chimiques, le découplage des photons observé au CMB et la formation des grandes structures à partir d'un sprectre primordial de la matière généré après une période d'inflation.
En ce qui concerne l'évolution de la DM, il est communément admis qu'elle fut en équilibre thermique et chimique avec les particules du SM. Quand l'expansion de l'univers fut plus importante que le taux d'annihilation dû à la transition au régime non-relativiste de la DM, elle n'a pratiquement plus vu changer sa densité en nombre. C'est le mécanisme du *freeze-out* (FO). De même, l'arrêt des collisions élastiques fixe la distribution de densité, cruciale pour la formation des structures.
Le candidat type est le WIMP : une particule ayant des interactions de l'ordre de l'interaction faible, massive, de sorte qu'elle obtienne naturellement la densité relique via le FO. Les candidats de DM de physique des particules sont issus de théories allant au-delà du SM, et correspondent souvent à des WIMPs. Une telle théorie est la Supersymétrie (SUSY). Parmi les candidats supersymétriques de DM on trouve le neutralino, un WIMP.

Les recherches de détection de la DM sont très avancées. En ce qui concerne les collisionneurs, l'exercice est modèle-dépendant et consiste à observer n'importe quel type de signal prédit par le modèle soujacent. Suite au manque de manifestations de nouvelle physique, les résultats restent des limites sur les configurations possibles. La DM est présente dans notre environnement, dans notre galaxie. Il est donc possible de contraindre ses collisions élastiques avec les noyaux via la DD sur terre, et ses annihilations via la ID, c'est-à-dire de la détection des produits des annihilations dans la Voie Lactée et ailleurs. Ainsi, les résultats du LHC, du Tevatron, de CDMS-II, de XENON100, de DAMA, de CoGeNT, de Fermi-LAT sont à tenir en compte dans la construction de modèles.

Chapitre 2 : Histoire thermique de la Matière Sombre (Résumé)

La présence de la DM dans notre entourage est due à sa création dans l'univers primordial. L'abondance de DM est déterminée par son départ de l'équilibre chimique avec les autres particules du plasma chaud. L'évolution de la densité en nombre de particules est déterminée par l'équation de Boltzmann, équation cinétique qui traduit l'impact des interactions dans l'espace des phases d'une espèce dans un fluide. La dynamique d'expansion et le refroidissement de l'univers y sont inclus par les dépendances spatiales, temporelles et dynamiques de la fonction de distribution des particules. Ainsi, on obtient une équation qui permet de calculer la densité en nombre des particules à tout instant. La solution, pour un cas générique de particules évoluant dans l'univers primordial, est réalisée à l'aide d'un traitement numérique avec une très bonne précision. Des outils très sophistiqués, notamment le code micrOMEGAs, permettent de traiter des modèles particuliers en incluant des corrections allant au-delà du premier ordre des interactions.
La densité relique de la DM est déterminée par la transition au régime non-relativiste, lui-même arrivant au moment où la température du plasma atteint une valeur comparable à celle de la masse de la DM. Plus la DM est légère, plus elle reste longtemps en équilibre. Par contre, la quantité de particules restantes dépend surtout de la section efficace d'interaction, qui, elle, détermine le moment auquel le départ de l'équilibre s'achève. Vu que ceci arrive pendant la transition non-relativiste, et que celle-ci est exponentielle, une petite variation de la valeur de la section efficace se traduit en un changement conséquent de la densité relique. Pour des masses de l'ordre de 100 GeV, c'est une section efficace de $3 \times 10^{-26}\ cm^3 s^{-1}$ qui convient pour expliquer la densité de DM requise.
Par ce mécanisme on peut contraindre les interactions d'annihilation de la DM, relevantes dans l'univers environnant pour les recherches de signaux indirects. Par contre, la dépendance en vitesse de la section efficace peut engendrer un comportement très différent dans l'univers primordial, d'autant plus que la différence de température des gaz primordiaux et galactiques de DM s'élève à un facteur $\sim 10^5$. En effet, cette différence peut signifier des sections effi-

caces d'annihilation en galaxie très différentes des primordiales, surtout dans les cas où des résonances, des canaux vitesse-dépendant ou l'effet Sommerfeld sont dominants. Il se peut aussi que l'annihilation ne soit pas le mécanisme fixant la densité relique : d'une part, s'il y a des particules dégénérées en masse elles peuvent se co-annihiler ; d'autre part, le freeze-in représente un tout autre moyen d'obtenir la densité relique, faisant intervenir d'autres espèces complètement découplées du plasma, et relâchant les contraintes sur les sections efficaces d'annihilation.

Chapitre 3 : De la formation de structures aux halos de Matière Sombre (Résumé)

A partir du spectre primordial de matière, la formation de structures se fait par l'effondrement gravitationnel des surdensités locales au-dessus d'un seuil. La DM étant dominante, cet effondrement implique toujours la présence de DM. Pourtant, les baryons peuvent échapper à ce processus dans les objets trop peu massifs, incapables de dominer la pression baryonique. Au-dessus de $(10^6 - 10^7)$ masses solaires, les baryons sont présents, mais on s'attend à des objets sombres aussi légers que 10^{-6} masses solaires. La formation des structures est un problème non-linéaire, dont le meilleur traitement est celui des simulations à N-corps.
La DM se distribue de forme diluée, dans des halos qui contiennent les galaxies et amas de galaxies. Ces halos sont sphériques en première approximation. Le modèle standard de halo est décrit par un profil de densité dit de Navarro-Frenk-White (NFW) et une distribution de vitesses Maxwellienne. La densité locale de DM atteindrait $\sim 0.3\ GeV\ cm^{-3}$, tandis que les vitesses de dispersion et d'échappement locales sont estimées à $220\ km\,s^{-1}$ et $(575 - 700) km\,s^{-1}$ respectivement.
Ce modèle est contesté et n'est pas définitif. Le profil de densité peut mieux correspondre à un profil d'Einasto dans les simulations à N-corps, plus plat que celui de NFW au centre du halo ; tandis que les courbes de rotation indiquent que les galaxies naines ont des profils de densité encore plus plats. Des études récentes suggèrent que la densité locale semblerait être plus importante que les estimations standard, plutôt autour de $(0.38 - 0.43) GeV\ cm^{-3}$. D'autre part, les vitesses pourraient avoir une distribution assez différente d'une Maxwellienne, avec des dispersions non isotropes. Le halo canonique est toujours utilisé, mais il faut tenir compte des déviations, au moins en tant qu'incertitudes, lors des interpretations des observations et des prédictions théoriques.

Deuxième Partie : Particules de Matière Sombre : modèles et contraintes (Résumé)

Chapitre 4 : Contraintes Cosmologiques et d'Astroparticules (Résumé)

Parmi les processus bien établis en comologie on retrouve la synthèse primordiale des éléments et le CMB. Le premier cas s'agit d'une chaîne de réactions nucléaires qui commencent à des températures d'environ 100 MeV, après le découplage des neutrons du plasma à des températures d'environ 86 keV, moment qui marque le début de la formation de deutérieum. La proportion de neutrons donne la proportion de noyaux d'Hélium par rapport à l'Hydrogène. Bien que la correspondance entre les prédictions et l'observation est infructueuse pour le Lithium, l'accord est remarquable pour le reste des éléments légers. Il est donc essentiel de ne pas perturber ce processus par l'injection d'énergie lors du découplage chimique de la DM au moment de la nucléosynthèse. En général nous prenons la précaution d'exiger que le FO de la DM arrive avant le découplage des neutrons. Dans le CMB peut être observé le spectre de masse primordial ainsi que les perturbations introduites au moment du découplage cinétique de la DM. Si la DM est relativiste à cette transition, les petites fluctuations seront lavées, ce qui ne pourrait pas expliquer l'existence de galaxies, les plus petites structures observées. C'est pourquoi la DM doit découpler dans le régime non-relativiste (pour la CDM), ou au plus quasi-relativiste (pour la DM tiède, ou WDM).
En ce qui concerne la DD, le taux d'évènements de reculs nucléaires dépend de la section efficace d'interaction, de la densité locale de DM, du type de milieu dans lequel les interactions se passent (notamment des noyaux mis en jeu et de leur densité), de la distribution de vitesses de la DM au niveau de la terre (qui donne lieu à des signaux modulés par le mouvement de la terre autour du soleil, ou asymétriques par le mouvement du soleil dans la galaxie cherchés en particulier par les expériences de détection directionnelle), et de la réponse du détecteur. Les évènements sont attendus juste au dessus du keV pour des WIMPs, ce qui oblige à un traitement très pointu du seuil d'acceptation à basse énergie. En particulier, il semble impossible de voir des évènements issus de particules de masses en dessous de $\sim 5\ GeV$. Les résultats sont interprétés en termes de limites supérieures pour la section efficace pour une masse de DM donnée dans le cas de résultats négatifs, ou en termes d'un contour de pos-

sibilités de sections efficaces et masses dans le cas de résultats positifs. Les expériences DAMA et CoGeNT ont des résultats positifs, et voient de signaux modulés, qui pourraient être interprétés comme de la DM. Par contre, CDMS-II, Edelweiss, et particulièrement XENON100, ne montrent pas de signal et mettent des limites très contraignantes, au dessous des régions préferrées par DAMA et CoGeNT.
En termes de détection indirecte, les produits issus d'annihilation de DM sont cherchés sous forme de rayonnement γ ou de flux de rayons cosmiques, en particulier d'antimatière, puisque ces annihilations ne génèrent pas, en principe, d'assymétrie particule/antiparticule. Pour les photons, le flux reçu dépend du carré de la densité locale de DM sur la ligne de visée, de la section efficace d'annihilation et du spectre généré. Les particules d'antimatière sont plus difficiles à traiter, puisqu'elles voyagent dans le milieu interstellaire avant de parvenir sur terre. La propagation est un sujet très incertain dû à la méconnaissance du champ magnétique traversé par les particules, entre autres. Les meilleures contraintes sont celles des photons venant des galaxies naines orbitant la Voie Lactée, car ce sont des objets très dominés par la DM, dont certains sont en plus dans des régions du ciel dépourvues du fond émis par le disque galactique et en particulier par le centre de la galaxie.

Chapitre 5 : Contraintes de Physique de Particules (Résumé)

Le SM décrit les interactions électrofaible et forte, ainsi que le spectre de particules observées jusqu'à présent dans toutes les expériences de physique des particules. La matière est décrite par des champs fermioniques et se divise en deux types : les leptons, interagissant faiblement et de charges entières, et les quarks, interagissant faible et fortement, colorés et de charges fractionnelles. Les interactions sont assurées par les bosons de jauge, le photon, médiateur électromagnétique, les bosons faibles Z et $W^{\pm}$, et les huit gluons assurant les interactions fortes. Le mécanisme de Higgs explique l'origine des masses des particules, et prédit l'existence du boson de Higgs, la seule particule du SM non-observée jusqu'à présent. Les états de masse des quarks ne correspondent pas à leurs états propres électrofaibles. Par ailleurs, ce ne sont pas des états libres dans la nature et ne se trouvent que confinés dans des baryons (protons et neutrons), i.e. des états liés de trois quarks, et les mésons, des états liés de deux quarks.
Le SM est très performant, et la place pour de la nouvelle physique aux échelles déjà explorées est très restreinte. Les recherches de nouvelles particules mettent des limites sur les masses des états cherchés. Par exemple, le boson de Higgs du SM doit être plus lourd que 114.4 GeV. Tout modèle allant au-delà du SM et comprenant le mécanisme de Higgs doit donc respecter ces recherches et des limites équivalentes. De même pour toute autre nouvelle particule. En particulier, la masse des partenaires supersymétriques des quarks-top doivent être plus lourdes que ~ 500 GeV, d'après les résultats les plus récents du LHC. D'autres ob-

servables sont aussi contraintes par les mesures expérimentales. Dans le secteur électrofaible, la désintégration du boson Z en particules invisibles est très bien connu et est en très bon accord avec les trois familles de neutrinos, ce qui contraint les couplages de nouvelles particules neutres et légères au Z, ce qui s'applique notamment aux particules de DM légère. Dans le secteur des mésons, les oscillations et désintégrations rares, effets à boucle résultant du mélange dans le secteur des quarks, sont des cas très prometteurs pour l'apparition de nouvelle physique, où les contributions attendues peuvent être du même ordre que celles du SM.

Chapitre 6 : Modèles supersymétriques (Résumé)

SUSY est la plus populaire des théories au-delà du SM (BSM). Elle consiste en l'incorporation d'un opérateur quantique de spin 1/2 assurant la transition d'états bosoniques en états fermioniques et vice-versa. Ainsi, toutes les particules du SM auraient leur partenaire supersymétrique. Cette nouvelle symétrie est sévèrement brisée dans la nature, puisqu'aucune correspondance de ce type n'est observée chez les particules connues. Ceci élève le rang de masses des particules supersymétriques au moins aux alentours de l'échelle électrofaible. Ainsi, le lagrangien est divisé en une partie qui conserve la supersymétrie et une partie qui la brise explicitement. La théorie contient une symétrie supplémentaire, donant lieu à la R-parité. Si celle-ci est conservée, alors la plus légère des particules supersymétriques doit être stable. C'est donc un moyen de prévoir un candidat de DM.
La réalisation la plus simple de SUSY est le Modèle Standard Supersymétrique Minimal (MSSM). Il consiste en une supersymétrisation du SM où chaque particule acquière un superpartenaire. Ainsi sont générés les squarks gauches et droits et sleptons gauches droits, toutes des particules scalaires, superpartenaires des quarks et leptons ; et les jauginos de spin 1/2, superpartenaires des bosons de jauge. Les masses sont générées grâce à un mécanisme de Higgs avec deux doublets, qui donnent lieu à un spectre de particules de Higgs : deux scalaires et un pseudoscalaire neutres, et un couple de Higgs chargés. Les champs supersymétriques des champs de Higgs génèrent à leur tour des higgsinos. Les paramètres sont nombreux. Parmi les plus importants pour la phénoménologie à l'échelle électrofaible on compte le rapport des valeurs d'espérance de vide des deux doublets de Higgs, le terme de masse des Higgs et higgsinos μ, les masses du pseudoscalaire, des squarks et des sleptons et les masses des jauginos. Le mélange des jauginos et higgsinos neutres donnent lieu aux neutralinos, dont le plus léger est un candidat de DM. Sa nature est dominée par le plus léger parmi les jauginos et higgsinos, ce qui a des conséquences sur ses couplages. En dessous de 100 GeV, le neutralino doit être dominé par le bino, les autres jauginos étant plus contraints. Le neutralino est aussi un candidat dans le NMSSM, une extension du MSSM. Le MSSM n'a pas d'explication pour l'échelle du paramètre μ. Ce paramètre peut acquérir naturelle-

ment une valeur correcte par l'introduction d'un champ scalaire supplémentaire, singulet du SM. L'addition de ce scalaire est la différence entre le MSSM et le NMSSM. Les bosons de Higgs sont plus grands en nombre et ont une nouvelle composante venant du singulet, et les neutralinos peuvent maintenant être singlino. Comme le singulet n'interagit pas avec le SM, les contraintes sur la masse du Higgs ainsi que bien d'autres sont levées, ce qui ouvre la possibilité de bosons de Higgs très légers ($\ll 100\ GeV$). Les conséquences phénoménologiques sont riches et intéressantes, notamment pour les neutralinos légers ($\ll 100\ GeV$).

Chapitre 7 : Candidats de Matière Sombre Scalaire (Résumé)

Les scalaires sont une façon novatrice d'expliquer la DM. On introduit ici de nouvelles particules, des scalaires, couplées aux fermions du SM et à de nouveaux fermions via des couplages de Yukawa. Ces nouveaux fermions partagent la plupart des caractéristiques des fermions du SM. Une parité conservée (comme la *R*-parité en SUSY) assure la stabilité des particules les plus légères, que nous supposons sont les scalaires. Ceux-ci sont aussi neutres et sans couleur, et constituent ainsi des candidats de DM.
Les particules scalaires peuvent obtenir une densité relique acceptable pour des masses plus petites que les fermions, ce qui ouvre la possibilité d'avoir de la DM plus légère que le GeV. On s'intéresse en particulier aux possibilités de grands couplages des scalaires aux quarks, ce qui serait visible au LHC. Ceci impose des contraintes sur la masse des scalaires :$1\ MeV \lesssim m_S \lesssim 135\ MeV$. Cet intervalle est choisi pour ne pas perturber la nucléosynthèse primordiale d'un côté, et pour que le FO ne dépende pas des interactions entre scalaires et mésons pi (le plus léger des mésons) de l'autre. Les interactions avec les leptons chargés sont contraintes par les moments magnétiques anomales. Par contre, la raie à 511 keV provenant du centre galactique peut être expliquée par les annihilations en électrons et positrons, mais pour des sections efficaces trop petites pour achever une densité relique correcte via ce canal. On assume donc que la densité relique est obtenue par les échanges avec les neutrinos. Accessoirement ceci expliquerait la masse des neutrinos par des effets de boucle.
Ainsi les interactions avec les quarks sont peu contraintes. Les nouveaux vertex introduisent deux couplages de Yukawa, que l'on peut supposer unifiés pour les quarks, mais qui sont différents de ceux des neutrinos et leptons chargés. La masse des nouveaux fermions, ainsi que la masse des scalaires complètent les paramètres libres des interactions entre quarks, scalaires et nouveaux fermions. Ces nouveaux fermions sont colorés et chargés, ce qui impose des limites sur leur masse : elle doit être plus lourde que $\sim 250\ GeV$. Le fait qu'ils soient colorés implique aussi que ces fermions sont couplés aux gluons, couplage déterminé par les interactions fortes.

Troisième Partie : Analyse Phénoménologique et d'Astroparticules de la Matiére Sombre Légère (Résumé)

Chapitre 8 : Exploration de l'espace des paramètres (Résumé)

L'espace des paramètres dans le MSSM et le NMSSM est multidimensionnel, les configurations à neutralinos plus légers sont de moins en moins probables pour des masses de neutralinos de plus en plus légères. C'est pourquoi j'ai implémenté un code d'exploration [2], dont la stratégie est basée sur l'utilisation d'outils numériques, tels que micrOMEGAs, SuSpect et NMSSMTools. Ce code est une simulation Monte-Carlo à Chaînes de Markov (MCMC) qui génère une série de points (une collection de paramètres libres) évalués sur leur correspondance avec les configurations recherchées (point à solution physique, avec un neutralino comme particule la plus légère du spectre) et sur leur respect des limites et contraintes de cosmologie et de physique des particules (la densité relique des neutralinos est en accord avec la limite supérieure établie par la densité de DM observée, masses de nouvelles particules, effets électrofaibles, effets dans la physique des mésons B). Ainsi, une fonction de prior (correspondant aux attentes théoriques) et une fonction de vraisemblence (associée aux données expérimentales) servent à discriminer les points et leur donnent un poids total qui les caractérise. Un processus d'itération aléatoire basé sur un algorithme de Metropolis-Hastings assure une exploration efficace, ne gardant que les points les plus performants vis-à-vis des contraintes qu'on leur impose.

A chaque fois qu'un point est trouvé et gardé, des données sont générées. Parmi celles-ci on compte les paramètres libres du point, les masses des particules importantes (notamment des bosons de Higgs, de la deuxième particule la plus légère, entre autres), les composantes du neutralino le plus léger, la densité relique des neutralinos, les sections efficaces de collision élastique entre les neutralinos et les quarks (relevantes pour la DD), la section efficace d'annihilation aux vitesses galactiques, et les spectres de photons γ, positrons et antiprotons issus de ces annihilations. La plupart de ces données sont facilement obtenues à l'aide de micrOMEGAs. Ainsi, l'analyse de données est facile à effectuer, d'une part pour bien

comprendre les configurations trouvées, et d'autre part pour comparer leurs prédictions aux données expérimentales. Il est donc possible d'évaluer facilement si des configurations sont compatibles avec les signaux de DD de DAMA et CoGeNT, de contraindre les points avec les limites de XENON100 en DD et Fermi-LAT en ID, ainsi qu'évaluer l'impact de résultats récents du LHC comme ceux de CMS, LHCb ou ATLAS, et finalement de projeter la portée des expériences à venir, telles que celles de détection directionnelle.

Chapitre 9 : Recherches de neutralinos légers (Résumé)

Ce chapitre montre les résultats obtenus dans les recherches de neutralinos légers à l'aide du code introduit au chapitre précédent, et présentés en [2, 3, 4].
Dans le MSSM il est très difficile de générer des points avec des neutralinos plus légers que 15 GeV. On en trouve de deux sortes. D'une part, des neutralinos obtenant leur densité relique en s'annihilant à travers l'échange d'un boson de Higgs, et d'autre part, des neutralinos qui l'obtiennent en s'annihilant à travers l'échange d'un slepton. Les poids des points à échange de Higgs n'est pas très élevé, ce qui montre qu'il y a toujours un ou plusieurs critères de discrimination qui n'est pas bien accompli. En particulier, la physique des mésons B en est en grande partie responsable. L'analyse des configurations en termes des paramètres relevants pour la physique du boson de Higgs montre que les points du premier groupe sont en conflit avec les résultats les plus récents montrés par CMS. Ils prédisent aussi beaucoup trop de photons γ provenant de la galaxie naine Draco, la plus contraignante, et sont donc exclus aussi par Fermi-LAT. En termes de DD, les sections efficaces sont presque un ordre de grandeur au-dessous des régions de DAMA et CoGeNT, mais sont bien au-dessus des limites de XENON100. On en conclut que ces points sont très défavorisés. Les poids des points qui échangent des slpetons sont meilleurs, mais montrent qu'ils sont dans la limite de la découverte ou de l'exclusion de la physique des mésons B. Ils sont au-delà des contraintes de CMS et sont bien en dessous des limites de XENON100. Le flux de photons γ, montant à petite masse, atteint la limite de Fermi-LAT aux alentours de $\sim 12.6\ GeV$ (sachant que la plus petite masse trouvée est de $\sim 11\ GeV$). En conclusion, il est impossible d'expliquer les signaux de DAMA et CoGeNT avec des neutralinos du MSSM, et il est très difficile de croire qu'un tel neutralino puisse être plus léger que $\sim 12.6\ GeV$.
En revanche, dans le NMSSM on trouve beaucoup plus facilement des neutralinos plus légers que $\sim 15\ GeV$ et jusqu'au GeV. En effet, ici le mécanisme pour obtenir la bonne densité relique est celle de l'échange de Higgs légers via une résonance. Ces Higgs légers, scalaire ou pseudoscalaire, sont principalement constitués de singulets et échappent donc un bon nombre de contraintes applicables au MSSM. Le poids caractéristique de ces points est bien meilleur et presque idéal. Les résonances donnent lieu à des sections efficaces d'interaction dans un vaste intervalle de valeurs. Dans le cas des annihilations galactiques, l'échange résonant de

Higgs pseudoscalaires est favorisée et donne lieu à des flux de rayons γ très importants, exclus par Fermi-LAT, alors que les échanges de scalaires sont supprimés à petite vitesse. En ce qui concerne les interactions élastiques indépendantes du spin, ce sont les échanges de Higgs scalaires qui donnent lieu à de grandes sections efficaces, alors que les interactions via des pseudoscalaires sont supprimées. Ceci implique que quelques points, dont les couplages sont aussi maximisés, tombent dans les régions de CoGeNT et DAMA, alors qu'encore plus de configurations sont au-dessus des limites de XENON100. Par contre, la plupart des points ne sont ni dans l'un ni dans l'autre des cas, et échappent aux contraintes de physique des astroparticules. Cette phénoménologie riche est donc viable et doit être testée par d'autres moyens.

Chapitre 10 : Expériences de détection directionnelle et neutralinos (Résumé)

Les projections des collaborations en train de développer les futurs détecteurs directionnels de DM sont confrontées ici aux prédictions issues du MSSM et du NMSSM, grâce à l'application du MCMC. Ces projections visent à établir des sensibilités aux sections efficaces dépendantes du spin entre protons et WIMPs quelques ordres de grandeur en dessous des limites actuelles. Ces expériences pouvant capter une information sur la vitesse relative des particules de DM peut donner une piste assez précise de la masse et de la section efficace, en cas de détection d'un signal. Ainsi, ces projections donnent lieu à trois régions dans le plan des sections efficaces par rapport à la masse de la DM : une région de découverte, une région d'exclusion et une région d'insensibilité.
Des explorations plus vastes des possibilités de neutralinos allant jusqu'à $\sim 600\ GeV$ ont été effectuées pour établir les régions de l'espace des paramètres que ces expériences pourraient atteindre. Pour des neutralinos plus lourds que $30\ GeV$, les deux modèles sont très équivalents et ne se distinguent presque pas. Beaucoup de neutralinos pourraient être vus par ces détecteurs, et même découverts (leur masse et section efficace pouvant être déterminée). Pour les grandes masses, ceci n'est possible que jusqu'à $\sim 200\ GeV$, car la section efficace chute avec la masse de la DM. Par contre la limite d'exclusion coupe l'espace des paramètres pour des neutralinos jusqu'à $\sim 600\ GeV$. Dans les deux modèles, la plupart des neutralinos plus légers que $\sim 30\ GeV$ seront détectables. Vu que le principal canal pour ces collisions élastiques est l'échange d'un boson Z et que le couplage des neutralinos à celui-ci dépend du paramètre μ, c'est ce paramètre qui serait le plus facilement déterminé en cas de découverte. Mais le résultat le plus important de cette étude est l'évidente complémentarité des différentes techniques : DD, ID et détection directionnelle sont sensibles à des configurations différentes, et pas de contraintes d'un côté ne signifie pas du tout qu'il n'y en a point de l'autre. Ceci invite à mettre en relation ces résultats dans l'avenir, ainsi qu'avec ceux issus des collisionneurs.

Un article sur cette étude est en préparation.

Chapitre 11 : Matière Sombre scalaire légère dans les collisionneurs de hadrons (Résumé)

Dans ce chapitre sont étudiées les conséquences du modèle introduit au chapitre 7 dans la physique des collisionneurs, résultats présentés dans [1]. Les interactions entre quarks peuvent donner lieu à la création de paires de nouveaux fermions colorés F suite à l'échange de scalaires dans une voie t ou u. Une paire de F peut aussi être produite par fusion de gluons, dans une voie s via l'échange d'un gluon ou via une voie t ou u via l'échange d'un F. Finalement, des quarks peuvent échanger un gluon et générer une paire de F aussi. Des évènements à un F et un scalaire sont aussi possibles par des collisions gluon-quark par l'échange d'un quark en voie s ou d'un F en voie t. La génération de deux scalaires est moins intéressante puisque la signature ne correspondrait qu'à de l'énergie manquante. La section efficace de ces processus est d'autant plus importante que les F sont générés avec juste leur énergie de masse, ce qui est d'autant plus probable que les F sont légers.
En explorant les sections efficaces à l'aide de CalcHEP pour des combinaisons de masses, énergie de collision, configuration hadronique et couplages, des prédictions ont été données pour le Tevatron et pour le LHC. Avec les résultats pour le Tevatron, bien qu'une étude dédiée à ce modèle n'existe pas, on peut contraindre la masse des F avec les contraintes établies pour le modèle des Leptoquarks, à comportement assez similaire. Ainsi, des masses de F inférieures à $\sim 400\ GeV$ sont très défavorisées. Pour le LHC, nous avons généré des évènements et comparé les distributions cinématiques à celles des fonds les plus puissants, notamment $Z + jets$. Le signal serait assez différent du fond, et en tout cas séparable, quoi qu'il ressemble beaucoup à certaines prédictions de SUSY. On en conclut qu'il est important de mener une étude plus détaillée avec une simulation complète et exhaustive de ces évènements, puisque le LHC a largement le potentiel d'explorer la phénoménologie de ce modèle. En outre, il est aussi important de trouver des moyens d'identifier ces signaux de façon univoque, puisqu'un signal ressemblant à de la SUSY peut facilement correspondre au cas présenté ici.

Conclusion (Résumé)

Le sujet de la DM légère est sans aucun doute un sujet excitant et dynamique. D'après les travaux ici présentés, les neutralinos plus légers que $\sim 15\ GeV$ sont difficilement acceptables dans le MSSM, alors que dans le NMSSM ils sont encore possibles et avec de grands intervalles de masse et de sections efficaces. Puisque ces configurations correspondent à de faibles masses des bosons de Higgs, des signatures particulières à explorer en profondeur peuvent être attendues au LHC.
La DM scalaire à l'échelle du MeV représente une alternative intéressante. Notamment, elle prédit une signature observable au LHC, qui pourrait même imiter un signal de SUSY. Ceci motive des études plus approfondies de ce modèle et de ses conséquences pour la physique des collisionneurs. La DM scalaire légère pourrait aussi jouer un rôle important dans les instants primordiaux, particulièrement dans la nucléosynthèse primordiale, ou dans les explosions de supernovas par leur couplage aux neutrinos.
Le problème de la DM est toujours ouvert. Il est peut-être temps de réviser les hypothèses communément admises, puisque la nature des particules de DM nous échappe, puisque les interprétations de différents résultats expérimentaux semblent se contredire. De nouvelles expériences se déroulent et se conçoivent, des résultats arrivent. Il faut être préparé pour faire une synthèse pointue et inclusive de tous les éléments de ce puzzle, dont nous croyons deviner le paysage.

Bibliographie

[1] Daniel Albornoz Vásquez, Céline Boehm, and John Idárraga. Signature of Sub GeV Dark Matter particles at LHC and TEVATRON. *Phys.Rev.*, D83 :115017, 2011.

[2] Daniel Albornoz Vásquez, Geneviève Bélanger, Céline Boehm, Alexander Pukhov, and Joseph Silk. Can neutralinos in the MSSM and NMSSM scenarios still be light ? *Phys.Rev.*, D82 :115027, 2010.

[3] Daniel Albornoz Vásquez, Geneviève Bélanger, and Céline Boehm. Astrophysical limits on light NMSSM neutralinos. 2011. [arXiv :1107.1614]. Sent to Phys. Rev. D.

[4] Daniel Albornoz Vásquez, Geneviève Bélanger, and Céline Boehm. Revisiting light neutralino scenarios in the MSSM. 2011. [arXiv :1108.1338]. Sent to Phys. Rev. D.

The ant, the spider, and the bee

Those who have handled sciences have been either men of experiment or men of dogmas. The men of experiment are like the ant, they only collect and use; the reasoners resemble spiders, who make cobwebs out of their own substance. But the bee takes a middle course: it gathers its material from the flowers of the garden and of the field, but transforms and digests it by a power of its own. Not unlike this is the true business of philosophy; for it neither relies solely or chiefly on the powers of the mind, nor does it take the matter which it gathers from natural history and mechanical experiments and lay it up in the memory whole, as it finds it, but lays it up in the understanding altered and digested. Therefore from a closer and purer league between these two faculties, the experimental and the rational (such as has never yet been made), much may be hoped.

Francis Bacon
Novum Organum (1620)

Introduction

Physics underwent an important revolution during the past century. Fundamental theories were established that allowed to understand and describe the world of elementary constituents of matter and their interactions as well as the Universe. At this moment we are privileged to witness an outstanding parallel development of technology, and the implementation of remarkable experiments such as the Large Hadron Collider (LHC) or the Planck and Fermi satellites.

Indeed, the Standard Model (SM) of Particle Physics has been successfully established in order to explain the particle physics observables. The last of its predictions, the Higgs boson, is currently been searched for at the LHC and remains to be discovered to validate the SM construction. The Universe, in turn, is very well described by the consistent ΛCDM model that explains the genesis of elements, the cosmic background microwave radiation, the formation of large scale structures we observe at all scales, and the expansion of the Universe: the Standard Model of Cosmology, or ΛCDM. However, the nature of most of the constituents of the Universe is still mysterious. Among these we find the Dark Matter (DM) problem. While the elementary properties of the DM are still unknown, conclusive gravitational evidence points towards the existence of new neutral and stable particles. Thus, DM challenges both Particle Physics and Cosmology.

DM was introduced as a concept by Fritz Zwicky in 1933. As an astronomer, he investigated the Coma cluster of galaxies, observing its optical light emission and estimating its dynamics through the Doppler shift of emission and absorption lines. A cluster of galaxies is expected to be a gravitationally bound system of masses moving at non-relativistic velocities. Assuming the equilibrium of the system –or virialization–, it is possible to relate the total mass of the system M, i.e., the sum of all the individual mass points, to the mean square velocity $\langle v^2 \rangle$ and mean inverse distance $\langle 1/r \rangle$ of a point relative to the center of mass of the system. The virial formula thus reads

$$M = \frac{2\langle v^2 \rangle}{G\langle 1/r \rangle},$$

where G stands for the gravitational constant. Zwicky used this formula to relate his observation of velocities and distances to the total mass of the system. He could also estimate the luminous mass, the mass responsible for the emissivity of the system, by counting the

number of apparent galaxies in the cluster. He found that the luminous mass was more than a hundred times smaller than the virial mass. His findings lead him to introduce the necessity for some dark matter, i.e., a mass component which does not emit any visible light. While the method used by Zwicky to determine the non-luminous mass of a cluster of galaxies or an individual galaxy by measuring its rotation curve is still valid and still in use, the concept of DM has evolved since those early conceptions.

It is now widely accepted that there is a universal mass component manifesting itself through gravitational effects but not through electromagnetic interactions. A large fraction of the Universe energy budget must respond to this fundamental characteristic. Among the first particle candidates to explain the DM were neutrinos. However, it has been shown that the three generations of neutrinos cannot account for all of the DM in a standard Cosmology. Dark baryonic objects were also claimed to contribute to the DM component. However the baryonic fraction of matter, which has been independently estimated by means of the primordial nucleosynthesis, is too small to account for all the matter density in the Universe. Indeed, the fraction of baryons to the total matter is only about a fifth or sixth.

Since the present observed effects accounting for DM are only gravitational, the possibility of modifying gravity has been proposed. While phenomena such as structure formation or gravitational lensing can still be partially explained by such theories, they appear extremely complex and are expected to be challenged by the forthcoming results from the Planck experiment. In fact, even the most sophisticated approaches that have attempted to modify the general theory of relativity fail to give a description of the Universe without a DM component.

Hence, hints rather point towards the necessity of introducing new species of particles, yet to be described by a fundamental particle theory. These particles would be present nowadays in galaxies and galaxy clusters. This picture motivates the underground shielded experimental searches for DM collisions with nuclei (the Direct Detection technique (DD)) and the observation of their annihilation products in our galaxy and beyond (the Indirect Detection technique (ID)). Both of these techniques have shown very interesting results lately: unresolved background collisions in DD experiments could be explained by DM interactions with nuclei, while excesses (with respect to the astrophysical background) in antimatter and photon signals have been reported and might also coincide with the DM hypothesis. Furthermore, the DM is a key ingredient in the formation of large scale structures. The energy density of the Universe has to match the apparently flat spacetime in which we dwell. In particular, its matter component must be made of much more mass than the baryonic matter provides.

The SM failing to give a complete explanation to the particle physics phenomena and to provide a successful DM candidate, new theories have been proposed and thoroughly studied since more than three decades. In such theories, new fields and particles are introduced, and

some of them contain at least one particle accounting for the DM component of the Universe. The LHC is expected to probe these theories at the electroweak scale.

This work is inspired by this context, by this cross road between a description of the Universe and the understanding of its elementary constituents, and by the exciting possibility of probing the next generation of theories by the current generation of experiments. The point of view that we adopt is that of phenomenological studies. We reduce theories to models and study their plausibility and predictions regarding experimental results, we interpret experimental results in order to shed light on this dark constituent of our Universe. The investigations presented hereafter are devoted to study models of DM in a certain mass range pointed out by both DD and ID experimental results and subsequently state predictions for forthcoming observations and detections.
The research carried out throughout these three years yielded important results. Scalar DM candidates are a successful explanation of the DM problem, challenging the standard candidates with its MeV scale mass. In [1] it was shown that the possibility of such scalar particles being coupled to quarks implies the existence of new colored fermions which could be copiously produced at the LHC. Moreover, their signature would be very similar to canonical expectations from Supersymmetry (SUSY) –the preferred theory to expand the description of elementary particle physics–, which calls urgently for model-disentangling techniques. In the scope of SUSY and in the context of $(6-12)$ GeV DM particles being possibily observed at DD experiments, I developed a numerical analysis devoted to study the possibility of light neutralinos. It consists on an random walk algorithm that searches for parameter configurations in a minimal model and a non-minimal model of SUSY, integrating all particle physics constraints and testing the neutralino as a DM candidate. The results are very encouraging: while the minimalistic supersymmetric configurations with neutralino DM are very constrained, non-minimalistic scenarios could indeed generate neutralinos with the right interaction rate and mass in order to explain the effects observed in DD experiments [2]. These successful configurations were further studied using ID: astrophysical and astroparticle observables were computed and compared to experimental results [3]. Finally, the original numerical tool was improved and the analysis was enlarged in the scope of minimal models, yielding lighter neutralinos than what was previously found, however, ruling out more scenarios by the application of astrophysical and astroparticle limits [4]. Other applications of this code are in development, and its contents are being constantly updated with new results from the LHC.

The scope of this report is to adopt the particle DM hypothesis, to review its main features, to delineate its possibilities and to explore candidates of supersymmetric nature and of relatively light masses. Hence, we start by describing the DM problem in Part I, where we

give a review for evidence of the existence of DM, we set the cosmological framework in which we work and describe the history of DM from the Early Universe (EU), to the formation of structure and up to the current distribution of the DM in haloes. Then, in Part II, we go through the important Cosmological, Astroparticle and Particle Physics constraints to particle DM candidates and subsequently introduce models providing relatively light DM candidates, models of standard supersymmetric nature such as the Minimal Supersymmetric Standard Model (MSSM) and the Next-to-MSSM (NMSSM) with neutralino DM, and beyond $N = 1$ SUSY in a light scalar DM scenario inspired in $N = 2$ SUSY. Finally, in Part III we present the findings of the investigations carried out: we describe a numerical tool developed to scan the multidimensional supersymmetric parameter space, then we present an application of this tool to the search of light neutralino configurations in the MSSM and NMSSM as well as an application to the search for neutralino DM in directional detectors, and finally we discuss possible signatures of light scalar DM scenarios at the LHC.

Bibliography

[1] Daniel Albornoz Vásquez, Céline Boehm, and John Idárraga. Signature of Sub GeV Dark Matter particles at LHC and TEVATRON. *Phys.Rev.*, D83:115017, 2011.

[2] Daniel Albornoz Vásquez, Geneviève Bélanger, Céline Boehm, Alexander Pukhov, and Joseph Silk. Can neutralinos in the MSSM and NMSSM scenarios still be light? *Phys.Rev.*, D82:115027, 2010.

[3] Daniel Albornoz Vásquez, Geneviève Bélanger, and Céline Boehm. Astrophysical limits on light NMSSM neutralinos. 2011. [arXiv:1107.1614]. Sent to Phys. Rev. D.

[4] Daniel Albornoz Vásquez, Geneviève Bélanger, and Céline Boehm. Revisiting light neutralino scenarios in the MSSM. 2011. [arXiv:1108.1338]. Sent to Phys. Rev. D.

I

THE DARK MATTER PROBLEMATIC

1 Introduction to Dark Matter

1.1 Evidence of the existence of Dark Matter

We present some examples of evidence for DM. This is not meant to be an exhaustive list, but is just a sufficient sample of arguments to motivate the search for DM.

Critical energy density in the expanding Universe

The observation of the Cosmic Microwave Background radiation (CMB), and in particular, of its anisotropies, gives precious information about the total energy budget of the Universe. Indeed, they are an imprint of the matter fluctuations at the matter-radiation decoupling time. The analysis of the anisotropy multipoles, and in particular, the position of the main peak in Fourier space, suggest that the energy density of the universe is the critic density, that is to say, the energy density of a flat universe [1]. The Universe dynamics can be studied by measuring the expansion rate, which in turn needs the observation of velocities of objects at different scales, which means estimating the distance. The Supernova Cosmology Project and the High-z Supernova Search Team independently observed type Ia Supernovae, used as standard candles –thus the measure of luminosity is a measure of the redshift– for a large range of redshifts [2, 3]. Assuming a flat universe they showed the need of a cosmological constant –or equivalent component– and measured the matter fraction to be $\Omega_M \simeq 28\%$. Part of it is baryonic, some of it is DM. This means, in particular, that the universe is not solely constituted of matter (and a negligible contribution of radiation), but it also shows that the matter component is important.

Measuring the baryon density with X-rays

Assuming that the virialized systems are representative of the matter to luminosity ratio of the Universe it was shown that $\Omega_M \simeq 15\%$ by estimating the total luminosity of the Universe [4]. But also an estimate of the baryon to dark ratio can be estimated in such systems. Indeed, X-rays are produced by baryonic collisions. By estimating the temperature of gas clouds containing baryonic matter and measuring the X-ray luminosity, the baryonic density can be estimated. But the baryons are in hydrostatic equilibrium with the surroundings. The

study of this equilibrium relates the total and baryonic matter densities at a certain position in the system. By these means, and extrapolating the obtained ratio to be universal, it can be estimated that $\Omega_B/\Omega_M \simeq 10\%$ [5]. Dark Matter would thus be the dominant component of the matter content of the Universe.

Gravitational lensing

Gravitational lensing is another powerful tool to measure the matter content of an object (see [6] for a review on the subject). Gravity causes the curvature of spacetime, and light propagation following geodesics can thus describe curved trajectories. By observing deflection of the light from distant objects experiencing the screening of a foreground system, the mass accounting for the total deviation can be determined. Moreover, the weak lensing technique provides a tool to analyze a large number of systems and infer its mass distribution. It consists in the determination of the deformation of the background object apparent image after deflection. By statistical analysis of data, matter distribution can be derived and be compared to the foreground object emitting matter. Again, these studies confirm the existence of non-luminous matter.

The bullet cluster

Perhaps the most striking astrophysical evidence for non baryonic DM is the so called bullet cluster [7]. It consists of the double galaxy cluster 1E0657-558, which is believed to be the resulting collision of two individual subclusters. Clusters are made of galaxies, of hot baryonic gas and hypothetically of DM[1]. While galaxies are shown to be distributed in two well separated regions accounting for each of the subclusters, the hot gas, measured by its X-ray emission, lies in between the two systems. Clusters being diluted objects, the dense galaxies have little probability of colliding and thus are not affected by the collision of clusters. The hot gas interacts electromagnetically and by this friction is slowed down. Finally, making use of the lensing technique, the mass distribution of the system has been measured, showing that the dominant component follows the stars and not the dust, strongly favoring the presence of cold, collisionless DM. Moreover, the ratio of hot gas mass to total mass was estimated to be $1/6$, in very good agreement with the best estimations of the Ω_B/Ω_M ratio of the matter of the Universe.

Structure formation

Finally, let us briefly discuss the formation of structures. Structures have formed by gravitational collapse acting in opposition to the expansion of the Universe. This collapse is different for baryonic matter and DM, since the former –made essentially of electrons and

[1] Models of modified gravity can give an alternative explanation to this phenomenon [8].

protons– is electromagnetically interacting and thus has a non negligible pressure against collapse. The matter power spectrum can be deduced from the CMB. At that time structures did not exist, hence it is from that power spectrum that the bounding of a local amounts of matter started. If such power spectrum was made purely of baryonic matter, then forming structures fails because of the baryonic pressure. Therefore, the amount of DM in the matter power spectrum has to be sufficient to create large enough gravitational fields in order to overcome the baryonic pressure, and thus eventually allow the formation of stars, galaxies and clusters. Moreover, the comparison of the extraction of the matter power spectrum from the CMB to the surveys of large scale structures sets the amount of DM needed in the matter power spectrum. This amount is in a remarkable agreement with the other techniques giving estimations of the baryonic to dark ratios.

The measured Dark Matter density

The best estimation of the DM density comes from the thorough study of the CMB, for which the best results available are those of the 7-year results from WMAP [9]. Assuming ΛCDM to be a correct description of the Universe, all the information is then contained in the CMB in order to determine Ω_{CDM}. For example, by relating the CMB information about the radiative and massive energy density to the dynamical theory of primordial synthesis of elements, the CDM abundance can be disentangled from the baryon density. Furthermore, the current results from the WMAP satellite allow to estimate the abundance with a precision of $\sim 5\%$. The determination of Ω_{CDM} is the result of a likelihood analysis that fits all the parameters of the ΛCDM model. Thus it has been determined that $\Omega_{CDM}h^2 = 0.1120 \pm 0.0056$ –where h^2 is the Hubble parameter measuring the expansion rate in units of $100 km\,s{-}1\,Mpc^{-1}$– from which it is deduced that $\Omega_{CDM} \simeq (22.8 \pm 2.7)\%$. The Planck satellite is expected to further reduce the error band.

There is a large variety of evidence pointing towards the existence of DM. Actually, Cosmology is nowadays able not only to demonstrate the presence of heavy neutral and non-baryonic particles, but to measure its relative abundance with high precision, and constrain several of its characteristics.

1.2 Cosmological framework

1.2.1 ΛCDM: the concordance model

The Universe has been studied as a physical system since the introduction of the first non-local[2] physical theory, the general theory of relativity. In the framework of general relativity the energetic content of spacetime is related to its geometry through the Einstein equations. Defining an isotropic and homogeneous metric –motivated by the observation of the surrounding universe– and describing the energetic contents of the universe as a fluid with a given energy density and a pressure, the Einstein equations become the Friedmann equations, which described thus the dynamics of the Universe.
The XX^{th} century saw Cosmology turning into a science. In our century it has become a precision science. The discovery of the redshift of extragalactic objects suggested an expanding universe. These dynamics can enter the set of relativistic equations of the universe and set their solutions. The observation of the CMB, a black-body radiation arriving to Earth isotropically, in 1964 by the radioastronomers Arno Penzias and Robert Wilson confirmed an ancient stage of the Universe where the spacetime was filled with an opaque medium where photons could not free stream. Such a plasma is possible if the matter is denser and hotter, allowing electrons to elastic scatter with photons at large enough rates. Actually, the story goes backwards in time: there was a time when the Universe was a hot and dense plasma, time that ended when the density and temperature were low enough for photons to travel freely around. That transition happened, in a simplistic view, at the moment of the last scattering between photons and electrons, $T_{LS} \simeq 3000\,K \simeq 0.25eV$. Before that time, the photons were at equilibrium with a plasma. Hence at decoupling they had a blackbody spectrum peaked at the plasma temperature. After that the free streaming evolution only experienced the expansion of the universe, in a matter dominated stage: the spectrum shape was kept, but suffered from a redshift of order 1100. This gives the measured value of the peak. It was the beginning of a long road that lead to the construction of a concordance model able to explain astrophysical and laboratory data in light of the cosmological evolution. Furthermore, the study of the synthesis of the elements of the universe from an expanding, cooling Universe, initiated in the 1940s by Alpher and Gamow is in very good agreement with the astrophysical abundances observed. Finally, the formation of large scale structures is very well described by an early matter power spectrum which has evolved, in a first approximation, solely under the influence of gravity and the expansion rate after DM decoupled from other species.
The concordance model regrouping the coherent explanation of these phenomena is called ΛCDM or Standard Model of Cosmology. Its ingredients are the Friedmann equations with

[2] Non-local meaning here that the equations describing the system are not restricted in spacetime nor in phase space, and can therefore treat any physical point in the Universe. However, the local realization of the theory is, of course, explicitly dependent on the position in spacetime.

no curvature containing radiation, dark dominated matter and a cosmological constant – which origin is yet very obscure, efforts try to explain this component by introducing the so called Dark Energy. An early stage of inflation is also needed in order to account for fluctuations observed in the CMB and the large structures: a very accelerated expansion would have captured quantum fluctuations of a quantum fundamental size at the beginning of inflation, and translate them into energy density inhomogeneities at the end of inflation. Hence, inflation provides a matter power spectrum that can reproduce both the CMB anisotropies and the formation of structures as the Universe cooled. It is not our purpose to give a full review of the SM of Cosmology, neither is it to describe all the alternatives to it. This work is devoted to investigate the DM problem as a particle physics problem within ΛCDM. Nowadays the ΛCDM model is presented in textbooks such as [5, 10] and is broadly recognized as the best model for Cosmology so far, although it has important challenges to tackle, namely, the nature of the DM component. The DM is needed to be the dominant component of the matter in the Universe; it is preferably Cold DM (CDM), that is, it would decouple from SM particles at non relativistic stages in order to generate a suitable power spectrum for structures to form.

1.2.2 The Dark Matter decouplings

ΛCDM implies a hot thermal bath at early stages. The DM would have been present in such a bath. Interactions between particle DM and SM particles would ensure the DM thermal and chemical equilibrium at sufficiently high temperatures. We can follow the DM throughout the expanding EU, from its equilibrium state to its chemical and kinetic decouplings from the thermal bath.

Let us follow the useful description of the characteristic times of DM particles in the thermal bath given in [11]. An interacting particle –or species– can be characterized by its interaction radius. It represents the maximal distance between such a particle and any of its targets allowing an interaction to occur. It quantifies the strength of the interactions between the particle and the surrounding particles of the thermal bath. When divided by the mean velocity one obtains the interaction –or collision– time. If the typical distances between particles in the thermal bath are always larger than the interaction radius, if the thermal bath is too diluted to transgress this radius with a statistically important frequency, then the particle is decoupled from the thermal bath. We thus expect it to free stream, and its total number should be unchanged. This time scale should thus be compared to the time between two subsequent collisions, representing the probability of interaction. It is the ratio of the mean free path of the particle to its mean velocity. The simple consideration of a gaseous state leads us to establish that the collision time is smaller than the mean time between two subsequent collisions. Otherwise particles would form bound states. Then, we can define two different equilibrium time scales. Local equilibrium is quicker to attain as compared to global equilib-

rium. Indeed, if the Universe experiences fluctuations in density and temperature, then it is probable that some denser regions could be in local equilibrium while more diluted regions could fall out of equilibrium. The relaxation time defines the time needed to establish local equilibrium. If no region of the universe presents the conditions needed to establish local equilibrium for a time longer than the relaxation time, then there is no region in the Universe where equilibrium is represented. Finally, global equilibrium needs local equilibrium to propagate and thus transmit local equilibrium in a patch of spacetime to the neighbouring regions. This time is obviously larger than the relaxation time.

In the paradigm of an expanding and cooling Universe, all time scales depending upon the thermal bath characteristics, namely its composition, density and temperature, evolve with time. Whereas we expect the interaction time scale to be established by fundamental particle physics. Assuming that at large enough temperatures the global equilibrium time scale was small compared to the expansion rate, then particles are at equilibrium with the thermal bath. Annihilation into particles from the thermal bath is compensated by the reverse interactions in what is called the detailed balance in kinetic theory. The total number of particles is roughly maintained and their mean velocity is set by the temperature of the plasma. As the thermal bath cools down, mean velocities decrease and the volume is diluted. When particles attain the non relativistic regime, which happens roughly at temperatures of the order of $m/25$ to $m/10$ for CDM, then the equilibrium distribution is Boltzmann –i.e. exponentially– suppressed and the number of particles drops rapidly. The mean velocity slowing down, the collision, relaxation and equilibrium time scales grow. Also, particles in the thermal bath start statistically lacking the energy required to produce DM particles. When the interaction rate is sufficiently lowered by the dilution of DM particles and falls below the expansion rate of the Universe, the suppression stops and the number of DM particles is thus stable again. This is chemical decoupling. Because of the exponential nature of the Boltzmann suppression, this transition is extremely quick: usually the out of equilibrium transition is immediately followed by the particle number freeze out. This sets the amount of DM particles present nowadays in the Universe, which should match the measured value.

The local thermal equilibrium does not depend upon the density of DM particles, but on the density of the thermal bath. The elastic scattering rate is the product of the gas density to the interaction cross section, and thus evolves as the number density of the bath –which has not experienced a Boltzmann suppression–, or the inverse of the Universe volume. With decreasing temperature, at some point the interaction rate becomes smaller than the expansion rate and thus the collisions stop. However, local equilibrium can be lost before, since the interaction rate needed for relaxation is larger than the purely interaction rate, as it was discussed previously. Kinetic decoupling depends upon the moment at which the Hubble time becomes smaller than the relaxation time. Before decoupling the temperature of DM particles is that of the thermal bath, hence relativistic particles still communicate their kinetic

energy to the DM particles. After decoupling it falls quadratically with respect to that of the plasma, simply by the expansion rate of the Universe. The kinetic decoupling transition freezes the influence of interactions on the fluctuations in the distribution of DM. Hence, it is crucial to the final establishment of the matter power spectrum to be injected at the beginning of structure formation.

1.3 A physical overview

1.3.1 Candidates

We have argued that the DM evidence is purely gravitational. Hence either new particles accounting for the DM are introduced, either we need to change the theory of gravitation. At most scales the Newtonian theory is sufficient and accurate. Hence, any attempt to modidy gravity has to include all the well tested gravitational systems, which include the Earth, the Moon rotating around it, our entire solar system and its satellites, to say the least. Such an effort has been carried out and gave birth to the Modified Newtonian Dynamics (MOND) [12]. MOND was introduced to explain the rotation curves of galaxies and clusters, by modifying the very low acceleration behavior of the Newtonian theory. The threshold for this low acceleration regime would be lower than the acceleration stemming from the Sun gravitational field at the Earth position, and thus could not be tested. A relativistic construction which includes MOND at low velocities is TeVeS (the Tensor/Vector/Scalar theory) [13]. While these theories could explain the formation of structures and usual gravitational lensing effects, they usually fail to give a simultaneous solution to all phenomena. Furthermore, they could not explain the bullet cluster without adding rather heavy neutrino-like particles to the system. Even though these efforts are worth the try and are still not ruled out, we take the particle DM hypothesis in the following.
We have presented the ΛCDM paradigm in which the DM is cold. However, a valid alternative is the so called Warm DM (WDM), which would consist of particles decoupling at quasi-relativistic velocities. WDM is indeed plausible explanation for the DM in agreement with Cosmological and Astrophysical observables. Even though they have been put forward by recent model independent small scale simulations (see [14, 15]), we will not treat this case. We adopt the hypothesis of the standard model of Cosmology stating that the DM is made of neutral, almost collisionless, heavy particles (of masses that usually go from $\sim 100\,MeV$ to the TeV scale), which we will further study by investigating light candidates (of masses $< 100\,GeV$) aiming to account for it.
The SM of particle physics does not provide good candidates to account for these properties. Therefore there must be at least one new particle, a particle beyond the SM (BSM). Various theories have been proposed to extend the SM, and actually, most often independently of the

DM problem. Indeed, while it is very successful in describing standard processes related to the electroweak (EW) and strong interactions, and it is fully self-consistent, it has not been entirely probed. Indeed, all fields in the theory are exactly massless unless one introduces the Higgs mechanism. This elegant solution generates the mass terms of all particles by including a doublet scalar field having a non vanishing vacuum expectation value. The mechanism goes along with the prediction of the Higgs boson which is yet to be discovered in collider experiments. Nevertheless, even if the Higgs mechanism is confirmed, it is not sufficient to explain all masses: neutrinos have been proven to oscillate which implies they actually have mass, while in the SM they are exactly massless. Moreover, the Higgs mechanism does not provide an explanation to the scale of masses of the Higgs boson and of all particles of the SM. Indeed, if the Higgs boson is to account for the masses of particles, then it must be related to the gravitational force. However, its expected mass range is at the scale of EW scale, and not at the Planck scale, which is the scale at which quantum mechanics –hence quantum field theory– meets gravity[3]. Thus, the natural quantum contributions to the Higgs mass, of the order of the Planck mass, have to be cancelled within an extremely fine-tuned renormalization prescription. This is known as the hierarchy problem. Furthermore, there is no experimental evidence for CP violation in the strong interactions sector, while the SM contains terms which should naturally yield such a violation. The unnaturalness of the very small value of the θ angle –responsible for strong CP violation– is a mere observation for which there is no theoretical motivation in the SM. Also, the SM fails to explain the matter anti-matter asymmetry observed at very large scales of the surrounding Universe.

Thus, theories have been proposed to tackle these insufficiencies of the SM. These theories carry with them the existence of new particles and interactions, of physics BSM. They might also provide candidates for the DM. However, the requirements to fulfil are not very easily realized, thus it usually takes particular configurations in these theories in order to account for the DM –and more generally for a consistent Cosmology. DM particles have to be neutral and stable. Their density has to match the WMAP observations –or at least be smaller than the observed value. It has been shown that a neutral particle with EW interactions and with a mass of some $100\,GeV$ would naturally reproduce the right relic density from decoupling from its interactions with the SM particles in EU. It is the so called WIMP-miracle, consisting in the curious match between a Weakly Interacting Massive Particle and the DM.

Some BSM theories provide, indeed, WIMP-like DM candidates, but DM is not necessarily constituted of WIMP-like particles. In BSM theories we may found very well motivated DM candidates for either WIMP-like DM or other DM. An example of a WIMP can be found in the universal extra dimension theories. They imply the existence of a natural parity to be conserved, which in turn gives the suitable stability to the lightest new particle of the spectrum.

[3] Recall that the Planck mass is defined by $m_{Pl}\,c^2 \equiv \sqrt{\hbar c/G} \simeq 1.22 \times 10^{19}\ GeV$, a constant of Nature constructed with G, Newton's gravitational constant, $\hbar$, the Planck's constant and c, the speed of light in vacuum

This particle can indeed match the DM relic density [16]. Among non-WIMP candidates, we may quote Technicolor, an extension to the SM including QCD-like new particles and interactions. In this theory, a DM candidate would be asymmetric in its particle-antiparticle content, similarly to regular baryons [17]. Another example are axions, new scalar particles, have originally been proposed to solve the CP violation problem. They constitute a candidate to DM [18], however it seems impossible to account for both CP violation and the DM at the same time.
The theory of SUSY provides models with DM candidates. SUSY is a theory postulating a symmetry between bosons and fermions by introducing of a quantum operator transforming half-spin particles into integer-spin particles and vice-versa. It was first introduced in the 1960s and rediscovered in the 1970s. SUSY stabilizes the Higgs mass problem by making the supersymmetric fermionic and bosonic contributions to cancel. It also provides a natural unification of coupling constants of all interactions at high scale of energy thus explaining all SM interactions in their origin. The first predictive phenomenological supersymmetric model was proposed in 1976. It extends the SM of particle physics by applying one time the supersymmetric operator, thus doubling the particle spectrum, in addition to two Higgs doublets [19]. In such a model there is more than one candidate to account for the DM. Indeed, DM could be made of neutralinos, a mixed stated made of the superpartners (i.e. supersymmetric partners, or the resulting fields after the application of the supersymmetric operator on the SM fields) of SM bosons and Higgs bosons. Neutralinos are perhaps the most famous DM candidate, much hope is attached to the possibility of their existence and forthcoming detection. However other supersymmetric particles could also explain the DM, such as the gravitino (superpartner of the gravitational boson, or graviton) or the sneutrino (the superpartner of the neutrino).

1.3.2 Dark Matter experiments

Ideally, the best way to determine the DM characteristics would be to directly measure its mass and couplings at laboratory experiments, i.e. by producing it at colliders. It is unfortunately impossible due to the very nature of DM: all the means we have to detect whatever phenomenon are the electromagnetic interactions. Accounting for other interactions always invoke the understanding of the connection between electrically charged particles or photons with the studied process. That is why generating DM is so challenging. Even more if we consider that CDM is virtually collisionless, thus it seldom interacts with itself and with SM particles through the EW and strong interactions. If DM particles were produced, they would fundamentally generate ”non-events”, the missing energy in the reconstruction of interactions. Indeed, if BSM processes are indeed produced in the laboratory, then the probability of appearance of DM is rather large, since it is meant to be the lightest stable particle of the BSM spectrum. However, this also means that it would lead to an incomplete picture

of the BSM manifestation, because of the dark characteristic of its lightest stable particle. In any case, the prediction of the full theory is a very important complement to ensure the detection and identification of DM. Currently, the LHC is searching for SUSY, yet with null results so far. It was already the case in the Large Electron/Positron collider (LEP) at CERN and the Tevatron at Fermilab. Thus, the analysis of data have been focusing on constraining the plausible supersymmetric configurations, translating into bounds to the mass spectrum and the supersymmetric parameters. Thus, the very rich phenomenology motivated by SUSY has been progressively narrowed. This has consequences on the DM candidates as well: any configuration with a supersymmetric candidate implies avoiding all the limits that have been found so far.

While producing DM in laboratories seems rather difficult, we expect the DM to be naturally produced in the Early Universe. The remaining DM particles would be dominant in galaxies, such as the Milky Way (MW) or neighboring systems such as dwarf spheroidal galaxies (dSphs). Indeed, our galaxy holds together because of the presence of such particles, which distribution can be estimated by studying rotation curves and by analyzing the outcome of N-body simulations. An estimation of the local density of DM at the Earth position gives $0.3\,GeV\,cm^{-3}$, which, for a $\sim 30\,GeV$ DM candidate yields roughly ten particles per litre –roughly seven hundred particles of DM would be constantly going through an average person!

DM particles are expected to travel freely around with a certain velocity distribution. Nevertheless, if they happen to experience interactions with SM particles, although with very small rates, then by setting a very sensitive and shielded detector we may see unexpected events. It is the principle of DD. Detectors have been built to probe the nucleon-DM interactions with impressive sensitivity. Currently there are two sorts of claims from DD collaborations: null results (in such experiments as CDMS-II, Edelweiss or XENON100 [20, 21, 22]), and a potential signal which could be interpreted as the DM interacting with the detector (claimed by the DAMA and CoGeNT collaborations [23, 24, 25]). The former can only translate into upper limits on the interaction cross sections for a given mass of the DM particles. The latter stems from the observation of an annually modulated signal compatible with the oscillation of the Earth around the Sun, thus sweeping the DM cloud with a correspondingly oscillating velocity. CoGeNT also claims an unmodulated signal. While the two kinds of results seem to be in conflict, there also seem to be issues in the understanding of the detectors behavior at low energies, in the control of systematic errors and in the understanding of backgrounds. We cannot but take the results as they are published and use them to constrain or favor DM candidates. Indeed, these experiments are already scanning cross sections of about $10^{-44}\,cm^2$ for a $40\,GeV$ particle, configuration that can be provided by supersymmetric DM models, while the possible detection of DM would point towards $10\,GeV$ particles with a $\sim 10^{-40}\,cm^2$ cross section. Furthermore, it has been shown that future efforts in Directional

Detection, a technique that includes detecting the relative motion of the Earth with respect to the DM particles, would increase the sensitivity to interactions, and more interestingly, in case of a signal, they could resolve the DM mass and the interaction rates [26].
The presence of DM particles in the MW and other systems implies the possibility of two of them annihilating. Such processes would yield SM particles. After a decaying in the neighborhood of the interaction, the final products –photons, electrons and positrons, and/or protons and antiprotons– propagate and can reach Earth or satellite detectors. There is, hence a search for ID. On one hand, the annihilation cross section has to be large enough for these events to yield a detectable flux, and on the other, we would expect this to happen were the DM is more concentrated. This happens in the center of the galaxies, namely in ours and in surrounding dSphs. There is a large experimental effort to look for such signals, and there has been some excitement around results concerning unexpected rises in the flux of positrons observed by the PAMELA satellite at energies that would be compatible with DM annihilations, though at unexpectedly large rates [27]. The AMS-02 detector has recently been sent to the international space station to further explore the antimatter fluxes and other cosmic rays arriving to the Earth. The Fermi satellite with its Large Area Telescope (LAT) is observing the γ-ray sky and has established limits after null results –at energy ranges and directions relevant for DM annihilations. Other experiments such as EGRET, also a space telescope, and the MAGIC, VERITAS and HESS ground based telescopes complete the γ-ray sky survey. Fermi-LAT and HESS can also observe electrons and positrons. Furthermore, electrons and positrons produced in DM annihilations can emit synchrotron radiation when propagating through the magnetized the interstellar medium (ISM), hence, indirect signals can be searched for in radio frequencies. Thus, a new generation of experiments is looking for indirect signatures of the DM, with no conclusive results so far. Their sensitivity to the DM annihilation cross section is comparable to the interaction rate needed in the EU to provide the correct relic density. ID is, however, a very difficult tool. Indeed, signals depend on ISM where the original interactions occur, where they propagate, lose energy and produce further signals. Uncertainties on the composition of this medium and its characteristics, such as the magnetic field, make difficult the thorough estimation of DM signatures, as well as the background processes.
DM could also be trapped in the sun by scattering with its nucleons. Consequently the density of DM at the center would be large enough to produce a signal, though only visible in neutrinos which escape from our star. This technique is thus used by neutrino telescopes such as SuperKamiokande or IceCube to constrain both the elastic scattering and annihilation rates of DM particles.

2 Thermal history of Dark Matter

At early epochs of the universe particles were distributed in a dense plasma. Such a system can be treated using the kinetic theory, relativistic or classic, depending on the particle we aim to follow and the time we are interested in. Indeed, gaseous particles can be described using distribution functions, and a species evolution can be followed by computing all its interactions with other particles.
This chapter is devoted to the description of the CDM fate in the EU. If DM particles interact with SM particles, then the EU thermal bath must have contained such DM particles at equilibrium with SM particles down to some temperature. We know that decoupling must have happened at some point: DM is dark, which means it does not have any electromagnetic interaction and it is thus neutral. This sets its strongest interaction to be of the order of the EW interactions[1].

2.1 The Boltzmann equation

Let us now describe the evolution of a species of particles in the early stages of the Universe. As an example, let us assume this particle has a mass m and g internal degrees of freedom. If such particles interact with SM particles (photons, electrons, neutrinos, baryons), then they will be in thermal contact with these. Indeed, as long as the particle has a mass around the EW scale or smaller, then for T of the order of a few TeV down to at least $T \sim 1MeV$ the thermal bath has very large interactions, much larger than the expansion rate of the Universe. Hence, this context is that of statistical equilibrium of a gas. The species is thermally produced by annihilation processes as long as the temperature is larger than its mass and will annihilate: we may treat it using the Boltzmann equation accounting for chemical and thermal evolution.
Let us establish this equation by following the paths described in [28, 29, 10, 30]. We introduce the distribution function f, tracking the particles in spacetime and 4-momentum space. Therefore we have $f \equiv f(x,p)$. Thus, the mean particle number in the phase space infinitesimal element is given by $f\,d^3r\,dt\,d^3p\,dE$. The distribution function is easily related to the

[1] It could well be that DM is made of QCD-like particles with strong interactions: technicolor, a BSM theory, provides DM candidates, which we do not treat here.

species number density n in a given spacetime and 4-momentum 8-dimensional infinitesimal space (that we may take as the Universe and its configuration), as well as its pressure p and energy density ρ with the useful relations

$$n = \int dn = \int f(x,p)\,\frac{g d^3p}{(2\pi)^3} = \frac{g}{(2\pi)^3}\int f(x,p)\,d^3p, \tag{2.1}$$
$$p = \int dp = \int \frac{|\vec{p}|^2}{3E} f(x,p)\,\frac{g d^3p}{(2\pi)^3} = \frac{g}{(2\pi)^3}\int \frac{|\vec{p}|^2}{3E} f(x,p)\,d^3p,$$
$$\rho = \int d\rho = \int E f(x,p)\,\frac{g d^3p}{(2\pi)^3} = \frac{g}{(2\pi)^3}\int E f(x,p)\,d^3p.$$

Now, in order to follow the species evolution we must use a parameter λ (such as proper time for massive particles) and look at the distribution function variations with respect to λ. Any change in the distribution at a given value of that parameter has to be expressed through spacial, time, energy and 3-momentum evolution, taking into account all interactions that can alter particle number density and kinematics. In the absence of interactions we expect particles to suffer only the spacetime curvature together with its evolution, and thus stream freely throughout the expanding Universe. Let us then group all interactions on the right hand side (called the collisional term) containing both particles added and lost from a particular 8-dimensional infinitesimal spot due to microphysical processes, and keep the dynamical evolution between collisions on the left hand side. Thus we write the Boltzmann equation as follows

$$\frac{df}{d\lambda} = C(f).$$

Let us expand the (dynamical) left hand side into explicit x^μ and p^ν dependences. We may assume that mean free distances between particles are large as compared to interaction ranges (as in rarefied gas), therefore whenever particles are not interacting their trajectories obey the geodesic equation $\frac{dp^\nu}{d\lambda} + \Gamma^\nu{}_{\alpha\beta}\, p^\alpha p^\beta = 0$, since they evolve in a free fall frame. Thus

$$\frac{df}{d\lambda} = \frac{\partial f}{\partial x^\mu}\frac{dx^\mu}{d\lambda} + \frac{\partial f}{\partial p^\nu}\frac{dp^\nu}{d\lambda} = p^\mu \frac{\partial f}{\partial x^\mu} - \Gamma^\nu{}_{\alpha\beta}\, p^\alpha p^\beta \frac{\partial f}{\partial p^\nu}. \tag{2.2}$$

Now, in the standard model of cosmology, we use the Robertson-Walker metric

$$ds^2 = g_{\mu\nu}dx^\mu dx^\nu = dt^2 - \frac{R(t)^2}{1-kr^2}\,dr^2 - R(t)^2 r^2\,d\theta^2 - R(t)^2 r^2 \sin^2\theta\,d\phi^2,$$

from which we can deduce the set of Christoffel symbols –which are defined as usual by $\Gamma^\nu{}_{\alpha\beta} \equiv \frac{1}{2}g^{\mu\nu}\left(g_{\mu\alpha,\beta} + g_{\mu\beta,\alpha} - g_{\alpha\beta,\mu}\right)$– of interest. Before computing them, let us think about the dependences of distribution function f upon spacetime coordinates and 4-momenta. Indeed, we may assume that the distribution is homogeneous and isotropic, therefore it

does not vary with space coordinates nor 3-momentum angular distribution. Besides we know that a particle is always trapped in its mass shell, namely we always have the relation $|\vec{p}|^2 + m^2 = E^2$, meaning that we may drop either the dependence on energy or in 3-momentum amplitude. Thus we get a much simpler structure, namely $f \equiv f(t,E)$. Then, the final expression in (2.2) reduces to

$$E\frac{\partial f}{\partial t} - \Gamma^0{}_{\alpha\beta}\, p^\alpha p^\beta \frac{\partial f}{\partial E} = C(f).$$

We compute the following Christoffels

$$\Gamma^0{}_{00} = \Gamma^0{}_{0i} = \Gamma^0{}_{i0} = 0, \quad \Gamma^0{}_{ij} = -\frac{\dot{R}}{R} g_{ij} = -H\, g_{ij},$$

where we have introduced the Hubble parameter $H \equiv \dot{R}/R$. Thus we come to

$$\begin{aligned} &E\frac{\partial f}{\partial t} - H\left(-g_{ij}p^i p^j\right) = E\frac{\partial f}{\partial t} - H\,|\vec{p}|^2\,\frac{\partial f}{\partial E} = C(f), \\ &\frac{\partial f}{\partial t} - H\frac{E^2-m^2}{E}\frac{\partial f}{\partial E} = \frac{1}{E}C(f). \end{aligned} \tag{2.3}$$

2.2 Evolution of the number density of a species

2.2.1 The Boltzmann equation for the number density

It is interesting to follow number density evolution throughout cosmological evolution, therefore we may apply the (2.1) integral to (2.3)

$$\frac{g}{(2\pi)^3}\int\left(\frac{\partial f}{\partial t} - H\frac{E^2-m^2}{E}\frac{\partial f}{\partial E}\right)d^3p = \frac{g}{(2\pi)^3}\int\frac{1}{E}C(f)d^3p.$$

Let us develop the left hand side, integrating by parts the energy derivative

$$\begin{aligned} &\frac{g}{(2\pi)^3}\int\left(\frac{\partial f}{\partial t} - H\frac{E^2-m^2}{E}\frac{\partial f}{\partial E}\right)d^3p \\ &\quad= \frac{\partial}{\partial t}\left(\frac{g}{(2\pi)^3}\int f d^3p\right) - H\frac{g}{(2\pi)^3}\int\frac{E^2-m^2}{E}\frac{\partial f}{\partial E}d^3p \\ &\quad= \frac{\partial n}{\partial t} - H\frac{g}{2\pi^2}\int_m^\infty \left(E^2-m^2\right)^{\frac{3}{2}}\frac{\partial f}{\partial E}dE \\ &\quad= \frac{\partial n}{\partial t} + 3H\frac{g}{2\pi^2}\int_m^\infty E\sqrt{E^2-m^2}\,f\,dE \\ &\quad= \frac{\partial n}{\partial t} + 3H\left(\frac{g}{(2\pi)^3}\int f\,d^3p\right) \\ &\quad= \frac{\partial n}{\partial t} + 3Hn = \frac{g}{(2\pi)^3}\int\frac{1}{E}C(f)d^3p. \end{aligned} \tag{2.4}$$

Therefore, if we take a collisionless case using (2.4), then the Boltzmann equation reads

$$\dot{n} = -3Hn.$$

This means that whenever the species is not interacting, then the time evolution of its number density evolves purely with the expansion rate. An expanding Universe implies a positive Hubble parameter. Hence the decreasing number density expresses the dilution of the gas with the evolution of the spacetime, whereas the total number of particles does not evolve any more.

Let us now develop the interacting side of the Boltzmann equation. In principle we should take into account all possible interactions involving our particle species. This means regarding $1,2,...,N_i \to 1,2,...,N_f$ processes. In practice we will focus in just one type of process, being $2 \to 2$ scattering (results derived here may be rederived including more complicated processes without too much effort). Indeed, here our main concern is to understand key points in the particle species history. When it is meant to be at equilibrium, then we use equilibrium statistical properties. When a particle is frozen out and does not interact with others any more, then it is basically in free streaming regime. It is crucial to understand when it decouples chemically and thermally, though. The former takes place when the species total number stops changing because both annihilation and creation are no longer relevant. The latter takes place when the species stops elastic scattering on others, and its thermal evolution is no longer related to the characteristics of the rest of the species. Both moments determine important features. For example, chemical decoupling of a thermal dark matter candidate sets its relic density for later stages of the Universe evolution. Whereas details of thermal decoupling of cold dark matter particles will have an influence on structure formation. However, so far we have focused on number density. Elastic scattering processes, which thermalize particles and set their temperature to that of the thermal bath, do not change the number density. Therefore here we will address only annihilation processes.

So, let us label particles involved $1,2 \leftrightarrow 3,4$. If our particle species is represented by particle 1 in such a process, then we expect $1,2 \to 3,4$ to extract particles from our distribution function at some 8-volume, and $1,2 \leftarrow 3,4$ to add particles to it. Furthermore, those processes will depend on the transition probability, described by the squared amplitude of the process. Of course, all particles of the $2,3,4$ kinds will contribute, thus we have to integrate over the Lorentz Invariant Phase Space of all possible momenta ($d_{2,3,4}LIPS$) and spins, weighted by the corresponding distribution functions. Ensuring 4-momentum conservation for each transition, we have the general expression of the collisional term

$$C(f) = -\frac{1}{2}\sum_{spins}\int \left[f\, f_2 \left(1 \pm f_3\right)\left(1 \pm f_4\right) \left|\mathcal{M}_{12\to 34}\right|^2 - f_3 f_4 \left(1 \pm f\right)\left(1 \pm f_2\right) \left|\mathcal{M}_{34\to 12}\right|^2 \right]$$
$$(2\pi)^4 \delta^4\left(p + p_2 - p_3 - p_4\right) \frac{d^3 p_2}{(2\pi)^3 2E_2} \frac{d^3 p_3}{(2\pi)^3 2E_3} \frac{d^3 p_4}{(2\pi)^3 2E_4}$$

where the $1 \pm f_i$ factors come from Bose condensate enhancement $(+)$ or Fermi degenracy suppression $(-)$. From now on we will neglect these, since massive particles decoupling in early Universe are not expected to reach the density of a degenerate gas. The overall $1/2$ factor comes from the fact that in transition rates we cannot distinguish the initial state $(1,2)$ from $(2,1)$ for losses, nor $(3,4)$ from $(4,3)$ for added particles to f. In order to get a simple relation we must assume that the produced (or source) particles $(3,4)$ are in thermal and chemical equilibrium with the thermal bath, therefore $f_{3,4} \to f^{eq}_{3,4}$. Indeed, if we think of the thermal bath to be made of coupled species such as photons and electrons, then this holds safely. Note that equilibrium distributions are given by Fermi-Dirac $(+)$ or Bose-Einstein $(-)$ at temperature T, for a chemical potential μ by

$$f^{eq}(E) = \frac{1}{e^{\frac{E-\mu}{T}} \pm 1}.$$

Now, if our species is in equilibrium at high enough temperatures, then the detailed balance principle states that every single microphysical process must be balanced by its reverse process. This yields $f_1^{eq} f_2^{eq} = f_3^{eq} f_4^{eq}$, and thus we may integrate over $d^3p_3\, d^3p_4$ regardless of any distribution function. Furthermore, we shall notice that in the two transition rates appearing the only difference is the initial and final states, which are just interchanged. But we know from quantum mechanics that such microphysical processes are described by an S-matrix (from which the transition amplitude and therefore the squared amplitudes are computed), this matrix being unitary. This condition can be expressed in terms of $\left|\mathcal{M}\right|^2$ as follows[2]

$$\begin{aligned}
&\sum_{spins} \int (2\pi)^4 \delta^4 (p_1 + p_2 - p_3 - p_4) \left|\mathcal{M}_{34\to 12}\right|^2 \frac{d^3p_3}{(2\pi)^3 2E_3} \frac{d^3p_4}{(2\pi)^3 2E_4} \\
&\quad = \sum_{spins} \int (2\pi)^4 \delta^4 (p_1 + p_2 - p_3 - p_4) \left|\mathcal{M}_{12\to 34}\right|^2 \frac{d^3p_3}{(2\pi)^3 2E_3} \frac{d^3p_4}{(2\pi)^3 2E_4}.
\end{aligned}$$

Moreover, we see that

$$\begin{aligned}
&\sum_{spins} \int (2\pi)^4 \delta^4 (p_1 + p_2 - p_3 - p_4) \left|\mathcal{M}_{12\to 34}\right|^2 \frac{d^3p_3}{(2\pi)^3 2E_3} \frac{d^3p_4}{(2\pi)^3 2E_4} \\
&\quad = 4\, F\, g_1 g_2\, \sigma_{12\to 34} = 4\, E_1 E_2\, v_{Mol}\, g_1 g_2\, \sigma_{12\to 34},
\end{aligned}$$

were we introduced the total cross section $\sigma_{12\to 34}$ and the flux factor F in terms of the invariant Moller velocity defined (in units of $c = 1$) by $v_{Mol} = F/(E_1 E_2) = \sqrt{|\vec{v}_1 - \vec{v}_2|^2 - (\vec{v}_1 \wedge \vec{v}_2)^2}$, which in the laboratory frame comes to $|\vec{v}_1 - \vec{v}_2|$, the relative velocity. Collecting all our sim-

[2] It is worth to notice that if the CPT (Charge-Parity-Time reversal) symmetry is conserved at the interaction vertex then automatically $\left|\mathcal{M}_{34\to 12}\right|^2 = \left|\mathcal{M}_{12\to 34}\right|^2$. This holds for all processes observed in Nature so far.

plifications, and integrating the collisional term

$$\begin{aligned}
&\frac{g}{(2\pi)^3}\int \frac{1}{E}C(f)d^3p \\
&\quad = -\sum_{spins}\int \left(ff_2 - f^{eq}f_2^{eq}\right)\left|\mathcal{M}_{12\to 34}\right|^2 (2\pi)^4\,\delta^4\left(p_1+p_2-p_3-p_4\right) \\
&\qquad \times \frac{d^3p}{(2\pi)^3\,2E}\frac{d^3p_2}{(2\pi)^3\,2E_2}\frac{d^3p_3}{(2\pi)^3\,2E_3}\frac{d^3p_4}{(2\pi)^3\,2E_4} \\
&\quad = -\int v_{Mol}\left(dndn_2 - dn^{eq}dn_2^{eq}\right)\sigma_{12\to 34} \\
&\quad \simeq -\left\langle\sigma_{12\to 34}v_{Mol}\right\rangle\int\left(dndn_2 - dn^{eq}dn_2^{eq}\right) \\
&\quad = -\left\langle\sigma_{12\to 34}v_{Mol}\right\rangle\left(nn_2 - n^{eq}n_2^{eq}\right),
\end{aligned}$$

where we introduced the thermally averaged cross section

$$\left\langle\sigma_{12\to 34}v_{Mol}\right\rangle = \frac{\int v_{Mol}\sigma_{12\to 34}dn^{eq}dn_2^{eq}}{\int dn^{eq}dn_2^{eq}}.$$

Finally, if $1\equiv 2$, we come to a very simple version of the Boltzmann equation, namely

$$\dot{n} = -3Hn - \left\langle\sigma v\right\rangle\left(n^2 - n_{eq}^2\right). \tag{2.5}$$

This is a Riccati equation. Most of the physical aspects of chemical evolution are apparent in (2.5). Namely, there are two competing processes ruling the density of particles: the expansion rate $-3Hn$ and the interaction rate $\left\langle\sigma v\right\rangle\left(n^2-n_{eq}^2\right)$. Therefore, a particle is in good thermal contact with the plasma whenever $\left\langle\sigma v\right\rangle\left(n^2-n_{eq}^2\right)\gg 3Hn$, or equivalently, $\left\langle\sigma v\right\rangle n\gg 3H$. This is indeed the equilibrium condition. When the expansion rate overcomes the interaction rate, then the particle is out of equilibrium, thus its total number does not evolve any more.

2.2.2 Expression in a radiation dominated era

We are following the evolution of a species in radiation dominated era. It is useful to express the time and the Hubble parameter as a function of the thermal bath temperature. Indeed we can write

$$\begin{aligned}
H &= H_0T^2 \\
t &= \frac{1}{2H_0T^2} \\
\frac{dT}{dt} &= -H_0T^3.
\end{aligned}$$

Moreover, we can introduce the y variable defined by

$$y \equiv \frac{n}{T^3}$$

and rewrite (2.5) in terms of y

$$\begin{aligned}\frac{dn}{dt} &= -H_0 T^3 \frac{dn}{dT} = -H_0 T^3 \left(\frac{dy}{dT} T^3 + \frac{3n}{T}\right) \\ &= -3H_0 T^2 n - \langle \sigma v \rangle T^6 \left(y^2 - y_{eq}^2\right),\end{aligned}$$

which comes to

$$\frac{dy}{dT} = \frac{\langle \sigma v \rangle}{H_0} \left(y^2 - y_{eq}^2\right) \tag{2.6}$$

i.e., a simpler Riccati equation.
Note that H_0 is a function of the total number of degrees of freedom at a given epoch. Thus for a specific period we can safely take H_0 to be constant. However, whenever a species decouples from the thermal bath, the value of H_0 consequently changes as well as the number density of all species. The energy and entropy of the decoupling species is transferred to the bath, thus changing its state.

2.2.3 Relativistic behavior at equilibrium

Whenever particles are relativistic, i.e., with temperatures such that $T \gg m, \mu$ and $|\vec{p}| \approx E$, we expect equilibrium number density to behave like $n^{eq} \propto T^3$. Indeed, for a particle following Fermi-Dirac (upper sign) or Bose-Einstein (lower sign) statistics, of mass m , having g internal degrees of freedom, of energy E and 3-momentum $\vec{p}$, being at equilibrium at a temperature T. If $f(\vec{p})$ is its distribution, then

$$f(\vec{p}) \equiv \frac{1}{e^{\frac{E-\mu}{T}} \pm 1},$$

where μ is the particle's chemical potential. We see that $f(\vec{p}) \equiv f(E)$. If we treat particles with no chemical potential, then $\mu = 0$. We take this hypothesis form now on.
Let us focus in the relativistic case, where the temperature of the particle at equilibrium is much larger than its mass (we use $k_B = c = 1$) $T \gg m$. To begin with, if we assume that the largest contribution in the distribution at equilibrium is for particles for which $\mid \vec{p} \mid^2 \simeq T^2$, then it is a good approximation to use $E^2 - m^2 \simeq E^2 \simeq \mid \vec{p} \mid^2$. We can recast the distribution to a more useful form

$$f(E) = \frac{1}{e^{\frac{E}{T}} \pm 1} = e^{-\frac{E}{T}} \left(\frac{1}{1 \pm e^{\frac{-E}{T}}}\right) = e^{-\frac{E}{T}} \sum_{k=0}^{\infty} (\mp 1)^k \left(e^{-\frac{E}{T}}\right)^k = \sum_{k=1}^{\infty} (\mp 1)^{k+1} e^{-\frac{kE}{T}}. \tag{2.7}$$

And replacing (2.7) into (2.1), we get

$$n_{rel} \simeq \frac{g}{2\pi^2} \sum_{k=1}^{\infty} (\mp 1)^{k+1} \int_m^{\infty} E^2 e^{-\frac{kE}{T}} dE.$$

If we integrate twice by parts to get rid of the E^2 factor, and finally integrating the exponential, we find

$$n_{rel} \simeq \frac{g}{2\pi^2} \sum_{k=1}^{\infty} (\mp 1)^{k+1} T^3 e^{-\frac{kE}{T}} \left(\frac{m^2}{kT^2} + \frac{2m}{k^2 T} + \frac{2}{k^3} \right) \simeq \frac{g}{2\pi^2} \sum_{k=1}^{\infty} (\mp 1)^{k+1} \frac{2T^3}{k^3},$$

since

$$\frac{m}{T} \ll 1 \Rightarrow \left[\frac{2}{k^3} \gg \frac{2m}{k^2 T} \gg \frac{m^2}{kT^2} \right] \& \left[e^{-\frac{kE}{T}} = \left(e^{-\frac{E}{T}} \right)^k \simeq 1^k = 1 \right].$$

So in the relativistic era of a given bosonic particle with no chemical potential we can approximate its number density by

$$n_{rel} \simeq \zeta(3) \frac{gT^3}{\pi^2} \simeq 1.202 \times \frac{gT^3}{\pi^2} \simeq 0.244 \times T^3, \tag{2.8}$$

and for a fermionic particle

$$n_{rel} \simeq \frac{3}{4} \zeta(3) \frac{gT^3}{\pi^2} \simeq 0.9015 \times \frac{gT^3}{\pi^2} \simeq 0.183 \times T^3, \tag{2.9}$$

where $\zeta(3)$ is the Riemann ζ-function of 3. Equations (2.8) and (2.9) imply that $y^{eq} = const$. So looking at (2.6), it is straightforward to realize that $y = y^{eq}$ is a stable solution. Therefore we expect the species to be at equilibrium for $T \gg m$. Noticing that $T^3 \propto V$ where V is a volume, we conclude that y is proportional to the total number of particles, which is thus conserved in the relativistic regime.

2.2.4 Non relativistic behavior: freeze out

As the Universe expands and cools down, the temperature approaches the value of the species mass, which we assume is still in thermal contact with the plasma. It suffers the transition to non-relativistic regime, $T \ll m$. Let us show that, neglecting chemical potential, $n^{eq} \propto T^{\frac{3}{2}} e^{-\frac{m}{T}}$. If we take the non-relativistic regime, then we can rearrange (2.7), since here $m \gg T$ and $E \geq m$, thus $0 < e^{-E/T} \ll 1$,

$$f(E) \simeq e^{-\frac{E}{T}} \tag{2.10}$$

where we approximate to the first order in $e^{-E/T}$, which is the Boltzmann distribution, and this for both Fermi-Dirac and Bose-Einstein cases. So, using (2.10), recasting (2.1) and upon integrating by parts we come to

$$n_{non-rel} \simeq \frac{g}{2\pi^2} \int_m^{\infty} E\sqrt{E^2 - m^2} e^{-\frac{E}{T}} dE = \frac{g}{2\pi^2} \frac{1}{3T} \int_m^{\infty} \left(E^2 - m^2\right)^{\frac{3}{2}} e^{-\frac{E}{T}} dE.$$

We now perform the following change of variable

$$x = \frac{E-m}{T} \Leftrightarrow E = Tx+m \Leftrightarrow \left(E^2-m^2\right)^{\frac{3}{2}} = (mT)^{\frac{3}{2}} \left(\frac{Tx^2}{m}+2x\right)^{\frac{3}{2}} \simeq (2mT)^{\frac{3}{2}} x^{\frac{3}{2}},$$
$$dE = Tdx.$$

Therefore

$$n_{non-rel} \simeq \frac{g}{6\pi^2} (2mT)^{\frac{3}{2}} e^{-\frac{m}{T}} \int_0^\infty x^{\frac{3}{2}} e^{-x} dx = \frac{g}{6\pi^2} (2mT)^{\frac{3}{2}} e^{-\frac{m}{T}} \Gamma\left(\frac{5}{2}\right).$$

Thus, replacing the gamma function of $5/2$, $\Gamma(5/2) = 3\sqrt{\pi}/4$, we finally get

$$n_{non-rel} \simeq g \left(\frac{Tm}{2\pi}\right)^{\frac{3}{2}} e^{-\frac{m}{T}} \simeq 0.127 (Tm)^{\frac{3}{2}} e^{-\frac{m}{T}}.$$

Therefore, as the species enters this stage it still follows its equilibrium distribution and gets exponentially suppressed along with it, as long as the interaction rate $\langle \sigma v \rangle n$ overcomes the expansion rate H. However, the exponential suppression of the particle number density implies that this rate decreases as well, and eventually becomes much smaller than the expansion rate. Thus particles do not encounter each other often enough any more, since they are non relativistic and diluted, therefore they cannot annihilate any longer. Conversely, it becomes less and less probable that two species of whatever other species have enough energy to produce two non-relativistic particles. These decouple from the thermal bath and thus suffer freeze out, behaving as $\dot{n} = -3Hn$, or equivalently $\frac{dy}{dT} = 0$. As already stated, we expect the species total number to be constant, and from now on, forever.

2.3 Numerical evaluation of freeze out

Our concern here is to solve the Boltzmann equation in order to get accurate values of the relic density. In order to do so we follow temperature as it falls down. We may safely set our initial condition of number density, or y, as being the quantity at equilibrium for an initial temperature such as $T \gg m$ (in practice, even at $T = m$ equilibrium is a good starting point). As we choose T as the crucial parameter, we must discretize it and follow it with a given step. At each step we will calculate the value of the next one using numerical methods. Let us first address the problem of equilibrium values, playing an important role in the computation of the rate of change at each point.

2.3.1 Equilibrium evaluation

If our distribution is that of a Fermi-Dirac (upper sign) or Bose-Einstein (lower sign) particle with no chemical potential, then

$$f(\vec{p}) \equiv \frac{1}{e^{\frac{E}{T}} \pm 1} = e^{-\frac{E}{T}} \frac{1}{1 \pm e^{-\frac{E}{T}}}.$$

Since both $E, T > 0$, then $0 < e^{-E/T} < 1$, we can expand f as the following sum

$$f(\vec{p}) = e^{-\frac{E}{T}} \sum_{k=0}^{\infty} (\mp 1)^k e^{-\frac{kE}{T}} = \sum_{k=1}^{\infty} (\mp 1)^{k-1} e^{-\frac{kE}{T}}.$$

Furthermore, if f depends only upon E, then we transform (2.1) in order to express it explicitely depending on E.

$$n_{eq} = \frac{g}{2\pi^2} \int_m^{\infty} dE\, E\sqrt{E^2 - m^2}\, f(E) = \frac{g}{2\pi^2} \sum_{k=1}^{\infty} (\mp 1)^{k-1} I_k,$$

where

$$I_k = \int_m^{\infty} dE\, E\sqrt{E^2 - m^2}\, e^{-\frac{kE}{T}}.$$

Integrating by parts and then introducing the variable $x = E/m$, we may express I_k as

$$\begin{aligned} I_k &= \frac{k}{3T} \int_m^{\infty} dE \left(E^2 - m^2\right)^{\frac{3}{2}} e^{-\frac{kE}{T}} = \frac{km^4}{3T} \int_1^{\infty} dx \left(x^2 - 1\right)^{\frac{3}{2}} e^{-\frac{kmx}{T}} \\ &= \frac{m^3}{3} \left(\frac{km}{T}\right) \int_1^{\infty} dx \left(x^2 - 1\right)^{\frac{3}{2}} e^{-\left(\frac{km}{T}\right)x}. \end{aligned}$$

Now, the integral representation of the Bessel functions of the first kind is

$$\begin{aligned} K_n(z) &= \frac{\sqrt{\pi} z^n}{2^n \Gamma\left(n + \frac{1}{2}\right)} \int_1^{\infty} dt\, e^{-zt} \left(t^2 - 1\right)^{n - \frac{1}{2}} \\ Re(z) &> 0 \;\; \& \;\; Re(n) > -\frac{1}{2}. \end{aligned}$$

Therefore, for $n = 2$ and using the fact that $\Gamma\left(\frac{5}{2}\right) = 3\sqrt{\pi}/4$:

$$K_2(z) = \frac{z^2}{3} \int_1^{\infty} dt\, e^{-zt} \left(t^2 - 1\right)^{\frac{3}{2}}.$$

Identifying z with km/T we come to

$$I_k = \frac{m^2 T}{k} K_2\left(\frac{km}{T}\right),$$

which finally yields

$$n_{eq} = \frac{gm^2T}{2\pi^2} \sum_{k=1}^{\infty} (\mp 1)^{k-1} \frac{K_2\left(\frac{km}{T}\right)}{k}.$$

If we transform from number density to y, then we have

$$y_{eq} = \frac{gm^2}{2\pi^2T^2} \sum_{k=1}^{\infty} (\mp 1)^{k-1} \frac{K_2\left(\frac{km}{T}\right)}{k}. \tag{2.11}$$

Thus we can compute the value of y at equilibrium at any T. Actually, the series converges really fast, and usually 3 terms are enough to get a good value. Anyhow, this can be automatized with a convergence criterion.

2.3.2 An implicit solution

Within numerical methods for integration, it is known that implicit resolutions give good results, though they are not always achievable. The Riccati equation allows us to use such a method. Here it is specially needed since we have a stiff equation: we already saw that the transition from the two conserved total number regimes is due to an exponential. If we use the trapezoidal rule for integration then we write:

$$y_{i+1} = y_i + h\left(\frac{1}{2}\frac{dy_{i+1}}{dT} + \frac{1}{2}\frac{dy_i}{dT}\right) + O\left(h^3\right), \tag{2.12}$$

where h is the step size, and i the step number, and where we made explicit the error. Now, here we can reexpress the values of $\frac{dy_j}{dT}$, using (2.6)

$$\frac{dy_j}{dT} = \frac{\langle\sigma v\rangle}{H_0}\left(y_j^2 - y_{eq,\,j}^2\right).$$

Therefore in (2.12) we will have the solution (namely y_{i+1}) in both sides of the equation, thus we can get an implicit solution to such a quadratic equation

$$y_{i+1} = \frac{H_0}{h\langle\sigma v\rangle}\left(1 \pm \sqrt{1 - 2h\frac{\langle\sigma v\rangle}{H_0} - \left(\frac{h\langle\sigma v\rangle}{H_0}\right)^2\left(y_i^2 - y_{eq,i}^2 - y_{eq,i+1}^2\right)}\right).$$

Here all terms are computable for T_i and $T_{i+1} = T_i + h$, namely using (2.11) for equilibrium values. The wanted solution is the one with the $-$ sign, since we expect y to decrease with decreasing T (our step h is negative).

2.3.3 Tools for freeze out

I produced a quick and small code computing the relic density of a particle together with its FO temperature, where the free parameters were the mass, internal degrees of freedom

and the thermally averaged interaction cross section. In Fig. 2.1 some results that were obtained by this method are shown. These describe exactly the behavior we expected: the red curve, representing the solution to the Boltzmann equation, follows the blue curve, which corresponds to the equilibrium distribution, down to a given point, even during a large part of the relativistic to non-relativistic transition period. Then is stops following it at a certain point. Here we display various behaviors for n, each changing only in the thermally averaged annihilation cross section. While the temperature of freeze out is strongly dependent upon the non-relativistic transition and thus upon the mass of the species, a change of a factor few in the cross section does not have much influence on it. However, the final amount of particles, the relic yield of the process, drastically varies with the cross section. This code reproduced the well established results. The correct relic density as measured by WMAP [31] is achieved for $\langle \sigma_{ann} v \rangle \simeq 3 \times 10^{-26} cm^3\, s^{-1}$, and $T_{FO} \simeq m/20$, depending on the DM particle mass.

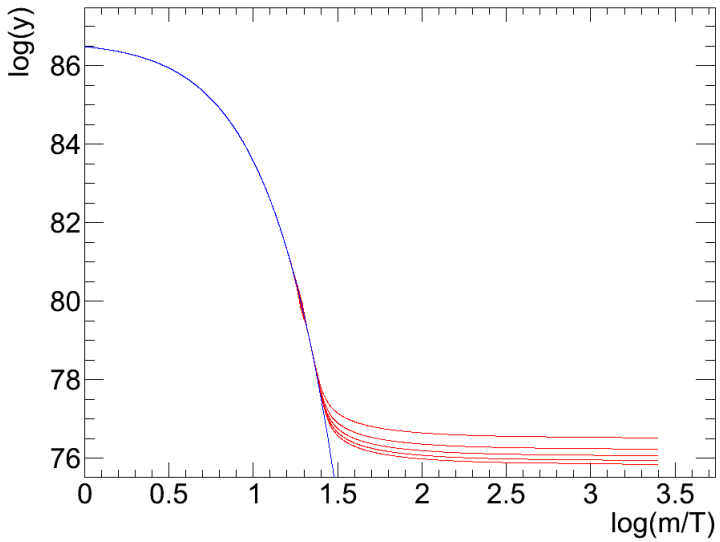

Fig. 2.1: Numerical solution of the Boltzmann equation for a CDM candidate. The red curves follow the evolution of the species while the blue curve describes that of the equilibrium distribution. Here four different cross section are shown. The decoupling and freeze out happen roughly at the same temperature, while the final number of particles is strongly depending on the annihilation rate. The larger the cross section the smaller the final number of particles.

Making this code was useful and enlightening. However it is very basic. For example, the cross section is a free parameter and its thermal average is not computed but assumed. No dependence on the temperature is considered. When we studied DM candidates in light of astrophysical and collider observables using particle physics models, we used well established tools. micrOMEGAs was built for this purpose [32]. Various particle physics models are included in the code. It computes the FO temperature and relic density of the DM candidate

in the model, including tree level and loop contributions in the estimation of the thermally averaged cross section. Finally, once the equation is solved and the stable state is obtained for the candidate, the fraction it contributes to the energy density of the Universe is computed by extrapolating the EU density thus obtained throughout the Universe expansion. This implies taking into account the exact number of relativistic particles at decoupling, since the relativistic degrees of freedom set the energy density evaluation during the radiation dominated era. Thus this fraction can be compared to the observed DM contribution at CMB and other observations.

2.4 Annihilation cross sections and temperature at the freeze out transition

Following the analytic treatment given in [10, 33] it can be established that

$$\frac{m}{T_{FO}} \simeq ln\left(\frac{0.038\, g\, m_{Pl}\, m\, \langle\sigma v\rangle}{\sqrt{g_* \frac{m}{T_{FO}}}}\right),$$

where g_* stands for the total number of effectively relativistic degrees of freedom at T_{FO} and $m_{Pl} \simeq 1.22 \times 10^{19}\, GeV$ is the Planck mass. This relation can be numerically solved knowing the value of the thermally averaged cross section and g_*, which in turn needs a certain knowledge of the period at which FO occurs. To account for the relic density one has to further follow the fate of the DM species by integrating the diluted interactions that may follow the decoupling time. By doing so we come to the useful expression

$$\Omega_{DM} h^2 \simeq \frac{1.07 \times 10^{19}\, GeV^{-1}}{J\,(m/T_{FO})\; g_*\, m_{Pl}},$$

where

$$J\,(x) = \int_x^{\infty} \frac{\langle\sigma v\rangle}{x'^2} dx'$$

is the integral accounting for residual annihilations. In numerical treatments this integral is performed in order to compute the present DM density and thus deduce $\Omega_{DM} h^2$. By imposing $\Omega_{DM} h^2 \simeq 0.1$ we come to the usual $\langle\sigma v\rangle \simeq 3 \times 10^{-26}\, cm^3\, s^{-1}$ annihilation rate needed for a typical candidate of the few tens of GeV range.

The temperature at which chemical decoupling happens depends upon the mass of the particle, responsible for the onset of the FO mechanism, and upon the annihilation rate at the time, however only with a logarithmic dependence on the latter. When a particle decouples from the thermal bath, it alters its characteristics. Indeed, the energy density and pressure –and hence the entropy– of the gas are just the sum of the individual contributions of each

species. Thus, it depends upon the number of relativistic degrees of freedom it contains. A decoupling particle escapes the bath carrying away its own contribution to the entropy of the gas. Thus, the equilibrium conditions of the remaining particles change. As it was seen, the transition from equilibrium to FO is extremely quick, thus, it consequently induces a very sharp transition in the behavior of those species that are still coupled to the bath. This transition could be at the origin of perturbations in ongoing processes, such as primordial nucleosynthesis, as it will be stated in Sec. 4.1.1.
We have showed that the final number of particles surviving the chemical decoupling and subsequent FO mechanism depends strongly on the annihilation cross section. This transition rate may depend or not upon the relative velocity of the particles, depending upon the very intrinsic nature of the interaction. If such is the case, while the FO transition requires a certain value of the thermally averaged cross section, this average is done at the very particular temperature T_{FO}, which sets the average velocities of the particles at the decoupling time. For example, for a typical $T_{FO} \simeq m/20\,GeV$ transition, we get $\langle v_{FO} \rangle \simeq 0.15 \times c$, which is indeed non-relativistic but still rather large velocity. This is not necessarily the velocity at which interactions would happen in the galaxies, where particles are expected to move at slower speeds. If the cross section has a velocity dependence, which allows a Taylor expansion for low v, then we have $\langle \sigma v \rangle \simeq a + bv^2$ where a and b are constants. Depending upon the dominant term in EU, the cross section at $v \ll v_{FO}$ can be very different: if the constant term is already dominant at high velocities then the cross section would remain the same at low velocities and thus be given by a, the s-wave term; however, if it is dominated by bv^2, the P-wave term, at $v = \langle v_{FO} \rangle$, then the expected annihilation rate at lower velocities is expected to be smaller. Thus, in galaxies the cross section may suffer of p-wave suppression and be smaller than the EU annihilation rate fixing the correct relic density via the FO mechanism.

2.5 Loosing the relation between early Universe and galactic annihilation rates

We have seen the example of the p-wave suppression which would induce a large sizeable difference between EU and galactic annihilation rates. However, there are other mechanisms that could provide the right relic density and have quite different behaviors. Here we briefly present the case of coannihilations, annihilation into forbidden channels and resonant processes which invoke particular kinematic relations in the dark sector (recall that the temperature at FO is lowered by a factor $\sim 10^5$ with respect to galactic temperature). Fortunately, all the cases we present here altering the standard FO picture are taken into account by micrOMEGAs. While the DM could intrinsically have very low couplings to SM particles, the annihilation rate at primordial times could be sufficiently enhanced to get a relic density below the experimental limit set by WMAP.

2.5.1 Coannihilation

Coannihilation is an example of how the DM could reach the measured relic density by other means than purely self annihilation [33]. If the DM candidate χ_{DM} is nearly degenerated in mass with another BSM particle χ', then the latter is expected to be present in the thermal bath for temperatures almost equal to T_{FO}. Indeed, their equilibrium would hold down to the non-relativistic transition, which would happen only a few instants before that of the DM candidate. In such a scenario, processes such as $\chi_{DM}\chi' \to XX'$, where X and X' are SM particles, are expected to enter in the collisional term of the Boltzmann equation, hence they alter the number density of the DM. While the decay of the nearly degenerated χ' ensures its null relic abundance, it might still be present at the decoupling time of χ_{DM} by the inverse relation, and by the $\chi_{DM}X \to \chi' X'$ process. Thus, the number density of χ' would be close to the equilibrium value as long as the χ_{DM} has not decoupled from the bath. Depending upon the degeneracy level –sizeable effects have been demonstrated to occur for $\sim 10\%$ degeneracy–, the interaction cross sections and the number of χ' particles, the co-annihilation rate could enhance the particle loss by a few tens to a few hundreds compared to self annihilation alone. This consequently translates into a lower self annihilation cross section of the DM.

2.5.2 Forbidden channels

The FO transition happens at non-relativistic speeds. Some processes suffer from large suppressions at low velocities. For example, the self annihilation of Majorana particles into scalar particles (such as neutralino annihilation into Higgs bosons) implies chiral couplings, and thus tends quadratically to zero with decreasing velocities. However, if the final state particles are also non-relativistic at the FO of DM, then the relevant thermally averaged cross section can no longer be approximated by $\langle \sigma v \rangle \simeq a + bv^2$, and has to include the velocity v' of the final state particles, thus turning into $\sigma v \simeq (a' + b'v^2) \times v'$ [33]. The v' velocity, in the thermal bath, depends upon the mass of the final state particles, and so will depend the annihilation rate. Therefore, for $2m_{DM} \gtrsim \sum m_{fs}$ where m_{fs} are the final state masses, we fall in the non-relativistic regime for v' around the DM FO. This configuration enhances the annihilation rate at decoupling by a large factor, depending upon the mass relation and the strength of the interaction. Thus, for these normally forbidden channels, one could expect dominant contributions within a certain range of mass relations. This consideration also holds for s-wave dominated processes, since its origin is purely kinematical.

2.5.3 Resonances

The annihilation rate at FO can be dominated by a resonant exchange. If X'' stands for the exchanged particle in the annihilation process, then, for example, $\chi_{DM}\chi_{DM} - X'' \to XX$ would be enlarged near $2m_{DM} = m_{\chi''}$. Actually, this relation is approximative, since we know

that the DM kinetic energy is small but not completely negligible at FO. Thus, depending on the nature of the X'' propagator, the relation responsible for a boost in the annihilation rate can include a tuning of v_{FO}, the decay rate of the exchanged particle $\Gamma_{\chi''}$, m_{DM} and $m_{\chi''}$. Such a case was also presented in [33] under the more general case of annihilations happening near poles of the cross section. Once again, depending on the interplay of the cited quantities, the annihilation rate could be greatly enhanced at T_{FO}, while it would present very different behavior at lower, galactic velocities.

2.5.4 Sommerfeld effect

Finally, the annihilation rate at low velocities could be enhanced by a Sommerfeld effect. Indeed, if the kinetic energy of the annihilating particles is very small, then the exchange of gauge bosons through the so-called ladder diagram –a sequence of t-channel exchanges of gauge bosons right before the interaction, constituting a multiple box diagram– could yield a large enhancement of the annihilation cross section. It is shown that the final enhancement factor S goes as $1/v$ (where v is the relative velocity) down to very small velocities. It also depends on the DM mass: the heavier the particles, the more efficient the Sommerfeld effect. Sizeable effects are expected for DM masses at the TeV scale and above –hence, not for light candidates. Moreover, for certain DM mass-gauge boson mass relations, bound states could be formed. They imply resonances that further increase the effect, potentially by many orders of magnitude. For example, for typical EW gauge boson masses and interaction strengths, a resonance could be expected at $m_{DM} \sim 4.5\ TeV$, for a global boost factor of 10^6 with respect to the annihilation rate at FO [34].

2.6 Freeze In: an alternative to freeze out

The novel freeze-in (FI) mechanism consists on a different way to obtain the relic density. It takes place when a species decouples from the thermal bath before the bath reaches the species Boltzmann suppression temperature. Then, two possibilities of achieving the correct relic abundance arise: the DM could be produced at temperatures around $(2-5) \times m_{DM}$ by the residual interactions of the thermal bath and thus acquire its relic density through FI; or the DM could reach its relic density after the decay of a frozen in unstable particle. Particles decoupling in such a way are called FIMP, for either Feeble Interacting or Frozen In Massive Particles. We follow the description in [35], in which also more details are given.

2.6.1 The freeze in mechanism

The general picture of the FI mechanism needs the assumption of a FIMP particle with a few particular characteristics. This particle needs to be decoupled from the thermal bath at

temperatures larger than the EW scale, independently of the FIMP mass. This means that equilibrium conditions are not met, thus the number density of the FIMP is not simply set by the thermal bath temperature as in (2.8) or (2.9). Assuming that after inflation the density of FIMP particles is null or very suppressed, they could only be produced by particles from the plasma annihilating into the FIMP. Such interactions can be described by a characteristic coupling λ. Thus, for example, Yukawa interactions would happen with a strength proportional to λ, while trilinear scalar interactions would involve λm_v, where m_v is the mass of the heaviest particle involved in the vertex, which could be from the thermal bath or the FIMP itself. It is convenient to assume m_v is of the order of the EW scale as well. Hence, it is assumed that $\lambda \ll 1$ so the interaction rate is low enough to prevent good thermal contact of the FIMP to the plasma.

The probability of two thermal particles to produce a pair of FIMPs is very suppressed, but not null. When $T < m_v$ the interaction suffers an exponential suppression because of the Boltzmann suppressed phase space of particles heavier than the temperature of the bath. This translates into a consequent dilution of the FIMP production. Therefore, the production of FIMPs happens mostly for $T \gtrsim m_v$. Thus, there is a transition, very similar to that of FO, after which the interaction modifying the total number of FIMPs are frozen: the FI transition. It is thus shown that the FIMP abundance at FI is

$$y_{FI} \propto \lambda^2 \frac{m_{Pl}}{m_v} \sim \lambda^2 m_v \frac{m_{Pl}}{m_v^2}, \tag{2.13}$$

where $y_{FI} = n_{FIMP}(T_{FI})/T_{FI}^3$, and $m_{Pl}/m_v^2 \simeq t_{FI}$ is a good approximation of the time at which FI occurs. The later FI occurs, the larger the yield of FIMPs.

2.6.2 *Freeze in and dark matter*

If the FIMP decay is prevented by an unbroken symmetry, then the FIMP can be by itself the DM candidate. Then, one needs a theory to provide a candidate behaving like a FIMP in EU, with such interacting rates that the relic density is met after the FI transition.

However, the FIMP could be unstable. In such cases, the DM would be another particle: the lightest of the FIMP decay spectrum. For an efficient decay rate the FIMP will produce the DM at a characteristic temperature T_{FD}. However, if it is efficient at temperatures for which the DM annihilation into SM particles is still possible, then the right relic density might not be achieved unless one invokes the FO mechanism. Therefore, the decay temperature must satisfy $T_{FD} < T_{FO} \sim m_{DM}/20$. Thus, if FIMP decay happens after the characteristic time of FO for the DM candidate, then the abundance of DM particles is solely determined by the FIMP decay rate. Thus, the relic abundance is set by the FIMP characteristics: the amount of FIMP particles produced as well as the decay rate of the FIMPs.

This is indeed a very interesting mechanism. For example, if we are interested in neutralino

DM, then by assuming its relic density achieved by the FI mechanism driven by the existence of a FIMP –accompanied or not by a whole new sector of particles and interactions– coupled to the neutralino, we may lift all constraints upon neutralino annihilation rates from EU.

3 From structure formation to Dark Matter haloes

The EU considerations set the initial conditions for structure formation. While the general mechanism that leads to DM objects –with or without the presence of baryons– is well understood, the details on DM halo properties are determined by N-body simulations. Let us describe both the generation of DM haloes and their basic properties. We follow the descriptions in [5] and particularly of the review [36].

3.1 From inhomogeneities to structures

In the ΛCDM model the structure formation is well described, specially for the large scales. The CDM inherits a power spectrum with fluctuations from inflation. This power spectrum appears to be naturally shaped to correspond to the needs of the subsequent formation of structures, however, inflation does not depend at all on CDM and its properties.Let us now quickly review the formation of large scale structures.

The structure formation starts when inhomogeneities in the matter distribution are sufficient to generate a gravitational attraction larger than the expansion rate. This happens first for small perturbations in the matter power spectrum. The behavior of this first step towards the gathering of matter can be followed by a linear treatment: overdensities get denser, underdensities become more diluted. The formation of the first structures, such as galaxy haloes and galaxy clusters –depending, of course, upon the size of the original inhomogeneity in the matter power spectrum– follows in a non-linear regime. From this point on the analytic treatment is trickier, but estimations can still be done. However this suggested the simulation solution, giving birth to N-body simulations. Indeed, a successful treatment of this problem is achieved by numerically following the formation of structures with billions of particles –though these particles are not elementary particles but rather large ($\gg M_\odot$, where $M_\odot$ is the mass of the Sun) groups of them–, from an initial power spectrum in agreement with the CMB to the present time.

However, these simulations do not account for the formation of galaxies nor stars, they just set the frame in which the baryonic objects are born. In principle, if a local collapsing patch of matter is large enough then baryons are trapped in the gravitational well together with the CDM. Nevertheless, if CDM is indeed an explanation of the formation of large

scales, namely of galaxy clusters and galactic haloes, it does not provide a mechanism for the formation of smaller objects such as stars or the baryonic component of galaxies. That particular problem is understood by an empiric model, the details of the mechanism being still in exploration. While kept bound by the gravitational potential, baryons start reaching densities that trigger radiative energy losses via electromagnetic interactions, and thus lose most of their energy, washed away by the emission of photons. This is the birth of proto-galaxies, large clouds of cooling gas which lead, eventually, to the formation of the earliest stars and galaxies. It is only due to the energy loss accretion that baryonic matter organizes in disk structures. DM particles, however, interacting at smaller rates, do not suffer from energy losses and remain distributed in spherically symmetric haloes, as a first approximation. Nevertheless, the gravitational interplay between the planar distribution of baryons and the surrounding DM has an impact in the shape of the DM halo thus formed. Also, in the central regions in haloes, the density is large enough for the treatment of the equilibrium states of both baryons and DM is not trivial. Thus, the late interactions between the baryons and the DM, distributed in quite different shapes, and sharing the very dense center of structures, give large uncertainties to the estimations of the actual distribution of the DM.

Large scale structures can be observed. Indeed, surveys of gravitational lensing can probe the distribution of matter, giving sizes, mass content and shapes as a function of the redshift. This way, the predicted formation of structures can be tested. The agreement is incontestable. The mechanism thus provided by the ΛCDM model is very successful in describing the formation of structures.

While the presence of baryons always implies the presence of CDM, the inverse is not necessarily true. Indeed, for halo masses above $(10^{11} - 10^{12})\,M_{\odot}$, the presence of baryons is always observed, whereas below $(10^{6} - 10^{7})\,M_{\odot}$ the presence of baryons is not observed. The latter mass range corresponds to the smallest dwarf galaxies observed[1]. Lighter structures are thus expected to be made entirely of DM. The evolution of the power spectrum in ΛCDM predicts these dark objects to exist down to scales of $\sim 10^{-6} M_{\odot}$, corresponding to $\sim 0.1\,A.U. \simeq 5 \times 10^{-7}\,pc$ with almost scale invariant abundances [37].

Since the smaller scale objects collapse earlier, they may fall into the larger haloes in later times, phenomenon that has been observed in N-body simulations. This yields a large number of satellites or even local overdensities in haloes. These have not been observed (not gravitationally nor, obviously, by any DM signal) and represent a challenge to the ΛCDM picture. Indeed, the smallest scales formed account for a rather small free streaming distance of the DM since the decoupling time, typically of this scale because of its cold nature. However, the smallest scales proven to exist, the dwarf galaxies observed, are not smaller than $\sim 1\,kpc$. If smaller structures were simply absent in the Universe, then warmer DM is

[1] This also corresponds to the Jeans mass of the system, mass below which baryonic pressure prevents gravitational stability for baryonic clouds and gravitational collapse for star formation, see [5].

needed, thus free streaming up to this scale in order to wash out the smaller structures. For the moment small dark satellites and local overdensities are absent, which is giving attention to the possibility of the DM being WDM rather than CDM.

3.2 Halo models and Dark Matter in the Milky Way

In order to identify the particle DM at present times we need to track the CDM in the surrounding Universe in great detail. In particular it is important to have as much information as possible about the distribution of the DM in the close-by objects and their velocities.

3.2.1 The standard halo

The scale invariance of the halos is also encountered in their shape. Early analytic considerations predicted radial density profiles with a steep power law as a function of r and of constant slope. However, N-body simulations have greatly improved the simplistic analytic models and have shown that the density profile has more features than just a power law [38]. Furthermore, a universal shape has been found independently of the mass of the halo, the initial power spectrum, and even the model of Cosmology as long as it assumes the DM to be explained by particle physics [39]. In such early data analysis the authors showed that the DM density can be fitted by the Navarro-Frenk-White (NFW) profile

$$\rho^{NFW}(r) = \frac{\rho_s r_s^3}{r(r_s+r)^2},$$

where r_s is a scale radius satisfying $\frac{d\,ln\rho}{d\,lnr}|_{r=r_s} = -2$ and $\rho_s = 4\rho(r_s)$ is a scale density. The scale radius r_s represents the transition from the innermost $\rho \propto r^{-1}$ to a steeper distribution at larger scales $\rho \propto r^{-3}$. For a MW sized galaxy r_s is taken to be $r_s = 20\,kpc$. The distance of the Sun to the galactic center of the MW (GC) is estimated at $r_\odot \simeq 8.5\,kpc$, while a local DM density of $\rho_\odot \simeq 0.3\,GeV\,cm^{-3}$. Solving ρ_s for these values gives $\rho_s \simeq 0.26\,GeV\,cm^{-3}$. Regarding the velocity distribution, it is observed to be isotropic, with the marginal exception of radial velocity dispersions at the outermost regions of the halo, which can be attributed to the continuous accretion [40]. Such an isotropic distribution yields a Maxwellian distribution with a cut-off at $v = v_{esc}$, the escape velocity of the system. Such a distribution needs a characteristic velocity, which for the MW is the mean dispersion velocity at the Sun radius v_0. Thus, the velocity distribution in the galactic frame reads

$$f(v) = \frac{4N}{\sqrt{\pi}v_0} exp\left(-\frac{v^2}{v_0^2}\right) \times \Theta(v_{esc}-v),$$

where N is a normalization constant, and the local velocity dispersion and escape velocity are estimated to be $v_0 \simeq 220\,km\,s^{-1}$ and $v_{esc} \sim (575-700)\,km\,s^{-1}$. This halo description has

become the standard DM density profile, widely used in all theoretical predictions for DD and ID, as well as in experimental data analysis to infer limits upon the DM interactions.

3.2.2 Drawbacks of the Navarro-Frenk-White-Maxwellian picture

Some deviations from the original NFW profile have been observed regarding the shape of the simulated haloes: it is not exactly spherical, but triaxial, with axis ratios of $b/a \sim c/b \sim (0.6-0.8)$. Furthermore, in [41] a revision of the DM density fitting N-body simulation haloes suggests that these are best described by the Einasto profile [42]:

$$\rho^E(r) = \rho_E exp\left(-\frac{2}{\alpha}\left(\left(\frac{r}{r_s}\right)^{\alpha} - 1\right)\right),$$

where r_s plays the same role as in the NFW profile, and α is characteristic of the haloes. The best fit gives $r_s \simeq 21.5\,kpc$ and $\alpha \simeq 0.17$. Using $r_\odot = 8.5\,kpc$ and $\rho_\odot = 0.3\,GeV\,cm^{-3}$, we get $\rho_E \simeq 0.054\,GeV\,cm^{-3}$ for the MW. The main difference between the Einasto and the NFW profiles is found towards $r \ll r_s$. Indeed, the Einasto profile yields a relative flattening towards the center of the structure. This is crucial for ID, since we expect the DM to annihilate the most were it is more concentrated. However, the discrepancy manifests for rather small radii. For example, for the MW parametrization, at $r = 10\,pc$ they differ by a factor ~ 2, while at $r = 1\,pc$ this factor is of ~ 6.5. This means that the observation of sizeable effects of the distribution would need high angular resolution detectors. Conversely, a low resolution observation of the core of a DM halo averages the uncertain inner region contributions over the solid angle, hence yielding smaller influence on uncertainties –and eventually a null effect if the resolution is sufficiently poor.

Furthermore, the fit of rotation curves is best performed by cored profiles, with flatter profiles in the inner halo. This is particularly true for low surface brightness galaxies, corresponding to dSphs, thus DM dominated objects. In such objects the NFW profile fails to fit the data [43]. This calls for a detailed study of the influence of baryons on the halo formation, problem which is so far beyond the N-body simulation reach.

Canonical values of the local DM density are also in discussion. While the standard density at Sun's position is always taken at $0.3\,GeV\,cm^{-3}$, there are arguments to believe it slightly larger. In a profile independent analysis, it has been shown that $\rho_\odot = (0.42 \pm 0.15)\,GeV\,cm^{-3}$ [44]; and in a Bayesian analysis it was determined that $\rho_\odot = (0.385 \pm 0.027)\,GeV\,cm^{-3}$ for an Einasto profile and $\rho_\odot = (0.389 \pm 0.025)\,GeV\,cm^{-3}$ for a NFW profile [45]. Hence, larger local densities seem to be favored.

The Maxwellian distribution is been questioned. Indeed, while more recent N-body simulations tend to show a deviation from the Maxwellian distribution, especially towards the outskirts of the haloes, the observation of rotation curves and derivations from first principles also point towards fundamental differences (see, for example [46] and references therein).

Isotropic but not Maxwellian configurations behave closer to observations and yield smaller escape velocities. In [46] it was shown that for a double power law density profile, the corresponding isotropic velocity distribution yields $v_0 = (200-280)\,km\,s^{-1}$ –though in agreement with the standard picture, this shows the very large uncertainties persisting in the most recent estimations– and $v_{esc} = (498-608)\,km\,s^{-1}$ at 90% confidence level. Furthermore, anisotropies are actually expected from tidal effects or violent relaxation processes in stellar formation. In addition, the velocity dispersion can be traced by the older halo stars. These measurements show a large tangential dispersion of about $80\,km\,s^{-1}$, and radial dispersion three times larger. There is no reason to think these stars should exactly trace the DM velocities, but since they have formed in very early stages of the halo formation and have been moving since then only in a gravitationally shaped trajectory, they can suggest the kind of dispersion suffered at the early stages of star formation by the matter in the halo. DM could have inherit some dispersion as well, though hardly larger than the observed (see [47] for a discussion in the subject).

Since the DM is present around us, in the MW and in the local structures, we expect observable effects. The possibility of observing collisions of DM particles and nuclei at Earth constitutes the principle of DD (see Sec. 4.2), while the detection of subproducts of galactic DM annihilations is the complementary ID technique (see Sec. 4.3). While, on one hand, the details of the interaction rates we may expect or constrain by these experimental techniques, the determination of the DM density and velocity distributions is a key point for the interpretation of the outcome of both DD and ID.

Bibliography

[1] P. de Bernardis et al. A Flat Universe from High-Resolution Maps of the Cosmic Microwave Background Radiation. *Nature*, 404:955–959, 2000.

[2] S. Perlmutter et al. Measurements of Omega and Lambda from 42 High-Redshift Supernovae. *Astrophys. J.*, 517:565–586, 1999.

[3] Adam G. Riess et al. Observational Evidence from Supernovae for an Accelerating Universe and a Cosmological Constant. *Astron. J.*, 116:1009–1038, 1998.

[4] S.R. Folkes, S. Ronen, I. Price, O. Lahav, M. Colless, et al. The 2df galaxy redshift survey: spectral types and luminosity functions. *Mon.Not.Roy.Astron.Soc.*, 308:459–472, 1999.

[5] Steven Weinberg. Cosmology. Oxford, UK: Oxford Univ. Pr. (2008) 593 p.

[6] Yannick Mellier. Gravitational lensing and dark matter. 2010.

[7] Douglas Clowe et al. A direct empirical proof of the existence of dark matter. *Astrophys. J.*, 648:L109–L113, 2006.

[8] J.R. Brownstein and J.W. Moffat. The Bullet Cluster 1E0657-558 evidence shows Modified Gravity in the absence of Dark Matter. *Mon.Not.Roy.Astron.Soc.*, 382:29–47, 2007.

[9] E. Komatsu et al. Seven-Year Wilkinson Microwave Anisotropy Probe (WMAP) Observations: Cosmological Interpretation. *Astrophys.J.Suppl.*, 192:18, 2011.

[10] Edward Kolb and Michael Turner. *The early universe*. Perseus Books, 1989.

[11] Torsten Bringmann and Stefan Hofmann. Thermal decoupling of WIMPs from first principles. *JCAP*, 0407:016, 2007.

[12] Mordehai Milgrom. MOND: A pedagogical review. *Acta Phys.Polon.*, B32:3613, 2001.

[13] Jacob D. Bekenstein. Relativistic gravitation theory for the MOND paradigm. *Phys. Rev.*, D70:083509, 2004.

[14] H.J. de Vega and N.G. Sanchez. Model independent analysis of dark matter points to a particle mass at the keV scale. *Mon.Not.Roy.Astron.Soc.*, 404:885, 2010.

[15] H.J. de Vega, P. Salucci, and N.G. Sanchez. The mass of the dark matter particle from theory and observations. 2010.

[16] Geraldine Servant and Timothy M. P. Tait. Is the lightest Kaluza-Klein particle a viable dark matter candidate? *Nucl. Phys.*, B650:391–419, 2003.

[17] S. Nussinov. Technocosmology: could a technibaryon excess provide a 'natural' missing candidate? *Phys.Lett.*, B165:55, 1985.

[18] John Preskill, Mark B. Wise, and Frank Wilczek. Cosmology of the Invisible Axion. *Phys.Lett.*, B120:127–132, 1983.

[19] Pierre Fayet. Supersymmetry and Weak, Electromagnetic and Strong Interactions. *Phys.Lett.*, B64:159, 1976.

[20] Z. Ahmed et al. Dark Matter Search Results from the CDMS II Experiment. *Science*, 327:1619–1621, 2010.

[21] E. Armengaud et al. Final results of the EDELWEISS-II WIMP search using a 4-kg array of cryogenic germanium detectors with interleaved electrodes. 2011.

[22] E. Aprile et al. Dark Matter Results from 100 Live Days of XENON100 Data. *Phys.Rev.Lett.*, 2011. Long author list - awaiting processing.

[23] R. Bernabei, P. Belli, F. Cappella, R. Cerulli, C.J. Dai, et al. New results from DAMA/LIBRA. *Eur.Phys.J.*, C67:39–49, 2010.

[24] C.E. Aalseth et al. Results from a Search for Light-Mass Dark Matter with a P-type Point Contact Germanium Detector. *Phys.Rev.Lett.*, 106:131301, 2011.

[25] C.E. Aalseth, P.S. Barbeau, J. Colaresi, J.I. Collar, J.Diaz Leon, et al. Search for an Annual Modulation in a P-type Point Contact Germanium Dark Matter Detector. 2011.

[26] J. Billard, F. Mayet, C. Grignon, and D. Santos. Directional detection of Dark Matter with MIMAC: WIMP identification and track reconstruction. 2011.

[27] Oscar Adriani et al. An anomalous positron abundance in cosmic rays with energies 1.5-100 GeV. *Nature*, 458:607–609, 2009.

[28] S. R. de Groot, W. A. van Leeuwen, and Christianus G. van Weert. *Relativistic kinetic theory : principles and applications*. North-Holland Pub. Co. ; Elsevier North-Holland, Amsterdam, New York, 1980.

[29] Jeremy Bernstein. *Kinetic theory in the expanding universe*. Cambridge monographs on mathematical physics. Cambridge Univ. Press, Cambridge, 1988.

[30] Paolo Gondolo and Graciela Gelmini. Cosmic abundances of stable particles: Improved analysis. *Nucl. Phys.*, B360:145–179, 1991.

[31] D. Larson et al. Seven-Year Wilkinson Microwave Anisotropy Probe (WMAP) Observations: Power Spectra and WMAP-Derived Parameters. *Astrophys. J. Suppl.*, 192:16, 2011.

[32] G. Bélanger, F. Boudjema, A. Pukhov, and A. Semenov. micrOMEGAs 2.0.7: A program to calculate the relic density of dark matter in a generic model. *Comput.Phys.Commun.*, 177:894–895, 2007.

[33] Kim Griest and David Seckel. Three exceptions in the calculation of relic abundances. *Phys.Rev.*, D43:3191–3203, 1991.

[34] Massimiliano Lattanzi and Joseph I. Silk. Can the WIMP annihilation boost factor be boosted by the Sommerfeld enhancement? *Phys.Rev.*, D79:083523, 2009.

[35] Lawrence J. Hall, Karsten Jedamzik, John March-Russell, and Stephen M. West. Freeze-In Production of FIMP Dark Matter. *JHEP*, 1003:080, 2010.

[36] James E. Taylor. Dark Matter Halos from the Inside Out. *Advances in Astronomy*, 2011.

[37] Jurg Diemand, Ben Moore, and Joachim Stadel. Earth-mass dark-matter haloes as the first structures in the early universe. *Nature.*, 433:389–391, 2005.

[38] Julio F. Navarro, Carlos S. Frenk, and Simon D.M. White. The Structure of cold dark matter halos. *Astrophys.J.*, 462:563–575, 1996.

[39] Julio F. Navarro, Carlos S. Frenk, and Simon D.M. White. A Universal density profile from hierarchical clustering. *Astrophys.J.*, 490:493–508, 1997.

[40] Julio F. Navarro, Aaron Ludlow, Volker Springel, Jie Wang, Mark Vogelsberger, et al. The Diversity and Similarity of Cold Dark Matter Halos. 2008.

[41] D. Merritt, A. W. Graham, B. Moore, J. Diemand, and B. Terzić. Empirical Models for Dark Matter Halos. I. Nonparametric Construction of Density Profiles and Comparison with Parametric Models. *The Astronomical Journal*, 132:2685–2700, December 2006.

[42] J. Einasto and U. Haud. Galactic models with massive corona. I - Method. II - Galaxy. *Astronomy and Astrophysics*, 223:89–106, October 1989.

[43] Rachel Kuzio de Naray, Stacy S. McGaugh, and J.Christopher Mihos. Constraining the NFW Potential with Observations and Modeling of LSB Galaxy Velocity Fields. *Astrophys.J.*, 692:1321–1332, 2009.

[44] P. Salucci, F. Nesti, G. Gentile, and C. F. Martins. The dark matter density at the Sun's location. *Astron. Astrophys.*, 523:A83, 2010.

[45] Riccardo Catena and Piero Ullio. A novel determination of the local dark matter density. *JCAP*, 1008:004, 2010.

[46] Mariangela Lisanti, Louis E. Strigari, Jay G. Wacker, and Risa H. Wechsler. Dark matter at the end of the galaxy. *Phys. Rev. D*, 83(2):023519, Jan 2011.

[47] Anton N. Baushev. Principal properties of the velocity distribution of dark matter particles on the outskirts of the Solar System. 2011.

II

PARTICLE DARK MATTER: CONSTRAINTS AND MODELS

4 Cosmological and Astroparticle constraints

4.1 Early Universe constraints

Taking into account the chemical and thermal decoupling of DM particles from the thermal bath implies estimating the possible effects –those needed and those to be avoided– of these particular transitions in ongoing and subsequent processes in the evolution of the Universe. Thus, a model providing a DM candidate has to fulfil requirements and not overcome constraints, both linked with the influence of the thermal presence of DM particles in the EU.

4.1.1 Primordial nucleosynthesis

One of the most strikingly successful features of the standard Cosmology picture is the explanation of the synthesis of light elements in the EU. On one hand it predicts the abundance of hydrogen and helium, the main components of baryonic matter, to a high consistency with observations. It has minor but persistent drawbacks, such as the prediction of the subdominant lithium abundance. While the measurement of relative abundances by observation at all scales of the universe, specially by focusing in those systems which have experienced little nuclear evolution since the EU, is not an easy task, the origin of the discrepancy between the current state of observations and the predictions from ΛCDM is still undetermined. This suggests some room for BSM physics to help solving the problem. However, the impact of the participation of BSM particles has to leave untouched the well behaving part of primordial nucleosynthesis. We will follow descriptions from [1, 2] in what follows.
Nucleosynthesis occurs when nucleons have not enough energy to escape bound states, such as nuclei. Since in EU neutrons and protons are sufficiently coupled to other SM particles, they are in thermal and chemical equilibrium. Thus, when they decouple, bound states may form. However, the decoupling of protons and neutrons happen way later than the standard FO picture. Indeed, the decoupling depends upon the small mass difference between neutrons and protons rather than the individual masses. EW reactions ensure the good thermal contact between neutrons and protons, and electrons and neutrinos via the following interac-

tions

$$n + \nu_e \rightleftarrows p + e^-,$$
$$n + e^+ \rightleftarrows p + \bar{\nu}_e,$$
$$n \rightleftarrows p + e^- + \bar{\nu}_e.$$

Since the frozen amount of protons and neutrons (total and relative) is the ingredient of the current abundance of nuclei (total and relative), the FO transition of nucleons is the first step to compute the yield in nuclei. Following the Boltzmann equations of nucleons and electron and neutrinos coupled through the EW interaction mentioned above leads to the determination of the neutron FO temperature at roughly

$$T_{nFO} \simeq \left(\frac{\sqrt{g_*}}{m_{Pl} G_F}\right)^{\frac{1}{3}} \simeq 1\,MeV,$$

where G_F is the Fermi coupling constant. While the FO temperature does not depend upon the nucleon masses, the relative amount of neutrons surviving this transition does. Indeed, assuming that at FO $X_n^{FO} \simeq X_n^{eq}$ where $X_n = n_n/(n_p + n_n)$ is the fraction of number density of neutrons among total number density of nucleons and X_n^{eq} is this value at equilibrium. The latter is set by the equilibrium distributions of both protons and neutrons, and since at FO both are non-relativistic, we have

$$X_n^{FO} \simeq X_n^{eq} \simeq \frac{1}{1 + exp\left(\frac{\Delta m}{T_{nFO}}\right)}$$

where $\Delta m \simeq 1.29\,MeV$ is the neutron-proton mass splitting. Notice that $\Delta m/T_{nFO} \simeq 1$, hence the yield of neutron fraction is not at all negligible. Indeed, $X_n^{FO} \simeq 27\%$. This implies that nuclei containing both neutrons and protons form in EU. Moreover, the Helium nucleus having a large binding energy, most surviving neutrons are eventually trapped in Helium nuclei. However, between freeze out and the nuclei formation, neutrons experience β-decay into protons, electrons and anti-neutrinos.

The start of formation of stable nuclei is determined by nuclear interaction rates. Indeed, while the binding energy of Helium is $\sim 7\,MeV$, the nuclear reaction chain that leads to its formation is slow enough for this to happen later than at an equivalent temperature of the nucleons. Following the evolution of neutron fraction by including the subsequent losses from decay down to $T_{NS} \simeq 86\,keV$ [3], the temperature at which deuterium, the first bound state to be formed, traps the neutrons, sets a fraction of 12.2% of neutrons [3]. Assuming most neutrons follow the formation of deuterium, tritium, ^3He and eventually are stabilized in ^4He, and knowing that there are two neutrons per ^4He nucleus, this yields 24.5% [3] of helium nuclei, the remaining being mostly protons, thus Hydrogen atoms in the older Universe. This is a rough estimate, but it sets the trend with a spectacular agreement with

observational data, as it will be commented later on.
A more complete treatment of the determination of relative nucleic abundances includes revising in detail the first nuclear reactions. The formation of Deuterium follows mainly from

$$p + n \rightleftarrows \gamma + D$$

reactions. These include thus the participation of photons, which are still in chemical equilibrium in the plasma. Thus, the photons being numerous, the rate of this interaction is sufficient to keep Deuterium in chemical equilibrium. With decreasing temperature further nuclear reactions yield the formation of the heavier nuclei, including in particular ^4He and ^7Li. Since the presence of D is a must for the rest of the nucleosynthesis process, the relative abundance of baryons to photons η is a key quantity to determine the precise final yields of the nuclear reaction chain. Thus, including the influence of η gives a set of abundances where this relative abundance is the only external parameter to be measured to complete the picture (notice that nuclear reactions carry their theoretical uncertainties relaxing a little the intervals for the abundances allowed for a given value of η). Fortunately η can be measured in the CMB by the peak of the blackbody spectrum generated by the decoupling of photons and baryons. Indeed, $\Omega_b h^2 \simeq 3.65 \times 10^7 \times \eta$. By confronting the observed abundances to the theoretical predictions for a measured η fixes the baryon abundance. This is once again evidence for the need of DM, since for $\eta \simeq (6.190 \pm 0.145) \times 10^{-10}$ [4] this exercise yields $\Omega_b h^2 \simeq 0.0226$, which is much lower than the measured value of $\Omega_M h^2$.
The success of primordial nucleosynthesis lies in the very good agreement between the observed relative abundances and the prediction. Nevertheless, the measurement of the relative abundances is far from being obvious. For a detailed discussion see [1]. The results show an overall agreement for most predictions, but for ^7Li where the theory overpredicts the relative abundance by a factor $\sim (2-3)$. This discrepancy has survived the many reconsiderations done, including the search for unaccounted effects in the nuclear reaction rates estimations.
Discussing the relation between DM and primordial nucleosynthesis can be viewed in two different ways. First of all, DM is generally a feature of a BSM including more particles and interactions. The Cosmology has to be thus explained by this BSM entirely. This implies that the BSM has to add little difference to the primordial nucleosynthesis, since it is well established and relies only upon SM physics –although it yields an argument for the insufficiency of the SM to explain $\Omega_M h^2$. We have argued that the chemical decoupling of DM yields some influence on the thermal bath, namely in its entropy, deeply related to the effective degrees of freedom of the plasma. In turn, primordial nucleosynthesis sets the present particles in thermal contact at the $T_{nFO} \simeq 1\,MeV$ and $T_{NS} \simeq 86\,keV$ temperatures. Thus, a DM particle experiencing its chemical decoupling around these temperatures would yield instabilities which might affect the nucleosynthesis process. Furthermore, if DM is still rel-

ativistic at these temperatures, it has an influence in their determination and thus changes the estimation of the time at which neutrons decouple and the subsequent nuclear chain of reactions happens. CDM is, in most cases, expected to experience FO before the beginning of primordial nucleosynthesis, because of its mass. However, for the lighter CDM possibilities, precautions have to be taken about its FO temperature in order to avoid disturbing the synthesis of light elements. Its further kinematic equilibrium has little impact in the fate of the species in the thermal bath, hence does not represent a feature to be cautious about. Second, and in a more constructive way, one could imagine that the discrepancy in the Lithium relative abundance could be solved by BSM theories. These efforts require a detailed treatment of all the possible influences a BSM theory could have in the entire process, namely in nuclear reactions and in temperatures in the thermal bath. In this work we restrain our DM models to have no impact on the primordial nucleosynthesis of light elements.

4.1.2 Dark Matter imprints in the CMB

As it was discussed in Sec. 1.2.2, kinetic decoupling typically occurs well after chemical decoupling. Indeed, the number of targets for elastic scattering, i.e. thermal particles, is not Boltzmann suppressed after FO. Decoupling occurs when the interaction rate keeping the DM in thermal contact with the plasma falls below the expansion rate. It has been shown that for DM interactions of the EW strength with light SM fermions this transition is expected to happen at $T_{kd} \sim m_{DM}^{1/4} m_Z / (m_{Pl}^{1/4} (G_F m_W^2)^{1/2}) \sim O(110)\,MeV$ [5], when neutrinos and electrons are indeed still relativistic and thus well represented in number density. See also [5] for more detailed and precise estimations of T_{kd} by expanding the squared amplitude of the interactions responsible for elastic scattering around the decoupling temperature.
After decoupling, though, the scattering rate is still large enough to allow some interactions. In other words kinetic decoupling is not equivalent to the last scattering surface of DM. These interactions can indeed affect the density distribution and therefore the size of inhomogeneities of the DM. The transition between an interacting fluid state of the DM particles to a kinetic state in which particles freely stream in a gravitational field is obtained by the dilution of the elastic scattering rate, but in between there is a compromise between both. The late interactions maintain the temperature of the DM closer to the bath temperature than the temperature of a completely decoupled particle. Thus, the velocity of the particles is maintained by these collisions.
Kinetic decoupling sets the beginning of an era of free streaming of DM particles. After this transition, particles will keep the initial inhomogeneities in the matter power spectrum down to the total free streaming length until the gravitational collapse starts. Hence the free streaming length sets the scales of the structures that will form. Then, the matter power spectrum, dominated by CDM, evolves with gravity. The collapse of particles starts first for the smallest inhomogeneity scales. However, a fundamental cut-off must exist in order to

explain the size of the smallest structures we observe, which is that of stars and galaxies. The smaller inhomogeneities are also imprinted in the CMB anisotropies, but at larger multipoles. That is why precision measurements by Planck can throw some light on the kinetic characteristics of DM from kinetic decoupling to the last scattering moment.

Two classes of DM can reproduce the matter power spectrum, which is measured in the CMB. Indeed, the fluctuations in the initial –in the sense of the beginning of structure formation– matter power spectrum can be extracted from the multipole analysis of the CMB anisotropies. The greater the precision, the larger multipoles that can be attained, the smaller the fluctuations that can be measured, the smaller the scale of the smallest structures predicted. Thus, high precision measurements give upper limits to the smaller inhomogeneities needed. We already argued that the main component of the matter power spectrum is DM, hence its shape constrains the DM physics. In particular, the size of the smaller fluctuations measured has to be respected by the DM evolution since decoupling. If the DM is sufficiently rapidly moving after kinetic decoupling, then the free streaming by itself would wash out the small scale inhomogeneities. Larger velocities at decoupling time mean that the kinetic decoupling transition happened for temperatures closer to the mass of the particle. It has been shown that relativistically decoupling particles erase scales down to equivalent fluctuations that have been extracted from CMB. Also, the absence of such fluctuations makes hard to explain the formation of the smallest structures observed. Thus, DM decoupling at high temperatures compared to its mass, so called Hot DM (HDM), is ruled out. However, CDM is not the only consistent model for decoupling the DM. Between the relativistic regime at decoupling and the cold decoupling of, for example, a typical WIMP, lies the quasi-relativisitc regime. Particles decoupling in these conditions are called WDM. For typical interaction rates, WDM would have masses of $\lesssim O(MeV)$.

The late interactions of DM, either cold or warm, with the radiative components of the Universe between kinetic decoupling and the last scattering surface can wash out the inhomogeneities that would yield unobserved structures, and would otherwise be kept by the free streaming at lower velocities of the particles. In some sense, the radiative, faster particles, would collide with inhomogeneities giving enough momentum to some DM particles to escape the well in which they had been gathered. The effect was first shown to happen for photons, thus at the recombination time when photons started diffusing with large mean free paths. The mechanism is called diffusion damping or Silk damping [6]. However, photons are not coupled to the DM, thus the effect of photon diffusion is mostly applied to the baryonic overdensities. Baryons can then transmit to the DM the Silk damping they experienced. Though, the effect is generic in the sense that neutrino diffusion can also transmit enough energy to reduce small scale overdensities, if they are coupled to the DM. This is called collisional damping [7, 8]. Finally, for warm enough DM, its self-interactions can also contribute to the collisional damping. See [7] for a detailed discussion.

Another impact of DM particles in the CMB is the injection of energy through annihilation into SM particles. Indeed, this would inject energetic electrons, positrons and photons. The effect is the ionization of the medium and the subsequent modification of the opacity encountered by the decoupled photons. The standard ionization history is obtained by following the Boltzmann equation of photons after decoupling, and contains both an effective recombination rate and an effective photoionization rate stemming from the presence and temperature of baryons. The effect on CMB photons depends on the free-electron fraction. The injection of energetic particles by DM annihilations increases the standard value of the free electron fraction, which induces a damping of the photon anisotropies. Hence, the ionization history from redshift ~ 1000 up to now leaves traces in the CMB photons, particularly at high multipoles (small scale anisotropies). Stringent limits on the cross section vs. mass plane have been already obtained with WMAP, and Planck will scan the light WIMP range down to $\langle \sigma v \rangle \simeq 10^{-27}\, cm^3\, s^{-1}$ for a $10\, GeV$ DM particle (see [9, 10] for a detailed and updated description of this effect).
With all these considerations, we see that by the observation of the large scale structure of the Universe and the CMB anisotropies, the elastic scattering interactions of CDM with the lighter leptons and radiation can be constrained. This, in turn, can give important information about what models can and cannot imply regarding interactions rates, thus, representing a constraint to be respected. A thorough study on these constraints has been performed in [8]. The typical WIMP candidate behaves as CDM and is not yet heavily constrained by these considerations, while we are waiting for the forthcoming results of Planck, whose striking precision will enhance the analysis by including higher multipoles, thus attaining information so far hidden in unobserved precision CMB features.

4.2 Direct Detection techniques

The presence of DM in the MW with a local density of about $0.3\, GeV\, cm^{-3}$ and a relative velocity of a few hundred $km\, s^{-1}$ implies that we are permanently surrounded and run through by CDM particles. If these were thermally produced in EU, then they weakly interact with SM particles. The possibility of DM particles leaving an imprint in detectors at Earth by colliding with nuclei and giving them a certain amount of detectable recoil energy is what we call the DD of DM. This possibility was first pointed to by Goodman and Witten in 1984 [11]. Since then a lot of experimental progress has been achieved, scanning DM interaction cross sections down to $7 \times 10^{-45}\, cm^2$ [12]. Furthermore, future efforts will carry on the lowering of the sensitivity curves, exploring an important part of the $(5 - 2000)\, GeV$ mass range DM candidates interacting with nucleons. Nowadays, the field is very active: tens of collaborations are developing sophisticated techniques to improve the experiments, while new competitive results have been appearing with a high frequency. Let us discuss the

principles of detection, the current experiments and their results as well as the forthcoming detection searches.

4.2.1 The density of a Dark Matter candidate

Testing a given DM candidate with DD (and ID) detection requires the assumption of the knowledge of the density of the candidate at Earth for DD and at the system observed for DD. We have given the canonical NFW distribution which is widely used to model the DM distribution in the MW and in other systems. This allows to estimate the local density for interactions at Earth and wherever an indirect signal is expected to be produced and observed. The estimation of the density of a DM candidate relies on the knowledge of the relative abundance of DM in the Universe. Indeed, the density of DM particles in any object we may consider is a result of the DM evolution throughout cosmological ages. Thus, we take the hypothesis that the local density of DM assumed to be of $0.3\,GeV\,cm^{-3}$ corresponds to the measured density of DM $\Omega_{CDM}h^2 \simeq 0.11$.
However, a DM candidate i does not need to represent all the DM. As long as the candidate behaves as CDM, and the BSM sector provides another particle j (or whole sector of stable and neutral particles) also behaving as CDM, the sum of the total contributions from the i and j type of candidates to the global DM sector density is the value that has to exactly fit the observed DM density, namely $\Omega_i + \sum_j \Omega_j = \Omega_{CDM}$. Hence,

$$\xi = \frac{\Omega_i}{\Omega_i + \sum_j \Omega_j} = \frac{\Omega_i}{\Omega_{CDM}} \tag{4.1}$$

stands for the i fraction to the total density of DM. This factor is expected to be representative in local systems as well, since all CDM particles would suffer roughly the same fate since the generation of the matter power spectrum to the present state of structures. In the investigations discussed later on we give a more precise definition of ξ taking into account the lower limit of the 95% confidence level interval given by the WMAP 5-year results [13]. If the calculated relic density lies above this lower limit but below the upper bound, the contribution of the particle is set to 100%. Below the lower end of the measured interval the proportionality is assumed. Hence, for a given candidate, after computing its relic density $\Omega_i h^2$ and assuming that $\Omega_i h^2 \leq 0.1165$, we define

$$\xi = Min\left(\frac{\Omega_i h^2}{0.1097},\ 1\right). \tag{4.2}$$

Thus, for all DD (and ID) calculations depending upon the CDM candidate density in a given object, we scale the expected DM density in the object by the ξ factor, therefore $\rho_i = \xi\rho_{CDM}$.

4.2.2 The direct detection principle

The local DD of DM in the MW halo is possible by its energy deposition on nuclei in a terrestrial detector after a scattering event. In most cases, elastic scattering is assumed to be the mechanism to manifest –and we focus on this case–, however, inelastic scattering events could produce nuclear recoils as well. Such interactions depend upon the mass of the given nucleus, that of the DM particles and the relative velocity of the DM with respect to the Earth. In turn, the recoiled nucleus would transmit its energy to the surrounding media by ionizing it, or by transmitting phonons in case of a crystal detector. The expected event rate is low compared to the background. Thus, experiments have to deal with shielding and resolving all possible sources of background, such as neutrons, muons, electrons and possibly neutrinos running into the detector. Hence, experiments are usually realized underground, in mines or tunnels in order to benefit from the shielding of the surrounding rock. In the same order of ideas, the cryogenic technique is also common to various experiments, seeking to reduce the thermal noise. Also, it is suitable to have as many exposed nuclei as possible in order to increase the interaction probability. This means building detectors as large as possible and letting them run as long as feasible in stable conditions.

Dark Matter interactions with nuclei

The recoil energy of an elastic scattered nucleus is

$$E_R = \frac{\mu^2}{m_N} v^2 \left(1 - \cos\theta^*\right),$$

where μ is the reduced mass of the nucleus-DM system, m_N is the nucleus mass, v is the relative velocity and θ^* is the scattering angle in the center of mass frame. This yields an energy of $\sim 10\,keV$ for a ^{73}Ge nucleus, a $\sim 50\,GeV$ DM candidate and a relative velocity of $\sim 400\,km\,s^{-1}$. The DM velocity distribution being peaked at some $220\,km\,s^{-1}$, this implies that a low energy threshold of the detector is a particularly difficult and important feature to achieve. Furthermore, from the detection point of view, for a given recoil energy there is a minimum velocity required for the event, which is

$$v_{min} = \sqrt{\frac{E_R m_N}{2\mu^2}}.$$

If the threshold of a ^{73}Ge experiment is, say, $10\,keV$, thus it would be sensitive to $50\,GeV$ DM particles of velocities above $\simeq 192\,km\,s^{-1}$, and of $\simeq 634\,km\,s^{-1}$ for $10\,GeV$ particles. Moreover, the energy deposition is the most efficient for $m_N = m_{DM}$. Thus DD can test particles in the $(5-2000)\,GeV$ range.

Let us express the event rate following the description in [14]. The event rate includes an

integration over the velocity distribution of DM particles in the Earth reference frame, and a sum over the contributions of all the DM particle species. Also, the detection of the energy deposition E_{det} is at most that of the actual event: $E_{det} \leq E_R$. The K function takes into account the energy resolution of the detector. Finally a detector can contain more than one type of target nucleus, hence a sum over all possible recoiling nuclei has to be performed. Thus, the rate of detected events per unit time, per unit energy and per unit of detector mass is expressed by

$$\frac{dR}{dE_{det}} = \frac{\xi\rho_{\odot}}{m_{DM}} \int_{v_{min}}^{v_{esc}} \sum_{x=nuclei} N_{T,x} \left(\int_{E_{min}}^{E_{max}} K_x \left(E_{det}, E_R\right) \frac{d\sigma_x}{dE_R} \left(E_R, v\right) dE_R \right) v\, f\left(\vec{v}\right)\, d^3\vec{v},$$

where $N_{T,x}$ is the number of x type target nuclei per unit mass of the detector and $f\left(\vec{v}\right)$ is the velocity distribution of DM in the Earth frame.

The interaction cross section can generally be expressed by its DM-nucleon contributions split into a spin-independent (SI) and a spin-dependent (SD) interaction rates. Hence,

$$\frac{d\sigma}{dE_R} = \left(\frac{d\sigma}{dE_R}\right)_{SI,p} + \left(\frac{d\sigma}{dE_R}\right)_{SI,n} + \left(\frac{d\sigma}{dE_R}\right)_{SD,p} + \left(\frac{d\sigma}{dE_R}\right)_{SD,n}.$$

In many cases, such as the supersymmetric neutralino DM, the SI effective couplings to protons and neutrons λ_p and λ_n satisfy $\lambda_p \simeq \lambda_n$. Hence, SI interactions can usually be factorized giving a $\lambda_p A^2$ behavior (where A is the total number of nucleons). Indeed, the point-like nucleus cross section reads [15]

$$\sigma^{SI} = \frac{4\mu^2}{\pi} \left(\lambda_p Z + \lambda_n \left(A - Z\right)\right)^2 \simeq \frac{4\mu^2}{\pi} \lambda_p^2 A^2,$$

where Z is the number of protons in the nucleus. Thus, heavy nuclei enhance the SI interaction cross section.

The SD cross section can be expressed in terms of the total spin of a nucleus J, the mean values of the nucleon spins in the nucleus $\langle S_p \rangle$ and $\langle S_n \rangle$ and the ξ_p and ξ_n effective SD couplings of the DM particle to the nucleons. Thus, in the point-like approximation

$$\sigma^{SD} = \frac{16\mu^2}{\pi} \frac{J+1}{J} \left(\xi_p \langle S_p \rangle + \xi_n \langle S_n \rangle\right)^2.$$

The dominant component of the total spin of a nucleus is carried by its unpaired nucleons, in case it has an odd-number of protons and/or neutrons. An unpaired proton (neutron) implies $\langle S_p \rangle \left(\langle S_n \rangle\right) \simeq 0.5$, and an even number of protons (neutrons) yield $\langle S_p \rangle \left(\langle S_n \rangle\right) \simeq 0$. For SD interactions the effective couplings can be very different.

Thus, experiments can resolve the interpretations of the results in term of the individual processes, and give limits to the most sensitive cross section in their media. As an example, DM particles interacting with a ^{19}F nucleus, made of 10 neutrons and 9 protons, could yield limits on (or the observation of) SD DM-proton interactions, while the SI sensitivity is lesser

than in heavier nuclei such as ^{73}Ge or ^{131}Xe.
The point-like cross sections are a good approximation to understand the general behavior, however, their computation includes the estimation of the effective couplings of DM to nucleons. These couplings are estimated by the convolution of the fundamental quark-DM couplings and the quark form factors of the nucleons. In the case of SI interactions the $\lambda_p \simeq \lambda_n$ approximation holds precisely because of the similar behavior of SI energy dependent form factors for both nucleons, and the small dependence on the valence quark involved in the interaction. In the SD case, however, the difference in the quark content can yield quite different results for the nucleons, since the quark nature is determinant in the SD fundamental processes. See [15] for a discussion on the subject. In both cases, the precise knowledge of the quark content of the nucleons is required for a good estimation of the cross sections. This is a field which is still evolving, since it needs a compelling treatment of QCD processes.
Ideally the experiments are designed to be zero background experiments. This means that a negative result is translated into a zero total number of events integrated in the time and mass of exposure. Thus, the upper limit on interactions can be derived by imposing, for example, a 5% probability to have one or more events in the integrated exposure, and thus get an upper bound in the interaction rate at 95% confidence level for zero events. More sophisticated techniques are actually used for this case and for the case of some events recorded to derive the constraints, but this gives a rough idea of how cross sections can be excluded. The constraints that can be derived on cross sections have to be scaled to the relative abundance of the candidate at the Earth position ξ. This is a model dependent quantity, thus it is simpler to establish the limits –as experimental collaborations actually do– for $\rho_\odot$, and apply the ξ factor to the predicted interaction rate of the given candidate for a meaningful comparison between predictions and constraints.
Finally, throughout this brief description we have introduced many uncertain parameters. The DM density and the velocities at the Earth position, the comprehension of the behavior of detectors in the recollection of the recoil energies, the nuclear form factors entering the determination of the interaction cross sections, all these aspects call for a cautious use of the DD limits.

Annual modulation

The Earth is rotating around the Sun, the relative velocity is in constant oscillation. Since the interaction rate depends upon the velocity distribution, we expect to have a modulation effect in the count rate if events are to be observed [16]. It is the principle of annual modulation, which is looked for in long exposure rates of experiments such as DAMA and CoGeNT. Hence, while the average velocity, that of the Sun, gives a constant contribution to the total event rate, the annual modulated part accounts for a sinusoidal oscillation on top of it. The

Earth velocity projected in the galactic plane and expressed in the galactic frame is

$$v_E = v_\odot + v_\oplus cos\gamma\, cos\left(\omega(t-t_0)\right) = v_0 + \delta_\odot + v_\oplus cos\gamma\, cos\left(\omega(t-t_0)\right),$$

where $\delta_\odot = v_\odot - v_0 \simeq 12\,km\,s^{-1}$ is the Sun deviation from the local dispertion velocity, $v_\oplus \simeq 30\,km\,s^{-1}$ is the Earth's orbital velocity around the Sun, γ is the inclination of the solar system plane with respect to the galactic plane and $\omega = 2\pi\,yr^{-1}$ is the orbital pulsation of the Earth. Thus we would expect

$$\frac{dR}{dE_R} = \frac{dR}{dE_R}_{|v=v_\odot} + \left[v_\oplus cos\gamma \left(\frac{\partial}{\partial v} \frac{dR}{dE_R} \right)_{|v=v_\odot} \right] \times cos\left(\omega(t-t_0)\right) + O\left(\left(\frac{v_\oplus cos\gamma}{v_\odot} \right)^2 \right).$$

Directional detection

The directional detection technique exploits the fact that the Sun velocity in the galactic reference frame is non zero [17]. This means that we are running through a DM cloud in a particular direction. That direction is roughly that of the Cygnus constellation ($l_\odot = 90^\circ$ and $b_\odot = 0^\circ$ in galactic coordinates). To concretize such a detection implies solving the direction of the recoil track in the detector. To such purposes, low pressure fluid detectors made of rather light nuclei are needed in order to have a sizeable imprint of the recoil event. Light nuclei are more sensitive to SD interactions because of the relative weight of the odd nucleons in the light nuclei with respect to heavier ones. New observables (in addition to the interaction cross section and the DM mass entering the event rate) include the three velocity components of the local velocity dispersion vector. This technique is also dependent on the anisotropy of the velocity distribution, making urgent a good understanding of what shall be expected in this respect for the DM behavior in the halo.

4.2.3 State of the art

Positive results have been claimed by annual modulation DD experiments. Indeed, the DAMA collaboration has recently updated their data analysis by adding new data sets and thus show a 8.9σ modulation observation in cumulative exposure [18]. While the DAMA collaboration is not widely trusted by the community, and hard criticism has been issued to their treatment of the acquisition and analysis of the data, the recent CoGeNT claim for a modulated signal gives more credit to these observations [19]. In principle these results point towards an annual modulated signal. Nevertheless, the interpretation of these findings in terms of the observation of DM is not obvious, since there is not a thorough investigation on the modulated backgrounds that could be mimicking a DM modulated signal. However, if the signal turns to be due to DM particle, it would be a major discovery. The CoGeNT collaboration had previously claimed unresolved signals at low energies independently of the annual modulation [20]. Both detectors have low thresholds: $2\,keV$ for DAMA and $0.4\,keV$

for CoGeNT. In both cases, the signal is found to be a rise towards the energy threshold, thus implying rather light DM. Interpretations suggest masses from $7\,GeV$ to $15\,GeV$, for SI interactions of $7\times10^{-39}\,cm^2$ to $3\times10^{-40}\,cm^2$ (see [21] fot a recent discussion on the matter). This has triggered the reconsideration of SUSY DM at that particular scale as will be discussed in chapters 8 and 9.

Regarding null results, let us discuss the most stringent limits obtained so far. Originally the DD experiments were meant to be zero background detectors, however the latest data acquisitions show unresolved events. While these events pass all cuts, their origin is not necessarily well understood. However their characteristics strongly suggest that they are marginal neutron or electron recoils which have somehow escaped the event discrimination. Nonetheless, stringent limits can be derived, even assuming the background events to be DM signals. It is the case for all the most recent and competitive limits established. In December 2009 the CDMS-II collaboration published their analysis of $612\,kg\,days$ of data acquired with their cryogenic ^{73}Ge detectors. The analysis yielded two unresolved events. The probability of having two or more events from background nature was of 23%. This motivated the community to interpret these events as being of DM collision nature. The recoil energy measure were of $12.3\,keV$ and $15.5\,keV$ respectively, not far above the $10\,keV$ energy threshold. While based upon two events it is impossible to set the DM mass, this would point towards the $(10-60)\,GeV$ range. The exclusion limit established at 95% confidence level is in conflict with most of the DAMA preferred regions.

In 2010 the XENON100 collaboration published their first results. The experiment consists of $62\,kg$ of liquid ^{131}Xe with scintillation detectors to estimate the recoil energy. The results obtained with only 11.17 days of exposure yielded very stringent limits, achieving a sensitivity of $3.4\times10^{-44}\,cm^2$ for a $55\,GeV$ mass [22]. The exclusion limits would exclude the CoGeNT and DAMA regions. However, these results were severely questioned because of the treatment of the efficiency of the scintillators for recoil energies near the threshold. While there were no experimental studies about the threshold of the scintillators set at $8.7\,keV$, the first results were established by assuming a constant behavior below the value measured at the lowest energy of $\sim10\,keV$. This triggered a harsh discussion [23, 24, 25], since the lower end of the energy sensitivity is exactly the region which would exclude the light DM pointed out by DAMA and CoGeNT. A new limit was thus established by the XENON100 collaboration taking further precautions, however their treatment on the efficiency was indeed more sophisticated than just a constant extrapolation. It was the result of a global fit to the available data. Their result was practically unchanged. Furthermore, in 2011 XENON100 published a new statistical method for data analysis taking into account various uncertainties, such as systematic uncertainties in the energy scale of the detectors and astrophysical uncertainties such as the value of the escape velocity [26]. This was closely followed by new results based on $100\,days$ of data acquisition [12]. The latter are by far the most stringent limits on elastic

scattering, confirming the exclusion of the DAMA and CoGeNT regions, and attaining the impressive sensitivity to SI interactions of $7 \times 10^{-45}\, cm^2$ for a $50\, GeV$ DM mass. These results, though, included once again the presence of three unresolved events.

The best limits from ^{73}Ge detectors come after the EDELWEISS collaboration results [27]. This experiments consists on an array of ten $0.4\, kg$ detectors, and the data acquisition is of $384\, kg\, days$. They reported five nuclear recoil events while the background expectations yielded only three. Four of them lie really close to the $20\, keV$ threshold of the experiment. While their data alone is not better than the CDMS-II results, the two collaborations made a common analysis [28] lowering the CDMS-II results, though not substantially. The most stringent limits to the DM SI interactions are still those of XENON100.

In the SD sector the SIMPLE collaborations has recently published their latest results of their long-life superheated droplet detectors [29]. They consist in a total active mass of $0.215\, kg$ of C_2ClF_5 gas. With a threshold at $8\, keV$, this experiment has achieved a sensitivity of $4.3 \times 10^{-39}\, cm^2$ for a $35\, GeV$ DM particle, with null results. their limits are thus the most competitive in the σ_p^{SD} vs. m_{DM} plane. They also have shown limits for SI interactions, however these are competitive with XENON100 only for $m_{DM} \lesssim 6\, GeV$. However, it is important to note that in the σ^{SI} vs. m_{DM} plane they almost completely exclude the CoGeNT and DAMA preferred regions.

A new analysis on SuperKamiokande data also constrains the preferred regions for DAMA and CoGeNT [30]. Their study includes fully contained upgoing muons, and upward stopping events. This neutrino detector is sensitive to the neutrino flux from the Sun. They compute DM trapping and annihilation in the Sun, and their yielding in neutrinos for various fermionic annihilation channels. Thus, they deduce constraints in both SD-proton and SI cross sections. This is a very model dependent technique, but which is showing to be very competitive for those models falling into the SuperKamiokande analysis. The best neutrino detector results have been published by the IceCube collaboration [31], and their analysis already constrain enhanced DM annihilation [32], though these results have not yet been analyzed in light of elastic scattering interactions trapping DM in the Sun with subsequent annihilation into neutrinos. Such results are expected to come soon and give probably the most competitive sensitivity to SD-proton interactions so far, however for particles of masses $\lesssim 40\, GeV$. In the SD-neutron side, the best limits so far obtained are still those from the XENON10 experiment [33]. While the XENON100 experiment has, in principle, gathered enough data to push the sensitivity down by an order of magnitude at least, such an analysis has not been produced so far.

Regarding directional detection, the current state of the field is that of the development of prototypes, hence no results are yet available, at least not competitive results. Because of its good ionization properties and its nuclear composition, the CF_4 gas has been pointed out as a well adapted medium for a good sensitivity. Efforts are made by several collaborations, such

as DRIFT [34], DM-TPC [35], D^3 [36], Emulsions [37], NEWAGE [38] and MIMAC [39]. The prospects look promising. Not only the projected sensitivity to SD proton interactions will be significantly lowered by the first generation of detectors, but the perspectives of resolving the mass, the interaction cross section and even of constraining the halo models are exciting [40].

4.3 Indirect detection

The presence of particle DM in haloes with non-relativistic velocity dispersions makes the encountering of two particles a rare yet possible event. Depending upon the nature of the DM, it may annihilate and produce SM particles. These particles can decay, lose energy, diffuse, and maybe come to Earth to be observed. It is the principle of ID searches. The field is far from being simple. Indeed, while annihilations are more probable in the highest concentrations of DM particles such as in the GC of our MW, the medium in which the interactions occur is not necessarily well understood. The propagation of charged particles in the diluted yet possibly charged and magnetized ISM is a complicated process to be solved. However, measurements can be and are being done. Thus, fluxes are observed, in antiparticles and photons channels, the most promising indirect signals from DM. By comparing the results to the expected backgrounds from standard astrophysical processes –another difficult task and a whole subject by itself–, limits on the annihilation rates can be obtained, provided a certain parametrization of the DM halos and the propagation of the DM annihilation final states. We only treat the ID possibility in annihilating DM cases, and not in decaying DM.

4.3.1 Annihilation in galaxies

Self annihilating stable DM can only produce lighter, SM particles. Annihilation processes may occur wherever DM is present. The rate of annihilation depends upon the annihilation cross section σ, the relative velocity v of DM particles, and the DM density ρ_{DM}. As we have already discussed, for a DM candidate i the density could be less than that of the total DM contribution, thus, the predictions a given model would yield have to include this scaling. Since DM self annihilation depends upon the probability of presence of two particles, the rate of interaction depends upon the square of the density at the observed place.
Observations are made by detectors pointing towards a given region within the solid angle defined by the detector resolution. Thus, the estimation of the flux of particles received at Earth for any given process depends upon the integral over the line-of-sight (l.o.s.) l and within an angular opening ψ. The interaction rate and further decay into final states does not, in principle, strongly depends upon the choice of the observed direction, however the amount of DM at the interaction point does. If the medium between the production of the signal of a k species and Earth is completely transparent for the received particles, then the

energy spectrum dN_k/dE depends only upon the production process[1]. Hence, the flux at Earth of a given channel is usually split into two contributions: the so called astrophysical (dimensionless) $J(\psi)$ part and the particle physics part $\phi_k^{PP}(E)$ responsible for the production of the channel and its energy spectrum:

$$\begin{aligned}\phi_k(E,\psi) =& \left[\int_{l.o.s.} dl(\psi)\,\xi^2\rho_{DM}^2(l(\psi))\right] \times \left[\frac{1}{2}\frac{\langle\sigma v\rangle}{4\pi m_{DM}^2}\frac{dN_k(E)}{dE}\right] \\ =& J(\psi)\times\phi_k^{PP}(E)\,.\end{aligned}$$

Note that the annihilation rate $\langle\sigma v\rangle$ is averaged for the characteristic range and distribution of velocities of the observed object. However, little spread is actually expected, since all objects at present contain cold DM, thus we are always in the non-relativistic regime. Large enhancements or suppressions with respect to the EU annihilation rates can indeed occur, since here the expected velocities are of $v \sim (10^{-4} - 10^{-2}) \times c$ depending on the medium observed. This might lead to a $p-wave$ suppression, or induce a large enhancement for resonances, as discussed in Sec. 2.5. Also, there could be inhomogeneities in the haloes, local clumps of DM enhancing the local distribution at a given position, thus locally increasing the annihilation probability.

As it was discussed for DD, a null result can be translated into a limit for the annihilation cross section. However, in principle, the constraint applies rather to $\phi_k^{PP}(E)$ than to σ. Going from one to the other implies a certain assumption of the spectrum of production of the observed species, which is, of course, DM model dependent.

The particle species that represent a great interest are those that can be detected and disentangled from background. The first criterion puts forward the charged particles and photons. The second, selects antimatter over matter. Indeed, while astrophysical objects suffer from baryon asymmetry and thus would yield asymmetrical fluxes of particles, the product of annihilating DM would be made of both particles and antiparticles. Thus, for the best comparison of signal to background, we expect the positron, antiproton and antideuteron channels to be the most promising.

Moreover, when looking at the GC of the MW, an ideal scenario for large annihilation rates in our vicinity, the propagation of particles might be more complicated than just straight lines from production to detection. Indeed, the GC is a relatively dense medium, which can contain ionized gas in movement. Thus in general particles propagate through electric and magnetic fields. Energy losses and spatial diffusion have thus to be treated, at least for charged particles such as positrons and antiprotons, for both signals and backgrounds. Also, the choice of the direction of observation has to be realistic. On one hand, DM has to be

[1] This is obviously not the case of charged particles. This simplification is correct for photons produced at the annihilation event, but not for positrons nor antiprotons, for which it is needed to include the propagation as briefly discussed later on.

concentrated enough in order to produce enough flux, and on the other hand the diffusion of the produced particles has to be able to reach us and not be trapped in local trajectories. For charged particles this restricts the range of observation to our galaxy. Photons are, however, much less sensitive to the medium they travel in. Thus we can expect some flux from the nearby dSphs which orbit around our GC. Neutrinos are also free to travel around, however very large fluxes are needed for a detection.

4.3.2 Antimatter

The production of antimatter would be a distinctive signature of DM annihilations. Among the possible products of DM annihilations we find positrons and antiprotons. The latter requires $m_{DM} \geq m_p$. Both of these fluxes can be estimated, however via the inclusion of a propagation model. The study of the propagation of charged particles is very complex. While numerical and semianalytical efforts have shown great progress in the matter, the errors in the treatment of the diffusion equation are still very large. This implies that the cosmic ray background estimations are not very precise either. The background estimations include the estimation of production of positrons via the spallation of the ISM by very energetic particles. For example, very energetic protons colliding with hydrogen atoms would produce energetic charged pions, which in their decay chain would give rise to ultrarelativistic positrons. A similar process is responsible for the production of antiprotons. For a review on propagation and background processes, refer to [41].
The antimatter sector captured the attention a few years ago with the results shown in the positron fraction flux observed by the PAMELA satellite [42]. A rise in the flux at $\sim 10\,GeV$ and up to the $\sim 100\,GeV$ was promptly interpreted as a possible DM signal by many groups. The main difficulty to explain such a result lied in the fact that no similar excess was reported in the antiproton fraction –calling for preferred annihilations into charged W bosons which have a $\sim 20\%$ probability to decay into muons or electrons, thus reducing the antiproton yield with respect to the positron production–, and that cross sections with large boosts (of a few thousand) with respect to the EU canonical annihilation rates was needed. Nowadays interpretations tend to give the preference to astrophysical interpretations, such as nearby pulsar emissions.
In any case, if a DM model predicts fluxes of positrons or antiprotons well above the background, including its error margins, then we may exclude the model. That is the philosophy of the checks we have performed in the works presented in the following chapters.

4.3.3 Photon signals

Photon signals are maybe the easiest ID case. It was first proposed in 1978 that γ-rays could be produced for massive neutrinos [43]. While photons are not directly coupled to the DM,

they might be produced in final state radiation, in form of lines in initial state radiation or via loop interactions, and as part of the decay of the annihilation products. Furthermore, the energy loss of particles produced in DM annihilations can consist upon photonic radiation, such the synchrotron radiation. Many experiments are devoted to study the sky at many wavelengths. Here we will discuss the cases of γ-rays and radio waves which will be used later on to constrain supersymmetric DM.

γ-rays

Let us discuss the search of γ-rays from DM annihilations. Cherenkov telescopes have been built in order to observe the flux at Earth. Current experiments include HESS, MAGIC, CANGAROO and VERITAS. In outer space, the Fermi satellite and its Large Area Telescope (LAT) is acquiring data in the *GeV* range. This detector is also sensible to antimatter (as well as HESS), since in its conception it is closer to a particle physics detector than to a telescope [44]. For the mass ranges we treat in what follows, we are mostly interested in the recent Fermi-LAT results.

As it was previously stated, the GC –typically with a 10° extension– is a very interesting region to look at. However, the background tends to be large as well, the DM signal is not clean and competes with standard processes. However, the possibility of observing dSphs is very appealing and the most competitive limits are coming from such searches. Another interesting MW based analysis is to look at the regions surrounding the GC, where background is less strong. Also, neighbouring galaxy clusters and the diffuse γ background are thoroughly studied by Fermi-LAT. Among the searches that can be devoted to DM signals, the γ-lines are the most precise in terms of the particular signature expected. However, a diffuse spectrum analysis from dSphs has proven to be the most constraining analysis so far achieved.

Indeed, Fermi-LAT has published negative results upon observation of γ-ray fluxes from dSphs [45]. They focus their analysis in a selection of eight dSphs: Ursa Major II, Coma Berenices, Bootes I, Ursa Minor, Sculptor, Draco, Sextans and Formax. The dSphs, although DM dominated objects, have some baryons. Resolving the positions and velocities of these light emitting objects and using a NFW DM density profile, they have fitted the DM distribution in each of the 8 studied systems. This, in turns, allows them to estimate the $J(\psi)$ integral, giving error bars stemming from their likelihood analysis. Thus, in order to compute γ-ray fluxes for a given candidate, what remains to be done regarding the astrophysical part of the flux estimation is to scale $J(\psi)$ by the ξ factor of a given configuration: $J(\psi) \to \xi^2 J(\psi)$. Finally, to complete the flux calculation, the resulting energy spectrum of the model has to be multiplied by $\xi^2 J(\psi)$. Thus, the negative results have been translated into flux limits for

a given energy spectrum, which is usually a power law

$$\frac{dN}{dEdAdt} = N_0 \left(\frac{E}{E_0}\right)^{-\Gamma},$$

where A is the detector surface, and E_0 and N_0 are normalization constants. The case of annihilating DM in the Fermi-LAT range is better represented by $\Gamma = -1$ (among the limits given in [45]). We use these limits and the information provided for the astrophysical $J(\psi)$ integral to constrain supersymmetric scenarios with annihilating neutralino DM in the $(1 - 500)\,GeV$ range.

Radio waves

The DM annihilation final states would include electrons and positrons. For annihilations occurring in magnetized regions, the electrons and positrons, in their propagation, would lose energy via synchrotron radiation among other processes. The synchrotron flux thus produced can be computed, for assumptions of the magnetic fields, and taking into account all the relevant energy losses that may affect the leptons. Observations of the sky in the radio wavelengths are copious. Thus the comparison to data is possible in almost any direction.
The synchrotron emission is thus expected to be produced in the GC of the MW where the DM density would provide enough electrons and positrons, and where the ISM is believed to be magnetized. Also, galaxy clusters are a good prospect, where large ionized clouds also yield magnetic fields that would be enough to produce synchrotron emissions. For a generic study in the field, see [46].
Electrons and positrons injected at relativistic velocities interact immediately with the ISM. Various processes can happen throughout the history of the lepton. However, at high energies, the dominant energy losses stem from synchrotron radiation, inverse Compton scattering of microwave background, stellar radiated and thermal dust emitted photons, and bremsstrahlung.
The averaged power lost by an electron of energy E passing through a magnetic field of strength B by synchrotron radiation is given by

$$-\left(\frac{dE}{dt}\right)_{sync} = \frac{4}{3}\sigma_T c \frac{B^2}{2\mu_0}\beta^2\gamma^2 = \frac{4}{3}\sigma_T c U_{mag}\left(\frac{E^2}{m_e^2 c^4} - 1\right).$$

where μ_0 is the permeability of free space, σ_T is the Thomson scattering cross section, $\beta = v/c$, $\gamma = (1 - v^2/c^2)^{-1/2}$ and v is the velocity of the electron/positron. Inverse Compton processes yield

$$-\left(\frac{dE}{dt}\right)_{IC} = \frac{4}{3}\sigma_T c U_{rad}\gamma^2 = -\left(\frac{dE}{dt}\right)_{sync}\left(\frac{U_{rad}}{\beta^2 U_{mag}}\right) \simeq -\left(\frac{dE}{dt}\right)_{sync}\left(\frac{U_{rad}}{U_{mag}}\right).$$

Where U_{rad} is the radiative energy density. Bremsstrahlung processes involve various targets. The relativistic electron sees different kinds of charges. It has been shown that for targets at rest and for the higher part of the emitted photon spectrum, free electrons and free protons behave in the same manner [47]. However, when these are in atoms and nuclei respectively, screening affects the interaction. The ISM being mainly formed by atomic and ionized H and He, we shall take these into account.

$$-\left(\frac{dE}{dt}\right)_{brems} = -\left(\frac{dE}{dt}\right)^{H}_{brems} - \left(\frac{dE}{dt}\right)^{He}_{brems} - \left(\frac{dE}{dt}\right)^{p,e,\alpha}_{brems} - \left(\frac{dE}{dt}\right)^{He^+}_{brems}.$$

For a fully ionized gas, the Bremsstrahlung losses can be written as

$$\begin{aligned} -\left(\frac{dE}{dt}\right)^{ionized}_{brems} &= 4\alpha r_e^2 c \left(\sum_Z n_Z Z(Z+1)\right)(ln\gamma + 0.36)E \\ &\simeq 6.9488\ 10^{-17}\left(\sum_Z \left(\frac{n_Z}{cm^{-3}}\right) Z(Z+1)\right)(ln\gamma + 0.36)E\, s^{-1} \end{aligned}$$

where α is the fine-structure constant, r_e is the classical electron radius, n_Z is the number density of the species Z having Z charges in the nucleus. The (Z) electrons are taken into account, contributing as Z and not Z^2 as the nuclei. This expression holds for protons, alpha particles and the electrons released by the ionization of hydrogen and helium yielding these. However, the case of He^+ is trickier. We need to include the contribution of the ionized part of the nucleus (and the free electron), as well as the contribution of the neutral part of these ions. So, for the valence proton only (and the correspondent free electron), this expression also holds, but keep in mind that it does not fully treat the He^+ case. These considerations could further help to estimate the losses in a more accurate way, if radio signals were found. The radio spectrum is given by [48, 49]

$$j(\omega) = \frac{\sqrt{3}e^3 B \sin\alpha}{8\pi^2 \varepsilon_0 c m_e} F(x),$$

where

$$F(x) = x\int_x^\infty K_{5/3}(z)dz,$$

$K_{5/3}$ is a modified Bessel function of order $5/3$, ε_0 is the permittivity of free space and α is the angle between the propagating lepton and the magnetic field direction. This yields a maximum emission at

$$\nu \simeq \frac{87}{1600}\frac{eB}{m_e}\sqrt{1-\left(\frac{m_e c^2}{E}\right)^2}\left(\frac{E}{m_e c^2}\right)^2$$

which yields a relation between the frequency and the energy of the electron or positron. Thus, in the monochromatic approximation

$$E(\nu,B) \simeq \frac{1}{2} \times \left(\frac{\nu}{MHz}\right)^{\frac{1}{2}} \times \left(\frac{B}{\mu G}\right)^{-\frac{1}{2}} GeV$$

This way, the electron and positron spectrum can be translated into a spectrum of radio emission. By propagating the leptons and including the main energy losses, the radio flux due to DM annihilations can be estimated, via an integral of the l.o.s. and a model of the DM halo. In particular assuming a NFW profile makes the integration rather easy as shown in [46].

Hence, by focusing in a given frequency, and estimating the magnetic field –expected to lie between $20\mu G$ and $100\mu G$– at the GC, one can compare, for example, the DM yield at $\nu = 330 MHz$ to the $360 Jy$ observed, and thus constrain a given model. Similarly, the flux can be estimated for the Coma cluster for a multifrequency approach. In such a system the magnetic field can be estimated at $4.7\mu G$. We use these observables to constrain supersymmetric configurations in this work.

5 Particle Physics constraints

Throughout the years the Standard Model of particle physics (SM) has proven to be a successful description of most laboratory phenomena at different energy scales. The confidence on its accuracy and its fundamental relation to phenomena has been strongly supported by the successful prediction of particles and excitations. It also provides strikingly precise estimations of masses and effects, such as M_W or the anomalous magnetic moment of the electron, in almost perfect agreement with the experimental measurements. However there are phenomena which the SM cannot account for.
In what follows we briefly discuss the main features of the SM, and subsequently review open physical problems that it cannot account for.

5.1 Brief introduction to the Standard Model of particle physics

The SM is based on the quantum field theory formalism and the gauge theory. It explains remarkably well the electromagnetic, weak and strong interactions, and includes a description and classification of all observed particles. For definitions of the objects we introduce and for a thorough presentation of the structure of the underlying theory of the SM, see [50]. This brief summary is inspired by [51, 52, 53].
The SM structure is given by the $SU(3)_C \times SU(2)_L \times U(1)_Y$ gauge symmetry group, where C, L and Y stand for color, left chirality and weak hypercharge quantum numbers that the fields carry. This gauge symmetry group is an internal symmetry of the Poincaré group of spacetime symmetry. The inhomogeneous Lorentz transformations define the Lie algebra of the Poincaré group over the four dimensional Minkowski flat spacetime given by the metric $\eta_{\mu\nu} = diag(1, -1, -1, -1)$. In the usual representation of the Lorentz algebra, a subset of the Poincaré algebra, fields are represented by spinors that transform under the action of the γ^μ matrices.
All observed matter correspond to spin-$1/2$ particles, the lepton and quark fields. The electromagnetic charge Q_f of a particle f is related to its weak hypercharge Y_f and its left chiral weak isospin T_{3L}^f by the relation $Q_f = T_{3L}^f + Y_f/2$. Thus, electroweak quantum numbers define whether a particle is charged, showing the fundamental unified structure of the weak and electromagnetic forces. However, at the low energy scales we are able to test at colliders,

these forces manifest quite differently. The left and right chiral fields are in fact the chiral projections $f_L = \frac{1}{2}(1-\gamma_5) f$ and $f_R = \frac{1}{2}(1+\gamma_5) f$ of f, where $P_{R/L} = \frac{1}{2}(1 \pm \gamma_5)$ are the chiral projectors. All fermion fields are chiral and thus they are coupled to the electroweak sector. The electroweak gauge transformations act on fields as follows: left chiral fields transform as doublets of $SU(2)_L$ while right handed fermions transform as singlets. Thus, left chiral fermion fields transform as under the $SU(2)_L \times U(1)_Y$ gauge transformations with left chiral and hypercharge gauge couplings respectively, while the right chiral fermion fields only transform non trivially under $U(1)_Y$. The only fermion fields having non trivial transformations under the $SU(3)_C$ color group are the quarks. The non-abelian $SU(3)_C$ strong gauge interactions are described by the Quantum Chromodynamics (QCD) theory.

There are three families of leptons: electrons, muons and tauons. The left doublets are made of the negatively charged leptons and the corresponding neutrino, while the only right handed fields are the charged right handed leptons. The SM does not contain right handed neutrinos. It is not clear whether neutrinos are Dirac particles or Majorana particles in which case they are their own antiparticle. Quarks also are described by three families of an up-type $+2/3$ charged quark and a down-type $-1/3$ charged quark: up-down, charm-strange and top-bottom. There are three left-handed doublets of $SU(2)_L$, with the six corresponding charged conjugated right handed singlets.

Interactions are ensured by the gauge bosons. The $SU(2)_L \times U(1)_Y$ sector interaction carriers are the spin-1 $\vec{W}_\mu$ and B_μ fields. The strong colored gauge fields are the eight spin-1 g^a_μ gluons, where $a = 1, ..., 8$. All gauge fields transform according to the adjoint representations of their groups. So far all fermion fields and gauge bosons are exactly massless. Except for the fact that all fields but the photon and gluons have mass, the description of these fields and interactions is complete, and works, for example, in remarkable agreement with observations for relativistic processes. The fact that physical vector bosons do have mass implies a mix of states. The neutral component of $\vec{W}_\mu$ and the B_μ field mix with the θ_W mixing angle to yield the massless electromagnetic A_μ vector boson –the photon, responsible for the interactions described by Quantum Electrodynamics (QED)– and the charged $W^\pm$ and neutral Z weak massive vector bosons.

The mass of all particles is linked to the breaking of the $SU(2)_L \times U(1)_Y$ symmetry. The spontaneous symmetry breaking is due to the $SU(2)_L$ doublet scalar Higgs field $\phi = \begin{pmatrix} \phi^+ \\ \phi^0 \end{pmatrix}$. This doublet has a non vanishing vacuum expectation value (VEV): $\langle \phi \rangle = \frac{1}{\sqrt{2}} \begin{pmatrix} 0 \\ v \end{pmatrix}$. This phenomenon stems from the Higgs potential

$$V(\phi) = \mu^2 \phi^* \phi + \lambda (\phi^* \phi)^2,$$

where $\mu^2 \leq 0$ is a mass term and $\lambda \geq 0$ is a quartic scalar coupling. Imposing the minimum of the potential –i.e. the vacuum expectation value of ϕ– for $\phi\phi^* = \frac{1}{2}v^2$, implies that the relation $\mu^2 + \lambda|v|^2 = 0$ must hold. Since it is the value of v that gives the masses to the weak bosons with $M_W = \frac{1}{2}g_2 v$ and $M_Z = \frac{1}{2}\sqrt{g_Y^2 + g_2^2}\,v$, where g_2 is the $SU(2)_L$ coupling and g_Y is the $U(1)_Y$ coupling intervening in the respective gauge transformations, the measure of the masses yields $v = \left(\frac{1}{\sqrt{2}G_F}\right)^{1/2} \simeq 246\,GeV$. This sets the possible range for the μ mass term. The inclusion of the Higgs scalar field implies one Goldstone boson –which is absorbed in the longitudinal polarization of the gauge vector fields– and a massive boson, the Higgs boson. Regarding vertices, these preserve the baryon (here in the particle physics sense of the term) and lepton quantum numbers exactly. The fact that the photon and the gluons are massless is due to the fact that below the electroweak scale the unbroken symmetry group is $SU(3)_C \times U(1)_{em}$, of which they are the gauge bosons.

The coupling of the Higgs boson to the fermions via Yukawa couplings ensures the masses of the fermions. Indeed, we include them in the SM lagrangian:

$$\mathcal{L}_{SM} \supset f_{ij}^x \phi . l_i^x \bar{r}_j^x + h.c.$$

where f_{ij}^x are the Yukawa couplings, l_i^x the left handed matter fields, $\bar{r}_j^x$ the hermitian conjugate of the right handed matter fields, i and j span the three families of fermions, x stand for either lepton or quark fields, and $h.c.$ means hermitian conjugate. Each left field is thus coupled to its right partner and the Higgs. While all left quarks have a right handed companion as well as all charged leptons, the fact that there is no right handed neutrino implies the non-existence of such a term for the left handed neutrinos, which makes them strictly massless. In fact, by adding a right handed neutrino Dirac field, neutrinos would automatically acquire mass. However, in order to make them as light as they are ($m_\nu \leq 2\,eV$ [52]), a very unnaturally small Yukawa coupling would have to be introduced. In generation space, the charged lepton, up-type and down-type quarks have a mass matrix which components are thus given by the Yukawa couplings times the VEV of the Higgs field.

Quark fields can experience flavor-mixing when interacting via the charged currents $W^\pm$. This is due to the fact that all –left handed and right handed, and the six flavors– quarks obtain mass via the coupling to the Higgs, while the left handed act as doublets of the weak interaction. Thus the mass eigenvalues, obtained by diagonalization of the Yukawa coupling matrix coupled to the left and right physical quark matrices, do not correspond to the weakly interacting quark states. The $W^\pm$ thus interact with the physical states via a mixing matrix, the Cabibbo-Kobayashi-Maskawa (CKM) matrix.

Quarks are not free in Nature and do not manifest as isolated singularities. Schematically, the strong interaction does not decrease its strength with distance, which ensures that a quark has a high rate of exchange of gluons with the surrounding quarks, whatever distance separates them. Hence, quarks are confined to bound states. Two quark –quark and antiquark–

states are mesons, which are typically classified by the quark flavor, while baryons –such as protons and neutrons– are three quark states. At very high temperatures and densities a deconfined dense quark-gluon plasma can be achieved, as it has been shown theoretically and are being tested –with apparent positive results– at the Relativistic Heavy Ion Collider (RHIC) and the LHC-ALICE experiment.
The Higgs boson is the only particle of the SM that has not been observed at colliders, despite the efforts carried at LEP, Tevatron, and currently at the LHC.

5.2 Experimental measurements as constraints to physics beyond the Standard Model

The construction of the SM has been empirical, yet it progressively included very theoretical concepts such as symmetries and force unification. Indeed, the SM has never been proved to be wrong. It might be incomplete, namely it has no explanation for the DM, it might fail to explain all phenomena such as neutrino masses, but it is very accurate in the accordance to experimental results of those phenomena it does describe. However, theoretical estimations always carry uncertainties. Indeed, while the masses of charged leptons and weak gauge bosons are precisely measured, the quark masses are much more complex, leading to larger uncertainties. Moreover the Higgs mass is still unmeasured. These mass values are parameters playing an important role in the estimation of observables, and thus propagate their errors. Furthermore, computation of observables to all relevant orders in perturbation theory is not always an easy task. Thus, there is not necessarily a final word in SM estimations of various observables. Some effects are generated only at the loop level in the SM. In such cases BSM contributions are expected to be of the same order as the SM contributions. Any attempt to build a BSM theory has to thoroughly reproduce the SM results. The additional features have to respect the narrow room left by the experimental measure of observables.

5.2.1 Unobserved particles

The Higgs boson, though the most important of the current SM predictions, has not yet been observed. Its mass range has been already severely constrained by the LEP and Tevatron colliders, with the best lower limit still coming from LEP in the $e^+e^- \to H^0Z$ channel yielding $M_H \geq 114.4\,GeV$ [52]. Any BSM model which would include the Higgs mechanism and a SM-like Higgs boson has to deal with this limit, or with an adapted yet similar constraint.
The best experimental evidence for a BSM theory would be the direct observation of non-SM particles. This would need a distinctive signature as well as an experiment able to see it. Detectors are able to track electromagnetic interactions only. This is how they have been able to demonstrate the manifestation of the other fundamental interactions. Thus, the easiest

signals to look for are charged particles. The energy of the experiment has to be sufficient for the kinematics to allow the new mass to be generated and the interaction cross section has to yield enough events to overcome the SM background. So far there is no evidence for new particles which translates into constraints on their masses and interaction rates.
The signatures of new particles are very model dependent. Thus, the analysis of data, and hence the exclusion limits that can be drawn, are also model dependent. That is why the lower bounds on masses are determined for individual particles in searches specific to a particular model, and not in a general manner. The detector collaborations –such as CDF [54] and DØ [55] at the Tevatron, or CMS [56] and ATLAS [57] at the LHC– have several work groups to analyse the physics results.
For example, fourth generation leptons have now been ruled out for masses below $100.8\,GeV$, a fourth generation up-type quark would be heavier than $256\,GeV$ and a down-type quark heavier than $199\,GeV$ [52]. In contrast, the latest LHC results imply that the supersymmetric top-squark would have to be heavier than $\sim 500\,GeV$ and gluinos heavier than $\sim 700\,GeV$.
For a review on limits classified by model see [52].

5.2.2 Electroweak measurements

The physics of the EW sector has been thoroughly studied at LEP. This electron/positron collider had a very good sensitivity to all phenomena related to the EW Z and $W^{\pm}$ bosons, and clean leptonic final states. To quote an example, the Z mass is now known at a precision of $\sim 2.3\,10^{-3}\%$. These measurements can be used to test BSM theories.
The SM decay modes of the Z are very well defined, including the invisible contribution explained by the $Z \to \nu\bar{\nu}$ neutrino channels. This sets a limit upon couplings to the EW interaction for BSM neutral particles of mass lighter than $M_Z/2 \simeq (91.1876 \pm 0.0021)/2\,GeV$. The full width is $\Gamma_Z = (2.4952 \pm 0.0023)\,GeV$, while the invisible contribution reads $\Gamma_{inv} = (499.0 \pm 1.5)\,MeV$ [52]. The SM provides an estimation of $\Gamma_{Z\to\nu\bar{\nu}}$ which leads to $\Gamma_{inv}/\Gamma^{SM}_{\nu\bar{\nu}} = 2.984 \pm 0.009$ (assuming the top mass at $m_t = 173.1\,GeV$ and the SM Higgs mass at $M_H = 117\,GeV$). This confirms the number of neutrino flavors and leads to a stringent constraint on BSM contributions.
One of the best precision measurements of particle physics is the anomalous magnetic moment of the electron and the muon. The latter is generally sensitive to BSM contributions, while the former gets BSM suppressed contributions since the electron is too light as compared to the EW scale. The world average reads $a_\mu^{exp} = \frac{g_\mu - 2}{2} = (1165920.80 \pm 0.63) \times 10^{-9}$, which includes QED, EW and QCD processes. The SM contribution is computed for all these processes $a_\mu^{SM} = (1165918.90 \pm 0.44) \times 10^{-9}$. The agreement is remarkable, but the difference between the measured value and the SM estimation is much larger than the experimental and theoretical errors. Hence, this calls for a BSM contribution helping to conceal the theoretical and experimental values. One possibility would be the supersymmetric loop

contributions of the lightest charged particles, namely that of the chargino or of the sleptons.

5.2.3 *B*-meson physics

Another interesting field in which BSM contributions could play an important role are the *B*-meson phenomena, such as decays and oscillations. These phenomena are studied at *b*-factories such as Belle, BaBar, and LHCb.

In the SM, the decays and oscillations of mesons are the result of loop transitions, usually via the exchange of *u*-quarks and $W^{\pm}$ bosons. Since these are effects generated at loop level, the BSM effect can be important, thus these phenomena are a good field to look for new physics. Since these decays depend upon flavor changing, invoking the EW interaction, it includes the components of the CKM matrix.

The $b \to s\gamma$ weak transition is a small but measurable loop effect in the SM. This transition can for example occur via a triangle loop of two *t*-quarks and a W^- boson, at leading order (LO). The actually measured process is the branching ratio of the radiated photon at the *B*-meson decay into a strange meson $\bar{B} \to X_s\gamma$. Currently the estimations at next-to-LO (NLO) and next-to-NLO (NNLO) proves to be quite important, setting the SM contribution at $(3.15 \pm 0.23) \times 10^{-4}$ [58], which is 0.45×10^{-4} less than the NLO prediction. Going NNLO implies including QCD corrections which can be non-perturbative and imply uncertainties of the α_s strong constant. The world average of the measurements is $(3.52 \pm 0.34) \times 10^{-4}$ [59].

Another example is the triangle exchange of a W^- boson by the *s* and $\bar{b}$ of the B_s^0 meson into a pair of top-quarks leading to a *Z* which finally yields $\mu^+\mu^-$ in the final state. This is the $B_s^0 \to \mu + \mu^-$ decay, which is very suppressed with respect to other decays. In the SM the prediction is still below the sensitivity of experiments, which in turn set upper limits to its branching ratio. Even the LHCb previsions do not attain the SM estimation in this observable. Thus, any BSM contribution has to be below the current world averaged limit of 4.7×10^{-8} for the branching ratio [59].

Regarding *B*-meson oscillations, they quantify the rate of meson/antimeson conversion. For example, a B_d^0 meson –made of a *b*-quark and a $\bar{d}$-antiquark– can exchange *u*-quarks and *W* bosons in a box diagram to yield its antimeson $\bar{B_d^0}$. Replacing the *d* flavor contributions by strange quarks and antiquarks leads to the same type of oscillation but for B_s^0 and $\bar{B_s^0}$.

6 Supersymmetric models

From all the BSM theories and models available, Supersymmetry is the most popular theory and its models are the most searched for in current experiments. Theoretical efforts have constructed not only its algebraic framework but also have explored the closest phenomenologies to the SM.
Here, we give a brief description of the basics of the supersymmetric framework. Then we focus on the Minimal and Next-to-Minimal Supersymmetric Standard Models, and emphasize configurations with neutralino lightest supersymmetric particle (LSP). We refer to [51] and references therein throughout all this section.

6.1 Brief introduction to Supersymmetry

The theory of SUSY is based upon the assumption of a symmetry between bosons and fermions. Such a symmetry postulates a new charge, the supercharge –carrying a spin-$1/2$–, which ensures the transition between the two kinds of particles. All SM particles would have at least one superpartner –the corresponding sparticle– carrying half a spin less (or more), generating a whole new sector of particles yet unseen.
Among the first remarks that may be drawn is the fact that if the four-momentum operator P^μ and Casimir operator P^2 were to commute with the supercharge operator, then a SM particle and its superpartner would be exactly mass degenerated. In exact SUSY the vacuum expectation value of the supercharge operator is expected to give a vanishing energy. This is a very appealing property since it would cancel out divergences of loop diagrams of bosons and fermions. However, this leaves the unnatural scalar contributions without compensation: SUSY contains scalars and thus is not fully renormalizable. Moreover, experiments have not observed superparticles with such characteristics, which implies that SUSY is broken at a scale at least of the order of the minimal mass difference set by unfruitful new particle searches. Furthermore, the broken $SU(2)_L \times U(1)_Y$ at the weak scale by the Higgs mechanism suggests a link between SUSY breaking and the presence of scalar fields driving these spontaneous breaking mechanisms, leading to the expectation of sparticles to manifest at a scale of $\lesssim O(TeV)$.
SUSY is formulated as a field theory based on an algebraic formulation which includes

the fermion-boson symmetry. In order to include such a non-trivial transformation of the Poincaré group, graded Lie algebras have been included. These are an extension of the usual Lie algebras, but including anticommutation relations. Hence objects are expressed in terms of Grassman elements and variables. Thus, functions of Grassman variables can contain terms which are either commuting or anticommuting –by making the right combinations. They are able to treat fermion-like objects and boson-like objects in a single expression. Ordinary matter and gauge bosons are contained in a generic object, together with their superpartners. The so called chiral superfields describe the spin-$1/2$ SM fermions and their spin-0 scalar superpartners, the sfermions, while the spin-1 vector bosons of the SM are contained in the vector superfields, together with their superpartners, the spin-$1/2$ gauginos.
An important feature of SUSY is the existence of an axial $U(1)$ generator R which translates the invariance under a chiral rotation of the charge conjugation, commutation and anticommutation relations of the supercharge. It is shown that the $U(1)_R$ symmetry cannot be an exact symmetry in nature. However, its discrete subgroup Z_2, in turn, can fulfil such a requirement. The R generator is generally part of SUSY, and it leads to a R-charge for each field. R-parity is the discrete Z_2 charge carried by fields, with even and odd states. SM particles are usually taken to have an even R-parity and their superpartners to have an odd R-parity. If $U(1)_R$ is an exact symmetry of nature, then interaction vertices must conserve R-parity, hence they must be always constructed by an even number of R-odd particles. Thus, three-vertices are made of one SM particle and two SUSY particles. As a consequence, the decay of the lightest R-odd particle is forbidden. Hence, the LSP is stable. If it is also neutral and has the right interaction rates, it could be a good DM candidate.
As it was already stated, SUSY must be broken. By construction, the supersymmetric vacuum vanishes by the action of supersymmetric generators –the supercharge operator. In constrast with the SM field theory where the global minimum of the vacuum expectation value can be shifted at any given value, in exact supersymmetry, the global minimum has to be zero or positive. Hence, if the ground level does not correspond to zero energy, then the vacuum acquires a positive energy. Thus, if there is a fundamental scalar complex field ϕ which potential $V(\phi)$ has non vanishing minimum energy, then SUSY is spontaneously broken. Therefore, a classic Mexican-hat like potential with null global minimum value does not break SUSY, while the same potential lifted by a certain value does break SUSY. There are various ways to spontaneously break SUSY, and it is beyond the scope of this work to treat them. Instead, we assume the explicit break of SUSY at the EW scale.
Most of what has been discussed in this section regarding SUSY corresponds to a $N = 1$ configuration. N stands for the number of fermionic generators introduced in this framework. In principle SUSY can be extended to an arbitrary number of generators. The theoretical interest of going beyond the case of $N = 1$ is of a vast variety. In $N = 2$ SUSY, for example, there are fermionic mirror partners of each SM fermion. Another example is the $N = 4$ supersym-

metric Yang-Mills theory is claimed to be finite and thus allows to solve analytically many complex processes such as loop amplitudes. However in this phenomenologically orientated work we only treat aspects of $N = 1$ SUSY.

6.2 Minimal Supersymmetric Standard Model

We now introduce the minimal model that can be constructed based on $N = 1$ SUSY: the MSSM. The MSSM is described by 124 free parameters including the soft (explicitely breaking) SUSY terms. Some constructions of the MSSM make use of theoretically motivated constraints to increase the degeneracy of the full parametrization, hence describing the MSSM with as few as 5 parameters. Nevertheless, here we are interested in the scenarios where the vastest phenomenological implications can be drawn. We will give a quick review of the main physical features of the MSSM and then we will focus on the neutralino, which is the DM candidate we study in this scope.

6.2.1 Description of the minimal supersymmetric standard model

The MSSM is the minimal supersymmetric replication of the SM. All matter in the SM is described by spin-$1/2$ fermions, which, by virtue of the supersymmetric fermion generator, acquire spin-0 scalar superpartners. Thus, the left handed leptons and quarks give rise to the left-handed sleptons and squarks. These are called left-handed only because of their intrinsic relation to the $SU(2)_L$ doublets. There are, equivalently, the right handed sfermions, superpartners of the right-handed singlets of the EW interaction. Notice that the superpartners of both charged leptons and quarks carry themselves a charge. Hence, there are lower bounds on their masses, since they have not been observed in particle physics experiments. Typically this sets a limit of $O(100\,GeV)$ –however this value is rapidly evolving with the LHC negative results–, though each family has to be treated individually. Indeed, the selectron case is constrained by the LEP, which has thoroughly scanned electron interactions up to $209\,GeV$. However, the stau could be lighter, down to $O(80\,GeV)$. Sneutrinos cannot be arbitrarily light either since they are coupled to the Z-boson, but the limits on their masses are somewhat looser than those of charged particles. In particular, a right handed sneutrino, superpartner of a right handed neutrino added to the SM, is a good DM candidate, which we do not treat in this study. Squarks are further constrained by strong interactions. Indeed, the Tevatron hadron collider explored these interactions up to $1.96\,TeV$ yielding limits on the squark masses of the order of $O(300\,GeV)$. The LHC has recently given even more stringent constraints by the analysis of $3.5\,TeV$ collisions, rising these limits to $O(500\,GeV)$. Therefore, these experimental bounds are translated into limits on the parameters of the MSSM, which we will further describe in Sec. 6.2.2.

The gauge bosons of the SM get supersymmetric gaugino partners. There is a vector super-

field including each one of the gauge fields B_μ, $\vec{W}_\mu$ and g^a_μ and the corresponding $\tilde{B}$, $\tilde{W}$ and $\tilde{g}_a$ gauginos. The latter are spin-$1/2$, 4-component, Majorana fields which left and right chiral components are charge conjugated.
A single scalar doublet field ϕ was enough in the SM to give mass to all massive particles and bosons. For reasons of structure this implies that the charge conjugated ϕ^C of the $Y = 1$ hypercharged ϕ has to carry a $Y = -1$ hypercharge. This, in turn, allows the same field to account for the up and down type of quark and lepton masses. In SUSY, however, the Higgs sector must be described by a superpotential, which needs to be an analytic function of the left chiral superfields. In order for the right handed fermions to acquire mass, a second scalar doublet needs to be introduced[1], hence the Higgs fields are h_1 and h_2. Thus the non-zero VEV ensuring the EW symmetry breaking is carried by both Higgs fields. The Higgs spectrum is enlarged to two physical CP-even scalar fields h and H, where h is the lightest, a CP-odd pseudoscalar A and a pair of charged Higgses $H^\pm$. The superpartners of the Higgs fields are spin-$1/2$, 4-component, Majorana fields, just like gauginos. Thus the superpotential of the MSSM is minimally constructed with the Higgs superfields H_1 and H_2 containing both the Higgs and higgsino $\tilde{h}_1$ and $\tilde{h}_2$ fields. Hence, the superpotential reads

$$\mathcal{W}_{MSSM} = \mu H_1.H_2 - f^e_{ij} H_1.L_i \bar{E}_j - f^d_{ij} H_1.Q_i \bar{D}_j - f^u_{ij} Q_i.H_2 \bar{U}_j$$

where i and j span the three families of fermions, L_i, Q_i are the matter superfields containing the left-hand side leptons and quarks and E_j, D_j and U_j are the matter superfields containing the right-hand side leptons, down-type quarks and up-type quarks, and the f^e_{ij}, f^d_{ij} and f^u_{ij} are the Yukawa couplings.

6.2.2 Soft supersymmetric terms and MSSM parameters

We do not intend to treat SUSY breaking mechanisms, nor to treat the renormalization of the theory. We only assume that there is a mechanism that breaks SUSY, which implies the presence of the so called soft terms in the lagrangian. Since SUSY is broken at low scale, the soft terms are decisive for the phenomenology at colliders, EU and galactic physics scales. The aim is to explore as many supersymmetric phenomenologies as possible for the mass sectors and interaction rates we are interested in our studies. Note that this makes sometimes difficult to apply the best limits inferred from particle physics experiments, since these are model dependent and usually obtained for constrained or minimal supergravity constructions of the MSSM. Here we introduce the crucial parameters entering the description of the supersymmetric interactions with particles of the SM.
A spontaneous EW symmetry breakdown sets the generalized Higgs-higgsino mass term μ to be of the order of the EW scale. The Higgs sector involves two fields with two different

[1] The supersymmetric Lagrangian has to be holomorphic, implying that it cannot contain the term involving the hermitian conjugate of the SM Higgs field.

VEVs. Even though they are related, there is no intrinsic reason to set the two VEVs equal. The ratio of the H_1 to H_2 VEVs is given by the $\tan\beta$ parameter: $\tan\beta \equiv v_2/v_1$. The μ and $\tan\beta$ are completed by the CP-odd Higgs mass M_A. At tree level, the Higgs masses are given by

$$M^2_{H,h} = \frac{1}{2}\left[M_A^2 + M_Z^2 \pm \left(\left(M_A^2 + M_Z^2\right)^2 - 4M_Z^2 M_A^2 \cos^2 2\beta\right)^{\frac{1}{2}}\right],$$
$$M^2_{H^\pm} = M_A^2 + M_W^2$$

resulting of the mixing of the h_1 and h_2 fields. The mixing angle leading to the h and H fields from h_1 and h_2 is α. This mixing angle is strongly linked to β, M_A and M_Z. Choosing values for β and M_A automatically sets α, hence it is not a free parameter (once β and M_A are already set as free parameters). We have now introduced all the parameters and quantities that allow to express the Higgs interactions. To quote an example, the coupling of the h to the SM fermions (divided in up-type and down-type) are proportional to the SM Higgs couplings times the following expressions:

$$hf_d\bar{f}_d \propto -\frac{\sin\alpha}{\cos\beta},$$
$$hf_u\bar{f}_u \propto \frac{\cos\alpha}{\sin\beta}.$$

This allows, for example, to set limits on M_h in terms of the β angle and the M_A parameter by studying the unseen h SM-like Higgs field and its decay modes into SM fermions. LEP has set $M_h \leq 114.4\,GeV$ [52] for most M_A values, though being less stringent for very close values of M_A and M_h. The tree level mass of the lightest Higgs cannot fulfill this requirement, since it is smaller than M_Z. However, various loop corrections of the most coupled particles to the Higgs fields, namely the top-quark, can bring it up to values above the limit. However, the lightest Higgs boson in the MSSM cannot be much heavier than $\sim 130\,GeV$ (see [60] for a review).

While there are supersymmetric scenarios with unification of gaugino masses, here we do not impose such conditions. We will treat the least constrained configurations, and thus, in principle, will consider as a free parameter each mass of a new particle. Indeed, the gaugino masses M_1, M_2 et M_3, the sfermion masses $M_{\tilde{u}_L}$, $M_{\tilde{u}_R}$, etc, are taken as free parameters, unless otherwise stated. These parameters are the soft masses of the sfermions, which, however, can mix between left and right sfermions of the same flavor to yield two different physical masses. For example, while usually $M_{\tilde{\tau}_L}$ and $M_{\tilde{\tau}_R}$ are the free parameters, the physical staus will be given by $\tilde{\tau}_1$ and $\tilde{\tau}_2$ where the former is the lightest of the two, hence, the mass of which is constrained by experiments.

Soft SUSY breaking also includes trilinear couplings of scalar fields. For example, a sfermion-sfermion-Higgs coupling is determined by such a trilinear $A_{\tilde{f}}$ coupling. Therefore, we introduce three free parameters, one for each type of superpartner coupled to the Higgs: A_t for the

up-type squarks, A_b for the bottom-type squarks and A_τ for sleptons. The trilinear couplings play a role in the mixing matrices of the left and right sfermions.
We had discussed that charged particles are rather heavily constrained. The $\chi^+_{1,2}$ charginos are a mix of the charged winos and higgsino states. Thus they are spin-$1/2$ charged particles. The lightest chargino thus constructed would be mainly made of the lightest of the two components, thus with a mass which is roughly $M_{\chi^+_1} \sim Min(M_2, \mu)$. By constraining the lightest chargino mass one can infer constraints upon these two mass terms, which also contribute to the neutralino mass.
Further constraints can be drawn by computing the MSSM contributions to precision observables in the EW and B-meson fields. We will take into account these considerations in our searches.

6.2.3 Neutralino dark matter

We focus in scenarios in which the LSP is the lightest of the neutralinos. Neutralinos are Majorana particles, made of the mix of the neutral weak gauginos and the neutral higgsinos. There are four neutralino states, usually ordered by mass, and are denoted by χ^0_k where $k = 1, ..., 4$. Hence, we focus in the case of χ^0_1 LSP. The neutralino masses depend upon the masses of the $\tilde{B}$, the $\tilde{W}$ and the higgsinos, as well as the mixing terms of the EW sector –namely the Weinberg θ_W phase–, and the Higgs sector mixing given by β. Thus the mass matrix is

$$\mathcal{M}^n_{MSSM} = \begin{pmatrix} M_1 & 0 & -M_Z s_w c_\beta & M_Z s_w s_\beta \\ 0 & M_2 & M_Z c_w c_\beta & -M_Z c_w s_\beta \\ -M_Z s_w c_\beta & M_Z c_w c_\beta & 0 & -\mu \\ M_Z s_w s_\beta & -M_Z c_w s_\beta & -\mu & 0 \end{pmatrix}, \tag{6.1}$$

where c_w (s_w) and c_β (s_β) are the cosine (sine) of the θ_W and β mixing angles respectively. This matrix can be diagonalized. Hence the lightest neutralino is given by

$$\chi^0_1 = N_{11}\tilde{B} + N_{12}\tilde{W} + N_{13}\tilde{H}_d + N_{14}\tilde{H}_u.$$

The lightest neutralino is thus dominated by the lightest of the gauginos and/or higgsinos available. Since the μ mass term is common to both higgsinos, the contribution of these states is usually of the same order (with always a larger fraction of $\tilde{H}_d$ given by the fact that $\tan\beta \geq 1$). Furthermore, we saw that μ and M_2 are severely constrained by unfruitful chargino searches and are roughly $\mu, M_2 \gtrsim 100\,GeV$. This is why $M_{\chi^0_1} \ll 100\,GeV$ implies a large $\tilde{B}$ contribution. Actually, by forcing the determinant of the diagonalizing matrix to vanish one could ensure a massless lightest neutralino. However, throughout this work we will rather look at neutralinos of the order of the EW scale and down to the GeV scale. Thus, it is expected that the neutralino behaves as CDM regarding Cosmology, and that it should manifest itself at the LHC.

Neutralinos are coupled to the Z-boson via the higgsinos components. Also, the higgsino, bino and wino are coupled to the h, H and A bosons, allowing thus the coupling of the neutralino to these bosons as well. These vertices at tree level are expressed by

$$\begin{aligned}
Z\chi_1^0\chi_1^0 \equiv & i\frac{g_2}{2\cos\theta_W}\gamma_\mu\gamma_5\left[N_{13}^2 - N_{14}^2\right], \\
h\chi_1^0\chi_1^0 \equiv & i\,g_2\left[\left(N_{12} - \tan\theta_W N_{11}\right)\left(\sin\alpha N_{13} + \cos\alpha N_{14}\right)\right], \\
H\chi_1^0\chi_1^0 \equiv & i\,g_2\left[\left(N_{12} - \tan\theta_W N_{11}\right)\left(\cos\alpha N_{13} + \sin\alpha N_{14}\right)\right], \\
A\chi_1^0\chi_1^0 \equiv & g_2\left[\left(N_{12} - \tan\theta_W N_{11}\right)\left(\sin\beta N_{13} - \cos\beta N_{14}\right)\right].
\end{aligned}$$

The neutralino has, of course, many other interactions, among which we stress the importance of the $f\tilde{f}\chi_0^1$ vertices. The expression of such vertices is rather complex and includes an interplay of all the parameters related to the neutralino mixing and mass, sfermion mixing and masses, Higgs sector mixings and the EW parameters.
The neutralino annihilation rates are a crucial point for both the obtention of the relic density and the ID searches, while elastic scattering is important for thermal equilibrium in EU and in the case of the quark-neutralino interactions for DD efforts. Since the neutralino is the LSP we expect it to annihilate into SM particles or Higgs bosons at low energies. In such cases, the vertices we have discussed are the most important ones to take into account. Indeed, neutralinos can annihilate into fermions via s-channel exchanges of Higgs bosons or a Z-boson, or via t and u-channel exchanges of sfermions. Annihilations into Higgs bosons can happen via the exchange of a neutralino in a t or u-channel, and by the s-channel exchange of a Higgs boson. Regarding elastic scattering off quarks, the interactions happen through a t-channel exchange of a Higgs boson or Z boson, the former contributing only to spin independent interactions, while the latter yields spin dependent interactions. Also quarks and neutralinos can exchange a squark through a s-channel. This diagram contributes to both cases, spin dependent and spin independent interactions. We illustrate such diagrams in Fig. 6.1. In general, the squark masses are large compared to M_Z and M_h, assuming M_h is SM-like. Thus, interactions are dominated by boson exchanges. However, for marginal configurations with the lightest possible squark masses, we may encounter a mixed contribution from these diagrams. Squark interactions can be destructive in the combination with the boson driven, thus lowering the total interaction rate instead of increasing it.

6.3 Next-to-Minimal Supersymmetric Standard Model

We now introduce the Next-to-MSSM. We will only stress the main differences with the MSSM and the aspects of interest for neutralino phenomenology and the configurations that go along. For a complete review on this model we refer to [61].

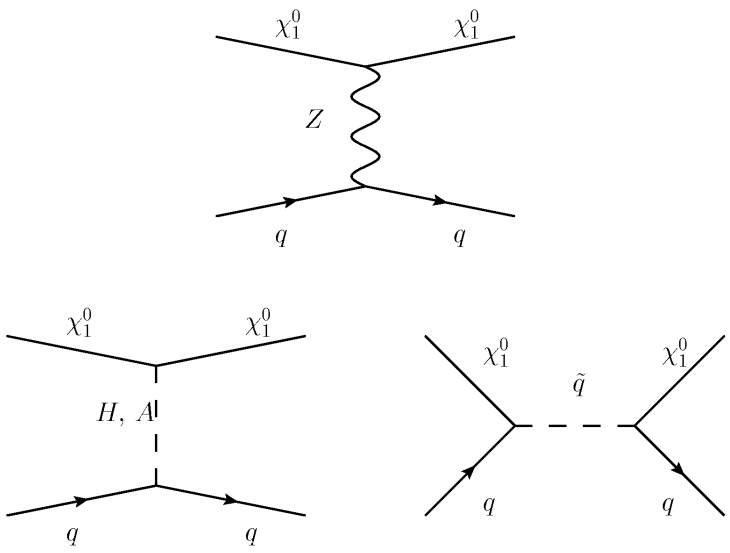

Fig. 6.1: Neutralino-quarks elastic scattering processes at tree level.

6.3.1 Introduction to the next-to-minimal supersymmetric standard model

The NMSSM consists of a simple extension of the MSSM. It is motivated by the unnatural scale of the μ mass parameter in the MSSM supersymmetric lagrangian, which is needed to be at the range of the weak scale. However, there is no fundamental mechanism making this only by a structural reason rather than a consequence of scale considerations of other sectors of the theory. As a mass term, it does not carry any fundamental quantum number of the SM symmetry group. It is an invariant of SUSY, which makes its natural values either zero or the unification scale. In the Higgs mechanism the mass spectrum of the particles is successfully explained by the VEV of a fundamental scalar field. In order to ensure an emergent μ mass parameter a similar path can be taken. Adding one extra field to the Higgs sector with a non vanishing VEV naturally generates the mass range, avoiding any fine-tuned definition. The MSSM superpotential is thus modified by the inclusion of the S superfield containing the new s Higgs field and its superpartner, the singlino $\tilde{S}$. This scalar field is taken as a singlet of $SU(2)_L$ in particular, and in general of the SM symmetry group. Indeed, we do not want any effect of such a scalar field upon SM physics nor in the EW symmetry breaking mechanism. The superpotential in the NMSSM can be expressed in terms of the MSSM superpotential as follows

$$\mathcal{W}_{NMSSM} = (\mathcal{W}_{MSSM} - \mu H_1.H_2) + \lambda S H_1.H_2 + \frac{1}{3}\kappa S^3,$$

which is equivalent to the following transformation

$$\mu H_1.H_2 \to \lambda S H_1.H_2 + \frac{1}{3}\kappa S^3.$$

Thus, we have introduced the dimensionless λ and κ Yukawa couplings. This is not the most general inclusion in the superpotential. Indeed, one could in principle leave the μ term untouched, include a second mass term coupled to S^2 and a supersymmetric tadpole for S with a mass-squared dimension parameter. However, including such terms would imply introducing more parameters which then would be to be set by hand at the EW scale, as it was the case for the μ in the MSSM superpotential. Hence, we restrain to this configuration. Now, the MSSM μ mass parameter is set by $\langle s \rangle$, hence, strictly speaking, μ is not a free parameter any more. However, we may define the effective μ-term

$$\mu_{eff} = \lambda \langle s \rangle .$$

Thus, by fixing the VEV of s and the λ coupling, the effective mass term is fixed, which is what motivates the inclusion of S and makes the terms we choose not to write in the general NMSSM superpotential rather unwanted. However, in light of all the understanding of the MSSM that has been built throughout the years, it is generally preferred to take μ_{eff} as a free parameter and thus adjust $\langle s \rangle$ to its choice. From now on, in the NMSSM frame, whenever we quote μ we refer actually to the effective μ term.
Regarding SUSY breaking schemes, the NMSSM is also rich in mechanisms leading to a well motivated configuration at low energies. Furthermore, constrained scenarios also exist in the NMSSM. We pursue in our wide view of the EW scale possibilities.

6.3.2 *Impact of the S superfield*

The inclusion of s to the Higgs sector gives rise to new bosons in the Higgs spectrum. Hence, there are now three neutral Higgs CP-even bosons $H_{1,2,3}$ and two neutral CP-odd Higgs bosons $A_{1,2}$, in both cases ordered by mass. The three scalar and the two pseudoscalar mass eigenstates now contain contributions from the singlet scalar field from the weak interaction basis. The second novel implication of the S superfield is the singlino state. Singlinos are spin-$1/2$ neutral particles coupled to the regular higgsinos. Hence they also contribute to the mixed neutralinos.
The soft part of the NMSSM lagrangian includes the usual terms from the two Higgs doublets and their mixed physical fields, enhanced by the new scalar features. These affect the trilinear couplings in the Higgs sector (which imply the the doublet-doublet-singlet A_λ and the triple singlet A_κ trilinear couplings, two new free parameters), the couplings of the Higgs bosons to sparticles and gauginos, and the singlino couplings to the Higgs, sparticle and gaugino sectors. This implies that the parametrization with the S superfield implies the replacement of the MSSM μ and M_A free parameters by λ, κ, A_λ, A_κ, $\langle s \rangle$, with, in practice, $\langle s \rangle$ being replaced by μ_{eff}.
As a general statement, all the Higgs and neutralino phenomenologies get new features. However, most of these features are only slight deviations from the MSSM phenomenology.

Nonetheless, the extreme cases yield rather interesting supersymmetric particle spectra and interactions. A singlet dominated lightest Higgs does not behave at all as a SM-like Higgs. Indeed, its couplings to the SM particles would be severely suppressed, since they are carried by the doublet fractions. This implies that a singlet dominated Higgs cannot be thoroughly scanned at colliders regarding production and decays for direct signatures, nor in the loop and high-order contributions to EW and B-meson physics –however, the charged Higgs and chargino phenomenology is not really modified. Thus, many scenarios can easily fall below all limits established for SM-like Higgs bosons or MSSM-like pseudoscalars. Hence, there is now a possibility of lightest Higgs bosons lighter than $\lesssim 100 GeV$. Light Higgs bosons generate very interesting conditions for neutralino interactions and collider physics. For the latter, unexpected (in MSSM) kinematic configurations could lead to very characteristic signatures (supersymmetric, yet particular to the NMSSM), which motivates dedicated searches for NMSSM scenarios at the LHC. On the other hand, the SM-like Higgs mass gets a new correction from the singlet component. If the singlet field is rather heavy (which corresponds to $\kappa \langle s \rangle \ll |A_\lambda|, |A_\kappa|$), then M_H^{SM} could reach up to $\sim 140\, GeV$.

6.3.3 Neutralino dark matter

In the NMSSM the neutralino weak eigenstate vector acquires a new component: the singlino. Hence, the neutralino mass matrix in the NMSSM reads

$$\mathcal{M}^n_{NMSSM} = \begin{pmatrix} M_1 & 0 & -M_Z s_w c_\beta & M_Z s_w s_\beta & 0 \\ 0 & M_2 & M_Z c_w c_\beta & -M_Z c_w s_\beta & 0 \\ -M_Z s_w c_\beta & M_Z c_w c_\beta & 0 & -\mu & -\frac{\lambda v_1}{\sqrt{2}} \\ M_Z s_w s_\beta & -M_Z c_w s_\beta & -\mu & 0 & -\frac{\lambda v_2}{\sqrt{2}} \\ 0 & 0 & -\frac{\lambda v_1}{\sqrt{2}} & -\frac{\lambda v_2}{\sqrt{2}} & \frac{2\mu\kappa}{\lambda} \end{pmatrix}. \tag{6.2}$$

The singlino component comes in the fifth row and columns. The top-left 4×4 matrix is exactly the MSSM neutralino mass matrix, with the caveat that μ is here an effective quantity and not really a parameter. The bottom-right 3×3 matrix shows the only singlino mixing terms, which correspond to the higgsino sector. Namely, there is no mixing with the gauginos. The lightest neutralino is now given by

$$\chi_1^0 = N_{11}\tilde{B} + N_{12}\tilde{W} + N_{13}\tilde{H}_d + N_{14}\tilde{H}_u + N_{15}\tilde{S}.$$

Neutralino crucial couplings do not change in their nature with respect to those in the MSSM. However, the expression of the vertices must now include the singlet (singlino) components of Higgs bosons (neutralinos) whenever they are involved. Thus, the vertices containing physical Higgses and neutralinos include the components of the Higgs and neutralino diagonalized mass matrices. If we name $\mathcal{H}_{ij}$ and $\mathcal{A}_{kl}$ (with $i, j, l = 1, 2, 3$ and $k = 1, 2$, i and k

spanning mass eigenstates and j and l the corresponding doublets and singlet contributions) the CP-even and odd Higgs mass matrices, then we get

$$\begin{aligned}
H_1\chi_1^0\chi_1^0 \equiv & i\frac{\lambda}{\sqrt{2}}\left[\mathcal{H}_{11}\left(N_{14}^2-N_{15}^2\right)+\mathcal{H}_{12}\left(N_{13}^2-N_{15}^2\right)+\mathcal{H}_{13}\left(N_{13}^2-N_{14}^2\right)\right] \\
& -i\sqrt{2}\kappa\mathcal{H}_{13}N_{15}^2+i\frac{g_Y}{2}\left[\mathcal{H}_{11}\left(N_{11}^2-N_{13}^2\right)+\mathcal{H}_{12}\left(N_{11}^2-N_{14}^2\right)\right] \\
& +i\frac{g_2}{2}\left[\mathcal{H}_{11}\left(N_{12}^2-N_{13}^2\right)+\mathcal{H}_{12}\left(N_{12}^2-N_{14}^2\right)\right], \\
A_1\chi_1^0\chi_1^0 \equiv & \frac{\lambda}{\sqrt{2}}\left[\mathcal{A}_{11}\left(N_{14}^2-N_{15}^2\right)+\mathcal{A}_{12}\left(N_{13}^2-N_{15}^2\right)+\mathcal{A}_{13}\left(N_{13}^2-N_{14}^2\right)\right] \\
& -\sqrt{2}\kappa\mathcal{A}_{13}N_{15}^2+i\frac{g_Y}{2}\left[\mathcal{A}_{11}\left(N_{11}^2-N_{13}^2\right)+\mathcal{A}_{12}\left(N_{11}^2-N_{14}^2\right)\right] \\
& +\frac{g_2}{2}\left[\mathcal{A}_{11}\left(N_{12}^2-N_{13}^2\right)+\mathcal{A}_{12}\left(N_{12}^2-N_{14}^2\right)\right],
\end{aligned}$$

while the $Z\chi_1^0\chi_1^0$ remains unchanged as well as the $f\tilde{f}\chi_1^0$ coupling.
The exchange of light Higgs bosons –in annihilation and elastic scattering processes– enlarges the possibilities of interactions rates the neutralino can have. However, lighter Higgs bosons mean large singlet components, which in turn translates into small couplings. Thus, real boosts in cross sections could only be obtained for limiting cases of kinematic configurations between the exchanged particles.

7 Scalar Dark Matter candidates

Among the new particles generated by the application of a second supersymmetric charge, there would be scalars and mirror partners of the SM fermions. This motivates the possibility of the DM being actually made of scalar particles. Without fully constructing a prescription to obtain such scalars, we just use the fact that they might exist and develop some phenomenological aspects of Yukawa couplings of scalar particles to SM fermions and their mirror partners. Hence we can address the possibility of the DM being constituted of neutral scalar particles. A complete study on the matter of construction of such a model is still missing, however we focus on the phenomenological implications of this hypothetical scenario, following the steps of [62].

7.1 New scalars and fermions

The scenario here presented relies on the existence of both scalars S –with no relation to the singlet superfield in the NMSSM– and mirror partners F to the SM fermions f. These three particles are coupled through Yukawa couplings. Hence, annihilation and elastic scattering interactions between scalars and SM particles can happen. For the newly introduced scalar particles to represent a DM candidate we also need it to be stable, neutral and colorless. While the two latter characteristics imply electromagnetic and QCD null quantum numbers, the former implies the existence of a broken symmetry stabilizing the particle. Hence we assume the existence of a discrete Z_2 symmetry, called M-parity in contrast with the $N = 1$ SUSY case, which yields a parity quantum number. The scalars are thus supposed to be the lightest M-odd particles, therefore stable.

While the scalar is only weakly coupled to the SM, the mirror partners of the SM fermions would carry some of their quantum numbers. For instance, if we focus in the electron e_R^- and e_L^-, then we need to introduce both F_L^e and F_R^e, both carrying a -1 electromagnetic charge. By repeating this for all SM fermions, we get the full spectrum of the mirror partners, which are chiral Dirac fermions. This implies that the ν mirror partners F_ν are neutral and the quark mirror partners F_q carry a color charge. Hence, the full lagrangian includes such terms as

$$\mathcal{L} \supset S\, \delta_{ij}\, \bar{F}_x^{\,i}\, (c_l^x P_r + c_r^x P_L)\, q^j.$$

where x stands for the type of fermion –all leptons and quarks–, i and j span flavor and color, $P_{R,L}$ are the right and left chiral projectors introduced in Sec. 5.1, and c_l^x and c_r^x are the non-universal Yukawa couplings. These new interactions imply a new subset of parameters, which we do not connect to any SUSY breaking scheme nor any high energy unification, which are simply the Yukawa couplings and the masses of the particles acquired via a Higgs mechanism, though we do not detail the Higgs sector in this work.
We will discuss in what follows $O((1-100)MeV)$ DM candidates with the correct relic density. We will further study their collider predictions for the LHC in Chapter 11.

7.2 Light scalars

The deepest motivation for the construction of this model is its LSP, a scalar which represents a DM candidate. In principle, its mass m_S may be as light as one could imagine. However, we restrict our considerations to plausible scenarios regarding cosmology.

7.2.1 Lee-Weinberg bound

Very general bounds on DM mass can be drawn by relating it to interaction rates with SM particles. Indeed, the DM energy density of $\Omega_{CDM}h^2 \simeq 0.1109$ [63] is not to be exceeded by any relic particle. If the relic density of a stable particle is determined by the the FO mechanism, then the interaction rate at the FO temperature is deeply related with the relic density found. This way, one may find a limit on the DM mass by constraining its annihilation rate in EU. This was first done for heavy neutrinos as DM [64], but the extension to any kind of fermionic DM is straightforward. One finds that $m_{DM} \gtrsim O(1\,GeV)$.
However, this bound applies just to fermions. Indeed, the mass enters in the cross section expression when computing the interaction amplitude and including the particle mass in the spinor. If the DM candidate is a scalar, there is no spinor, hence no mass dependence in the annihilation rate. Thus, $\langle\sigma v\rangle$ is roughly independent of m_S [62]. The bound is therefore lifted for scalars. Hence, we can address $m_S \lesssim 1\,GeV$ scenarios, which can reproduce the right relic density through FO.

7.2.2 Interactions in early universe and the scalar mass interval

Since we want large (enough) production rates at the LHC, we want to maximize the scalar coupling to the quarks, SqF_q, where the quark mirror partners F_q also intervene. However, if this coupling is very large, we expect large interactions with protons, neutrons and pions in EU. In particular, annihilation into these particles can bring the scalar relic density to zero. Nevertheless, we may invoke kinematical reasons to avoid this, setting m_S below the lightest meson or baryon. Indeed, this way the DM annihilation processes involving

SqF_q interactions are forbidden by the lack of a phase space. We take then $m_S \leq m_{\pi^0}$ ($\simeq 134.9766 \pm 0.0006\,MeV$ [52]). To achieve the correct relic density, scalar will annihilate into lighter particles: muons, electrons and/or neutrinos.
In addition, the scalar interactions with quarks could have an influence in the primordial nucleosynthesis processes. While there are still details to solve regarding the abundance of some marginal elements like ^6Li and ^7Li, the bulk of the theory works so well as it is that we should safeguard it. Therefore, in order to be cautious regarding primordial nucleosynthesis, we ask the scalars to freeze-out before the primordial nucleosynthesis takes place, that is to say $T_{NS} \leq T_{FO}$. As seen in Section 4.1.1, primordial nucleosynthesis starts at $T_{NS} \simeq 100\,keV$. It has been shown that for m_S in the $[1-100]\,MeV$ range, $T_{FO}/m_S \simeq [11-19]$ [62]. Hence, for this analysis, we restrict the scalar mass to be $m_S \gtrsim 1\,MeV$. An interesting question that is yet to be investigated concerns the impact lighter scalars could have on primordial nucleosynthesis, could it help solving the lithium problem?
With these considerations we have defined the following range for the scalar mass: $1\,MeV \lesssim m_S \lesssim 135\,MeV$.

7.3 Interactions with charged leptons

As scalars annihilate into light particles, we now analyse annihilation into charged leptons, namely muons and electrons.

7.3.1 *Constraint from* $(g-2)_{e,\mu}$

The SeF_e and $S\mu F_\mu$ coupling responsible for triggering scalar annihilation into electron/positron pairs and muon pairs, also yield other interactions. Indeed, we expect contributions to the lepton anomalous magnetic moments, measured by the $(g-2)_{e,\mu}$ observables. Their deviation to the measured values allows the BSM contributions to exist, but they cannot account for more than the difference between the SM prediction and the measured value. Hence, their contribution cannot exceed $\sim 10^{-9}$ for muons and $\sim 10^{-11}$ for electrons. Assuming $m_S \ll m_{F_{e,\mu}}$, this contribution behaves as $\delta\alpha_{e,\mu} \propto \frac{c_l^{e,\mu} c_r^{e,\mu}}{m_{F_{e,\mu}}}$. $\langle \sigma_{SS\to l^+l^-} v \rangle$, where $l \equiv e, \mu$, is actually also proportional to this term. This way a stringent constraint is to be respected by annihilation into charged leptons, namely $\langle \sigma_{SS\to\mu^+\mu^-} v \rangle \lesssim 10^{-29} cm^3 s^{-1}$ [62]. This value is too small to achieve $\Omega_{CDM}h^2$ relying on annihilations into charged leptons.

7.3.2 *Smaller interactions for electrons and the 511 keV line from the galactic center*

Among indirect detection observables are γ-ray fluxes. If S interacts with leptons, and namely electrons, we expect to have such signals from the galactic center for energies below m_S. On one hand, the interaction rate could be constrained by the observed fluxes, and on the other

one could try to fit the observed value if there is room for a signal with the characteristics of DM annihilations.
In [65] the SPI spectrometer in the INTEGRAL satellite reported a rather bright $511\,keV$ line with a potential diffuse morphology [66], although observations with better resolutions suggest a correlation with astrophysical objects, thus favoring rather standard explanations for the measured flux. Annihilating scalars could actually reproduce this signal because of kinematic reasons: low energy production of positrons would allow the production of positronium atoms with the subsequent decay into photon pairs after electron/positron annihilation quasi at rest. This however requires a very suppressed velocity dependence in $\langle \sigma_{SS\to e^+e^-} v \rangle$ which is not natural for annihilation through the F. Therefore, either the EU annihilation rate is drastically reduced to values $\lesssim 10^{-31}\,cm^3 s^{-1}$ (where the largest possible value is obtained for a flat dark matter halo profile towards the galactic center), either too many $511\,keV$ photons [67] and γ-rays in general [68] would be produced at the galactic center. This further constrains the possibility of achieving relic density via annihilation into charged leptons.
Further studies show the plausibility of scalar DM producing the observed signal from the MW GC [69, 70]. Although this possibility is still very interesting and not completely ruled out by standard astrophysical sources, there is no need to stick to this phenomenological configuration. Instead we only keep the upper bound to the annihilation cross section into light charged leptons.

7.4 Interactions with neutrinos

For the range of masses we are interested in only annihilation into neutrinos can proceed at sufficiently large rates to reproduce the correct relic density of DM.

7.4.1 Annihilation into neutrinos

In principle there is no other constraint coming from neutrino annihilation other than EU FO of scalar particles. This requirement sets then the annihilation cross section to $\sim 10^{-26}\,cm^3 s^{-1}$. However, at this rate and for part of the mass range of the scalar DM, the inverse reaction could be responsible for scalar production in core-collapse SN explosions, where the core temperature can reach a few tens of MeV [71]. Then, the question of energy transport arises, since a huge amount of energy is indeed carried away by neutrinos: what influence can the presence of such scalars have in the explosion mechanism? This is another open question.

7.4.2 An interesting implication: neutrino masses explained?

In [72] the possibility of a link between thermally produced scalars and neutrino mass is explored. Indeed, by modelling the interaction with an effective coupling, the authors show

that the annihilation cross section –which is $\langle\sigma_{SS\to\nu\nu}\rangle \simeq \frac{g^4}{4\pi}\frac{m^2_{F_\nu}}{(m^2_S+m^2_{F_\nu})^2}$, where g is an effective coupling– is in direct relation with the scalar and F_ν contribution to the neutrino mass. Through a loop exchange of such particles, the effective neutrino mass is $m_\nu = \sqrt{\frac{\sigma v}{128\pi^3}} m^2_{F_\nu}\left(1+\frac{m_S}{m_{F_\nu}}\right) ln\left(\frac{\Lambda^2}{m^2_{F_\nu}}\right)$, where Λ is an effective electroweak cut-off of the effective theory. It is easy to see that for a choice of masses and cut-off scale, the neutrino mass can have a suitable value. However, no stronger conclusion is to be taken hereafter, since no neutrino interaction is really expected at the LHC.

7.5 Interactions with quarks

Let us now focus on the scalar interactions with quarks, the most relevant for the LHC. Since we can safely assume the relic density is achieved through neutrino interactions, and the mass range of the scalars was chosen in order not to modify the primordial nucleosynthesis physics nor to annihilate into colored particles, the relevant vertices are so far unconstrained in this scenario.

7.5.1 Vertices

Since we are interested in new particle production at the LHC, we need to consider interactions involving these new particles –the scalar and the quark mirror partners F_q– as well as the partonic content of the proton –hence u, d and s quarks, as well as gluons. The term responsible for SqF_q interactions to include in the lagrangian is

$$S\,\delta_{ij}\,\bar{F}_q^{\,i}\,(c_l^q P_R + c_r^q P_L)\,q^j. \tag{7.1}$$

Here, δ_{ij} ensures flavor and color conservation. Here c_l^q and c_r^q are the Yukawa couplings exclusively related to these vertices (not universal with scalar-lepton interaction couplings), and P_R and P_L are the chiral projectors as defined in Sec. 5.1. The corresponding vertex is displayed in Fig. (7.1).

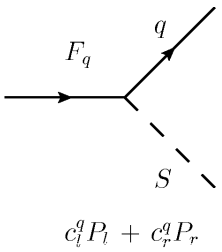

Fig. 7.1: Vertex introduced by the Yukawa interaction of scalar DM, quarks and their mirror partners F_q. Notice that for $m_{F_q} \geq m_S, m_q$, the decay of F_q is represented by this diagram.

The F_q are colored particles, therefore we also expect them to interact with gluons. In analogy to the usual QCD lagrangian, we then have the term

$$g\, G^a_\mu \bar{F}_i \gamma^\mu T^a_{ij} F_j, \tag{7.2}$$

where g is the strong interaction coupling, G^a_μ are the gluon fields, γ^μ are the Dirac matrices, T^a_{ij} are the generators relevant to the SU(3) group. a runs from 1 to 8 for the eight gluon fields, i and j span the color values, green, red and blue. Such a vertex is represented in Fig. (7.2).

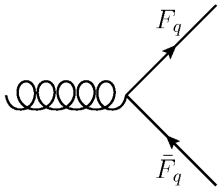

Fig. 7.2: QCD-like vertex for colored F_q particle interactions with gluons.

7.5.2 Free parameters

The free parameters to scan for LHC production of F_q and S are thus the couplings $-c^q_l$ and c^q_r- and the new particle masses m_S and m_{F_q}, the latter taken to be universal for all quark flavors, for simplicity.

Couplings cannot be arbitrarily large. On one hand, we want perturbative theory to hold for simplicity of calculations. Hence we do not allow c^q_l and c^q_r to be ≥ 3. It is arguable that couplings as large as 3, even though perturbative, may yield anomalies which would have been seen in particle physics experiments, however, since specific studies on the matter have not been carried out, and we are making a proof of concept, we still explore such large values. We will actually rule out the largest values by studying signals at the Tevatron and the LHC. On the other hand, we are interested in observable phenomenologies, therefore we restrict our analysis to large enough couplings, say ≥ 0.1.

The scalar mass range has already been determined by other interactions as discussed in 7.2.2. Regarding the F_q, these are charged particles. The search for new charged particles at colliders can set a limit on m_{F_q}. For example, if one assumes that the F_q could be similar to heavier generation quarks, we may apply the lower limits on b' and t'-like particles, which currently are $268\,GeV$ and $256\,GeV$ [52]. We will see later on more stringent constraints for m_{F_q}, which involve the production of such particles at the Tevatron and the LHC.

Bibliography

[1] Subir Sarkar. Big bang nucleosynthesis and physics beyond the standard model. *Rept.Prog.Phys.*, 59:1493–1610, 1996. Dedicated to Dennis Sciama on his 67th birthday.

[2] Steven Weinberg. Cosmology. Oxford, UK: Oxford Univ. Pr. (2008) 593 p.

[3] Jeremy Bernstein, Lowell S. Brown, and G. Feinberg. Cosmological Helium production simplified. *Rev.Mod.Phys.*, 61:25, 1989. Revised version of CU-TP-386.

[4] E. Komatsu et al. Seven-Year Wilkinson Microwave Anisotropy Probe (WMAP) Observations: Cosmological Interpretation. *Astrophys.J.Suppl.*, 192:18, 2011.

[5] Torsten Bringmann and Stefan Hofmann. Thermal decoupling of WIMPs from first principles. *JCAP*, 0407:016, 2007.

[6] Joseph Silk. Cosmic Black-Body Radiation and Galaxy Formation. *Astrophys.J.*, 151:459, 1968.

[7] Céline Boehm, Pierre Fayet, and Richard Schaeffer. Constraining the strength of dark matter interactions from structure formation. pages 333–344, 2002.

[8] Céline Boehm and Richard Schaeffer. Constraints on dark matter interactions from structure formation: Damping lengths. *Astron.Astrophys.*, 2004.

[9] Silvia Galli, Fabio Iocco, Gianfranco Bertone, and Alessandro Melchiorri. CMB constraints on Dark Matter models with large annihilation cross-section. *Phys.Rev.*, D80:023505, 2009.

[10] Silvia Galli, Fabio Iocco, Gianfranco Bertone, and Alessandro Melchiorri. Updated CMB constraints on Dark Matter annihilation cross-sections. 2011.

[11] Mark W. Goodman and Edward Witten. Detectability of Certain Dark Matter Candidates. *Phys.Rev.*, D31:3059, 1985.

[12] E. Aprile et al. Dark Matter Results from 100 Live Days of XENON100 Data. *Phys.Rev.Lett.*, 2011. Long author list - awaiting processing.

[13] E. Komatsu et al. Five-Year Wilkinson Microwave Anisotropy Probe (WMAP) Observations:Cosmological Interpretation. *Astrophys. J. Suppl.*, 180:330–376, 2009.

[14] R. Bernabei, Pierluigi Belli, F. Cappella, R. Cerulli, F. Montecchia, et al. Dark matter search. *Riv.Nuovo Cim.*, 26N1:1–73, 2003.

[15] G. Belanger, F. Boudjema, A. Pukhov, and A. Semenov. Dark matter direct detection rate in a generic model with micrOMEGAs 2.2. *Comput.Phys.Commun.*, 180:747–767, 2009.

[16] A.K. Drukier, K. Freese, and D.N. Spergel. Detecting Cold Dark Matter Candidates. *Phys.Rev.*, D33:3495–3508, 1986.

[17] David N. Spergel. The motion of the Earth and the detection of WIMPs. *Phys.Rev.*, D37:1353, 1988.

[18] R. Bernabei, P. Belli, F. Cappella, R. Cerulli, C.J. Dai, et al. New results from DAMA/LIBRA. *Eur.Phys.J.*, C67:39–49, 2010.

[19] C.E. Aalseth, P.S. Barbeau, J. Colaresi, J.I. Collar, J.Diaz Leon, et al. Search for an Annual Modulation in a P-type Point Contact Germanium Dark Matter Detector. 2011.

[20] C.E. Aalseth et al. Results from a Search for Light-Mass Dark Matter with a P-type Point Contact Germanium Detector. *Phys.Rev.Lett.*, 106:131301, 2011.

[21] Marco Farina, Duccio Pappadopulo, Alessandro Strumia, and Tomer Volansky. Can CoGeNT and DAMA Modulations Be Due to Dark Matter? 2011.

[22] E. Aprile et al. First Dark Matter Results from the XENON100 Experiment. *Phys.Rev.Lett.*, 105:131302, 2010.

[23] J.I. Collar and D.N. McKinsey. Comments on 'First Dark Matter Results from the XENON100 Experiment'. 2010.

[24] The XENON100 Collaboration. Reply to the Comments on the XENON100 First Dark Matter Results. 2010.

[25] J.I. Collar and D.N. McKinsey. Response to arXiv:1005.2615. 2010.

[26] E. Aprile et al. Likelihood Approach to the First Dark Matter Results from XENON100. 2011.

[27] E. Armengaud et al. Final results of the EDELWEISS-II WIMP search using a 4-kg array of cryogenic germanium detectors with interleaved electrodes. 2011.

[28] Z. Ahmed et al. Combined Limits on WIMPs from the CDMS and EDELWEISS Experiments. 2011.

[29] M. Felizardo, TA Girard, T. Morlat, A.C. Fernandes, F. Giuliani, et al. Final Analysis and Results of the Phase II SIMPLE Dark Matter Search. 2011.

[30] Rolf Kappl and Martin Wolfgang Winkler. New Limits on Dark Matter from Super-Kamiokande. 2011.

[31] R. Abbasi et al. Measurement of the atmospheric neutrino energy spectrum from 100 GeV to 400 TeV with IceCube. *Phys.Rev.*, D83:012001, 2011.

[32] Ivone F.M. Albuquerque, Leandro J.Beraldo e Silva, and Carlos Perez de los Heros. Constraints on Enhanced Dark Matter Annihilation from IceCube Results. 2011.

[33] J. Angle, E. Aprile, F. Arneodo, L. Baudis, A. Bernstein, et al. Limits on spin-dependent WIMP-nucleon cross-sections from the XENON10 experiment. *Phys.Rev.Lett.*, 101:091301, 2008.

[34] E. Daw, J.R. Fox, J.-L. Gauvreau, C. Ghag, L.J. Harmon, et al. Spin-Dependent Limits from the DRIFT-IId Directional Dark Matter Detector. 2010.

[35] S. Ahlen, J.B.R. Battat, T. Caldwell, C. Deaconu, D. Dujmic, et al. First Dark Matter Search Results from a Surface Run of the 10-L DMTPC Directional Dark Matter Detector. *Phys.Lett.*, B695:124–129, 2011.

[36] S. Vahsen. Talk at the 3rd international conference on directional detection of dark matter (cygnus 2011). Aussois, France, 8-10 June 2011.

[37] Tatsuhiro Naka, Mitsuhiro Nakamura, Osamu Sato, Toshiyuki Nakano, and Kimio Niwa. Directional direct detection with nuclear emulsion. *PoS*, IDM2008:004, 2008.

[38] Kentaro Miuchi, Hironobu Nishimura, Kaori Hattori, Naoki Higashi, Chihiro Ida, et al. First underground results with NEWAGE-0.3a direction-sensitive dark matter detector. *Phys.Lett.*, B686:11–17, 2010.

[39] D. Santos, J. Billard, G. Bosson, J.L. Bouly, O. Bourrion, et al. MIMAC : A micro-tpc matrix for directional detection of dark matter. 2011.

[40] J. Billard, F. Mayet, and D. Santos. Markov Chain Monte Carlo analysis to constrain Dark Matter properties with directional detection. *Phys.Rev.*, D83:075002, 2011.

[41] P. Salati, F. Donato, and N. Fornengo. Indirect Dark Matter Detection with Cosmic Antimatter. 2010.

[42] Oscar Adriani et al. An anomalous positron abundance in cosmic rays with energies 1.5-100 GeV. *Nature*, 458:607–609, 2009.

[43] J.E. Gunn, B.W. Lee, I. Lerche, D.N. Schramm, and G. Steigman. Some Astrophysical Consequences of the Existence of a Heavy Stable Neutral Lepton. *Astrophys.J.*, 223:1015–1031, 1978.

[44] Melissa Pesce-Rollins and for the Fermi-LAT Collaboration. Extending the Galactic Cosmic Ray electron + positron spectrum measured by the Fermi LAT. 2009.

[45] A. A. Abdo et al. Observations of Milky Way Dwarf Spheroidal galaxies with the Fermi-LAT detector and constraints on Dark Matter models. *Astrophys. J.*, 712:147–158, 2010.

[46] Céline Boehm, Joseph Silk, and Torsten Ensslin. Radio observations of the Galactic Centre and the Coma cluster as a probe of light dark matter self-annihilations and decay. 2010.

[47] G. R. Blumenthal and R. J. Gould. Bremsstrahlung, Synchrotron Radiation, and Compton Scattering of High-Energy Electrons Traversing Dilute Gases. *Reviews of Modern Physics*, 42:237–271, 1970.

[48] M.S. Longair. High-energy astrophysics. Vol. 1: Particles, photons and their detection. 1992.

[49] M.S. Longair. High-energy astrophysics. Vol. 2: Stars, the galaxy and the interstellar medium. 1994.

[50] C. Itzykson and J.B. Zuber. *Quantum Field Theory*. McGraw-Hill, New York, 1980.

[51] M. Drees, R. Godbole, and P. Roy. Theory and phenomenology of sparticles: An account of four-dimensional N=1 supersymmetry in high energy physics. 2004.

[52] K. Nakamura et al. Review of particle physics. *J.Phys.G*, G37:075021, 2010.

[53] F. Halzen and Alan D. Martin. Quarks and Leptons: an introductory course in modern particle physics. 1984.

[54] The Collider Detector at Fermilab. http://www-cdf.fnal.gov/.

[55] The DØ experiment. http://www-cdf.fnal.gov/.

[56] The Compact Muon Solenoid. http://cms.web.cern.ch/.

[57] ATLAS experiment. http://atlas.ch/.

[58] M. Misiak et al. The first estimate of B(anti-B -¿ X/s gamma) at O(alpha(s)**2). *Phys. Rev. Lett.*, 98:022002, 2007.

[59] E. Barberio et al. Averages of $b-$hadron and $c-$hadron Properties at the End of 2007. 2008.

[60] Marcela S. Carena and Howard E. Haber. Higgs boson theory and phenomenology. *Prog.Part.Nucl.Phys.*, 50:63–152, 2003.

[61] Ulrich Ellwanger, Cyril Hugonie, and Ana M. Teixeira. The Next-to-Minimal Supersymmetric Standard Model. *Phys.Rept.*, 496:1–77, 2010.

[62] C. Boehm and Pierre Fayet. Scalar dark matter candidates. *Nucl.Phys.*, B683:219–263, 2004.

[63] D. Larson et al. Seven-Year Wilkinson Microwave Anisotropy Probe (WMAP) Observations: Power Spectra and WMAP-Derived Parameters. *Astrophys. J. Suppl.*, 192:16, 2011.

[64] Benjamin W. Lee and Steven Weinberg. Cosmological Lower Bound on Heavy Neutrino Masses. *Phys.Rev.Lett.*, 39:165–168, 1977.

[65] Pierre Jean et al. Early SPI/INTEGRAL measurements of galactic 511 keV line emission from positron annihilation. *Astron. Astrophys.*, 407:L55, 2003.

[66] Jurgen Knodlseder, V. Lonjou, P. Jean, M. Allain, P. Mandrou, et al. Early SPI / INTEGRAL contraints on the morphology of the 511 keV line emission in the 4th galactic quadrant. *Astron.Astrophys.*, 411:L457–L460, 2003.

[67] C. Boehm, Pierre Fayet, and J. Silk. Light and heavy dark matter particles. *Phys.Rev.*, D69:101302, 2004.

[68] C. Boehm, T.A. Ensslin, and J. Silk. Can Annihilating dark matter be lighter than a few GeVs? *J.Phys.G*, G30:279–286, 2004.

[69] Céline Boehm and Yago Ascasibar. More evidence in favour of light dark matter particles? *Phys.Rev.*, D70:115013, 2004.

[70] Yago Ascasibar, P. Jean, C. Boehm, and J. Knoedlseder. Constraints on dark matter and the shape of the Milky Way dark halo from the 511-keV line. *Mon.Not.Roy.Astron.Soc.*, 368:1695–1705, 2006.

[71] Adam Burrows, Michael S. Turner, and R.P. Brinkmann. Axions and SN 1987a. *Phys.Rev.*, D39:1020, 1989.

[72] Céline Boehm, Yasaman Farzan, Thomas Hambye, Sergio Palomares-Ruiz, and Silvia Pascoli. Is it possible to explain neutrino masses with scalar dark matter? *Phys.Rev.*, D77:043516, 2008.

III

PHENOMENOLOGICAL AND ASTROPARTICLE ANALYSIS OF LIGHT DARK MATTER PARTICLES

8 Scanning the parameter space

The supersymmetric parameter space is multidimensional. If we are interested in thoroughly looking for phenomenologically interesting configurations then a scan of such a space is required. Finding a suitable point in the supersymmetric parameter space can be translated into a series of criteria to be respected. To this purpose we have developed a code using the well tested and user friendly numerical tools, which make the analysis of supersymmetric configurations rather easy. Using these tools, a random walk algorithm was built to scan parameter spaces taking into account the constraints to be respected. Each time a good point was found, its parameters, mass spectra and phenomenological outcome was kept. This code was first introduced in [1].

8.1 Tools

In principle there is not necessarily a unique set of parameters that fits the data and to which we expect to converge. There might be many different configurations equivalently well fitting the data. The search for those configurations has to be automatized. In order to solve the spectrum of many points and compute their yield –a set of observables–, it is essential to make use of the best numerical structures available.
That is why the code was constructed using micrOMEGAs (mO) [2]. Regarding supersymmetry, micrOMEGAs is a code, a framework and a library of functions. It provides tools to the user, allowing easy computation of supersymmetric spectra –by making use of other, well tested codes–, comparison of mass spectra to new particle searches limits, finding of the LSP and computation of its FO relic density, analysis of its annihilation channels, computation of the suypersymmetric configuration contribution to electroweak precision parameters, to leptonic anomalous magnetic dipole momenta, to rare meson decays, and give predictions to direct and indirect detection of DM. The user can choose the SUSY breaking scheme.
Both the MSSM and NMSSM are implemented in a number of usual paradigms. Since we are interested in widely exploring phenomenological configurations, we only used the so called EW symmetry breaking (EWSB) scheme. Unification of parameters is not assumed at the GUT scale, allowing the user to freely define the sfermion soft masses, non-universal gaugino masses, the Higgs sector parameters and trilinear couplings. However a mecha-

nism that breaks SUSY is to be assumed. For each set of free parameters, the configuration is tested by checking whether the renormalization group equations driven SUSY breaking mechanism from GUT scale parameters down to the EW scale can actually lead to such a choice of EW scale parameters. Higher order corrections are taken into account in the computation of masses, which are especially important in the Higgs sector. In the MSSM, mO calls the SuSpect [3] spectrum calculator to achieve this task, whereas in the NMSSM, mO has implemented the NMSSMTools package [4], and more specifically the NMHSpec function [5] and the NMHDecay function [6, 7] to compute the spectrum and Higgs sector decays, as well as various particle physics constraints (see Sec. 8.3.3).
In the particular case of the MSSM, the latest searches (presented in [8]) included a limit on the Higgs mass which was not implemented in mO (and not used in [1]). In this case it was necessary to interface mO with the HiggsBounds (HB) package [9, 10]. This package needs all the Higgs couplings to SM particles in the MSSM (or whatever model is being evaluated) for the given configuration. The tree-level couplings are computed by mO while the loop induced couplings (such as Higgs-photon-photon or Higgs-gluon-gluon) were computed with SUSY-HIT package [11]. The link between these two supplementary packages and mO was performed by A. Pukhov and G. Bélanger, specially for the late searches in the MSSM.
Once interesting supresymmetric configurations are found and data is generated, the representation of different parameters or observables in correlating planes is a very useful analysis tool. Analysis routines have been written to get these representations systematically. The tool used to this purpose is ROOT [12], the data analysis framework developed at CERN.

8.2 A Monte-Carlo Markov chain algorithm

8.2.1 A random walk approach

The aim of our study was to meticulously search for supersymmetric configurations yielding neutralino DM with an acceptable relic density and respecting particle physics constraints. Within the vast multidimensional parameter space there is a high probability to fall into choices that will not meet all the requirements, starting with the spectrum calculation. Therefore it is wiser to look within some range in each dimension. Once such a box is properly defined by prior knowledge of the model, we would like to explore it automatically. One way to come through this exploration is to iterate in the search. This way, if start from a point –i.e. a set of values for each of the free parameters that we are scanning–, a subsequent set can be generated by making a step towards a given direction. A new set of variables is thus defined. It can be tested regarding all the constraints we wish to consider. If the point is satisfactory to this respect (in fact, if it passes the acceptance requirement, which is a slightly different requirement as we will develop in what follows), it is kept, and thus becomes a source for the

next iteration. If not, a new one is generated until we find a suitable point. This procedure is that of random walks, or Markov Chain Monte-Carlo (MCMC), in which the conditional probability distribution of a point is given as a function of the previous point alone and does not depend on all previous kept points. Therefore, we ensure the generation and suitability of a point to depend only on its local (with respect to the parameter space) behavior and only on its intrinsic characteristics (and not on the way the iteration has evolved at all previous steps). The exploration will be oriented and determined purely by the properties of each of the configurations visited during the random walk. The question of the initial point is then to be addressed, and it turns out to be not a trivial issue. Also, the generation of new points determines how the code will walk in the parameter space. Finally, and what is the most interesting feature for us, all kept points will yield a number of predictions: their cross sections for DD and ID can be computed.
Evaluating a set of variables is both evaluating whether it is a configuration which corresponds to our theoretical expectations and whether its phenomenology is in contradiction with experimental data. This way we can define two quantitative functions of a given set of variables: its prior and its likelihood. The former represents its match with the kind of model we are looking for, and the latter checks whether experimental constraints are respected. Priors and likelihoods will be discussed in detail below. Their distinction is purely abstract, the numerical evaluation of these functions is not compelled to follow a certain order. In other words, one may compute the likelihood before the prior, or the inverse. In practice, both the prior and likelihood are composite functions, since both include several criteria.

8.2.2 Metropolis-Hastings algorithm

With this in mind we constructed a Metropolis-Hastings algorithm [13]. Its iteration procedure is the following. In an n-dimensional parameter space we start by finding a starting point. This could be achieved by imposing it as an input, or by using a flat probability distribution over parameter space, namely, generating n random variables within a n-dimensional box, or by using a more sophisticated method (see later on for a detailed discussion on the starting point). Then, we use it to generate the next point. The generation of a point $j+1$ from a point j requires, first of all, the choice of a generator. Let us define it following the probability distribution function $\vec{G}\left(\vec{\theta}^k|\left(\vec{\theta}^j,\vec{\sigma}\right)\right)$, an n-dimensional normal distribution centered at the variable set $\vec{\theta}^j$ with a variance vector $\vec{\sigma}$:

$$G^{k|j}=\prod_{i=1}^{n}G_i\left(\theta_i^k|\left(\theta_i^j,\sigma_i\right)\right)=\prod_{i=1}^{n}e^{-\frac{\left(\theta_i^k-\theta_i^j\right)^2}{2\sigma_i^2}}.$$

The new set of variables $\vec{\theta}^k$ is then tested regarding the prior $\mathcal{P}^k\left(\vec{\theta}^k\right)$ and the total likelihood $\mathcal{L}^k\left(\vec{\theta}^k\right)$. In principle it is suitable to evolve towards better total weights. Hence, if a new

point has a better weight than its predecessor it will be accepted automatically. However, it is in the nature of the Metropolis-Hastings algorithm to allow some steps back in the evolution of the weight throughout the chain, although with a lesser probability. This way it is possible to avoid being trapped in a well. Thus, the new point will be accepted with a probability

$$min\left[\frac{G^{k|j}\times\mathcal{P}^{k}\left(\vec{\theta}^{k}\right)\times\mathcal{L}^{k}\left(\vec{\theta}^{k}\right)}{G^{j|k}\times\mathcal{P}^{j}\left(\vec{\theta}^{j}\right)\times\mathcal{L}^{j}\left(\vec{\theta}^{j}\right)},\ 1\right]. \tag{8.1}$$

If accepted, $j+1\rightarrow k$. Otherwise $j+1\rightarrow j$. Of course, since $G^{k|j}\equiv G^{j|k}$, the generator function does not contribute to the acceptance probability. This reinforces the MCMC characteristic of the random walk, avoiding the influence of a configuration generation on the evaluation of the configuration itself. We define the weight of a point j to be

$$Q^{j}=\mathcal{P}^{j}\times\mathcal{L}^{j}. \tag{8.2}$$

Each different variable set kept has a given multiplicity, which is the number of times the code stayed at that point before accepting a different one. A total number of points was asked for a chain –typically 10^4 or 10^5. Then, it is a good thing to ask the run to make several chains –a few tens, typically–, so we may avoid the results depending on a particular choice of a starting point. Furthermore, this allows us to compare the yield of two different chains, and so to explore potentially disconnected regions of parameter space. The number of different points within a chain depends on how easy it is to jump from one point to the next and how many points are rejected. This is determined by the interplay between the density of healthy configurations –in which is included the possibility of fine-tuned solutions– and the mean deviation, the size of the step with which we generate new candidates, determined by the variance in the generator function. For a given deviation, the denser a region is in healthy points, the easier to find a successful point. For a given density of healthy points, the smaller the deviation, the easier to find a successful point. It is interesting to have not too large deviations, so the probability of falling out of a healthy region with each step is not too large, but too short deviations may prevent the chain to explore the parameter space and stay trapped in a single region. This interplay is relative to the way we define $\mathcal{P}$ and $\mathcal{L}$, and thus depends on the run. The best choice of the mean deviations is found by trial and error. Namely, the code does not contain a smart and automatic way to choose how large will be the step.

8.2.3 Finding a starting point

The starting point represents a problem by itself. Indeed, if we are trying to find rare configurations in the parameter space, then it is not obvious to randomly find a point j for which simultaneously $\mathcal{P}^{j}\left(\vec{\theta}^{j}\right)\neq 0$ and $\mathcal{L}^{j}\left(\vec{\theta}^{j}\right)\neq 0$ in order to have $Q^{j}\left(\vec{\theta}^{j}\right)\neq 0$, and therefore be

able to define a meaningful probability of acceptance for $j+1$ using (8.1). The rareness of a configuration may be interpreted as fine-tuning. If a subset of variables, or parameters after the spectrum calculation, have a strong influence on the phenomenology of the point, and if they are needed to follow some relation with a narrow tolerance, then such a configuration is fine-tuned. And the narrower is the tolerance, the more fine-tuned is the point. For example, the neutralino mass is a parameter at the origin of fine-tuned requirements, specially towards masses lighter than $\sim 30\,GeV$. If the configurations needed are intrinsically fine-tuned, then randomly finding a starting point is actually looking for a needle in a haystack. In these cases, we may use a efficient tool to find such an unflinching starting point: a MCMC made of a chain which is not retained but which purpose is to approach the desired region in parameter space. We call this first MCMC the pre-MCMC. Thus, the search for a starting point can be decomposed into two steps. First we relax some of the most stringent conditions we want the chains to respect. For the neutralino mass case this is achieved by defining a different form of the prior imposed on its value, namely, giving it an exponential distribution. The mass prior at the pre-MCMC level does not have a sharp edge at the upper bound any more as required at the MCMC, but very heavy neutralinos will be strongly disfavored. A heavier neutralino point, with a very low total weight $Q_{pre-MCMC}$, is good enough to launch the pre-MCMC. Thus we force this preliminary random walk to exponentially fall into lighter mass regions. This way we allow more points to help us finding a suitable one, by letting them generate a random walk which is conceived to converge towards the region of interest. Secondly, once we fall into an interesting region, we evaluate the weight of the given point with respect to the criteria chosen for the run. Finally, when the weight of a point overcomes a given threshold, then it becomes the starting point, and the MCMC iteration is eventually launched, the subsequent chain will be stored. This threshold is to be defined with respect to the total weights one is expecting to get. In general, the maximum weight that we get is $\gtrsim 0.5$. However, the MCMC can gain several orders of magnitude in a few steps, depending on the amplitude of the variance. This way, a threshold of 10^{-15} is reasonable. Although the first ten points or so might have very bad total weights, the thousands to come will successfully probe the region of interest.

Otherwise, if it is not difficult to pick a starting point out of absolute randomness, then the starting point may be generated by picking a set of variables with flat probabilities within each interval defined for each dimension of the parameter space.

Finally, sometimes we would like to make special checks at some particular configurations. Then, in order not to lose time in finding a starting point, we can use a forced initialization by imposing the starting point as an input. Of course, this way, a many chain run will always start at the very same point. In such cases, a low deviation is used, since the aim is to scan the surroundings of the given point. Otherwise, if the user has a set of suitable initial points which are not necessarily sitting very close to each other, it can be indeed interesting

to generate chains for each one of them and compare the different regions obtained, the total weights and the extensions of them, and whether the MCMC could build bridges between them.

8.3 Quantifying the performance of a set of variables: priors and likelihoods

8.3.1 Functions

In order to compute a point's weight –prior and likelihood– we call functions that will help us evaluate each partial weight. Then, the product of these partial weights will give the total weight. These functions are thus normalized to give a certain value between 0 and 1, quantifying thus the points behavior regarding a certain prior or likelihood. Depending on the nature of the criterion, we apply different functions, which are defined as follows.

1. For some points the actual probability is given by a Dirac delta function. This is the case, for example, of the spectrum calculator. Either it is able to compute the supersymmetric spectrum, or it is not. Here we cannot quantify a continuous value of the requirement. The criterion is thus binary. Hence, for a given point j, the probability of it surviving the test 0 is simply given by

$$F_0\left(x_j, x_0\right) = \delta_{x_0}^{x_j}.$$

2. For the various data fitting criteria imposed to the supersymmetric realizations, we used likelihood discrimination. Whenever a quantity was to be found within a certain range without a preferred value within it, we used a round-edged flat-distribution –instead of a Heaviside function for smoothing reasons. It means that besides defining the upper x_{max} and lower x_{min} limits tolerated for an x quantity, an exponentially decaying edge with a certain deviation σ is included.

$$\begin{aligned} F_1\left(x, x_{max}, x_{min}, \sigma\right) &= e^{-\frac{\left(x-x_{min}\right)^2}{2\sigma^2}} \;\; if \;\; x < x_{min}, \\ &= 1 \;\; if \;\; x_{min} \leq x \leq x_{max}, \\ &= e^{-\frac{(x-x_{max})^2}{2\sigma^2}} \;\; if \;\; x > x_{max}. \end{aligned}$$

   σ is chosen such that F_1 drops rapidly outside the interval, namely $\sigma \ll x_{max} - x_{min}$.

3. Whenever a criterion has to fit a preferred value μ with a certain deviation σ tolerated, we used a normal distribution centered in the former, the latter being the normal variance.

$$F_2\left(x, \mu, \sigma\right) = e^{-\frac{(x-\mu)^2}{2\sigma^2}}.$$

4. For those quantities that only have lower or upper bounds, we use

$$F_3(x,\mu,\sigma) = \frac{1}{1+e^{-\frac{x-\mu}{\sigma}}}.$$

With this definition, for an upper (lower) bound σ has to be negative (positive). For a small value of σ as compared to the bound μ and the variable x, this is similar to a step function of values 0 and 1 on each side of μ. Only, this function is differentiable.

The code does not treat all criteria at the same level. Indeed, all those making use of the F_0 function come first. If any point fails this test, then the computation of all the rest is useless. This allows to prevent the code of spending time on uninteresting calculations.

8.3.2 On priors

Part of the evaluation of a point is determined by its correspondence with our initial expectations, with the theoretical idea we want to test. Also, it has to meet numerical-physical sense. These are the priors. A detail of those which were implemented, always or for some runs, is given below.

1. The sprectrum calculator is called to get sparticle and Higgs masses. Both spectrum calculators return an error message if there is any during the spectrum calculation. Actually, whereas we ask SuSpect only for this job –albeit, in a consistent and reliable manner–, NMSSMTools does more with the variable set. Indeed, not only the spectrum is calculated, but also masses of squarks, sleptons, gluinos and charginos are compared to limits established by LEP. Furthermore, extensive limits on Higgses from the same experiment and from the Tevatron are checked, such as $e^+e^- \to hZ$, $e^+e^- \to hA$, the Z width, the decays $\tilde{t} \to bl\tilde{\nu}$ where l stands for a lepton, $\tilde{t} \to \chi^0 c$, $\tilde{b} \to \chi^0 b$. From CLEO, $\Upsilon \to A\gamma$ and the A width. From BaBar, the η_b mass difference. See [5, 6, 7] and references therein for details on these limits. One can switch on and off the verification of each constraint. Those listed above are those we kept, for the rest, we implemented them aside. Structural problems are also checked. These are common to both spectrum calculators and include the existence of Landau poles below the GUT scale, unphysical global minimum in the Higgs potential, Higgs mass scales above the SUSY breaking scale and the integration of the RGE. An error message is discriminated as an ill defined supersymmetric point. In this case the point is rejected straight away, and its attributed probability is null. This means this prior –which contains also a bit of likelihood, treating the mass limits and other data-fitting criteria in the case of NMSSM– responds to a delta function discrimination. A viable candidate k has to go through

$$\mathcal{P}^k_{SUSY} = F_0(k, SUSY) = \delta_{SUSY}.$$

2. In the case of NMSSM, mO has to check whether it is treating the Higgs correctly. It is achieved by looking to the Higgs self interaction coupling, which intervenes in the Higgs mass calculation. If this coupling is ≥ 1, the treatment of the Higgs sector might be wrong. We have to discriminate these points, not because they are necessarily excluded, but because we cannot trust the way mO is treating them. This coupling is called *laMAX* by mO. Thus, we impose the prior

$$\mathcal{P}^k_{laMAX} = \delta_{MSSM} + \delta_{NMSSM} \times F_3\left(laMAX_k, 1, -0.001\right).$$

3. If micrOMEGAs, while ordering the spectrum, is not able to find the LSP (error in the sortOddParticles function), we reject automatically the point. This prior is also evaluated by

$$\mathcal{P}^k_{spec} = F_0(k, spectrum) = \delta_{spectrum}.$$

4. We are looking for neutralino DM, whus we require the LSP to be the neutralino. Again, a binary criterion given by

$$\mathcal{P}^k_{LSP} = F_0(k, LSP = \chi^0_1) = \delta^{LSP}_{\chi^0_1}$$

is applied.

5. In a number of runs of the MCMC, we wanted to explore low mass neutralinos. Therefore we set an upper-limit for $m_{\chi^0_1}$ in order to avoid less fine-tuned, trapping regions. In some other cases, we wanted to explore larger masses without falling into these already explored regions. In which case we set a lower limit for the mass. In any case we impose $m_{\chi^0_1} \geq 1\,GeV$, which was decided to be the lower possible value for our searches for a simple reason: mO does is not trustworthy in the FO calculation for neutralinos below this limit. Hence, for the candidate k, we impose a neutralino mass interval. Thus, this prior calls

$$\mathcal{P}^k_{m_{\chi^0_1}} = F_1\left(m_{\chi^0_1,k}, m_{\chi^0_1 min}, m_{\chi^0_1,max}, 0.1\right),$$

with the values of $m_{\chi^0_1,min}$ and $m_{\chi^0_1 max}$ depending on the run. All quantities are to be expressed in GeV.

6. The search for interesting points is performed inside a box. Indeed, we require each variable to lie in a certain interval. The phenomenology we are looking for defines these intervals. Therefore, for a candidate k, we define the prior on the variables as

$$\mathcal{P}_{\vec{\theta}^k}\left(\vec{\theta}^k\right) = \prod_{i=1}^{n} F_1\left(\theta^k_i, \theta_{i,min}, \theta_{i,max}, \sigma_{\theta_i}\right),$$

where maxima, minima and tolerances depend on the run.

Finally, the total prior of a candidate k is given by

$$\mathcal{P}^k = \mathcal{P}^k_{SUSY} \times \mathcal{P}^k_{laMAX} \times \mathcal{P}^k_{spec} \times \mathcal{P}^k_{LSP} \times \mathcal{P}^k_{m_{\chi_1^0}} \times \mathcal{P}_{\vec{\theta}^k}.$$

As discussed previously, when the portion of parameter space able to produce healthy configurations is very narrow, getting a starting point forces the use of a pre-MCMC, in which some of the priors may be changed. It is the case of low mass neutralino searches. In this case, the pre-MCMC takes a different prior for the neutralino mass, with the aim to force the pre-MCMC towards lower masses. The strategy is then to accept any point with a non vanishing total weight, regardless of the neutralino mass, and apply an exponential prior on top of it. For example, when we were looking for neutralinos lighter than $m^{max}_{\chi_1^0} = 15\,GeV$, the exponential prior took the form

$$\mathcal{P}^k_{m_{\chi_1^0} \leq m^{max}_{\chi_1^0}} = \frac{10\,GeV}{m^{max}_{\chi_1^0}} exp\left(-10\frac{m_{\chi_1^0}}{m^{max}_{\chi_1^0}}\right) = \frac{2}{3} exp\left(-\frac{2}{3}\frac{m_{\chi_1^0}}{GeV}\right).$$

This prior replaced $\mathcal{P}^k_{m_{\chi_1^0}}$ in the pre-MCMC. However, when a point for which $m_{\chi_1^0} \leq m^{max}_{\chi_1^0}$ and $Q \geq Q_{threshold}$, the MCMC was started with the flat prior on the neutralino mass. For the case where $m^{max}_{\chi_1^0} = 15\,GeV$, $Q \geq Q_{threshold} = 10^{-12}$.

8.3.3 On likelihoods

The rest of the determination of the total weight of a point relies on its comparison to several data-fitting criteria. Observations have to be respected, and that is why we associate likelihoods to the most constraining limits emanating from experiments in particle physics. We take only these into account (and not DD nor ID limits) since we are trying to find a particle physics candidate. We will analyze its behavior in the galaxy and universe later on. A part of the outcome of the NMSSM spectrum calculation should be included in the total likelihood. However, for the sake of simplicity, we let those criteria evaluated by a test 0 along with the spectrum calculation itself. Here are enumerated the likelihoods taken into account.

1. The relic density of a stable neutralino can be computed via the FO mechanism introduced in the Sec. 1.2.2, or may be assumed to be accomplished through the FI mechanism as described in Sec. 2.6. The former case is achieved by a call to the DarkOmega function in mO. It returns $\Omega^{FO}_{LSP}h^2$. Here, the LSP is the neutralino. This value is then required to take into account the WMAP cold dark matter content measure. This estimation is composed of a central value $\Omega_{CDM}h^2$ and a 1σ error $\Delta_{\Omega_{CDM}}h^2$, and usually the interval $(\Omega_{CDM} \pm \Delta_{\Omega_{CDM}})h^2$ is considered. However, the nature of both ends of this interval are conceptually very different in their implications. The upper end is a strict limit, since there cannot be more neutralinos than the DM observed. However, the

lower end of the interval is to take as an indication for the total DM only. With this we have in mind the possibility of many particle DM, to which the neutralino would be a partial contributor. We still want the neutralino to represent, at least, an important fraction of the observed DM. The likelihood function we built takes then the upper end as a limit, but it allows the neutralino density fraction to be as low as $10\% \times \Omega_{CDM}h^2$. The interval has not evolved much in the last three years, namely, the WMAP 5-year result reads $(\Omega_{WMAP5} \pm \Delta_{\Omega_{WMAP5}})h^2 = 0.1131 \pm 0.0034$ [14], whereas the WMAP 7-year result gives $(\Omega_{WMAP7} \pm \Delta_{\Omega_{WMAP7}})h^2 = 0.1120 \pm 0.0056$ [15]. What is rather convenient is that both intervals have a similar upper value. We use the WMAP 5-year results in the analysis. For the FO case the likelihood of a candidate k was computed with $F_1\left(\Omega^{FO}_{\chi^0_1}h^{2,k}, 0.1 \times \Omega_{WMAP5}, \Omega_{WMAP5}, \Delta_{\Omega_{WMAP5}}\right)$. If the FI mechanism was assumed, then automatically $\Omega^{FI}_{\chi^0_1}h^2 = \Omega_{WMAP5}$. Hence, the likelihood associated to the relic density of the neutralino is given by

$$\mathcal{L}^k_{RD} = \delta_{FO} \times F_1\left(\Omega^{FO}_{\chi^0_1}h^{2,k}, 0.01131, 0.1131, 0.0034\right) + \delta_{FI}.$$

2. Runs aimed to probe regions opened by the FI ask for low $\Omega^{FO}_{\chi^0_1}h^2$ values. Indeed, the FI is an alternative to explain why configurations for which the relic density of neutralinos after FO would be too diluted to explain the DM in the universe. When probing this particular case, we ask $\Omega^{FO}_{\chi^0_1}h^2 \leq 0.1 \times \Omega_{WMAP5}$. In such cases, we want the tolerance to be strict. The likelihood

$$\mathcal{L}^k_{FI} = \delta_{FO} + \delta_{FI} \times F_3\left(\Omega^{FO}_{\chi^0_1}h^{2,k}, 0.01131, -0.00034\right).$$

is used. This criterion could easily be understood as a prior, since it is not really fitting any data, and is rather forcing a required configuration.

3. The first particle physics criterion requires the candidate point to have a sufficient, yet not too large, contribution to the magnetic dipole momentum of the muon. Recall that $g_\mu = 2(1 + a_\mu)$, the latest measurement giving $a_{\mu,meas.} = [255(63)(49)] \times 10^{-11}$ [16], were the first error is statistical and the second is systematic. Therefore we require the supersymmetric contribution of a point k, Δa^k_μ, calculated with the gmuon function in mO implemented for both MSSM and NMSSM, to lie within the allowed interval, using quadratic summation of the errors. Namely, we define

$$\mathcal{L}^k_{g_\mu} = F_2(\Delta a^k_\mu, a_{\mu,meas.}, \sqrt{63^2 + 49^2} \times 10^{-11}).$$

4. In the SM, the ρ-parameter quantifies the relative strength between the neutral and charged current interactions at zero momentum transfer. $\Delta\rho$ measures its deviation from unity. The MSSM corrections to this electroweak observable are computed by

the deltarho function in mO, and include the $\tilde{t}$ and $\tilde{b}$ loop contributions and two-loop QCD corrections. These corrections have to stay marginal in order not to perturb the low energy phenomenology of the EW interaction. An upper limit of ~ 0.002 is thus set, though with no precise definition. The deltarho function is not defined for the NMSSM. We include the likelihood

$$\mathcal{L}^k_{\Delta\rho} = \delta_{MSSM} \times F_3(\Delta\rho^k, 2\ 10^{-3}, -10^{-4}) + \delta_{NMSSM}.$$

5. The following limit is set by the first b-physics constraint: the $b \to s\gamma$ branching ratio. It is deduced from the measurement of the $\bar{B} \to X_s\gamma$ branching ratio, where X_s stands for any s-quark containing meson. The function bsgnlo computes this branching ratio for both MSSM and NMSSM taking into account NLO contributions. Nevertheless, it was shown that NNLO contributions are not negligible in the case of the SM alone, $\Delta^{b\to s\gamma}_{NNLO} \simeq 0.45\ 10^{-4}$ [17]. From this expression we take the theoretical error to set the tolerance, assuming it is of the same order for supersymmetric estimations. We choose to shift the value returned by the bsgnlo function by the SM NNLO contribution and only then compare it to the experimental bound, which sets the ratio to be $(3.52 \pm 0.34)\ 10^{-4}$ [18]. This shift is, of course, hypothetical, but a good enough approximation knowing that we take into account the theoretical as well as the experimental errors. Hence, we define

$$\mathcal{L}^k_{b\to s\gamma} = F_2\left((b \to s\gamma)^k - \Delta^{b\to s\gamma}_{NNLO}, 3.52\ 10^{-4}, \sqrt{(0.23)^2 + (0.34)^2} \times 10^{-4}\right).$$

In late runs the full NNLO computation has been included in the estimation of the supersymmetric contributions to this branching ratio, making useless the shift we have applied. However, most runs used the previously described form for this likelihood.

6. Similarly, we use the function bsmumu to compute the $B_s \to \mu^+\mu^-$ branching ratio in the MSSM and NMSSM, which takes into account various corrections, in particular those stemming from Higgs exchanges. The current experimental averaged bound is $4.7\ 10^{-8}$ [18]. Thus, we include the likelihood

$$\mathcal{L}^k_{B_s\to\mu^+\mu^-} = F_3\left(\left(B_s \to \mu^+\mu^-\right)^k, 4.7\ 10^{-8}, -4.7\ 10^{-10}\right).$$

7. Next we compute the likelihood of the candidate taking into account the branching ratio for $B_u \to \tau\nu_\tau$. The function btaunu computes the ratio of its value in the MSSM and NMSSM to its value in SM alone. This ratio should fit the value of 1.28 ± 0.38 [18]. Therefore, the

$$\mathcal{L}^k_{B_u\to\tau\nu_\tau} = F_2\left((B_u \to \tau\nu_\tau)^k, 1.28, 0.38\right)$$

likelihood is included.

8. The B_s^0 meson has a different mass from its anti-meson. This difference is called ΔM_s. The MSSM and NMSSM corrections to the SM predicted value may be of some importance. MicrOMEGAs includes the deltaMs function which returns the NMSSM contribution ΔM_s^{NMSSM} which is to be added to the SM value of $\Delta M_s^{SM} = (134.934 \pm 21.063) \times 10^{-13}\, GeV$ [19] before comparison with the experimental value of $\Delta M_s^{exp} = (117.0 \pm 0.8) \times 10^{-13}\, GeV$ [16]. It was only recently been implemented in the MSSM and was taken into account in the latest applications of the code. Using the theoretical and experimental errors quadratically summed as tolerance, the following likelihood is taken into account

$$\mathcal{L}^k_{\Delta M_s} = \delta_{MSSM} + \delta_{NMSSM} \times F_2 \left(\left(\Delta M_s^{NMSSM} \right)^k + 134.934 \times 10^{-13}\, GeV, \right.$$
$$\left. 117 \times 10^{-13}\, GeV, \sqrt{21.063^2 + 0.8^2} \times 10^{-13}\, GeV \right).$$

9. Similarly, the B_d^0 meson has a different mass from its anti-meson. ΔM_d^{NMSSM} is also computed in mO by the deltaMd function. The SM estimate reads $\Delta M_d^{SM} = (3.883 \pm 1.251) \times 10^{-13}\, GeV$ [19], while the latest experimental averaged value is $\Delta M_d^{exp} = (3.337 \pm 0.033) \times 10^{-13}\, GeV$ [16]. Again, this function it is been recently implemented in the MSSM and will be added to the analysis in the near future. Thus,

$$\mathcal{L}^k_{\Delta M_d} = \delta_{MSSM} + \delta_{NMSSM} \times F_2 \left(\left(\Delta M_d^{NMSSM} \right)^k + 3.883 \times 10^{-13}\, GeV, \right.$$
$$\left. 3.337 \times 10^{-13}\, GeV, \sqrt{1.251^2 + 0.033^2} \times 10^{-13}\, GeV \right).$$

10. The lightest Higgs mass has a lower limit that applies to the MSSM from unfruitful searches at LEP and Tevatron. In most MSSM configurations, it is required that $M_h \geq 114.4\, GeV$ [20]. We notice that for $M_A \lesssim 120\, GeV$ this bound could be translated into a coupling ratio, allowing lower values for M_h. Indeed, for example, in the dominant Z-boson exchange channel of Higgs production at LEP, if the final state is Zh or ZA, for close masses of the Higgses, these might be impossible to disentangle. Furthermore decays could mimic those of SM final states. Uncertainties become larger and thus constraints are less stringent. That is why, for late runs, a link to HiggsBounds and SUSY-HIT was implemented, to check more fine-tuned Higgs configurations, thoroughly checking all Higgs decay modes. To this purpose, all couplings between the lightest CP-even Higgs and the SM particles are computed, either by mO or by SUSY-HIT, and are sent to HiggsBounds, which checks their ratio to the SM values. The square of this ratio has to be smaller than one for all channels, and particularly, for the dominant channel. The code reads the message sent by HiggsBounds resulting from this evaluation. If the dominant channel has a ratio larger than one, then the point is

rejected, it is kept otherwise. The NMSSM has a richer Higgs sector and such limits on the lightest Higgs mass do not apply. Instead, a very complete Higgs study was performed by the spectrum calculator. Therefore we compute

$$\mathcal{L}^k_{M_h} = \delta^{early\ runs}_{MSSM} \times F_3\left(\left(\frac{M_h}{114.4\,GeV}\right)^k, 1, 0.01\right) + \delta^{late\ runs}_{MSSM} \times \delta_{HB} + \delta_{NMSSM}.$$

11. Masses of the supersymmetric spectrum ought to be checked. As it was seen in the spectrum calculator prior, for the NMSSSM this is done directly by the NMHspec routine. For the MSSM, the masslim function of mO does this check. However, this function returns an error if any of the new particles gets a forbidden mass. The criterion is translated into a test 0:

$$\mathcal{L}^k_{M_{SUSY}} = \delta_{MSSM} \times \delta_{masslim=error} + \delta_{NMSSM}.$$

The most constraining among these masses is the chargino mass, whose smallest allowed value is $94\,GeV$ [16].

12. The Z boson width is a very constrained observable. The only possible channels in which there might be an invisible supersymmetric contribution is the $Z \to \chi^0_1\chi^0_1$. Invisible decay modes cannot overcome $1.7 \pm 0.3\,MeV$ [16]. This criterion is taken into account in the spectrum calculator for the NMSSM, but for the MSSM is computed using the pWidth (which calculates the total width) and findBr (which allows to find a specified branching ratio) functions in mO. Hence,

$$\mathcal{L}^k_{Z\to\chi^0_1\chi^0_1} = \delta_{NMSSM} + \delta_{MSSM} \times F_3\left(\left(BR\left(Z \to \chi^0_1\chi^0_1\right) \times \frac{\Gamma_Z}{MeV}\right)^k, 1.7, -0.3\right)$$

was included in the total likelihood.

13. Finally we impose a constraint on the process $e^+e^- \to \chi^0_1\chi^0_{2,3}$ with subsequent decay of the heavier neutralinos into $Z\chi^0_1$, stemming from LEP searches. Similarly to the previous criterion, this is automatically checked in the NMSSM spectrum calculation, but has to be computed for the MSSM. It was accomplished by making use of the cs22 (which calculates a 2×2 process cross section), pWidth and findBr functions. To such processes the OPAL collaboration set a limit of $\simeq 1\,pb$ [21]. Therefore the following likelihood is defined

$$\mathcal{L}^k_{e^+e^-\to\chi^0_1\chi^0_{2,3}} = \delta_{NMSSM} + \delta_{MSSM} \times F_3\left(\left(\frac{\sigma_{e^+e^-\to\chi^0_1\chi^0_{2,3}}}{pb} \times BR\left(\chi^0_{2,3} \to Z\chi^0_1\right)\right)^k, 1, -0.01\right).$$

Thus, the total likelihood of the k candidate is

$$\mathcal{L}^k = \mathcal{L}^k_{RD} \times \mathcal{L}^k_{FI} \times \mathcal{L}^k_{g_\mu} \times \mathcal{L}^k_{\Delta\rho} \times \mathcal{L}^k_{b\to s\gamma} \times \mathcal{L}^k_{B_s\to\mu^+\mu^-} \times \mathcal{L}^k_{B_u\to\tau\nu_\tau} \times \mathcal{L}^k_{\Delta M_s} \times \mathcal{L}^k_{\Delta M_d} \times \mathcal{L}^k_{M_h} \times \mathcal{L}^k_{M_{SUSY}} \times \mathcal{L}^k_{Z\to\chi^0_1\chi^0_1} \times \mathcal{L}^k_{e^+e^-\to\chi^0_1\chi^0_{2,3}}.$$

8.4 Output and data analysis

8.4.1 Data generated

Each time a point was successfully evaluated and passed the acceptance criterion (8.1) data was generated. This data includes its characteristics: the set of free parameters and various observables. Different data are kept in different files. Each point has its own line in each of those files, with columns representing the different quantities stored. Each different chain is numbered and so are the corresponding files.

Regarding the code information, all the individual weights –all priors and all likelihoods– are written down, as well as a point's total weight and multiplicity.

The point itself is, of course, also written. However, only the free parameters are kept. For example, in all runs the trilinear coupling of the bottom sector was always set to zero. Thus, it was not written for each point. For many runs, the gluino mass M_3 was forced to be $3 \times M_2$. Again, M_3 was not written in those cases.

Not all the spectrum was written, however, the most important masses are kept, starting with the neutralino mass. The NLSP (which ever it is, though in most cases it is the chargino, the lightest stop or the second lightest neutralino) was always kept, since it plays a role in case of coannihilating DM. The chargino mass is written down, since it is one of the most interesting particles to predict at colliders: it has a good chance to be the lightest charged particle of the spectrum. Higgs masses are important for the phenomenology of a point and are thus stored as well.

The neutralino LSP is the main character of DD and ID. Its components are crucial parameters in the cross section computation. They are kept. Notice that the NMSSM includes a singlino component. It is useful to check to what extent these points differ from the MSSM configurations. It is also the case for the Higgs particles: their singlet components in the NMSSM show their deviation from the MSSM. Thus we also keep the singlet component of these particles.

Assuming either FO or FI, $\Omega^{FO}_{\chi^0_1}h^2$ is always useful. In the first case, its relative contribution to Ω_{CDM} sets the neutralino fraction ξ –as defined in (4.1)– of neutralinos in the DM density at Earth, Sun and galaxies. Thus, $\Omega^{FO}_{\chi^0_1}h^2$ and ξ are kept. For the FI case, it is still interesting to establish whether this mechanism can save configurations in which the neutralino would have annihilated too much in EU if it had suffered the FO mechanism. Along with

this, we keep the channels responsible for the neutralino annihilation in EU, since they will be helpful to understand the difference in behavior in the EU as compared to in the present astrophysical surroundings.

DD cross sections are computed for each successful point. Interaction cross sections are computed after the procedures seen in Sec. 4.2.2. Among the theoretical uncertainties on the interaction rates are the nuclear form factors. In these, the scalar coefficients are the main contribution to the error in SI interactions. They depend on the light quark masses and light quark fractions in nucleons. Whereas quark masses do not introduce large uncertainties, the fractions do. The latter are computed using the pion-nucleon sigma term $\sigma_{\pi N}$ and the σ_0 parameter evaluating the size of SU(3) symmetry breaking effect (see [22] for a more detailed discussion). There are three standard pairs of values for $(\sigma_{\pi N}, \sigma_0)$: $(55\,MeV, 35\,MeV)$, $(45\,MeV, 40\,MeV)$ and $(70\,MeV, 30\,MeV)$. The first is a medium value, whereas the second gives a lesser fraction of the most reactive *s*-quarks, and the third a bigger contribution of *s*-quarks. The spread between the lower value and larger is of about an order of magnitude. Recent lattice QCD developments suggest the *s*-quark contribution may be towards the lower estimates, namely with $\sigma_{\pi N} \simeq (50 \pm 10)\,MeV$ and $\sigma_{\pi N} \sim \sigma_0$ (see [23] and reference therein for a discussion). There is a small difference ($\lesssim 4\%$) between proton and neutron cross sections. Therefore, for each point, six values are stored for SI interactions: three estimates for both neutrons and protons. We choose to represent the lowest estimate from the three, for proton interactions. Thus, when ruling out a particular data set using current experimental limits, we are being conservative. For SD interactions, separate values are kept for neutralino-neutron and neutralino-proton cross sections. These cross sections also depend on a choice of parameters for the nucleon from factors. Three normalized nuclear structure functions are used to estimate the pure isoscalar, mixed isoscalar-isovector and pure isovector components of the squared SD amplitude [22]. They quantify the magnitude of the spin in the nucleon and the spatial distribution of the spin, and they depend on the exchanged momentum. These are computed using the quark content coefficients for each component. We take the mO default values given in Table 1 of [22].

Neutralino annihilation in galaxies can yield indirect signals. These interactions would happen at rather low velocities, as compared to what happened in EU. Therefore, not only the cross section might have a velocity dependence and thus be orders of magnitude larger or smaller, but the spectrum of SM particles thus created could be different as well. The annihilation rate σv at $v = 10^{-3}c$ is thus computed, along with the main channels into which the neutralino annihilates. As it was stated in Sec. 4.3.3, one easy way to constrain DM is using ID γ-rays from dSphs. Indeed, computing the γ-ray spectrum resulting from low velocity neutralino annihilations is the first of two factors to compute fluxes from dSphs observed by terrestrial and satellite γ-ray detectors. Upper limits for such fluxes are drawn by the Fermi collaboration for two different energy ranges [24]. Hence, using the likelihood fitted

DM distributions along with the l.o.s. integral furnished in the same study for eight different dSphs we can estimate the fluxes and thus constrain supersymmetric scenarios. Finally, other interesting ID spectra can be computed. These include antiproton and positron. For both, a potential signal is not only dependent on the production rates where the neutralino annihilation happens, but also on the way these particles propagate through the ISM to reach a detector. micrOMEGAs includes a quick treatment of the propagation. It is not necessarily the most sophisticated estimation in the matter –it does not include a detailed map of the ISM, hence it only gives an averaged approximation–, but it still represents a good tool to check whether some configuration could yield important signals, whether more detailed studies should be carried out, and this in a very short computing time. This, however, requires a longer calculation time and more data to be stored than just a number, but a collection of points in the flux vs. energy plane. This is why we only compute these fluxes for benchmark points, namely when it is important to check what those points which overcome all previous tests would imply regarding antimatter signatures. The case of radio light is treated in the same way. Indeed, electrons and positrons would radiate radio photons by synchrotron radiation. Here mO does not provide any estimate of the radiative processes, and can only provide the produced spectrum of electrons and positrons in the galaxy. The rest is treated independently by a code written by Céline Boehm, which takes the spectrum as an input, computes the radio signal yield (including the energy losses and spatial diffusion in the MW and the energy losses in galaxy cluster), and compares it to data in any given direction of the sky. Limits can be drawn this way for particular points.

8.4.2 Representing results

By reading a file containing basic information on a run, such as the number of chains, the number of points per chain, the number of variables and other, the data analysis routine is able to read data, discriminate it with different criteria and plot it. In general, when representing supersymmetric configurations with dots on a plane or by histograms, we attribute color shading to the total weight contribution. Points are classified in four different groups. The first group is composed of those points j for which $Q_1^j \geq 0.32 \times Q_{max}$, where Q_{max} stands for the maximum total weight of the run. The second corresponds to those points lying in $0.05 \times Q_{max} \leq Q_2^j \leq 0.32 \times Q_{max}$. The third group satisfies $0.003 \times Q_{max} \leq Q_3^j \leq 0.05 \times Q_{max}$. Hence, the first group is limited at 1σ, the second at 2σ and the third at 3σ away from Q_{max}. Finally, the fourth group contains the remaining points: $Q_4^j \leq 0.003 \times Q_{max}$. This classification is arbitrary and relative to each run, since it depends on its Q_{max}. The different nature of priors and likelihoods as well as the shape of the distributions associated to them make very difficult to have an absolute meaning of the total weight. When configurations are represented by dots, only the first three groups are represented: the first is the darkest and the third is the lightest. When the frequency of a given quantity is represented in a histogram,

then the weight attributed to a point j is Q^j/Q_{max}. Four histograms are represented. The same shades applied to dots are used for contributions from the first group alone, for the sum of the first two and the sum of the three groups. There is a darkest shading corresponding to all points.

Regarding colors, they allow the representation of a third dimension in a plane, by attributing a given characteristic to each dot. For histograms, different colors give distributions for a particular subset of points. These attributions are most often chosen by discriminating points with respect to a given limit or constraint. Usually, when none of these apply, we represent dots in blue. When just one such discrimination is done, then red shows points which are ruled out by the specified criterion, the rest still being tainted of blue. When more than one discrimination is used, then failing one criterion makes a point's dot yellow. When a point fails two criteria, then the corresponding dot turns red. If it fails three, then its dot goes black/gray. Safe points in these cases are represented in green. A special case arises when the groups of points failing to two different criteria have a null intersection. In such a case one can use two different colors for the two failing groups, namely, yellow for one, red for the other.

The limits that we use to discriminate points can also be drawn in the corresponding plane. We use Higgs sector constraints from a study realized by the Tevatron New Phenomena and Higgs Working Group, including results from both the CDF and DØ detectors [25]. This limit applies only to the MSSM, and excludes scenarios with a combination of light pseudoscalar mass $M_A \leq 200\,GeV$ and large $\tan\beta \geq 30$. These two supersymmetric parameters play a fundamental role in Higgs couplings to standard model particles and to sfermions. In this plane, thus, points are represented, together with the upper bounds given in [25], for two different benchmark scenarios: maximum mixing and no mixing at all in the stop sector [26]. The limits were established by analyzing $2.2\,fb^{-1}$ of data looking for Higgs boson production in the $\tau^+\tau^-$ final state associated with b-quarks, which are correlated for a given combination of M_A and $\tan\beta$. In very late runs we also include the recent CMS limit in the same plane from early 2011 results presented in [27].

The LHCb collaboration has estimated their projected sensitivity to the $B_s \to \mu^+\mu^-$ branching ratio with $1\,fb^{-1}$ of integrated luminosity (see [28] for the state of the art in the matter). They should be able to attain values of 6×10^{-9}, considerably lowering the current best limit established by the CDF collaboration. We use this projection to predict the possibility of observation of supersymmetric configurations by showing the $B_s \to \mu^+\mu^-$ branching ratio in the configurations found with respect to the LSP mass, together with the current CDF limit and the projected LHCb sensitivity.

DD was at the very motivation of our research for light neutralino configurations in the MSSM and NMSSM. In the plane σ^{SI} vs. $m_{\chi_1^0}$ we represented scenarios with the color codes already described. Superimposed to those we show the latest results from the CDMS collabo-

ration [29]. We did not use a more recent study for a lower threshold performed by the same collaboration [30] because it was somewhat controversial. The XENON100 collaboration published their earliest, more constraining results in 2010 [31]. Nevertheless, these results were not received without criticism [32]. Indeed, their assumptions on the efficiency of the scintillation detectors $\mathcal{L}_{eff}$ seemed to be too optimistic: they claimed that the extrapolation towards low energy, where no trustworthy experimental investigation has yet been done, was to be flat. The XENON100 collaboration replied to this criticism by estimating the spread of different estimations [33]. That is why we performed a reanalysis of their limits, assuming a decreasing efficiency towards low energies. This is a more conservative approach, which still gives more stringent constraints than the CDMS results. This was the limit we used to discriminate points regarding DD in our early results presented in [1]. In later studies we used the latest XENON100 results [34], where the error in the unknown $\mathcal{L}_{eff}$ is integrated in a more sophisticated statistical study. The new published limit is still a matter of discussion, however, we take it as it is and discuss the implications of such exclusions. In light neutralino searches in the NMSSM we will treat the CoGeNT preferred region and present results from configurations falling in the preferred region pointed out in [35]. Even though we also represented the equivalent results in the σ_p^{SD} vs. $m_{\chi_1^0}$ and σ_n^{SD} vs. $m_{\chi_1^0}$ planes, the best limits available are never constraining our configurations. However, future experiments might start scanning the relevant regions of these planes. Among these is the MIMAC detector, which could give precious information of nuclear recoil events [36]. Three different regions can be categorized regarding the expected performance of this detector: a region where DM could be detected and both the σ_p^{SD} rate and the DM mass can be determined. Then a region where the DM could be detected but where statistics are too low to get more information: if no signal is seen, scenarios falling into this region can still be excluded. The third region is where the MIMAC detector is not expected to have any sensitivity. This is a projection of future research. No point can be ruled out using these regions, however, it is very interesting to investigate what scenarios fall in them. That is why the data analysis routine can discriminate points among these three regions, and represent them with different colors. Blue was used for those scenarios which are unattainable by MIMAC, whereas points falling in the exclusion region are tagged in cyan, and the points which could be resolved are colored in magenta. In all these planes, we have to take into account the neutralino local density. Indeed, all limits are derived assuming a certain DM local density ($\rho_0^{DM} = 0.3\,GeV\,cm^{-3}$), and using a particular choice for the local mean velocity and velocity dispersion of the DM. Since not all our scenarios are supposed to represent the whole of the DM, instead of calculating the limits again for each point, we rescale the interaction by the ξ factor, introduced in Sec. 4.2.1 and defined by (4.2). Thus, what is indeed represented and discriminated are the $\xi\sigma^{SI}$ vs. $m_{\chi_1^0}$, $\xi\sigma_p^{SD}$ vs. $m_{\chi_1^0}$ and $\xi\sigma_n^{SD}$ vs. $m_{\chi_1^0}$ planes.

Regarding ID, as already described in Sec. 4.3.3, we used systematically the limits estab-

lished by the Fermi null results from γ-ray observation towards dSphs [24][1]. Among the eight dSphs studied, the most constrainting is Draco. Limits obtained from this dwarf galaxy are thus used to discriminate points, using the more conservative limit. Indeed, the l.o.s. integral, J^{NFW}_{Draco}, includes a fit of the DM distribution and is obtained using a NFW halo profile. The profile was fitted using a likelihood method, and thus, an estimate is established along with theoretical errors. Let us call them $J^{NFW,0}_{Draco}$, δJ^{+} and δJ^{-}. Hence, J^{NFW}_{Draco} is expected to lie in $\left[J^{NFW,0}_{Draco} - \delta J^{-}, J^{NFW,0}_{Draco} + \delta J^{+}\right]$. These errors are propagated into the flux estimate. Since it is not obvious to represent these errors in the flux for each point, we choose to rescale the limit given by Fermi. Thus, if the limit is ϕ^{Draco}_{lim}, then we also represented $\phi^{Draco}_{lim} \times (J^{NFW,0}_{Draco} + \delta J^{+})/J^{NFW,0}_{Draco}$ and $\phi^{Draco}_{lim} \times (J^{NFW,0}_{Draco} - \delta J^{-})/J^{NFW,0}_{Draco}$, and used the former to discriminate points, thus being conservative. Notice that the angular resolution of the LAT is of $\sim 0.5^{\circ}$, and thus the choice of the profile shape to use for the fit of the DM density is not as relevant, since the inner part of the dSph is largely contained in the area contained in an observed pixel. When computing the γ-ray flux from neutralino annihilations we weighted the J^{NFW}_{Draco} integral by ξ^2 in order to take into account the actual fraction of neutralinos in the dSph.
Other planes in which the results where projected are correlations of parameters or observables, useful to understand the scenarios found by the code, and useful to predict which scenarios may be tested by which experimental technique.

8.5 What the code does and does not do

The MCMC was conceived to find suitable configurations to explore the favored regions pointed out and explored by recent DD developments from DAMA [38], CoGeNT [35], CDMS [29], XENON100 [31] and more recently Edelweiss [39], for particle DM masses around $10\,GeV$ and SI interactions around $10^{-41}\,cm^2$. Its performance is to be evaluated with this in mind. However, it has shown some potential, and it is natural to imagine further applications and improvements of what has already been done.

8.5.1 General behavior

In general, we can say that we have explored the general configurations for neutralino DM between 8 and $500\,GeV$ in the MSSM, and between 1 and $500\,GeV$ in the NMSSM. Runs usually yielded a few 10^5 different points. This number usually is sufficient to get smooth parameter distributions. Nevertheless, it is not a precise criterion to say we found all possible configurations, but shows that at least the most frequent are found. What defines what is enough is whether we find interesting results regarding the possibility of explanations for

[1] Fermi-LAT has recently shown improved limits [37] which were not taken into account in this work, though they can be easily implemented in the near future, when a more detailed publication will be available.

possible DM signals, as well as exploring unseen configurations, particularly in the very light NMSSM neutralinos scenario. It was however difficult to escape some very probable regions, such as that in which the neutralino annihilates via the Z-resonance and thus $m_{\chi_1^0} \simeq M_Z/2$. That is why we introduced priors to force exploration in regions unlikely to be scanned otherwise, such as the light configurations in the NMSSM.

Usually the best total weight found was of about $0.5 - 0.8$. Having more than ten criteria potentially decreasing the total weight, these values are rather good. Again, this does not ensure we find the configurations with the best fit to the data, but it seems hardly possible to find better scenarios once we reach so large total weights. Therefore, we can be sure we found good configurations, although we cannot state that we found all of them.

Further developments have not been included for a simple reason: the data analysis had to be prepared and physical implications were to be drawn. The motivation was to get interesting phenomenological configurations and thus understand the results was far more important than further develop the MCMC. Indeed, once interesting data was gathered, it was more exciting and fruitful to analyze it rather than keep exploring. Furthermore, it took a long time to explore all the interesting correlations –taken in a broader sense than those of variables alone, but including analysis of correlations on observables– and plots. Also, the competition of other groups looking for similar results, as well the quick evolution of experimental limits and constraints, pushed towards quick production of results, which needs the dedication to the data analysis.

Furthermore, the tool as it is allowed me to successfully investigate other questions, such as the studies dedicated to the FI implications in supersymmetric configurations. Here it was very simple to use the same tool, only the likelihood on the relic density was to be adapted, and no prior on the neutralino mass to be taken (which is equivalent to allow a very large value for the maximum mass tolerated, and the same regarding its lower value). Similarly, for an investigation of the MIMAC potential on supersymmetric configurations only the prior on the mass was to be lifted, and the data could be generated straight away.

Adaptation is also easy, since including further variables and likelihoods to the algorithm represents a very small problem. Even though multiplying the number of variables to scan may dilute the parameter space and thus make the exploration more difficult, there is always the possibility of defining the intervals for a given variable in a smart way, as well as adapting the deviations.

Depending on the aim of the run, its computation time can change. Light neutralino searches can take several days in a local processor. Because of the fine-tuning of the desired configurations the pre-MCMC can take a day or so to find a suitable starting point, specially in the MSSM, where healthy configurations are not at all frequent. Otherwise, once a chain has started, it takes a few hours to find its few $\sim 10^4$ points. This depends on the deviations, since it is shorter to reject a point, specially by a binary criterion, than to compute all observables

and write down all the information of a given point. Thus a chain with less different points will be quicker than a very low multiplicity, denser chain.

8.5.2 Perspectives

The cuts introduced by priors on the neutralino mass suggest that the code is not really prepared to explore very fine-tuned regions. One way to explore them would be to further introduce priors on some observables, such as light Higgses in the NMSSM. This can only be applied to regions already known, or at least where some theoretical intuition leads to. Also, when rare configurations are found and the code enters such a region, we could define very small deviations to ensure we do not jump out of it as quickly as we enter them.
There is no convergence criterion applied. This could be a smarter way to make a chain stop. Once a very large total weight is found, and by some automatic adaptation of the deviations explored it thoroughly, it might be a good moment to stop a chain and start the procedure again with a new starting point, ideally quite different from the previously found.
In the same light, we could think of a fine-tuning measurement. It would be helpful and interesting to understand which realizations lie on narrow relations between parameters, masses, and couplings, and how narrow these relations have to be, with what tolerance a given scenario can be expanded. However, I do not think this is an important quantity for a discrimination between models: what if nature is very fine-tuned?
Regarding data analysis, correlation estimators are not used. On one hand, it seems not fundamental regarding variables, since many different configurations are explored. However, some variable values can be indeed crucial in the success of a point. It would be interesting to find, for each region found, what are those variables that need to be correlated in order to produce healthy configurations. In many cases this can be studied without sophisticated statistical tools, but it is undeniable that quantifying such correlations thoroughly can throw some light on the characteristics of the parameter space explored.
Other techniques exist to scan parameter space thoroughly. One of them is the nested sampling technique [40] in which a fixed number of points is kept. Iteration does not increase the amount of data, but replaces the worst behaving points by a new one, found by a random generation. This technique can be very useful to explore regions of parameter space that would be unnatural for the MCMC, if the starting point and deviations chosen do not allow the chain to attain it. One drawback is the needed amount of points for a large number of dimension in parameter space. However the algorithm would not need to evaluate such a large amount of points at each iteration, since only one at a time is to be evaluated. Here the most difficult step is therefore generating points. Unfortunately this points towards the same systematic weakness of starting point definition for the MCMC.

9 Light neutralino searches

9.1 Light neutralinos in the Minimal Supersymmetric Standard Model

Let us now discuss the outcome of the runs and data analysis in the MSSM. As it was stated, the very first motivation for this code to be written was the search of $O(1-15)\,GeV$ neutralino configurations. Thus we first focus in these searches. The first results obtained in this light were presented in [1]. We further explored the astrophysical implications of light NMSSM neutralinos in [41], and we revisited the results in the MSSM applying new constraints in [8].

Neutralino DM in the MSSM has been considered for a long time as an explanation to the cosmological DM problem (see for example [42, 43, 44, 45]). More recent studies have further extended the investigation of light ($\lesssim 50\,GeV$) neutralino by lifting gaugino mass unification and thus expanding the phenomenological configurations stemming from the MSSM [46, 47]. In [48] it was even considered that the neutralino could be hot DM being in agreement with CMB constraints and structure formation for $m_{\chi_1^0} \leq 1\,eV$. However, there is no a continuum of solutions as a function of neutralino mass, and they argue that if the neutralino was to account for the CDM, then lower bounds in the $(5-15)\,GeV$ range (depending on the analysis) are unavoidable. This is the philosophy of our study as well: is a light-but-cold relic neutralino in the MSSM plausible once we apply the latest constraints from collider searches to the widest variety of supersymmetric configurations?

We proceed by scanning the parameter space taking into account all the likelihoods described in Sec. 8.3.3, that is to say, we expect the neutralino to be a DM candidate, thus contributing to the DM relic density, as well as a product of a supersymmetric configuration which is not in conflict with particle physics experiments. Once such configurations are found, we compare the Higgs sector parameters found to constraints from unfruitful Higgs searches at the Tevatron. We then evaluate the possibility of astrophysical signals from DD experiments, in which, though, the astrophysical uncertainties enter in the errors.

Since we presented the first results in [1] we have extended the search to new regions in parameters space, changing our conclusions. We present our results chronologically, with the late investigation –which is currently in preparation for publication– being the most complete.

Parameter	Minimum	Maximum	Tolerance
M_1	1	100	3
M_2	100	2000	30
μ	0.5	1000	0.1
$\tan\beta$	1	75	0.01
M_A	100	1000	4
A_t	-3000	3000	100
$M_{\tilde{l}}$	100	2000	15
$M_{\tilde{q}}$	300	2000	14

Tab. 9.1: MSSM free parameter intervals for the first light neutralino searches (GeV units).

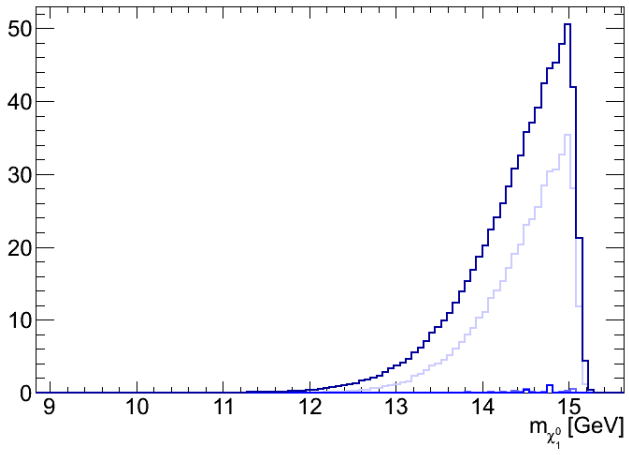

Fig. 9.1: Neutralino mass spectrum in the first light neutralino MSSM search. The color code is described in Sec. 8.4.2.

9.1.1 The first run

Neutralino mass below $15\,GeV$*: negative results*

We proceed to discuss the results presented in [1]. Since the aim is to find light neutralinos, here the prior on the neutralino mass was set by $m_{\chi_1^0\,min} = 1\,GeV$ and $m_{\chi_1^0,max} = 15\,GeV$. In this run we assumed the FO mechanism for the neutralinos to achieve an acceptable relic density. Thus, points had relic neutralino densities down to $10\%\Omega_{WMAP5}h^2$. Recall that we took a stringent and constant upper limit on the lightest Higgs mass. Priors on parameters

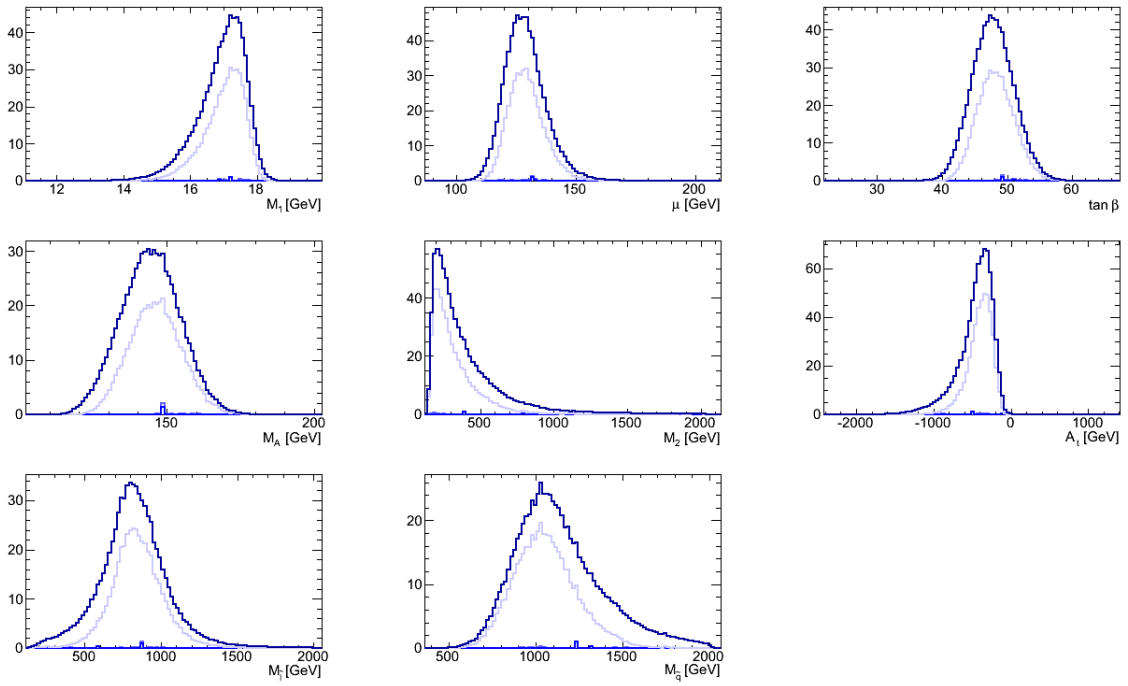

Fig. 9.2: Frequency distributions of free parameters in the first light neutralino MSSM search. The color code is described in Sec. 8.4.2.

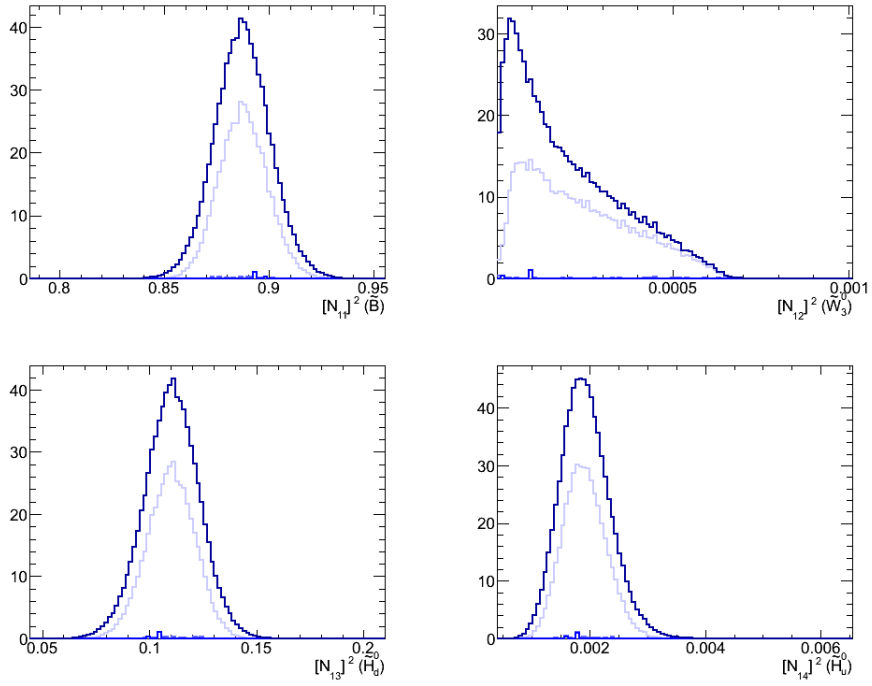

Fig. 9.3: Frequency distributions of the lightest neutralino components in the first light neutralino MSSM search. The color code is described in Sec. 8.4.2.

where taken as described in Table 9.1. These were defined to force a configuration where $M_1 \leq M_2, \mu$, so the neutralino is mostly bino. Also, allowing μ and M_A to be as small as possible as well as $\tan\beta$ as large as possible increases the chances to have large enough interactions via Higgs boson exchanges for the FO mechanism to yield a low enough relic density of neutralinos. We present only results for $\mu \geq 0$, nevertheless we have also explored negative μ scenarios, although the results in such case are not worth a discussion. We used one free parameter for soft slepton masses and one for soft squark masses.

A total number of 754186 points were kept and analyzed in this run. The best total weight is of only 0.226, which is rather poor. Furthermore, only two points are included in the first group of Q-weights (as defined in (8.2)), whereas only 34 can be found among the second group. The third is populated with 64301 points, less than 10% of the total. This already says that it is difficult to find good configurations in this region. When we analyze the mean individual likelihoods, the worst is $\mathcal{L}_{b\to s\gamma}$ with only 0.035. Among the rest, around $0.4-0.6$ we find the Higgs mass limit –which here is taken as the sharp lower limit of $114.4\,GeV$, see Sec. 8.3.3– and the contributions to the g_μ and the Z width. This gives an idea of what criteria are difficult to satisfy, however, the low weight of different points may be due to different criteria.

Neutralino masses found span from $8.9\,GeV$ to $15.5\,GeV$. However, Fig. 9.1 shows that very few configurations yield neutralinos lighter than $12\,GeV$. Furthermore, the very low curve of the points closer to Q_{max} only takes off from zero above $10\,GeV$.

Fig. 9.2 represents the free parameters found in this run, whereas Fig. 9.3 shows the lightest neutralino components. It is easy to see that among the parameters determining the neutralino mass –see (6.1)–, the lighter is by far M_1. The lightest neutralino is thus bino-like, with this component representing $\gtrsim 85\%$ of the LSP. The μ parameter is constrained to be larger than $\sim 100\,GeV$ since it is strongly correlated to the highly constrained chargino mass. Hence the higgsino components are rather small: $N_{13}^2 \lesssim 15\%$ and $N_{14}^2 \ll 1\%$. The wino mass is rather large. Even though sometimes it approaches the $\sim 110\,GeV$ range, it is not light enough to really contribute to $m_{\chi_1^0}$.

In order not to overproduce neutralinos in the EU, they need to annihilate enough, that is to say, attain annihilation cross sections of the order of $3\,10^{-26} cm^3 s^{-1}$. For neutralinos lighter than $15\,GeV$, the available channels for annihilation are all SM fermions but the top-quark. Since here neutralinos are heavier than $1\,GeV$, neutrinos final states are kinematically disadvantaged: the favored annihilation channels are the bottom-quark and the tau-lepton. Thus the only particles that can intermediate the interactions are vector bosons, sfermions and Higgs bosons. The couplings to EW carriers are heavily constrained: since here $m_{\chi_1^0} \ll M_Z/2$, the neutralino contributes to the invisible Z decay, which is constrained by $\mathcal{L}_{Z\to\chi_1^0\chi_1^0}$, ensuring this coupling to be small. Also, we observe rather heavy sfermion masses. Therefore the preferred exchange is through Higgs bosons. Here, the lightest Higgses have

masses well above $100\,GeV$. Thus the only way for neutralinos to annihilate enough is to have large couplings to Higgses, an important fraction of higgsino, and large couplings of the Higgs to the final state particles. Light M_A ensures a maximum splitting in the Higgs sector. The lightest Higgs couplings depend on the β angle (see Sec. 6.2.2). This is why we observe very large $\tan\beta$ values: it enhances the Higgs coupling to the b-quarks. The neutralino-Higgs couplings are determined by the α mixing angle –hence upon M_A–, the β angle, but mainly on the higgsino fraction, as it was seen in Sec. 6.2.2. Such large couplings manifest themselves in the SI nucleon-neutralino elastic scattering cross sections, since these occur mainly through the exchange of a Higgs boson through a t-channel, squark masses being too heavy to compete. Moreover, the need of a consequent fraction of higgsino in the LSP explains the concentration of the μ parameter towards the lower values allowed. This is also the origin of a poor value of likelihood devoted to the g_μ. The MSSM dominant contribution is given by the chargino-slepton-muon coupling and the chargino propagator [50]. This contribution is indeed maximized for low chargino masses, themselves attained for light charged higgsino and/or light charged wino, i.e., small μ and/or small M_2. The first case is realized here.

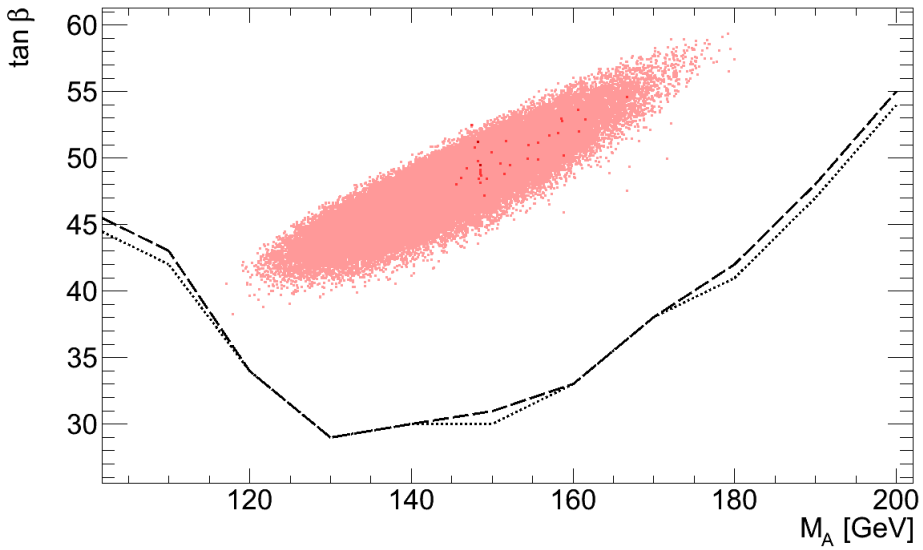

Fig. 9.4: Points of the first light neutralino MSSM search in the $\tan\beta$ vs. pseudoscalar Higgs boson mass M_A plane. Exclusion limits from a Tevatron Higgs are shown for two benchmark scenarios. The color code is described in Sec. 8.4.2.

In this particular run, the γ-ray constraints from the dSphs are not taken into account. The reason is simple, at the time these results were published the analysis of such observables had not been done yet. However, it is not necessary to look at those limits since, unfortunately, all points are already ruled out by those constraints that were successfully computed. Indeed, in Fig. 9.4 we see that all configurations found by the MCMC lie above the Tevatron limits

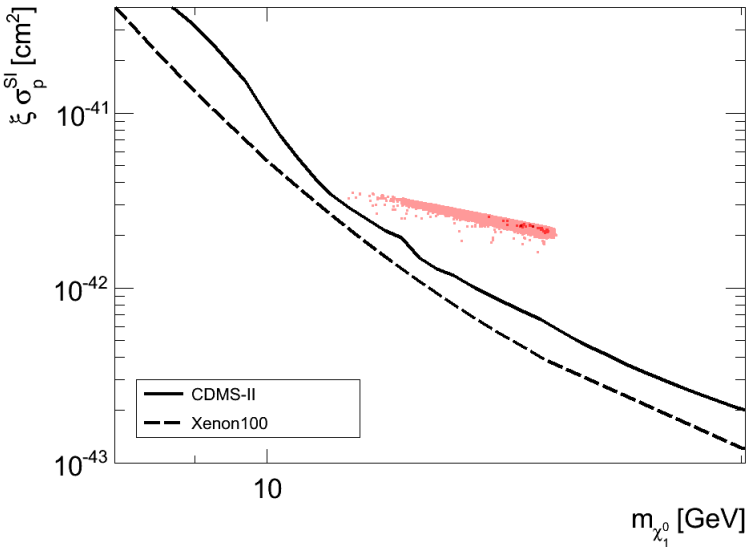

Fig. 9.5: Points of the first light neutralino MSSM search in the $\xi\sigma^{SI}$ vs. neutralino mass $m_{\chi_1^0}$ plane. Exclusion limits from CDMS-II and XENON100 (here, the 2010 rescaled results) are shown. The color code is described in Sec. 8.4.2.

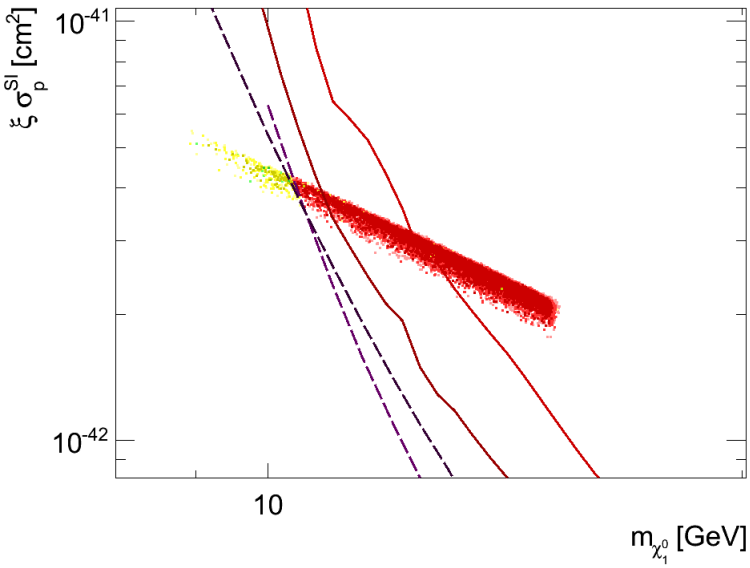

Fig. 9.6: Points in the $\xi\sigma^{SI}$ vs. neutralino mass plane for a light neutralino MSSM search without taking into account the limits on $B_s \to \mu^+\mu^-$. Exclusion limits from CDMS-II 2009 alone and combined results (solid lines), XENON10 [49] and the 2010 rescaled XENON100 limits (dashed lines) are shown. The color code is described in Sec. 8.4.2.

on the $\tan\beta$ vs. M_A plane. Similarly, Fig. 9.5 presents where configurations rest on the $\xi\sigma^{SI}$ vs. $m_{\chi_1^0}$ plane. As expected, all of them have rather large interactions and are thus excluded by the XENON100 limits established in their first results, and, of course, even more by the latest results from the same collaboration.

This run lead us to the following conclusions regarding light neutralino scenarios in the MSSM. On one hand it is very difficult to generate configurations without failing to any of the data fitting criteria we have defined. On the other hand, those configurations found are in disagreement with the exclusion limits of the Tevatron Higgs searches and of the XENON100 experiment.

To show the power of a particular constraint on the parameter space we performed a quick run in which $\mathcal{L}_{B_s\to\mu^+\mu^-} = 1$ for all points. This way, the $B_s \to \mu^+\mu^-$ exclusion limits where not taken into account, whereas all the rest was kept. Results are shown in the $\xi\sigma^{SI}$ vs. $m_{\chi_1^0}$ plane in Fig. 9.6. This figure shows that if there was no limit on BSM contributions to the $B_s \to \mu^+\mu^-$ BR, then, most of the points would be excluded by both DD experiments and the Tevatron (the red points). Of the remaining points, most would be excluded by one or the other criterion (yellow points). Only a few would survive to both (green points). Therefore, we conclude that every single constraint reduces the parameter space of healthy configurations, that even if one particular constraint is relaxed success is not guaranteed in largely expanding the parameter space allowed, and that it marginally increases the chances of having more points overcoming Tevatron and DD limits. Therefore, it is safe to claim that, given the constraints we have imposed, no successful configuration can be found for neutralinos lighter than $15\,GeV$ in the MSSM.

Search for a new lower limit for CDM neutralinos in the MSSM

Since the search for $O(1-15)\,GeV$ neutralinos overcoming all constraints applied failed to provide good candidates, we extended our study to larger neutralino masses, namely $m_{\chi_1^0} \leq 50\,GeV$. The aim was now to find the lightest healthy neutralino around $O(10)\,GeV$. For this second run the only change included in the code was the upper limit of the neutralino mass in the prior. Indeed, we set $m_{\chi_1^0,max} = 50\,GeV$. Thus we concluded that neutralinos could be as light as $\simeq 28\,GeV$ in the MSSM with the parameter space described in Table 9.1. The results of this run were also presented in [1].

This run generated 2954127 different points. The best weight was 0.750, whereas 30.2% of the points belonged to the Q^1 group and 88.8% of the points had a weight better than $0.003 \times Q_{max}$. This shows that this run is much more successful than the first and equivalent run that searched for light neutralinos, described in Sec. 9.1.1.

Neutralino masses spanned from $8.9\,GeV$ to $51.3\,GeV$. The code was able to scan towards light neutralinos, however that region has no statistical weight, as it can be seen in Fig. 9.7. In this figure we can see that the neutralino mass distribution presents a very pro-

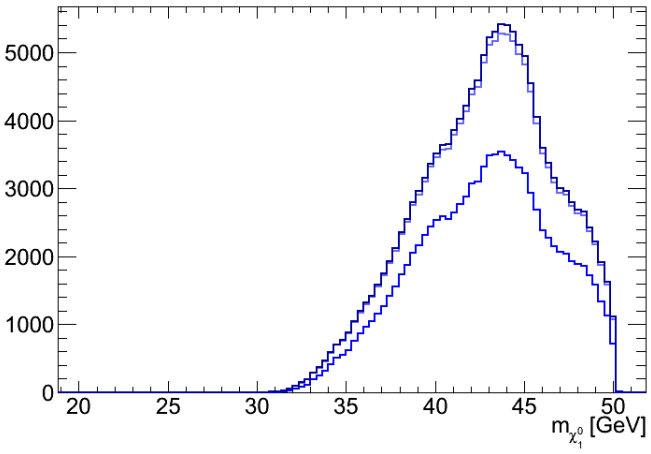

Fig. 9.7: Neutralino mass spectrum in the search for the new lower bound on cold neutralino masses in the MSSM. The color code is described in Sec. 8.4.2.

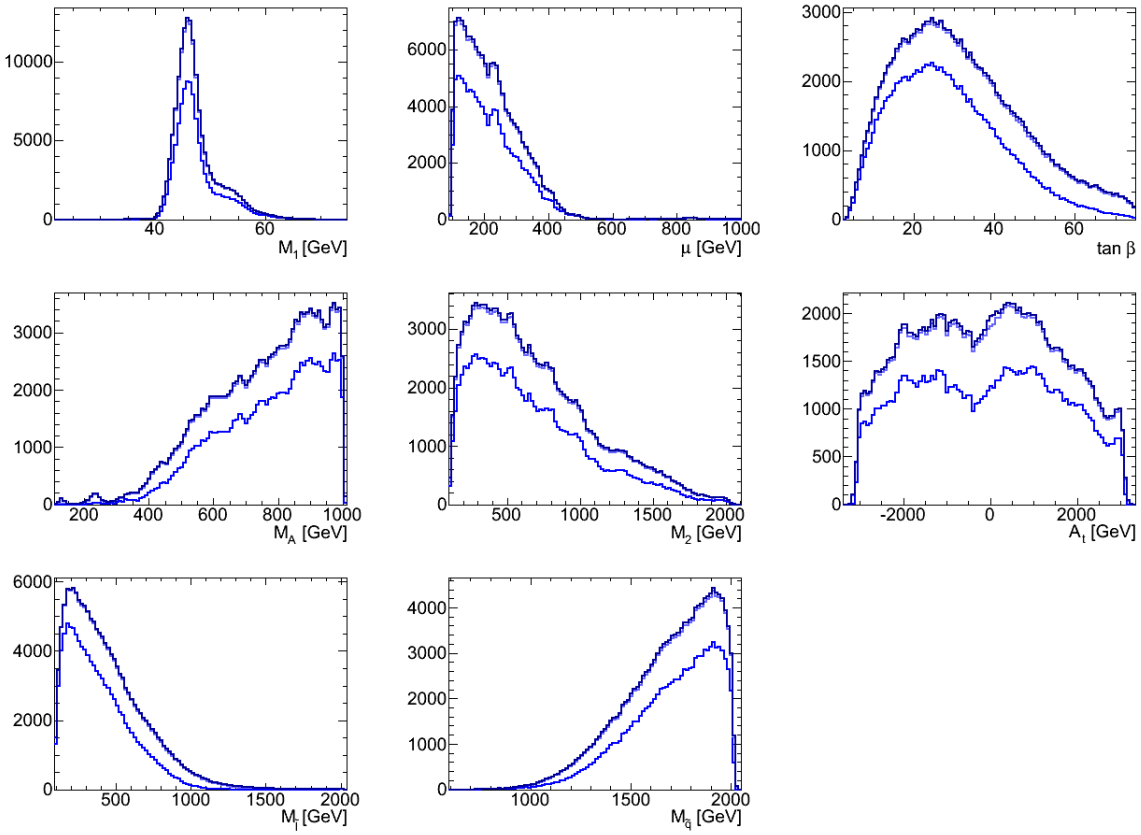

Fig. 9.8: Frequency distributions of free parameters in the search for the new lower bound on cold neutralino masses in the MSSM. The color code is described in Sec. 8.4.2.

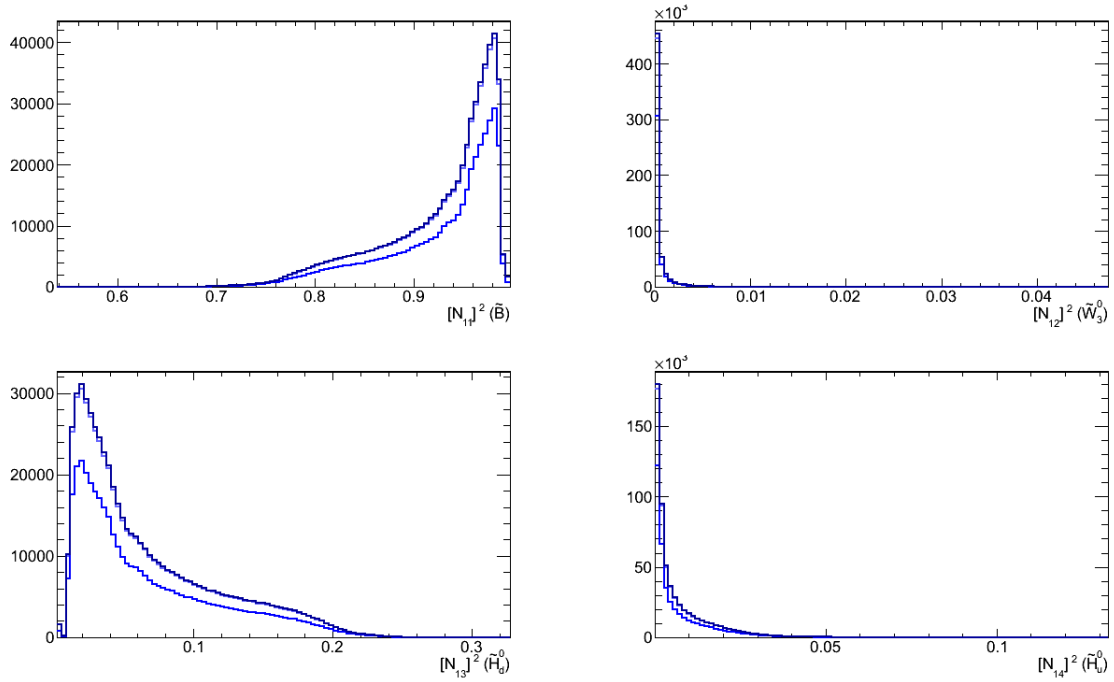

Fig. 9.9: Frequency distributions of the lightest neutralino components in the search for the new lower bound on cold neutralino masses in the MSSM.. The color code is described in Sec. 8.4.2.

nounced peak around $(42-45)\,GeV$, that is to say, around $M_Z/2 \simeq 45.56\,GeV$ [16]. It is not surprising: neutralino annihilations have to be strong enough in order not to overtake the observed relic density of DM. The neutralino annihilation into SM fermions via the exchange of a Z-boson through an s-channel behaves as $\langle\sigma v\rangle \propto \left(1-M_Z^2/s+iM_Z\Gamma_Z/s\right)^{-2}$. Since $\Gamma_Z \simeq 2.50\,GeV$ [16], this implies that this annihilation channel is most efficient when $s \simeq M_Z^2$, that is to say, through a resonance. The neutralino, as a WIMP in the EU, freezes-out for a temperature of roughly $T_{FO} \simeq m_{\chi_1^0}/20$, i.e., annihilation into fermions occurs at $s \simeq \left(m_{\chi_1^0}(2+1/10)\right)^2 = 4.41 m_{\chi_1^0}^2$, which leads to $m_{\chi_1^0} \simeq M_Z/2.1 \simeq 43.4\,GeV$. This value is even closer to the observed peak, confirming the EU resonance mechanism to obtain a low enough relic density through the FO mechanism.

The resonance in the exchange of a Z-boson is a very helpful mechanism: indeed, because of its convenient kinematics, other interactions which would have been invoked to help annihilating neutralinos are smaller, namely those which require Higgs exchanges. Light Higgs with large couplings to fermions lead to unhealthy implications in b-physics as well as the possible exclusion from the Tevatron limits, as it was seen in Sec. 9.1.1. That is what we observe in Fig. 9.8: a large span of values are found for $\tan\beta$, whereas M_A is actually more concentrated towards large values yielding small couplings. The coupling of neutralinos to the Z-boson depends upon the Higgsino fractions, N_{13}^2 and N_{14}^2. We observe in 9.9 that in this

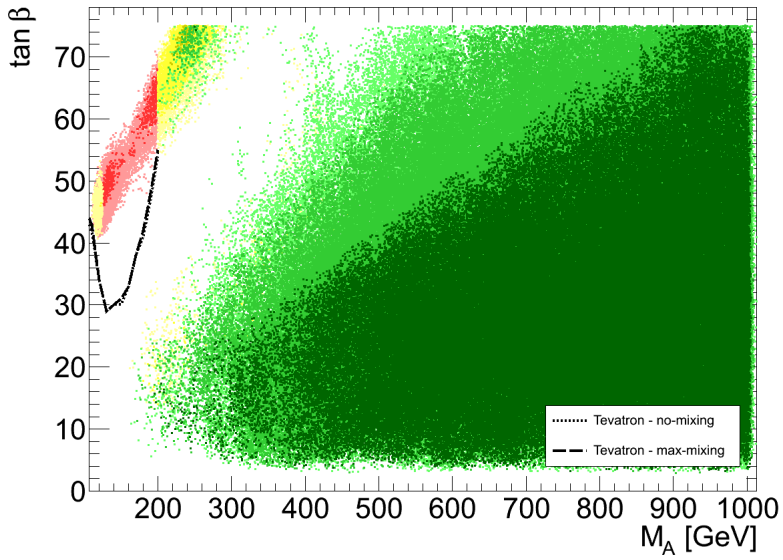

Fig. 9.10: Points from the search for the new lower bound on cold neutralino masses in the MSSM represented in the $\tan\beta$ vs. pseudoscalar Higgs boson mass plane. Exclusion limits from a Tevatron Higgs are shown for two benchmark scenarios. The color code is described in Sec. 8.4.2.

region of parameter space the neutralino is most of the times more than 90% bino. Consequently, the higgsino fractions are lower than in the light neutralino searches. Indeed, since the mechanism of annihiliation is sufficiently enchanced by kinematics, the coupling can drop to lower values. That is why the μ parameter can now span more values: for $\mu \gg M_1$, the bino fraction is much more important than the higgsino components, which is now allowed. We also observe that light sleptons are preferred whereas heavy squarks are also favored.

We saw that here the large $\tan\beta$ vs. light pseudoscalar intersection is not well represented among selected points. Indeed, Fig. 9.10 shows that only a fraction of points are excluded by Tevatron. Moreover, there are two disconnected regions, the largest being far away from the Tevatron limits. Following the color code we also see that the points excluded by DD are in the smaller cloud, of larger $\tan\beta$ values. In the $\xi\sigma^{SI}$ vs. neutralino mass plane, as we expected, the points form a v-shaped cloud with the tip around $M_Z/2$. Indeed, the closer a point is to the resonance, the smaller the couplings to the Z and the Higgs. The latter implies smaller SI elastic scattering with nucleons. That explains why the resonance induces the lowest interaction rates. The upper cloud is clearly related to the large $\tan\beta$ region, as color-tagging exposes. It suggests that its extrapolation towards lighter neutralinos corresponds to the points we were able to find in Sec. 9.1.1. That identification allows us to assign a larger higgsino component to these points (i.e., smaller μ values), which in turn explains the position of this cloud with respect to the $\xi\sigma^{SI}$ axis. In general, this type of configuration seems

to be unhealthy not only for light neutralinos. For reference we also show the SD interaction rates in Fig. 9.12. It is clear that the most stringent limits currently available are far away from the parameter space we explored. No further constraints can be obtained by looking at these interactions.
Using this run, thus, we can estimate a lower value of the neutralino mass. Indeed, with the likelihoods and priors as they were taken for these points as well as in Sec. 9.1.1, the healthy point yielding the lightest neutralino lies in the light tail of the Z-resonance cloud. By asking points with the lightest neutralino possible, for which the $Q \leq 0.32 \times Q_{max}$, not excluded by the Tevatron limits in the Higgs sector, and not ruled out by DD experiments, we came to the conclusion that in this search the lightest possible neutralino had a mass of $\simeq 28\,GeV$.

Caveats to the first search in the MSSM

It is important to notice that these runs do not take into account the possibility of Higgs bosons lighter than $114.4\,GeV$. If the pseudoscalar Higgs mass is close enough to that of the lightest scalar Higgs, then their production is more difficult to test in collider experiments. Thus, the constraint on the light Higgs mass can be translated into a limit on its couplings to the SM particles. Lighter Higgs bosons imply more possibilities for lighter neutralinos. Indeed it should be easier to achieve a safe relic density through the FO mechanism with a lighter exchanged particle. Also, we expect a better general behavior with respect to most constraints in which the Higgs plays a role, such as all limits on b-physics. This is why the lightest Higgs mass limit in the MSSM has been improved in mO and it will definitely be included in future releases. It is still under development, but with the current state of the code we could perform a new run taking into account this allowed region in order to complete our searches of light neutralinos in the MSSM. Also, compared to [60], we have restricted sleptons to be heavier than $\sim 100\,GeV$, while stauons could be as light as $81.9\,GeV$ and smuons as light as $94\,GeV$ [16].

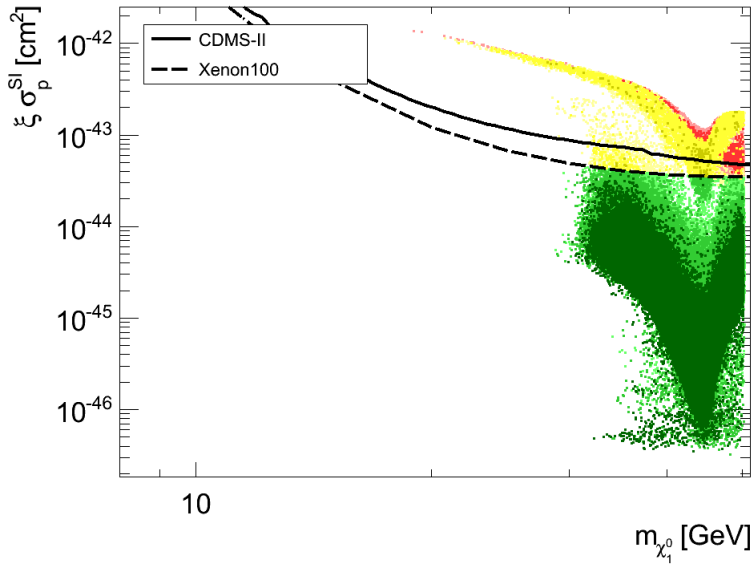

Fig. 9.11: Points from the search for the new lower bound on cold neutralino masses in the MSSM represented in the $\xi\sigma^{SI}$ vs. neutralino mass plane. Exclusion limits from CDMS-II and XENON100 (here, the 2010 rescaled results) are shown. The color code is described in Sec. 8.4.2.

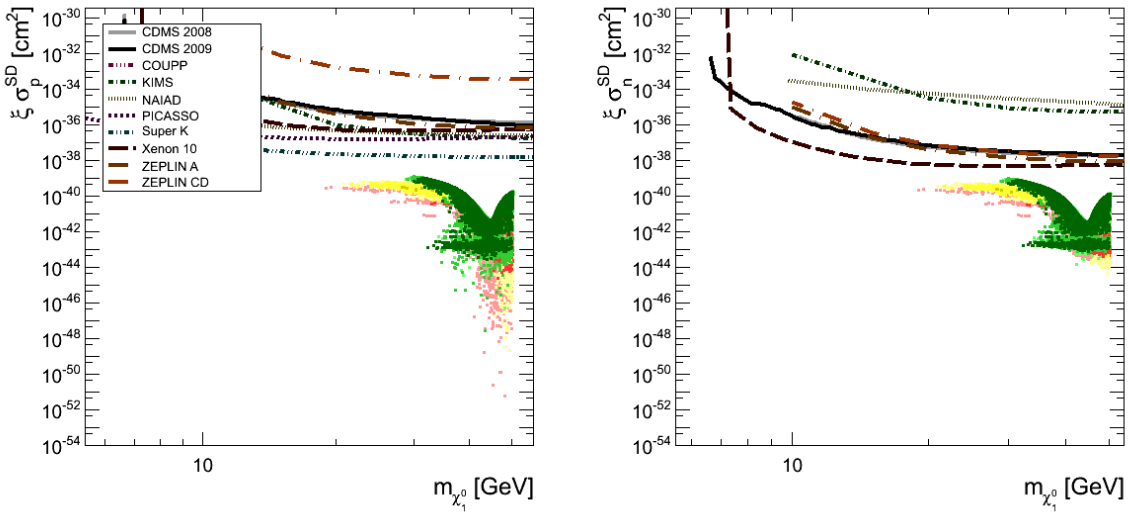

Fig. 9.12: Points from the search for the new lower bound on cold neutralino masses in the MSSM represented in the $\xi\sigma_p^{SD}$ vs. $m_{\chi_1^0}$ plane (left panel) and in the $\xi\sigma_n^{SD}$ vs. $m_{\chi_1^0}$ plane (right panel). Exclusion limits shown for reference: CDMS [51], COUPP [52], KIMS [53], NAIAD [54], PICASSO [55], SuperKamiokande [56], XENON10 [57] and ZEPLIN [58], whereas all data points were obtained at [59]. The color code is described in Sec. 8.4.2.

9.1.2 A second run: lighter Higgs and slepton configurations

We present now a more recent analysis of light neutralinos in the MSSM. The results here have been shown and updated in [8].

Neutralino masses below $15\,GeV$*: a new open region*

Parameter	Minimum	Maximum	Tolerance
M_1	1	1000	3
M_2	100	2000	30
M_3	500	6500	10
μ	0.5	1000	0.1
$\tan\beta$	1	75	0.01
M_A	1	2000	4
A_t	-3000	3000	100
$M_{\tilde{l}_L}$	70	2000	15
$M_{\tilde{l}_R}$	70	2000	15
$M_{\tilde{q}_{1,2}}$	300	2000	14
$M_{\tilde{q}_3}$	300	2000	14

Tab. 9.2: MSSM free parameter intervals for the a further light neutralino search (GeV units).

In this late run, thus, we took the improved limit on the Higgs mass by making use of the HiggsBounds package linked to mO. The prior on the neutralino mass was kept in order to scan masses lighter than $15\,GeV$. Furthermore, new free parameters were included: the gluino mass M_3 was no longer forced to be proportional to the wino mass M_2, and was instead taken as a free parameter with a wide range, squark masses were split into two free parameters, one for the first and second generations, and one for the third, and finally the sleptons were split into two free parameters, one for the left handed and one for the right handed sleptons. Indeed, we expect the sbottom mass to be more constrained since it plays an important role in the B-mesons loop corrections to rare decays and mass oscillations. Actually, the stop mass is also important but to yield enough destructive interferences to lower the supersymmetric contribution to the $b \to s\gamma$ branching ratio. If all squark masses were degenerated, then this tendency would be immediately transmitted to the other squark generations. Moreover, very light sleptons have been pointed out as a possibility for light neutralinos to annihilate enough in [60]. In particular, the physical mass of the sleptons is a mix of the left and right handed states. These new inclusions could open some new possibilities in parameter space in which constraints can be more easily respected: loop contributions

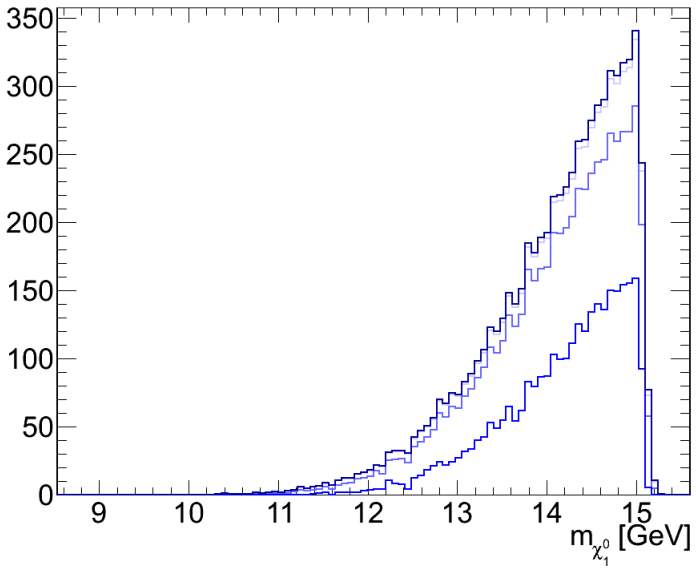

Fig. 9.13: Neutralino mass spectrum in the second light neutralino MSSM search. The color code is described in Sec. 8.4.2.

of squarks and gluinos could cancel out for some combination of their masses, therefore it is suitable to have them all as free as possible in order not to miss such configurations. However, we find out that this is not a crucial feature. We also relaxed the lower limit of the pseudoscalar mass and let the HiggsBounds package stop those configurations ruled out by this parameter being too small. Hence, we scan the set of parameters given in Table 9.1 together with their intervals and tolerance levels.

In this run we used a forced initialization technique. First, a few runs were used in order to explore possibilities, after which we chose a certain number of starting points and finally these were used to scan the parameter space. We found a total number of 301912 points, in two rather distinct regions: added to the old region we had explored –although enhanced by the possibility of lighter Higgs bosons– we found a light slepton region. Indeed, the best total weight was of 0.220, while the region corresponding to our previous findings could only reach weights of 0.085. Among all points 6506 points lied at $1\,\sigma$ from Q_{max}, 25217 at $2\,\sigma$, and only about a third had weights within $3\,\sigma$ of Q_{max}. Once again, the bad likelihoods are those of the $b \to s\gamma$, but more importantly in this run, the $B_u \to \tau\nu_\tau$ branching ratio. The best likelihoods are obtained for the new light slepton region where $b \to s\gamma$ is no longer constraining, and $B_u \to \tau\nu_\tau$ gives a likelihood of ~ 0.1. In the lighter Higgs region only an interplay of these two criteria can make a relatively good total weight, namely, both being between one and two σ away from the central value.

As it can be seen in Fig. 9.13, the situation has not changed dramatically from the first run: it is very difficult to find healthy configurations yielding neutralinos lighter than $(10-12)\,GeV$,

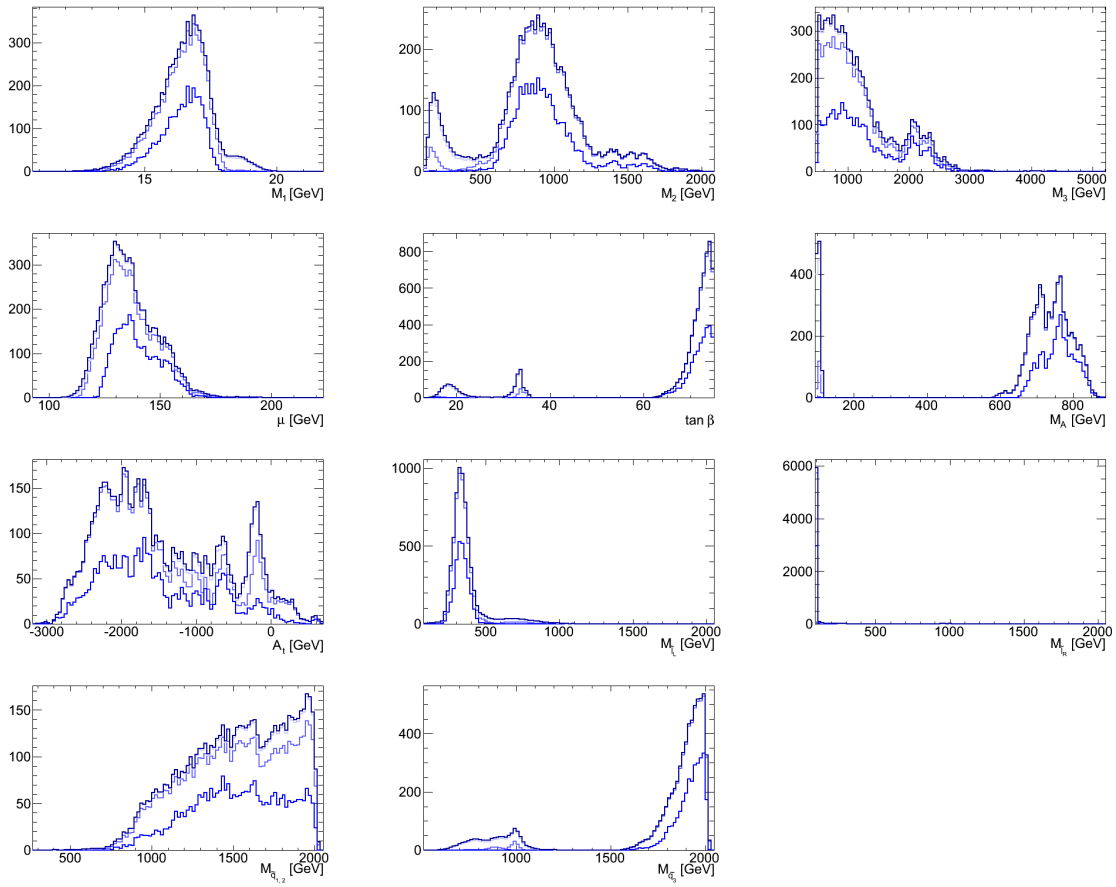

Fig. 9.14: Frequency distributions of free parameters in the second light neutralino MSSM search. The color code is described in Sec. 8.4.2.

and most points found are concentrated towards the prior upper bound. Actually in this run, masses were found from 8.6 to 15.4 GeV, almost exactly the same interval as previously found. Even though we could have expected more results towards lighter neutralinos, the constraints are so difficult to overcome that even in this more relaxed run the mass spectrum does not change drastically. However, the curve representing the best likelihoods is now much closer to the others, showing that there is a larger concentration around the best points, which correspond to the light sleptons.

The parameter space found is represented in Fig. 9.14. We readily see that the distributions are not shaped in quite the same way as in the previous run. We can distinguish three $\tan\beta$ regions: below 25, between 30 and 36, and above 60. We also can clearly observe two distinct M_A regions: around 100 GeV and above 600 GeV. Lighter pseudoscalars are associated to the two smaller $\tan\beta$ regions, which together imply rather light charged Higgses $H^{\pm}$. Thus the resulting enhancement in the supersymmetric contribution to the $B_u \to \tau\nu_\tau$ branching ratio lowers the total weight for these configurations. The split in M_A and $\tan\beta$

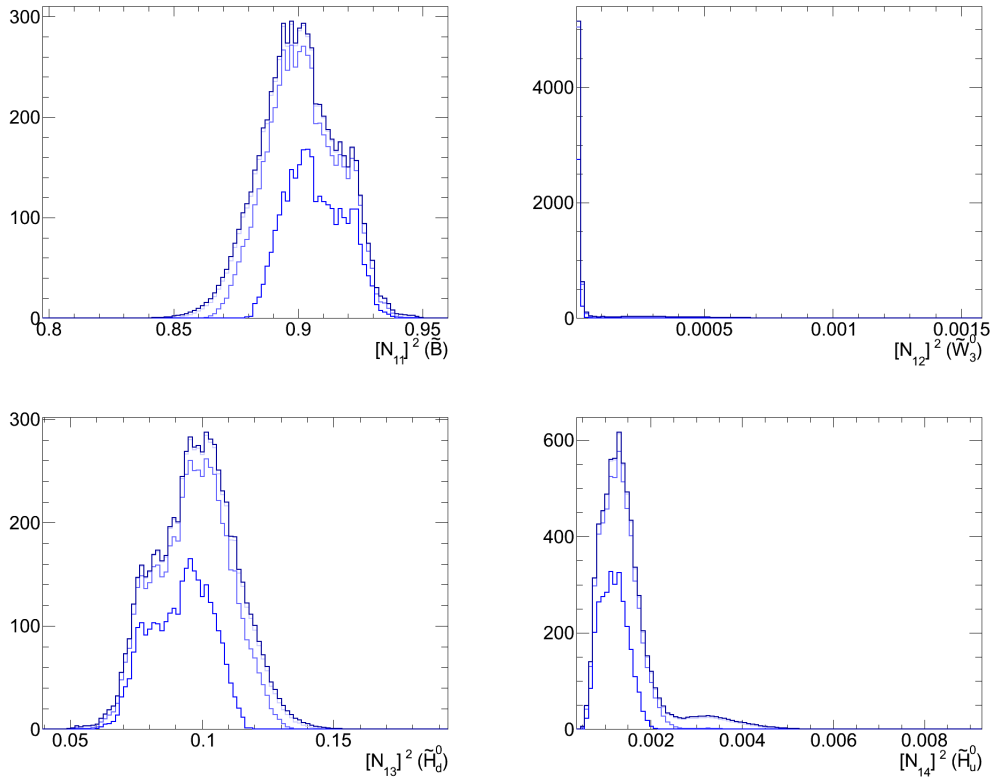

Fig. 9.15: Frequency distributions of the lightest neutralino components in the second light neutralino MSSM search. The color code is described in Sec. 8.4.2.

gives rise to the tendency to have two preferred regions in other parameter distributions such as those of M_2, M_3 or $M_{\tilde{q}_3}$. Notice that right handed sleptons are always as light as possible and that left handed sleptons are concentrated below $500\,GeV$, suggesting a large mixing of the states, and a relic density achieved through the exchange of sleptons, at least partially. Regarding the squark masses, we see that the first run interval and the current are similar for the third generation, albeit with two peaked regions appearing in the distribution shape, whereas the first and second tend to be heavier. This confirms our expectations: the third generation destructively contributing to the $b \to s\gamma$ was constraining the others in the first run. Relaxing the other masses shows that is is preferred to have heavier squarks, to reduce other loop contributions to b-physics observables. A very similar conclusion stems from Fig. 9.15: roughly the same intervals are spanned, but with slight differences and a tendency to have three separated peaks contributing. Indeed, the new peaks show an even more pronounced bino composition of the neutralino.

The main difference with the previous run takes place in two sectors: the Higgs and the sleptons. Indeed, whereas before the SM-like Higgs boson had a mass limited to $114.4\,GeV$, now it can be smaller. Furthermore, the neutralinos we found before were ruled out by the

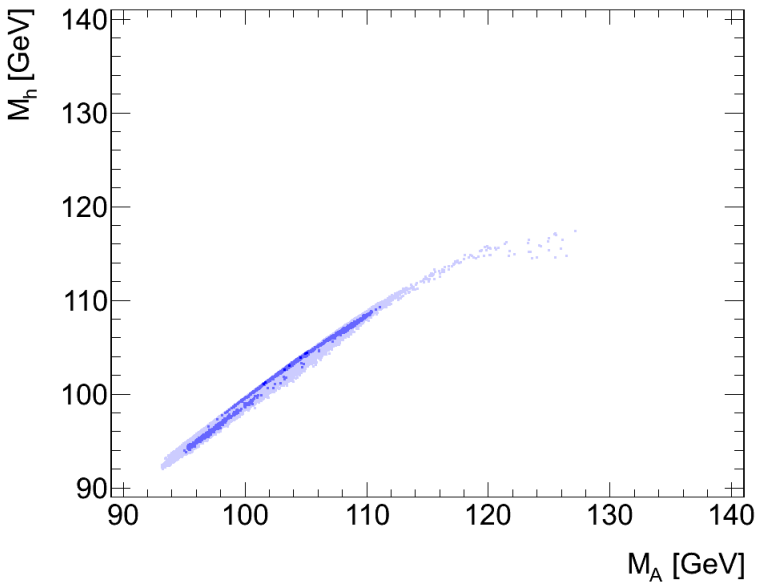

Fig. 9.16: Standard Model-like Higgs boson mass as a function of the pseudoscalar Higgs boson mass in the second light neutralino MSSM search. The color code is described in Sec. 8.4.2.

Tevatron limits in the $\tan\beta$ vs. M_A plane. This limit is taken into account by HiggsBounds, thus we are not finding those exact same neutralino configurations for light Higgses. Instead, lighter Higgs bosons are found together with a light pseudoscalar. Hence, these two masses are very correlated in this new region, as we can see in Fig. 9.16. Indeed, in order to overcome the limits on the Higgs mass, both Higgs bosons have to be light. It becomes obvious that all these points were impossible to be obtained in the previous run by looking at the range of the lightest CP-even Higgs mass. In this plot we cannot see the region corresponding to light sleptons though, as it is associated with heavier M_A.

The two new regions found, namely that of Higgs exchanging and that of slepton exchanging neutralinos, behave very differently regarding further constraints we apply from CMS, Fermi-LAT and XENON100. Let us start by discussing the limits on the $\tan\beta$ vs. M_A plane. In Fig. 9.17 we have splitted in two the two very different regions represented in this plane. In the top panel we observe the light Higgs configurations, corresponding to light pseudoscalars. Such a region is divided in two. The missing connecting sector is ruled out by limits on the $B_u \to \tau\nu_\tau$ branching ratio, while the apparent configurations are accepted at best at 1σ away from the central value for that observable. We observe only two colors in this plane: red and black. Therefore, all points in this region are excluded by both Fermi and XENON100. Moreover, the region on top corresponding to $\tan\beta \gtrsim 27$ is ruled out by CMS. The lower panel shows the rest of the configurations, corresponding to light slepton exchanges. Such a cloud is far away from the reach of CMS and can only be constrained by ID or DD searches.

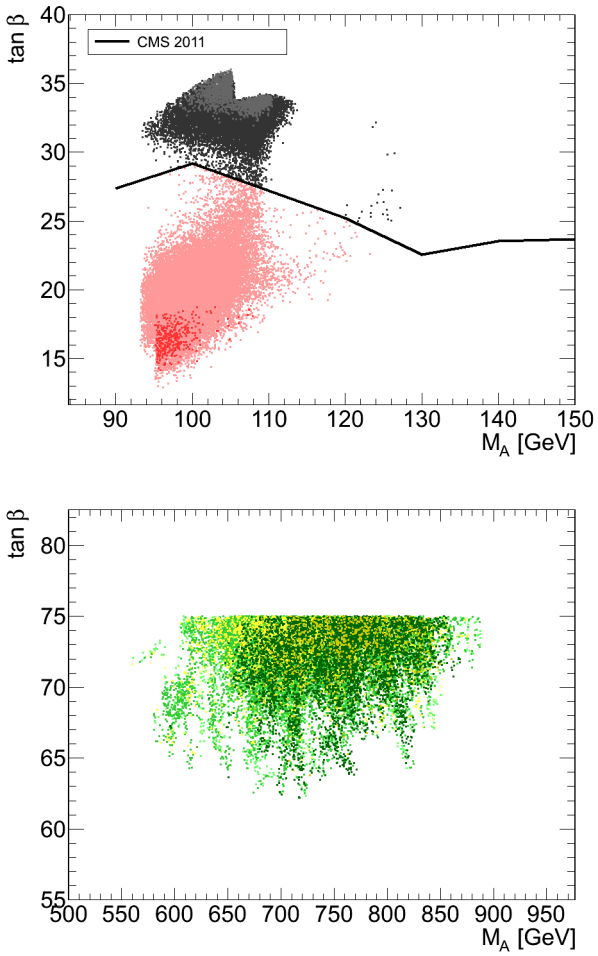

Fig. 9.17: Points of the second light neutralino MSSM search in the $\tan\beta$ vs. pseudoscalar Higgs boson mass plane. Exclusion limits from a CMS Higgs are shown in the top panel for the light Higgs region. The bottom panel shows the configurations characterized by light sleptons. The color code is described in Sec. 8.4.2.

Regarding γ-ray fluxes from the Draco dSph, the two regions yield different fluxes. Indeed, Fig 9.18 shows that, unfortunately, all Higgs-exchanging scenarios fall well above the Fermi-LAT limit from a factor 2 to 12, hence they are ruled out. However, the limit only partially exclude the second cloud. The lightest safe point has a neutralino mass of $12.6\,GeV$, all points yielding lighter neutralinos over-predicting the flux.

Fig. 9.19 represents the yields of this run in the $\xi\sigma^{SI}$ vs. $m_{\chi_1^0}$ plane along with limits from XENON100 and CDMS-II. On one hand the SI DD limit from XENON100 constrain the light Higgs scenarios, as it also did in the previous run. Even if we argued that we could have chosen more conservative nucleon form factors, it is impossible to move the cloud by more than an order of magnitude. It is thus safe to exclude all these points regarding this criterion. On the other hand, the light slepton cloud is safe with respect to XENON100.

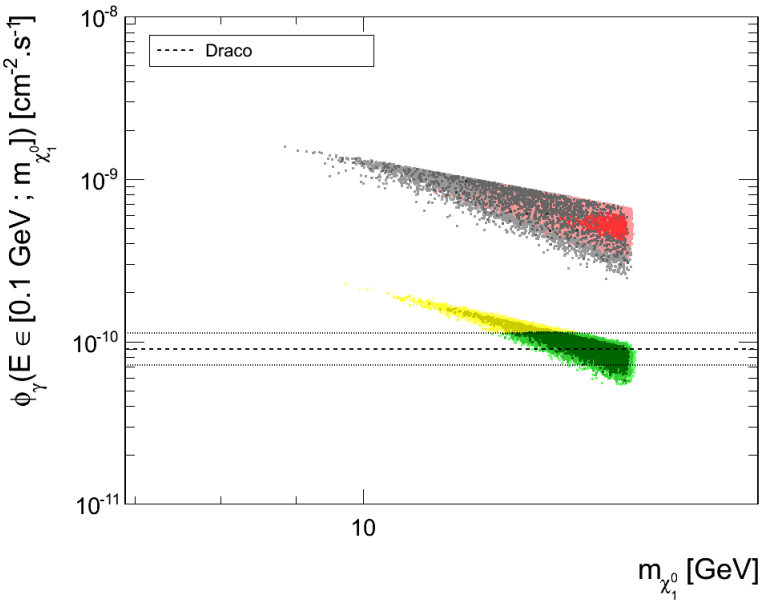

Fig. 9.18: Integrated γ-ray flux from the Draco dwarf spheroidal galaxy as a function of the neutralino mass in the second light neutralino MSSM search. The color code is described in Sec. 8.4.2.

Finally, in Fig. 9.20 we show the value of the estimation for the $B_s \to \mu^+\mu^-$ branching ratio in the MSSM. What we can see is that, once more, the two separate regions behave very differently with respect to this criterion. Indeed, while all points found are safe with respect to the current Tevatron limit accordingly to the code discrimination procedure, different conclusions can be drawn with respect to the LHCb projected sensitivity to the rare decay of B_s into muon pairs. The light Higgs points tagged in red and black would be in the reach of LHCb while the slepton exchanging points would escape the projected sensitivity. This means that if LHCb observes such decays, the slepton exchanging scenarios would be ruled out, since they do not predict any signal. Conversely, if no signal is observed, then a further criterion rules out the light Higgs exchanging points in the MSSM.

In conclusion, this run shows that there is a narrow window of configurations with very correlated values of the scalar and pseudoscalar Higgs boson masses that provide MSSM DM neutralinos which are safe regarding all particle physics constraints –although very borderline with respect to at least $B_u \to \tau\nu_\tau$ and $b \to s\gamma$. However, the astrophysical signatures of these points, specifically in the SI DD experiments and in the γ-ray signal from dSphs, are largely above the observations published by the XENON100 and the Fermi-LAT collaborations. Assuming that the *s*-quark content in nucleons could be overestimated –suggesting lower SI neutralino-nucleon cross sections– it is difficult to gain more than a factor ~ 10 in the interplay between cross section estimation and exclusion limits, and thus save some of these neutralinos with respect to the SI cross sections limits. Limits established by the null flux of γ-rays from Draco already take into account uncertainties, and the exclusion we

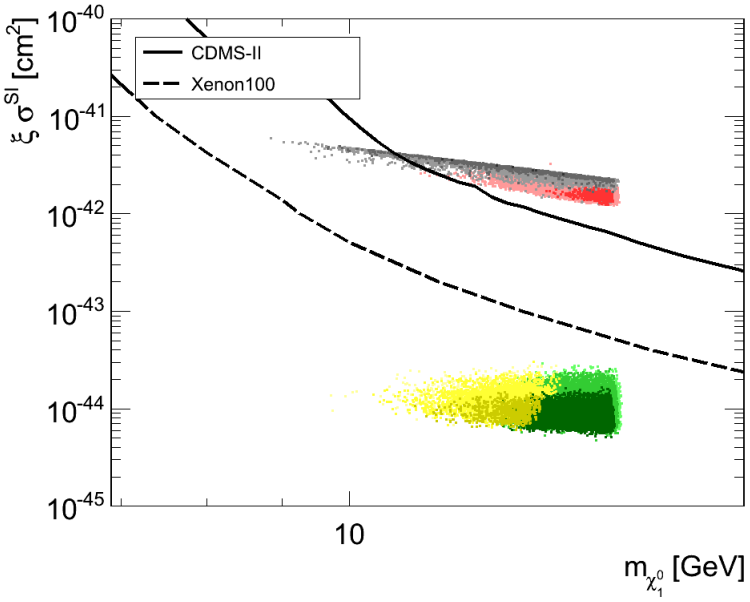

Fig. 9.19: Points of the second light neutralino MSSM search in the $\xi\sigma^{SI}$ vs. neutralino mass plane. Exclusion limits from CDMS-II and XENON100 (here, the 2010 rescaled results) are shown. The color code is described in Sec. 8.4.2.

show is already conservative to that respect. Roughly half of these configurations are also ruled out by the CMS Higgs decays into τ pairs searches. Nonetheless, we have successfully found a new region characterized by light sleptons. These sparticles ensure large enough annihilation rates in EU. The points associated to this region show better likelihoods in the very constraining rare B-meson decay criteria and reach total weights of 0.22. Furthermore, they completely escape the exclusion limits from CMS and XENON100, but are divided in two cases by the Fermi limits on γ-rays from Draco: neutralinos lighter than $12.6\,GeV$ are excluded, while heavier neutralinos are allowed. This is the lower limit we found for the neutralino mass, for configurations in agreement with particle physics and astrophysics experiments.

Further checks: neutralino masses up to $30\,GeV$

In light of the extended analysis we have presented in this section, we checked the consistency of our results by allowing larger neutralino masses. The aim here is to connect the two regions previously obtained towards the larger neutralino masses. To make such a run, we fixed the upper limit of the mass prior to $30\,GeV$, since we had previously obtained configurations yielding neutralinos at around $\sim 28\,GeV$ that passed all constraints. The parameters scanned can be checked in Table 9.2. We also included the CMS, Fermi-LAT and XENON100 limits and used them to further constrain the points in the analysis.

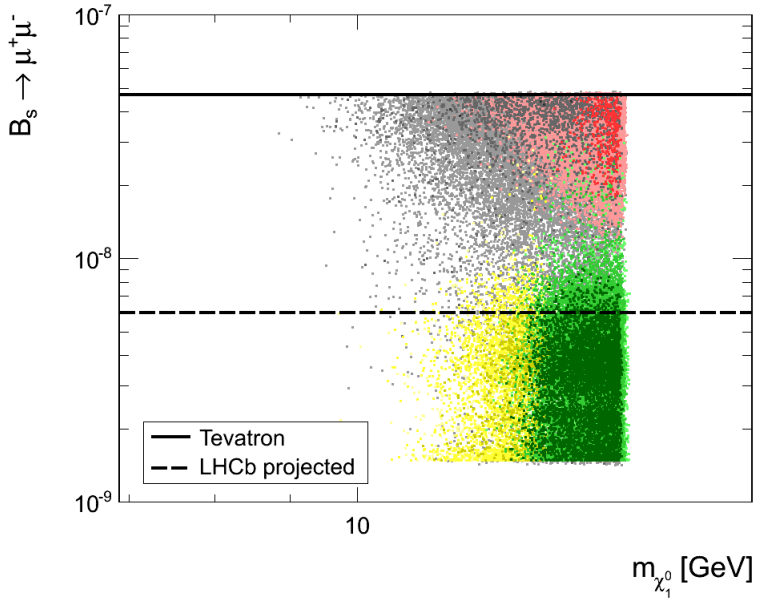

Fig. 9.20: Supersymmetric contribution to the $B_s \to \mu^+\mu^-$ branching ratio as a function of the neutralino mass for light neutralinos in the MSSM. The color code is described in Sec. 8.4.2. We include the current best limit obtained at the Tevatron, and the projected LHCb results for $1\,fb^{-1}$ analysed data.

The run produced 241824 points with a maximum local weight 0.718. About 2.9% of the points belong to best weight group, while 57.1% are in the first three groups. This makes the run highly successful in finding very good configurations, which are however not that dense. Hence, around the $M_{\chi_1^0} \sim 30\,GeV$ region is where we found the lightest point in perfect agreement with data. The worst likelihood tends to be that of the contribution to the anomalous magnetic dipole of the muon, followed by $B_u \to \tau\nu_\tau$ and the invisible Z-width contribution of χ_1^0 pairs.

The mean value of the prior on the mass is quite bad (0.69 for all points), implying that many points seat in the tolerance borders of the prior. It is indeed what we observe in Fig. 9.21: the mass distribution is very concentrated towards $30\,GeV$. The run found points with masses between $10.5\,GeV$ and $31.2\,GeV$, those in the $[30-31.2]\ GeV$ interval having thus lowered the mean mass prior. Below $\sim 20\,GeV$ very few points are found. Although we know that the light slepton configurations do populate the lighter regions down to $\sim 12\,GeV$ with weights up to ~ 0.2, it seems clear now that those scenarios are rather fine-tuned relatively to the $\sim 30\,GeV$ region.

Even if they are less represented, we do observe the same configurations than in the previous section. Parameter space distributions and neutralino configurations are shown in Fig. 9.22 and 9.23 respectively. The former also show the safe (with respect to CMS, Fermi-LAT and XENON100) configuration distributions in green. With this we deduce that most of the configurations ruled out have M_2 below the TeV, M_3 below $2.5\,TeV$, while it seems

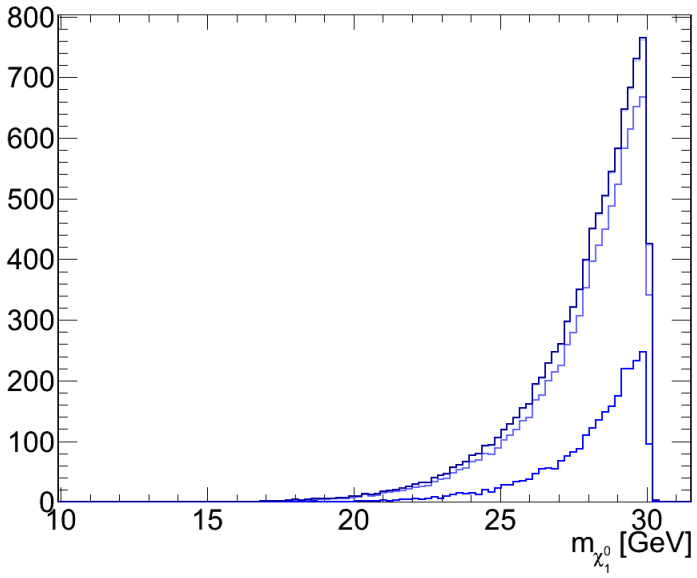

Fig. 9.21: Neutralino mass spectrum in the second search for the new lower bound on cold neutralino masses in the MSSM. The color code is described in Sec. 8.4.2.

very difficult to obtain healthy configurations with $\tan\beta$ below 20, M_A below $500\,GeV$ or $M_{\tilde{q}_3}$ below the TeV. All configurations show very light slepton masses, together with a bino dominated LSP. However, the safe points are indeed dominated by slepton exchanges since M_A is very heavy, hence Higgs exchanges are suppressed. Higgs exchanging scenarios imply around 20% of higgsino in the LSP as it was previously found, while the slepton exchanging neutralinos stem from bino-dominated neutralinos at 90% or more. In this run all neutralinos have masses which fall below the Z-boson resonance. In order to achieve an acceptable relic density for $\sim 30\,GeV$ neutralinos, such processes as $\tilde{\tau}$ exchanges in a t-channel for neutralino annihilation into $\tau\bar{\tau}$ have to contribute, or conversely, annihilation through the same Z-boson exchange has to be enhanced by having a larger $Z\chi_1^0\chi_1^0$ coupling (which, we recall, is $\propto N_{13}^2 - N_{14}^2$). The former is relevant for light slepton masses while the latter implies the smallest possible μ values (hence the largest higgsino contributions, thus the largest couplings to the Z) for the range of neutralinos we ask for. When we further reduce the neutralino mass, the Z-resonance is further away: either the higgsino contribution keeps increasing which worsens the Z invisible width contribution of the LSP, and a subsequent Higgs exchange is needed; or the light sleptons become the dominant mechanism of annihilation, which seems to be less problematic. Therefore, while both configurations can be unified at the Z-resonance mass range, when going below it they are characterized by two different ways to achieve the relic density and decouple in two separate regions, depicted by the other likelihoods such as that of the invisible Z-width contribution of $Z \to \chi_1^0\chi_1^0$. Finally, relaxing the squark masses and the gluino mass does not seem to help finding any new kind

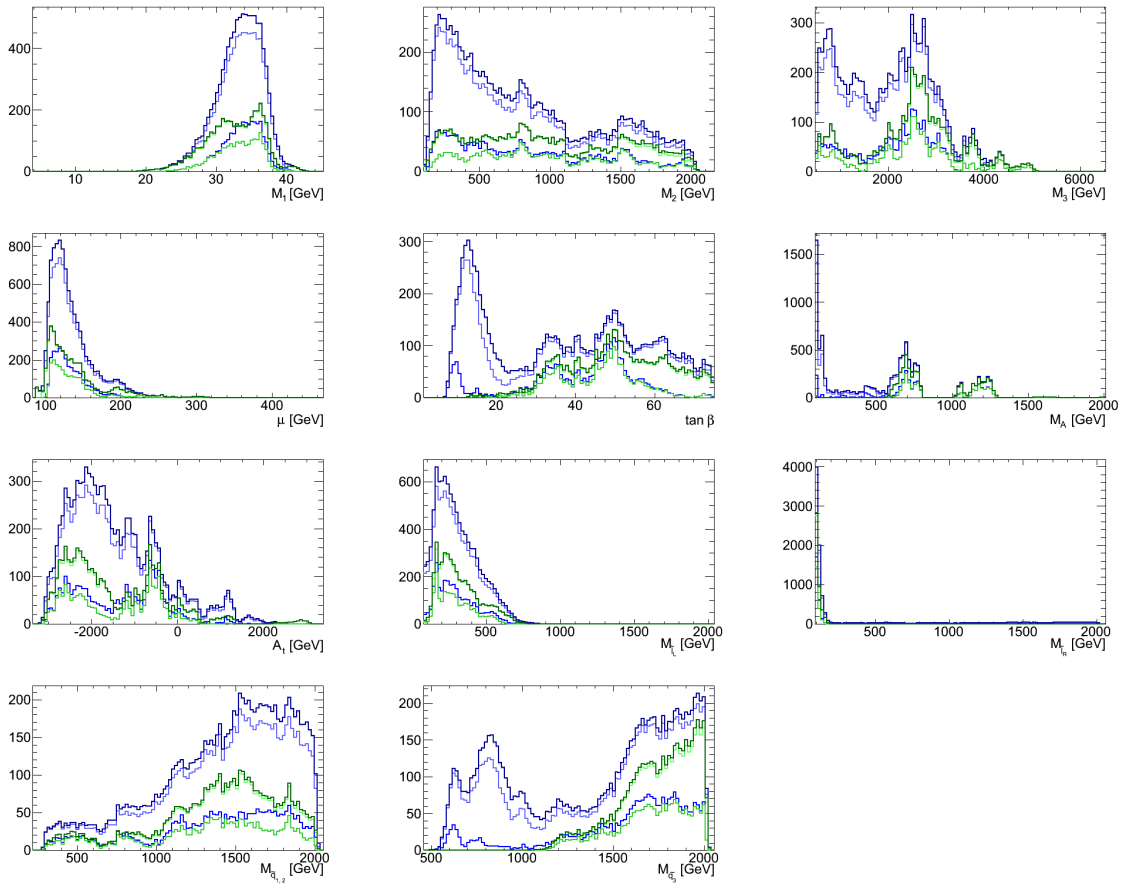

Fig. 9.22: Frequency distributions of free parameters in the second search for the new lower bound on cold neutralino masses in the MSSM. The color code is described in Sec. 8.4.2: the green curves represent the parameter distribution of the safe points only.

of configuration.

Let us now discuss further constraints. In Fig. 9.24 we show the spin independent interaction rates in the galaxy with respect to the neutralino mass. The XENON100 limits are also shown. Recalling the color code as described in Sec. 8.4.2, we see that the constraints are acting in a very correlated way, at least around $30\,GeV$ neutralino masses. Indeed, the XENON100 limit sets the transition from constrained to unconstrained points: all points below it are safe with respect to all other experiments as well. Hence it is the most stringent constraint on these points. Fig. 9.25 shows the γ-ray flux predicted from the Draco dSph for these configurations, together with the Fermi-LAT limits. This is the second most stringent limit for the larger masses. Nevertheless, we observe that the light end tail of the slepton exchanging points reach the limit for masses around $(12-13)\,GeV$. At these masses the XENON100 limits are not the most constraining. The change in behavior is explained because of the SI interactions: the dominating process is the exchange of a Higgs boson

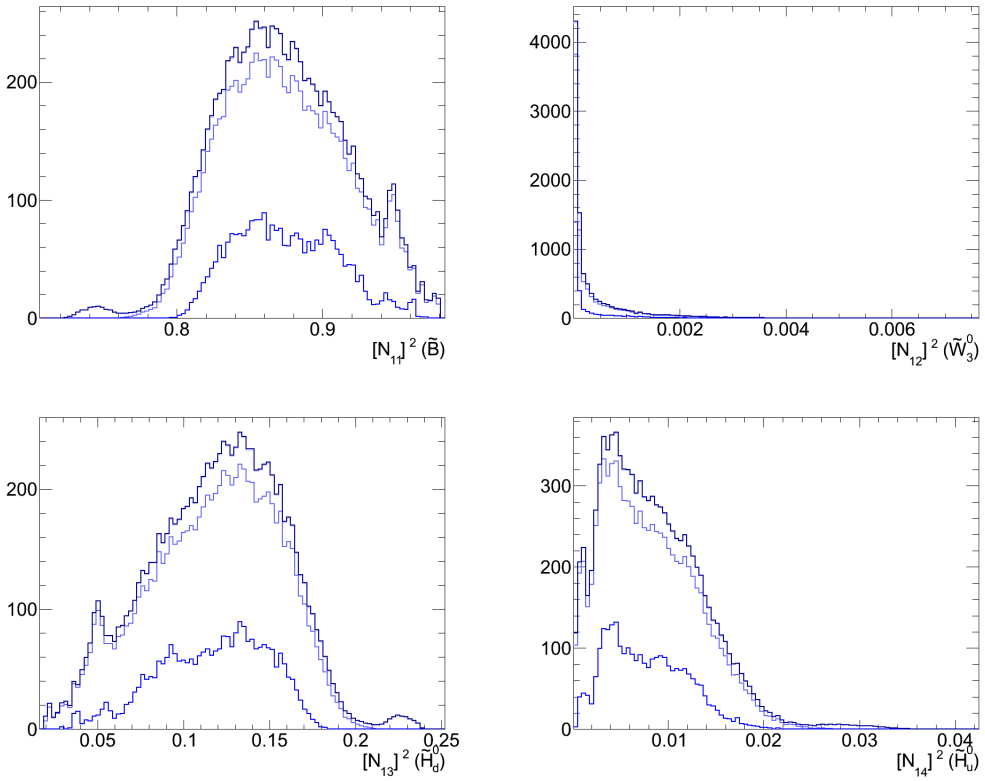

Fig. 9.23: Frequency distributions of the lightest neutralino components in the second search for the new lower bound on cold neutralino masses in the MSSM.. The color code is described in Sec. 8.4.2.

through a t-channel, as it was discussed in Sec. 6.2.3, which corresponds to the left diagram in Fig. 6.1. The neutralino coupling to the Higgs is not enchanced for the lighter masses of the slepton exchanging points, hence the elastic scattering interactions remain constant, while the exact opposite is observed for the Higgs exchanging points: the lighter the Higgs boson, the more efficient the annihilation process, the larger the elastic scattering of neutralinos off nucleons. In Fig. 9.26 we show the points in the $\tan\beta$ vs. M_A plane together with the most recent CMS limits for points corresponding to $M_A \leq 500\,GeV$. Even though there are many points with large M_A, we still rule out part of the parameter space due to this constraint. We have also checked the SD interactions which yield, however, too small cross sections to further constrain the configurations here presented.

For these points we have also explored the impact of the LHCb projected sensitivity to the $B_s \to \mu^+\mu^-$ branching ratio. We present the yield for this observable as a function of the neutralino mass in Fig. 9.27. The conclusion is very similar to the lighter neutralino run: most safe configurations are not expected to be in the range of sensitivity of LHCb, while the excluded regions would fall in the branching ratios LHCb will be able to explore. The different behavior of the two regions is given by the neutralino coupling to the Z. Indeed, the

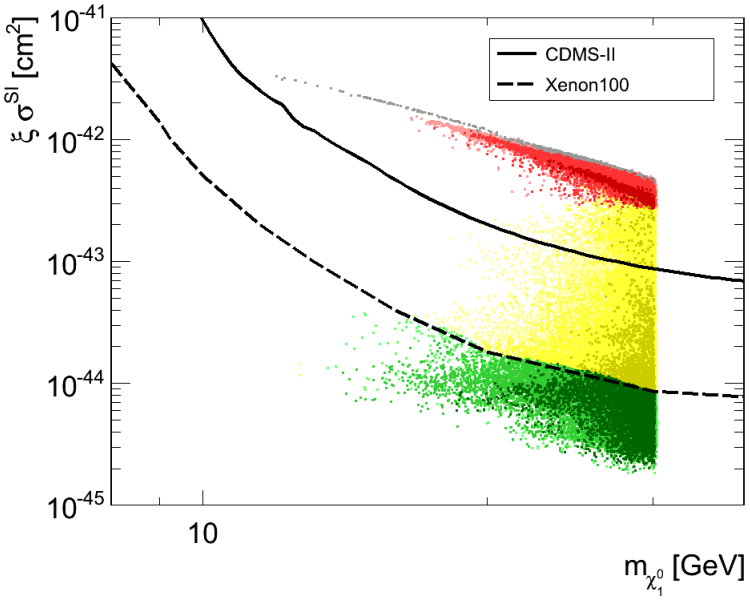

Fig. 9.24: Points from the search for the second new lower bound search on cold neutralino masses in the MSSM represented in the $\xi\sigma^{SI}$ vs. neutralino mass plane. Exclusion limits from CDMS-II and XENON100 are shown. The color code is described in Sec. 8.4.2.

dominant contribution to this branching ratio stems from a triangle loop: the s and $\bar{b}$-quarks exchange a charged W-boson to yield a pair of t-quarks which annihilate into a Z-boson which further decays into two muons. On one hand, the slepton exchanging points tend to be very bino dominated configurations, thus with a μ mass term not so small. On the other hand the Higgs exchanging points correspond to lighter μ, which translates into light charginos, which in turn contribute to the same kind of diagram in replacement of the charged W-boson. Hence, we do expect a larger contribution of the light Higgs configurations because of their larger higgsino fraction.

In conclusion, this region shows less fine-tuning than the lighter neutralino configurations, but have, however, very pronounced light slepton masses. We were able to connect the two separate regions found for neutralino masses below $15\,GeV$ at the light end of the Z-resonance. Constraints in this region are difficult to overcome for most points, in particular, those from XENON100. Nevertheless, there is still a cloud of points –tagged in green– overcoming all constraints, corresponding to heavy pseudoscalar masses, bino fractions above 90% in the neutralino composition and preferred slepton exchanges as the annihilation mechanism. Towards lighter masses, though, the Fermi limits from the observation of the Draco dSph turn to be more stringent for the slepton exchanging points. Indeed, these imply larger Higgs masses and smaller couplings to the Higgs, hence smaller SI cross sections, while the annihilation rate keeps growing towards lighter masses.

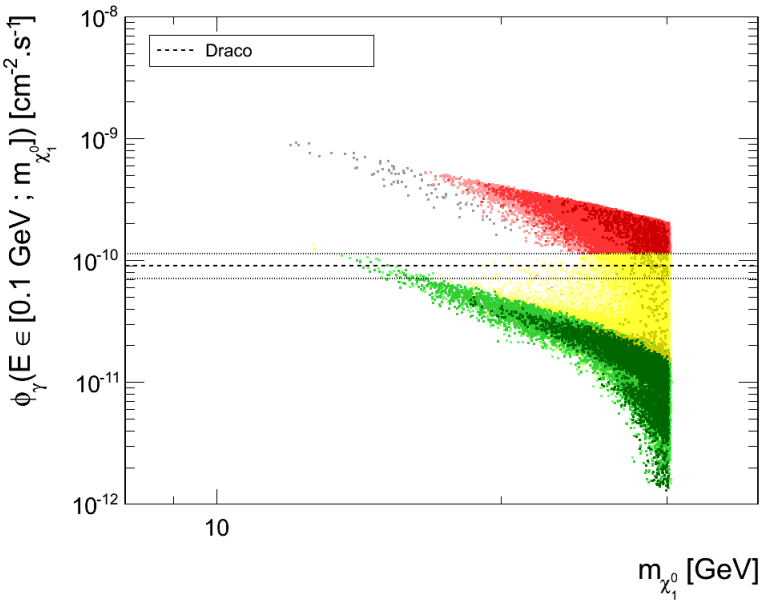

Fig. 9.25: Integrated γ-ray flux from the Draco dwarf spheroidal galaxy as a function of the neutralino mass in the second new lower bound search on cold neutralino masses in the MSSM search. The color code is described in Sec. 8.4.2.

9.1.3 Summary of the light neutralino searches in the MSSM

We have explored the light neutralino configurations in the MSSM with two different choice of parameter sets and parameter boundaries. The first search was published in [1]. We then considered two improvements: we implemented the HigssBounds package in order to allow Higgs bosons below $114.4\,GeV$ which have not yet been ruled out, and we have relaxed crucial parameters such as the slepton masses, now allowed to attain $70\,GeV$ and thus span the stau masses below $100\,GeV$. Thus we aimed to find the regions claimed in, for instance, [61] and [60] respectively. While we do find these regions in the second set of runs we performed with the MCMC code, we came to strong conclusion for the two configurations: the light Higgs configurations have rather bad likelihoods in the $B_u \to \tau\nu_\tau$ and $b \to s\gamma$ branching ratios, most of them are ruled out by CMS, all of them are ruled out by XENON100 and Fermi-LAT, and most of them would be seen in the LHCb search for $B_s \to \mu^+\mu^-$ decays; the light slepton scenarios are allowed down to $m_{\chi_1^0} \simeq 12.6\,GeV$, with lighter neutralinos beeing excluded by Fermi-LAT, and predict SI cross sections of $\sim 10^{-44}\,cm^2$ and no signal for the LHCb searches for $B_s \to \mu^+\mu^-$ decays. In any case, it seems rather very unlikely that the MSSM could yield neutralinos in the CoGeNT and DAMA preferred regions at $m_{\chi_1^0} \simeq 10\,GeV$ and $\sigma^{SI} \simeq 10^{-40}\,cm^2$.

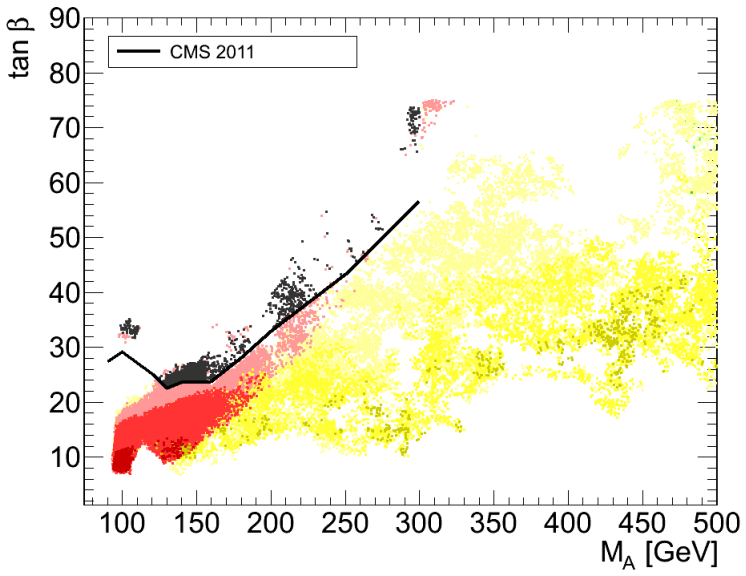

Fig. 9.26: Points from the second search for the new lower bound search on cold neutralino masses in the MSSM represented in the $\tan\beta$ vs. pseudoscalar Higgs boson mass plane. Exclusion limits from CMS are also shown. The color code is described in Sec. 8.4.2.

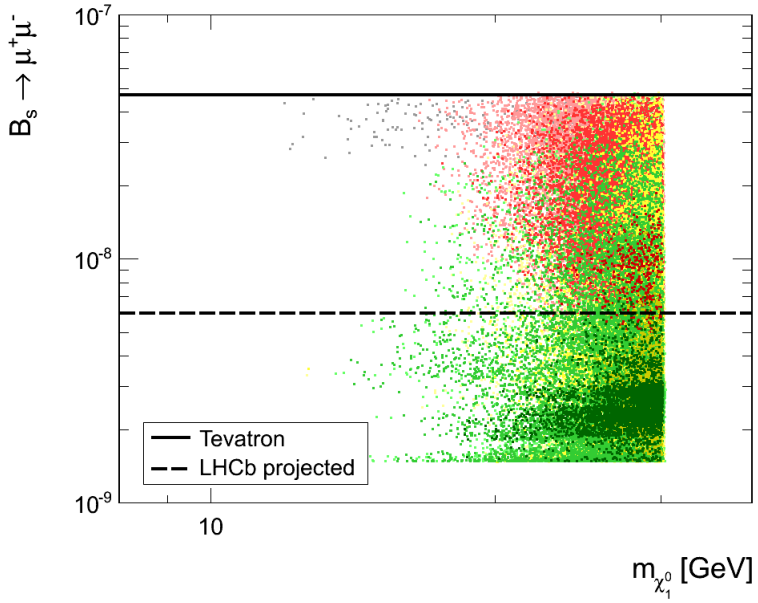

Fig. 9.27: Supersymmetric contribution to the $B_s \to \mu^+\mu^-$ branching ratio as a function of the neutralino mass for neutralinos lighter than $30\,GeV$ in the MSSM. The color code is described in Sec. 8.4.2. We include the current best limit obtained at the Tevatron, and the projected LHCb results for $1\,fb^{-1}$ analysed data.

9.2 Light neutralinos in the Next-to-Minimal Supersymmetric Standard Model

In Sec. 9.1 we looked for light neutralinos in the MSSM and failed to find healthy configuration below $12\,GeV$. The main motivation to extend our studies to the NMSSM was precisely because of the light configurations: the NMSSM is an extension of the Higgs sector [62, 63], which is at the origin of many relevant interactions for the neutralino LSP. The new particle spectrum it generates (see [64]) changes the phenomenology previously obtained in the MSSM [65], there is indeed an extension of possibilities and a large fraction of these escape constraints applying to the MSSM. Particularly, most constraints to the supersymmetric Higgs sector are obtained in the scope of the MSSM, and do not necessarily apply to the NMSSM [66], in which there are three CP-even neutral and two CP-odd neutral Higgs bosons. We aimed to test such modifications in light neutralino searches. Other studies have been carried out at roughly the same time with the same objective [67, 68, 69, 70, 71, 72]. Some were published before, some later. Our first results were presented in [1] and were extended in [41]. Although most results are found here and there, our scan seems to be powerful in the sense that it finds all configurations discussed otherwise individually, and in the most interesting cases it was the first to produce them.
The only differences with the MSSM have to come from the singlet components of the Higgs bosons and singlino component of the neutralino, and all results obtained in the MSSM can be reproduced by the NMSSM. Indeed, neutralinos now have a new component, the singlino. A singlino-like neutralino has been studied as a DM candidate throughout the history of the universe (see for example [73, 74, 75]). Here, of course, we will allow for all possible mixing of its components, as well as the singlet contribution to the Higgs bosons.
Thus, we expand the free-parameter space to the newly introduced λ and κ Yukawa couplings, as well as the A_λ and A_κ trilinear couplings (see Sec. 6.3). The Higgs sector now contains two pseudoscalar neutral Higgses, thus M_A is no longer a free parameter. In spite the fact that μ is, in principle, no longer a free parameter but an effective mass term, we choose to maintain it in replacement of the singlet VEV free parameter. We then follow the same path as in Sec. 9.1, namely, we make use of all the constraints discussed in Sec. 8.3.3 and proceed to scan the NMSSM parameter space using the MCMC. The Tevatron limits no longer apply to the configuration we found, however, we will still impose DD and ID limits to constrain the successful scenarios.

9.2.1 Particulars of the run

In this run we imposed, as it was done in the MSSM, a prior in the LSP mass: $m_{\chi_1^0\,min} = 1\,GeV$ and $m_{\chi_1^0,\,max} = 15\,GeV$. We look for neutralino DM assuming the FO mechanism by impos-

Parameter	Minimum	Maximum	Tolerance
M_1	1	200	3
M_2	100	2000	30
μ	0	1000	10
$\tan\beta$	0.1	65	3
λ	0	.75	0.1
κ	0	0.65	0.8
A_λ	-2000	5000	100
A_κ	-5000	2000	100
A_t	-3000	3000	100
$M_{\tilde{l}}$	100	2000	15
$M_{\tilde{q}}$	300	2000	14

Tab. 9.3: NMSSM free parameter intervals for the first light neutralino searches (GeV units).

ing $\mathcal{L}_{RD}$. As already stated, we included new free parameters: the Yukawa couplings λ and κ, which sign and upper limits have been chosen in light of a previous investigation of the relic density through FO for neutralinos in the NMSSM [4], as well as the trilinear couplings A_λ and A_κ, for which a minimum value and a maximum value have been respectively established in the same study. The rest is scanned the same way as in the MSSM. Small differences may be found, however, they are not really relevant for this run. The boundaries and tolerances of this scan are summarized in Table 9.3. A total number of 266904 configurations were successfully generated, with a best local weight $Q_{max} = 0.642$. With respect to weights, 21.9% of the points belong to the first group, 21.8% belong to the second, and 93.1% of the configurations satisfy $Q \leq 0.003 \times Q_{max}$. This is a good run in general. When analyzing individual weights, the most sensitive likelihood is $\mathcal{L}_{g_\mu}$, with a global mean value of only 0.34 when the global mean total weight is of 0.12. However, for those scenarios lying in the first group of points, those with better weights, their worst likelihood tends to be $\mathcal{L}_{b\to s\gamma}$ with a mean value within this group of 0.78. A likelihood with a rather poor value, however, constant for all runs in the NMSSM is $\mathcal{L}_{\Delta M_s}$ with a value of 0.68. Note that this sets the maximum weight of this run, which would otherwise approach unity, showing the extremely good performance of the run. We notice that $\mathcal{L}_{g_\mu}$ and $\mathcal{L}_{b\to s\gamma}$ are generally low for light neutralinos both in the MSSM and the NMSSM. Here, the contribution of neutralino channels to the $\Gamma_{Z\to invisible}$ is not quantified in terms of a continuous function, but by a test 0 in the NMSSMTools package. We cannot quantify what borderline extensions would have been induced this run if a smooth weight would have been established for this criterion. Thus we expect the configurations to explore other possibilities in the NMSSM.

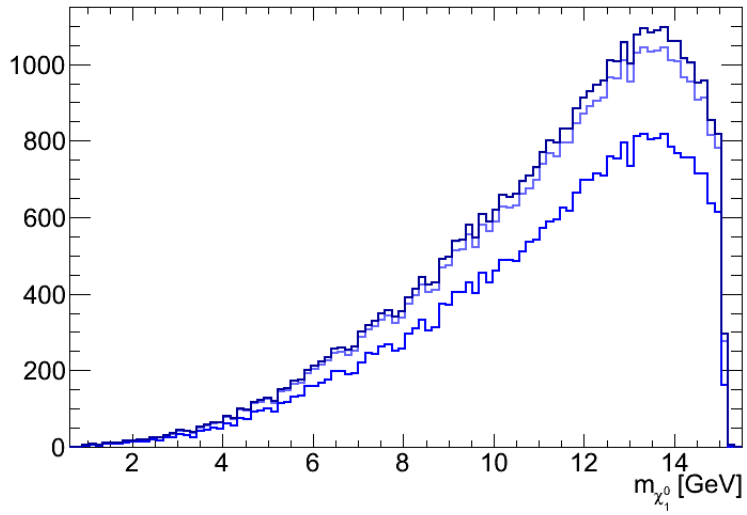

Fig. 9.28: Neutralino mass spectrum in the light neutralino NMSSM search. The color code is described in Sec. 8.4.2.

The neutralino mass range we found is $[0.6, 15.3]\ GeV$. Its frequency is shown in Fig. 9.28. The distribution is concentrated towards the prior upper limit. However, in no way it is comparable to the same phenomenon in the MSSM: here we find many more points towards lower masses, the distribution is much smoother. Furthermore, the curve representing the first group is rather close to that of all points. Recall that this curves are weighted by Q/Q_{max}. This shows that at all masses found there are healthy configurations. Although the density of points is lower towards lighter values, this suggests that a run with a lower upper bound in the prior would find many more healthy points with very light neutralinos. Nevertheless, we can already state that in the NMSSM going towards light neutralinos requires some amount of fine-tuning.

The parameter distributions are presented in Fig. 9.29. First of all, notice that the distribution of M_1, even though peaked at $(15-17)\,GeV$, is extended all the way up to its prior limit at $200\,GeV$. This implies that not all neutralinos are bino-like, and some of them are not at all bino. The wino mass, though, is spread without a strongly preferred region. We do not expect wino neutralinos. The effective μ parameter also spans a larger range of values, and seldom visits smaller values than $\sim 160\,GeV$. Thus we expect that in many cases the higgsino component should vanish. The singlino component is not determined by one particular parameter, but is the results of an interplay of conditions. Indeed, the lower 3×3 part of (6.2) indicates that for a large singlino contribution to the lightest neutralino, both $2\mu\kappa/\lambda$ and λ should be of the order or smaller than the competing M_1 and μ parameters. We see that for intermediate values of λ, but more importantly, for nearly null values of κ, these conditions should be met. Indeed, in Fig. 9.30 we observe that all LSP component distributions are

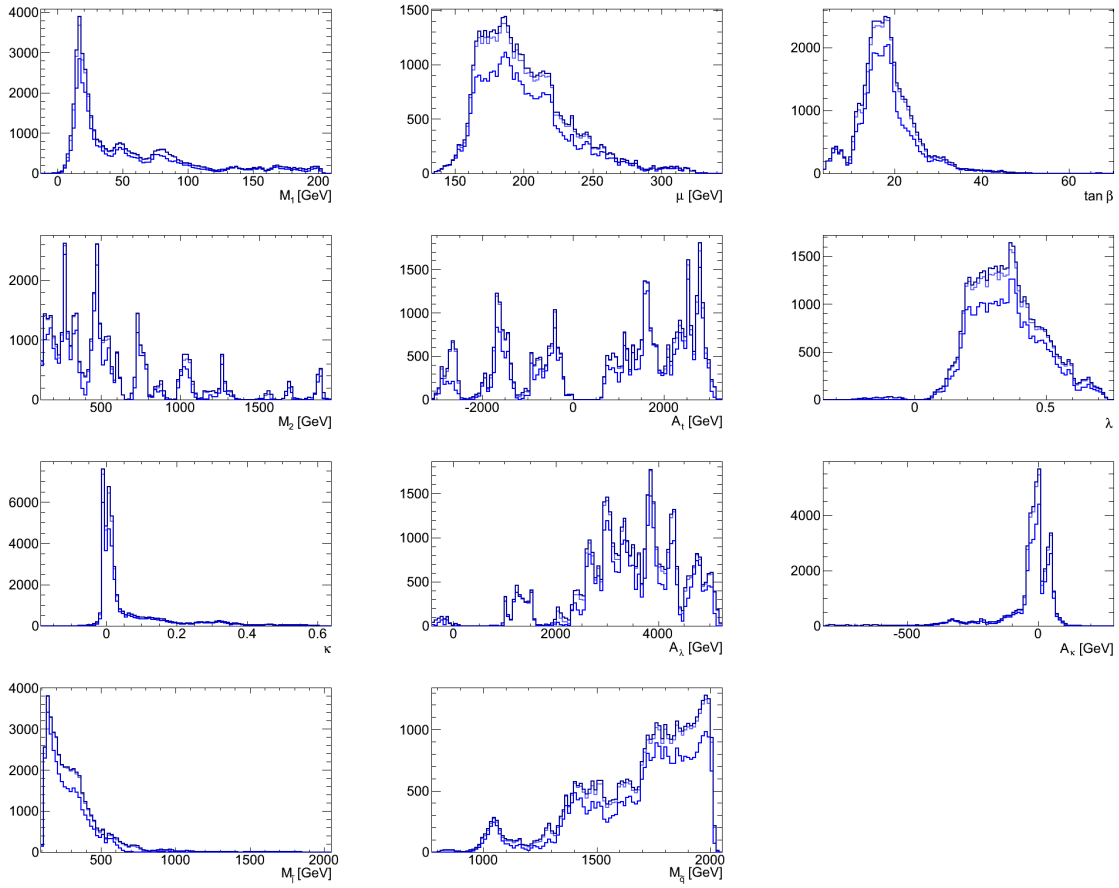

Fig. 9.29: Frequency distributions of free parameters in the light neutralino NMSSM search. The color code is described in Sec. 8.4.2.

peaked at zero. This shows that there is no one an only tendency dominating, but there is a variety of LSP realized. The two components accounting for a strong domination are bino and singlino, whereas wino is always negligible. Higgsinos are very often absent, and never larger than 10% each. Singlino configurations are thus present, which is consistent with the large peak at $\lesssim 0.02$ for the κ distribution and the large spread of values for λ and μ. Even though $\tan\beta$ is not small, it does not reach the large values it reached in the MSSM. Moreover, a vast majority of points have $\tan\beta \leq 20$. However, all kinematic reasons given before not to annihilate via the exchange of an EW gauge boson or sfermion are still valid.

9.2.2 Singlet light Higgses and relic density

We still expect the relic density to be achieved via Higgs exchanges. These have different and more complex couplings to all particles, in the NMSSM. The value of $\tan\beta$ –together with the pseudoscalar mass– is no longer so determinant. The expression of the couplings between neutralinos and Higgs bosons is long and can be dominated by different terms de-

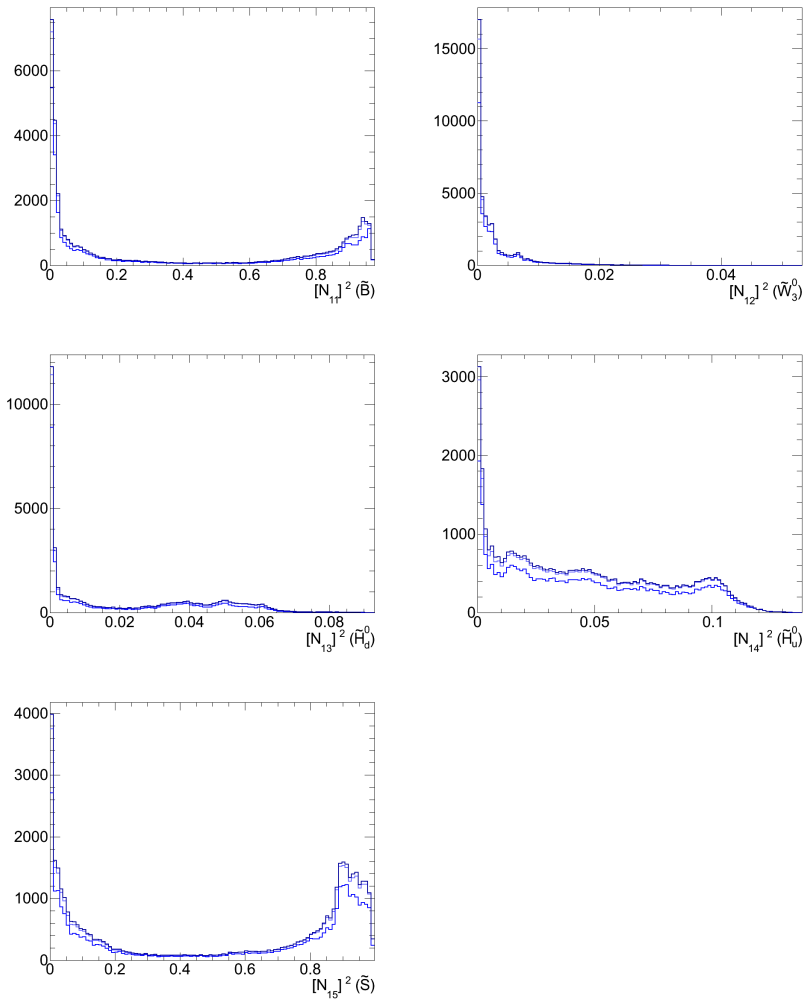

Fig. 9.30: Frequency distributions of the lightest neutralino components in the light neutralino NMSSM search. The color code is described in Sec. 8.4.2.

pending on the neutralino and Higgs compositions (see Appendix A in [63]). However, now the Higgs bosons may be lighter than the SM-like Higgs mass range. Also, it is clear that in order to achieve an acceptable relic density, the neutralino has to reach rather large interaction rates. Therefore, annihilation through light Higgs seems a good competitive manner to achieve the relic density.

Indeed, in order to obtain the correct relic density it is crucial to have an annihilating mechanism such as a resonance. In Fig. 9.31 we observe the lightest Higgs masses as a function of the neutralino mass. This shows that there are indeed very light Higgses down to $\lesssim 1\,GeV$. Hence we expect these Higgs bosons to be either mediators of neutralino annihilations through an s-channel and final states of neutralino annihilations via the exchange of a neutralino in t and u-channels. Moreover, the resonances can be seen in these figures: points

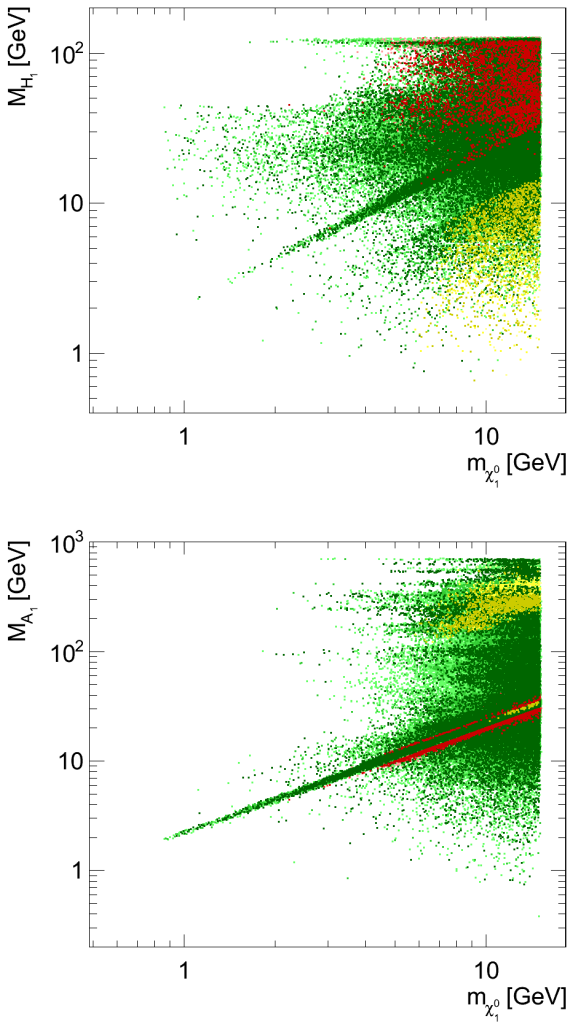

Fig. 9.31: Lightest CP-even (top panel) and CP-odd (bottom panel) neutral Higgs bosons mass as a function neutralino mass in the light neutralino NMSSM search. The color code is described in Sec. 8.4.2.

condensate towards the straight lines satisfying $M_{H_1} = 2m_{\chi_1^0}$ and $M_{A_1} = 2m_{\chi_1^0}$ respectively. Furthermore, we see in Fig. 9.32 that there is always either one or the other below $30\,GeV$, the artificial limit set by the neutralino mass prior. Indeed, the upper right hand side quarter of the M_{A_1} vs. M_{H_1} plane is empty. Colors will be discussed in Sec. 9.2.4.

We can check further that the resonance is always verified. Fig. 9.33 shows the points for which there is no resonance through the lightest pseudoscalar. It represents the frequency of points in the $m_{\chi_1^0} - M_{H_1}/2$ axis. When the difference between M_{A_1} and $2m_{\chi_1^0}$ is larger than $2\,GeV$ (top panel), we see a very large peak at $m_{\chi_1^0} - M_{H_1}/2 \simeq -2\,GeV$. Therefore, when there is not a narrow resonant relation between the lightest pseudoscalar and the LSP, there seems to be one between the latter and the lightest scalar Higgs. However, some points

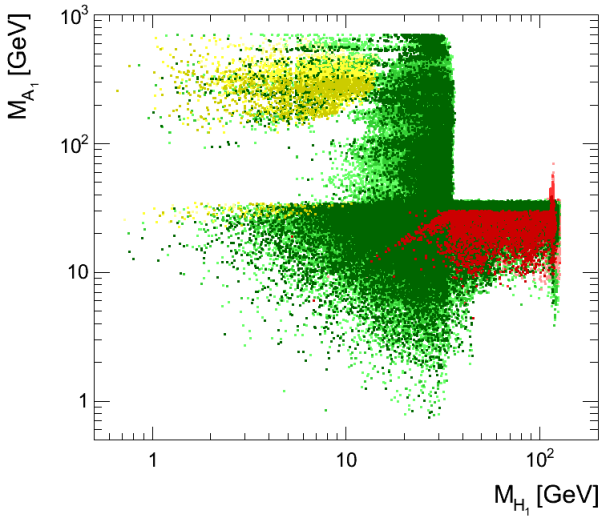

Fig. 9.32: Lightest CP-odd Higgs mass as a function of the lightest CP-even Higgs mass in the light neutralino NMSSM search. The color code is described in Sec. 8.4.2.

do not fall in this peak. When we allow the A_1-resonance to a spread up to $9\,GeV$ (bottom panel), all points on the left side of the peak, i.e., with light Higgses too heavy to mediate a resonance, disappear. These might be included in a larger mass difference resonance, or correspond to very light A_1. The peak is less prominent in the bottom panel, meaning that some points going through a CP-even resonance have a close-to-resonant CP-odd Higgs, or viceversa. Finally, even in the bottom panel we observe that some points have a CP-even Higgs lighter than the resonance level. For these points, and those with A_1 ligther than twice the neutralino mass, the light Higgs bosons turn out to be channels into which the neutralino can annihilate through neutralino exchange. In the case of A_1A_1 final state, through the exchange of a resonant H_1. In case of $\chi_1^0\chi_1^0 \to H_1H_1$ via the exchange of a neutralino, since it is not a resonant process, a light neutralino is needed as well as a sufficiently large $H_1\chi_1^0\chi_1^0$ coupling. This is basically achieved through a large fraction of higgsino-d, higgsino-u and/or singlino fractions in the neutralino composition together with the corresponding down, up and/or singlet component of the lightest CP-even Higgs.

Very light Higgs bosons are thus needed to find light neutralinos. This is why, by the way, we do not find these neutralinos in the MSSM. Moreover, if these Higgs bosons do not exist in the MSSM, they have to be dominated by the singlet component, and thus be mostly decoupled from the SM fermions and gauge bosons. This way, even if kinematically accessible to past experiments, the very light Higgses escape detection and constraints. Fig. 9.34 shows the singlet content of the lightest Higgs bosons. Indeed, for the CP-even Higgs, only when its mass approaches $\sim 100\,GeV$ the singlet component drops from 1. A_1 is always singlet dominated, even if for $M_{A_1} \sim (20-50)\,GeV$ this contribution could be as low as 67%. This

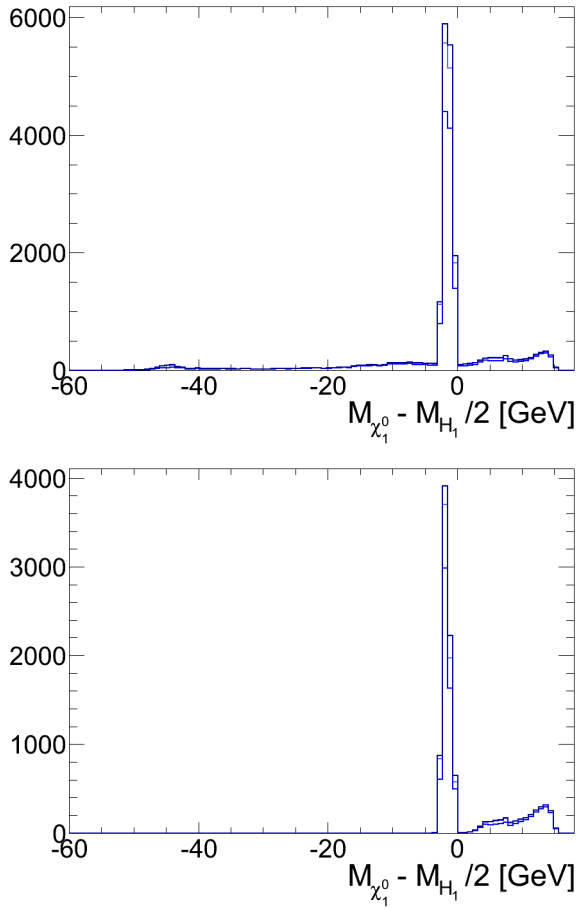

Fig. 9.33: Frequency of points satisfying $\mid m_{\chi_1^0} - M_{A_1}/2 \mid < 2\,GeV$ (top panel) and $\mid m_{\chi_1^0} - M_{A_1}/2 \mid < 9\,GeV$ (bottom panel) represented in the $m_{\chi_1^0} - M_{H_1}/2$ axis. The color code is described in Sec. 8.4.2.

confirms what we expected and explains why these bosons have escaped detection. Furthermore, this makes obvious that the configurations we found are characteristic of the NMSSM. Thus, the neutralinos annihilate via light Higgs bosons. The final states of annihilation in EU are shown in Fig. 9.35. The top four panels contain the available fermionic channels. We observe that when the neutralinos annihilate into fermions, the preferred channel is determined by the neutralino mass. For $m_{\chi_1^0} \leq M_c \simeq 1.29^{+0.05}_{-0.11}\,GeV < M_\tau \simeq (1.77682 \pm 0.16)\,GeV$ [16], the only available channel is the s-quark pair, and potentially lighter quarks and leptons, however these are very subdominant. Above this range and up to the running bottom mass $\simeq 4.16^{+0.18}_{-0.06}\,GeV$ [16] the dominant channel is the $\tau\bar{\tau}$. For the rest, the $b\bar{b}$ channel is dominant, however, very rarely at 100%. Usually an important contribution of $\tau\bar{\tau}$ and/or $c\bar{c}$ complement it. When the Higgs bosons constitute the final state, it is always in pairs of the same kind, namely the A_1H_1 channel does not contribute. Whenever the H_1H_1 channel contributes, it is dominant. It is easily understood: the exchanged particle can only be a neutralino in a t or

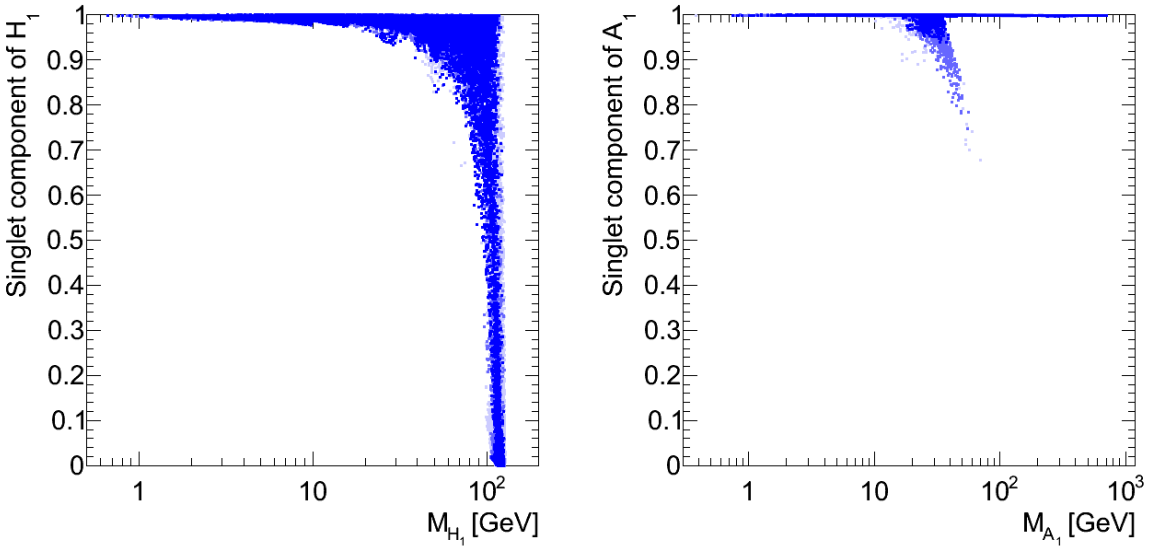

Fig. 9.34: Singlet components of the lightest CP-even Higgs as a function of its mass (left panel) and of the lightest CP-odd Higgs as a function of its mass (right panel) in the light neutralino NMSSM search. The color code is described in Sec. 8.4.2.

u-channel, since the $A_1H_1H_1$ coupling is CP-odd. It is not, thus, a resonant configuration. The only available particles for final state in such a process are Higgs bosons, thus there is no competition from fermions. When the final state is a pair of pseudoscalars, there is also the possibility of a H_1 resonant exchange. If such a channel is opened, then the annihilation may be shared with fermionic final states. If not, then it is dominant, in analogy with the H_1H_1 dominant final state. That is why the A_1A_1 final state spans more possibilities. Colors in Fig. 9.35 will be commented later on.

9.2.3 Annihilation in galaxies: cross sections at low velocities

Let us now address the production of SM particles in neutralino annihilation in our galaxy and other DM containing objects. The neutralinos we found contribute to the CDM component of the energy density of the universe. Neutralinos move around at low velocities in the galactic (or equivalent object) frame: typically $v_G \lesssim 1000\,km\,s^{-1} \sim 3.3\times10^{-3}c$. However, the annihilation rate determining the relic density is fixed at higher energies, namely, for temperatures of $\sim m_{\chi_1^0}/20$. Using the usual relation between temperature and mean particle velocity, $3T/2 \sim mv_{EU}^2/2$ (with T in energy units), we get $v_{EU} \sim \sqrt{3T/m_{\chi_1^0}} \sim \sqrt{3/20} \simeq 0.4c$. Now, it has been discussed in Sec. 2.2 that the annihilation rate could be strongly dependent on the relative velocity of the DM. If no particular mechanism is used, a simple expansion about the relative velocity can be made, thus $\langle\sigma v\rangle \sim a + bv^2$ where a and b are constants. If in EU the dominant term is the p-wave, i.e., $\langle\sigma v\rangle \sim bv^2$, then when $v \to 0$,

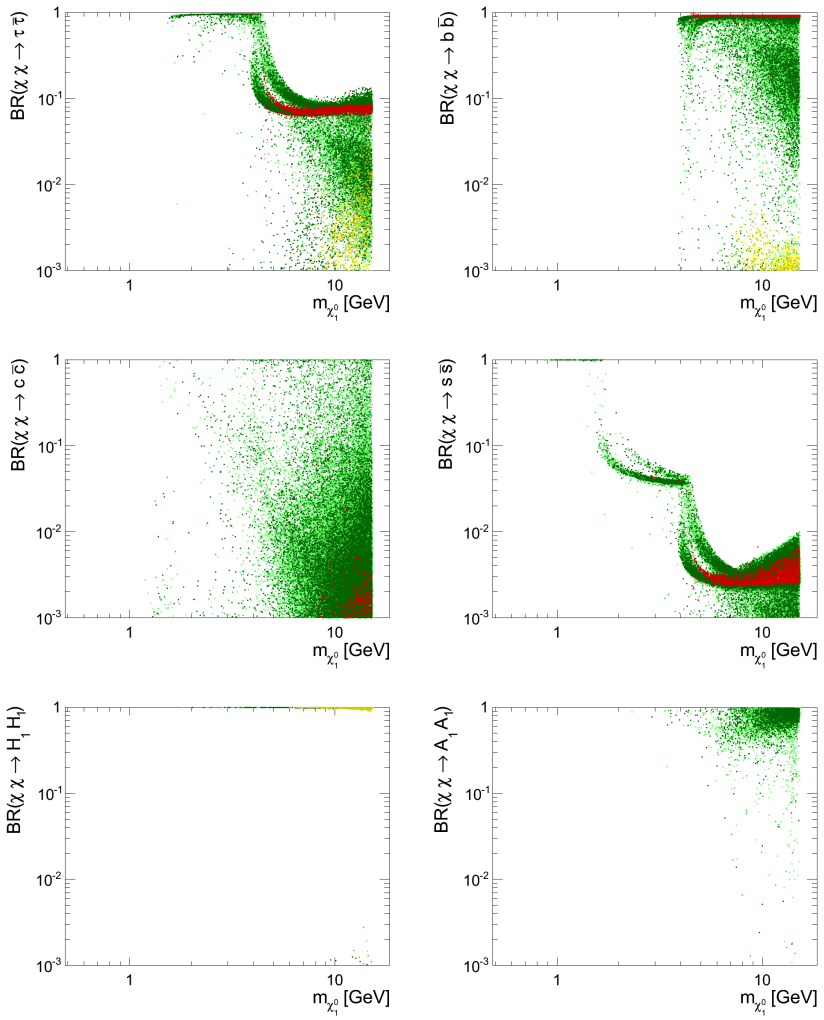

Fig. 9.35: Neutralino annihilation channels in the EU as a function of the neutralino mass in the light neutralino NMSSM search. The color code is described in Sec. 8.4.2.

$\langle\sigma v\rangle \to a \ll bv_{EU}^2 \sim bv_G^2 \times 10^4$. This is exactly the case of H_1 exchanges: p-wave cross section tends to zero at null velocity because of chirality suppresion, due to the Majorana nature of the neutralino. Here, other channels such as sfermion exchanges become dominant, however at lower rates. Thus, some processes with large enough cross sections in EU will be subdominant in galactic frames, and the total cross section itself will be much smaller than in EU. Furthermore, for resonant diagrams not suffering from this suppression at low energies, the cross section could suffer the inverse fate. It no longer could be expanded as a quadratic function of the velocity [76]. Similarly to what was explained for the case of the Z-boson

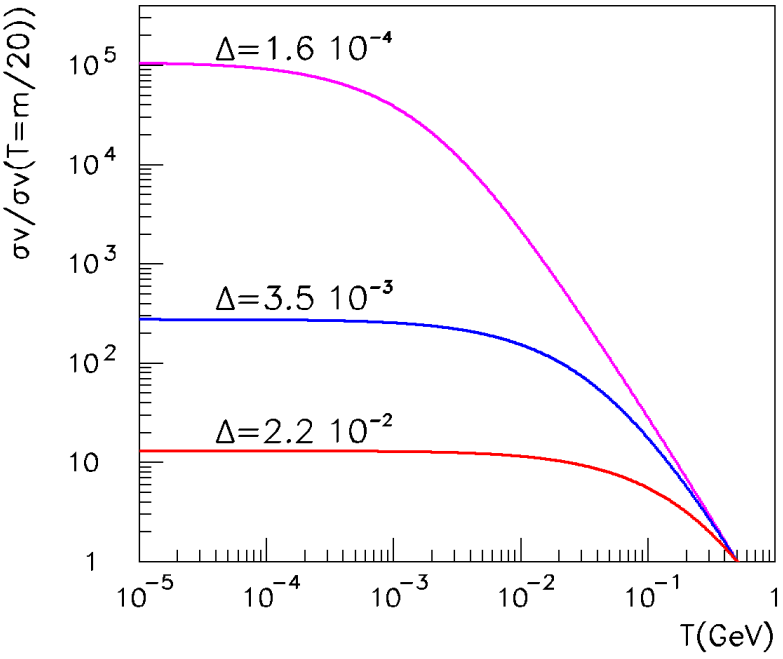

Fig. 9.36: Ratio of neutralino annihilation rates at a given temperature T to the EU typical approximation $T = m_{\chi_1^0}/20$ for resonant A_1 exchange processes for $m_{\chi_1^0} = 10.10\,GeV$ and $\Gamma_{A_1} = 1.1 \times 10^{-4}\,GeV$ as a function of temperature. Various values of the $\Delta = 1 - m_{A_1}^2/4m_{\chi_1^0}^2$ parameter are drawn.

resonance in 9.1.1, in A_1-resonant processes we have

$$\sigma v \propto \frac{1}{(s-M_{A_1}^2)^2+\Gamma_{A_1}^2 M_{A_1}^2} = \frac{1}{16m_{\chi_1^0}^4}\,\frac{1}{(\frac{v^2}{4}+\Delta)^2+\frac{\Gamma_{A_1}^2}{4m_{\chi_1^0}^2}(1-\Delta)} = \frac{1}{16m_{\chi_1^0}^4}\times\Pi, \tag{9.1}$$

where $\Delta = 1 - m_{A_1}^2/4m_{\chi_1^0}^2$. We see that if the resonance is very narrow, i.e. $\Delta \simeq 1$, and the A_1 width is small, i.e. $\Gamma_{A_1}/m_{\chi_1^0} \ll 1$, then the cross section attains its maximum value for $v \to 0$. We further checked this behavior by taking a particular point as an example, for which $m_{\chi_1^0} \simeq 10.10\,GeV$ and $M_{A_1} \simeq 20.12\,GeV$, thus $\Delta \simeq 7.9 \times 10^{-3}$, whereas $\Gamma_{A_1} \simeq 1.1 \times 10^{-4}\,GeV$. In such a case, by replacing these values in (9.1) we come to the approximated expression $\Pi \simeq ((v^2/4 + 7.9\times10^{-3}) + 2.9\times10^{-11})^{-1}$. Thus, slowing down from $v \simeq 0.4\,c$ to $v \simeq 3.3\times10^{-4}c$ implies increasing the interaction rate by

$$\frac{\sigma v_G}{\sigma v_{EU}} \simeq \frac{\Pi_G}{\Pi_{EU}} \simeq 36.7.$$

Therefore for this point we get a boost of more than an order of magnitude from EU to the galactic frames. Now if we freeze the value of Γ_{A_1} and $m_{\chi_1^0}$, allowing only the variation of

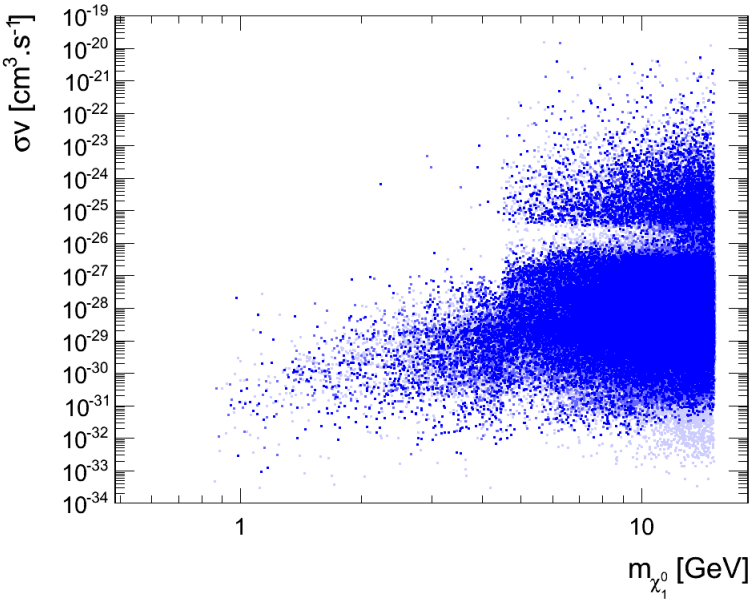

Fig. 9.37: Neutralino annihilation rates at $v = 10^{-4}c$ as a function of the neutralino mass. Various values of the $\Delta = 1 - m_{A_1}^2/4m_{\chi_1^0}^2$ parameter are drawn. The color code is described in Sec. 8.4.2.

M_{A_1}, thus of Δ, and furthermore express the ratio of the cross sections at a given temperature T to the cross section at $T = m_{\chi_1^0}/20$, then we get

$$\frac{\sigma v|_T}{\sigma v|_{T=m_{\chi_1^0}/20}} \simeq \frac{\left(\frac{3}{80}+\Delta\right)^2 + 3\times 10^{-11}\,(1+\Delta)}{\left(\frac{3T}{4m_{\chi_1^0}}+\Delta\right)^2 + 3\times 10^{-11}\,(1+\Delta)}. \tag{9.2}$$

This expression only depends on the choice of the temperature T and of the narrowness of the resonance Δ. In Fig. 9.36 we show the behavior of the boost represented by (9.2) as a function of the temperature for various resonance tunings. Notice that boosted processes are not expected to change their favored final states between EU and galactic interactions. We conclude that there are major differences between the neutralino annihilation rates in EU to that of the galaxies in some cases. Indeed, Fig. 9.37 shows a span of 14 orders of magnitude in $\sigma v|_{v=10^{-4}c}$, whereas at EU the cross sections oscillates around $3\times 10^{-26} cm^3\, s^{-1}$, the canonical value, without much spread. This can be also observed by comparing the EU annihilation channels (see Fig. 9.35) to those at low velocities represented in Fig. 9.38. Higgs channels are not represented simply because they do not contribute for low velocity annihilations. As it was explained, the chiral suppression eliminates the production of Higgs pairs. All points that were annihilating into Higgses in EU are now found in the fermionic channels. For some kinematical configurations the $s\bar{s}$ channel is dominant, however, in most cases $\tau\bar{\tau}$ and $c\bar{c}$ are the preferred final states. In particular, we see that now there are points

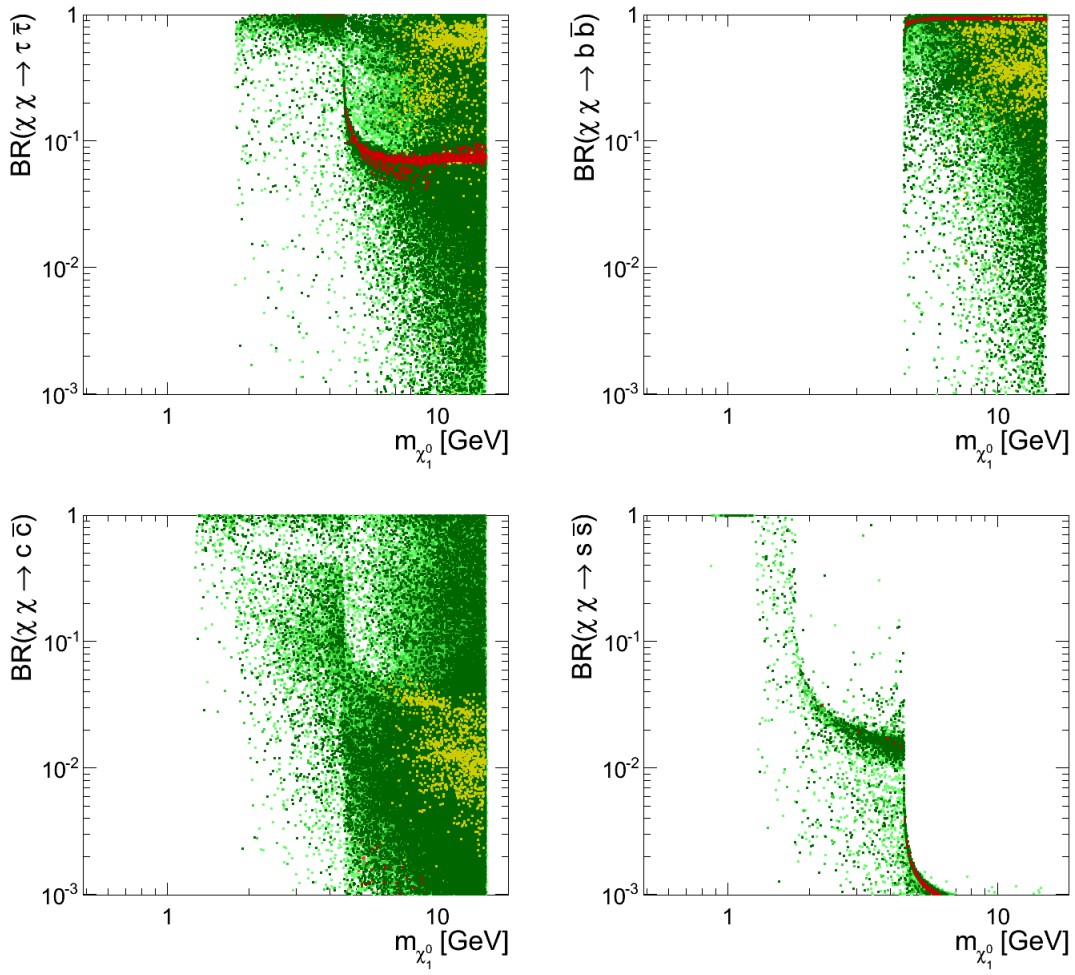

Fig. 9.38: Neutralino annihilation channels at low relative velocities as a function of the neutralino mass in the light neutralino NMSSM search. The color code is described in Sec. 8.4.2.

for which the dominant channel is $\tau\bar{\tau}$ at neutralino masses above M_b. That implies that the process occurs via the exchange of a $\tilde{\tau}$ rather than a Higgs exchange. Furthermore, leptonic final states are favored compared to hadronic final states because of the exchanged sfermion mass (see Fig. 9.29).
Fig. 9.39 summarizes the situation of EU light Higgs bosons resonant exchanges and their corresponding behavior at low energies, while Fig. 9.40 shows the same but for non-resonant EU neutralino exchanges.

9.2.4 Indirect detection contraints from γ-rays

We now proceed to constrain the parameter space using dSphs. Indeed, we computed the γ-ray flux coming from these DM dominated objects as it was described in Sec. 4.3.3. It was discussed that the most stringent constraints in the Fermi-LAT study come from the

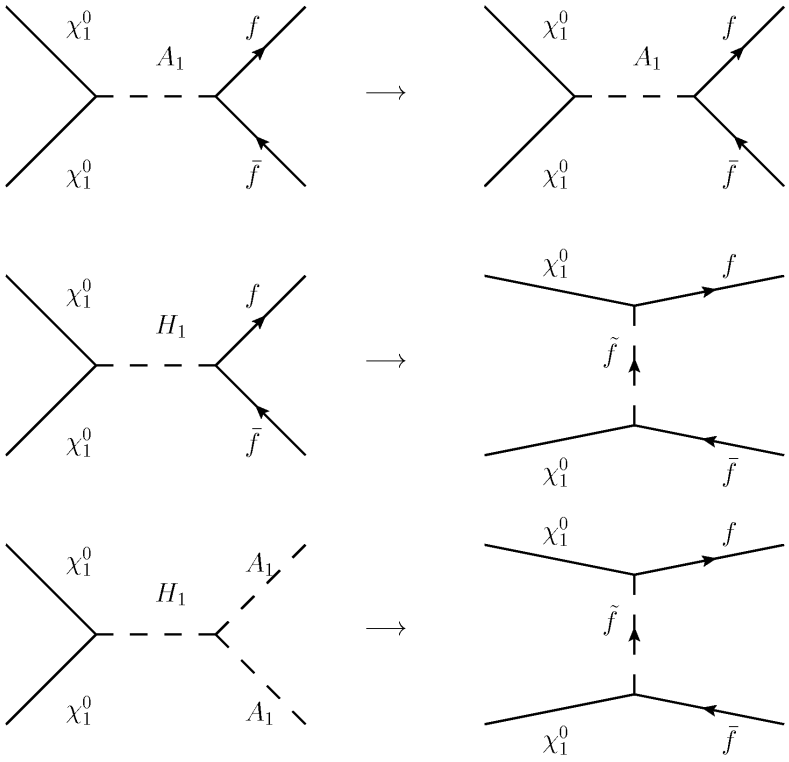

Fig. 9.39: Neutralino annihilation diagrams for dominant resonant exchange of light Higgs bosons at early universe (left) and their corresponding annihilation diagrams at low energy (right). While the resonant A_1 exchanges get a boost for low neutralino relative velocities, resonant H_1 exchanges are suppressed and are subdominant with respect to the sfermion exchanges at low energies.

analysis of the Draco galaxy. However, if for any reason this particular galaxy was to be misinterpreted, we show in Fig. 9.41 the γ-ray fluxes along with the limits for all eight galaxies chosen in [24] for establishing limits. The shape of the cloud of points found for in the γ-ray flux vs. neutralino mass is very similar to that of the annihilation cross section vs. neutralino mass. A slight difference can be found, and it is explained by the inclusion of ξ^2 in the computation of the flux. Also, there is a difference in the behaviors of fluxes from a same dSphs between the $\left[100\,MeV,\, m_{\chi_1^0}\right]$ and $\left[1\,GeV,\, m_{\chi_1^0}\right]$ integrated energies. Indeed, the maximum yield in the γ-ray spectrum produced by neutralino annihilation lies typically around a factor 10 below its mass. Neutralinos with masses around the *GeV* do not contribute too much to the $\left[1\,GeV,\, m_{\chi_1^0}\right]$ interval, whereas they can still deposit their γ-rays in the $\left[100\,MeV,\, m_{\chi_1^0}\right]$ interval. The most conservative Draco limits (taken from the first panel, second row in Fig. 9.41, see Sec. 8.4.2) translate into an upper bound for $\left(\xi/m_{\chi_1^0}\right)^2 \times \sigma v$: we found the condition $\left(\xi/m_{\chi_1^0}\right)^2 \times \sigma v \leq (2-5)\ 10^{-29}\, cm^3 s^{-1} GeV^{-2}$, depending on the neutralino mass, as can be seen in Fig. 9.42. Points excluded by the overprediction of γ-rays

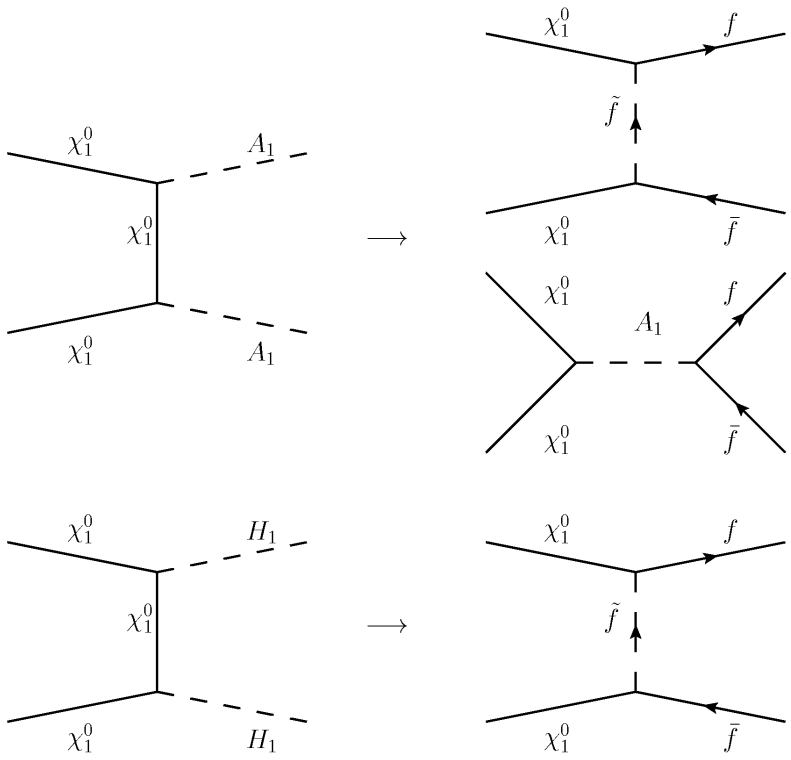

Fig. 9.40: Neutralino annihilation diagrams for dominant neutralino exchanges and light Higgs bosonic final states at early universe (left) and their corresponding annihilation diagrams at low energy (right). While the non-resonant A_1 exchanges are not suppressed at neutralino relative velocities and thus compete with sfermion exchanges, non-resonant H_1 exchanges are suppressed and are subdominant with respect to the sfermion exchanges at low energies.

from the Draco dwarf spheroidal galaxy are tagged in red in this figure and all others in this section. Thus, these points can be seen in Fig. 9.38, that is to say, in the annihilation channel repartition. Indeed, the points excluded by Draco annihilate into the most conventional channels: a mix of $b\bar{b}$ and $\tau\bar{\tau}$ for masses larger than the bottom-quark mass, and $\tau\bar{\tau}$ below. Points excluded share their dominant channels in EU and in galaxies, as it can be seen in Fig. 9.35, which is consistent with our arguments about A_1-resonances and boosts. The same conclusion can be drawn from Fig. 9.31: in the bottom panel, all the points excluded by γ-rays lie in the resonance line. The fact that they do not fall in the middle of it is easily understood: those points are excluded by the relic density since they would annihilate too much in EU and yield a too small density at present. The center of the resonance is actually set by $E^{EU}_{\chi_1^0} = m_1^0 + K = M_{A_1}/2$, where K stands for the neutralino kinetic energy, which in turn is set by the temperature at FO. If this relation is too fine-tuned the relic density would be too small, unless they have small enough couplings. Then, if it is still plausible regarding relic density to be sitting in the very center of the EU resonance, then at lower velocities, the

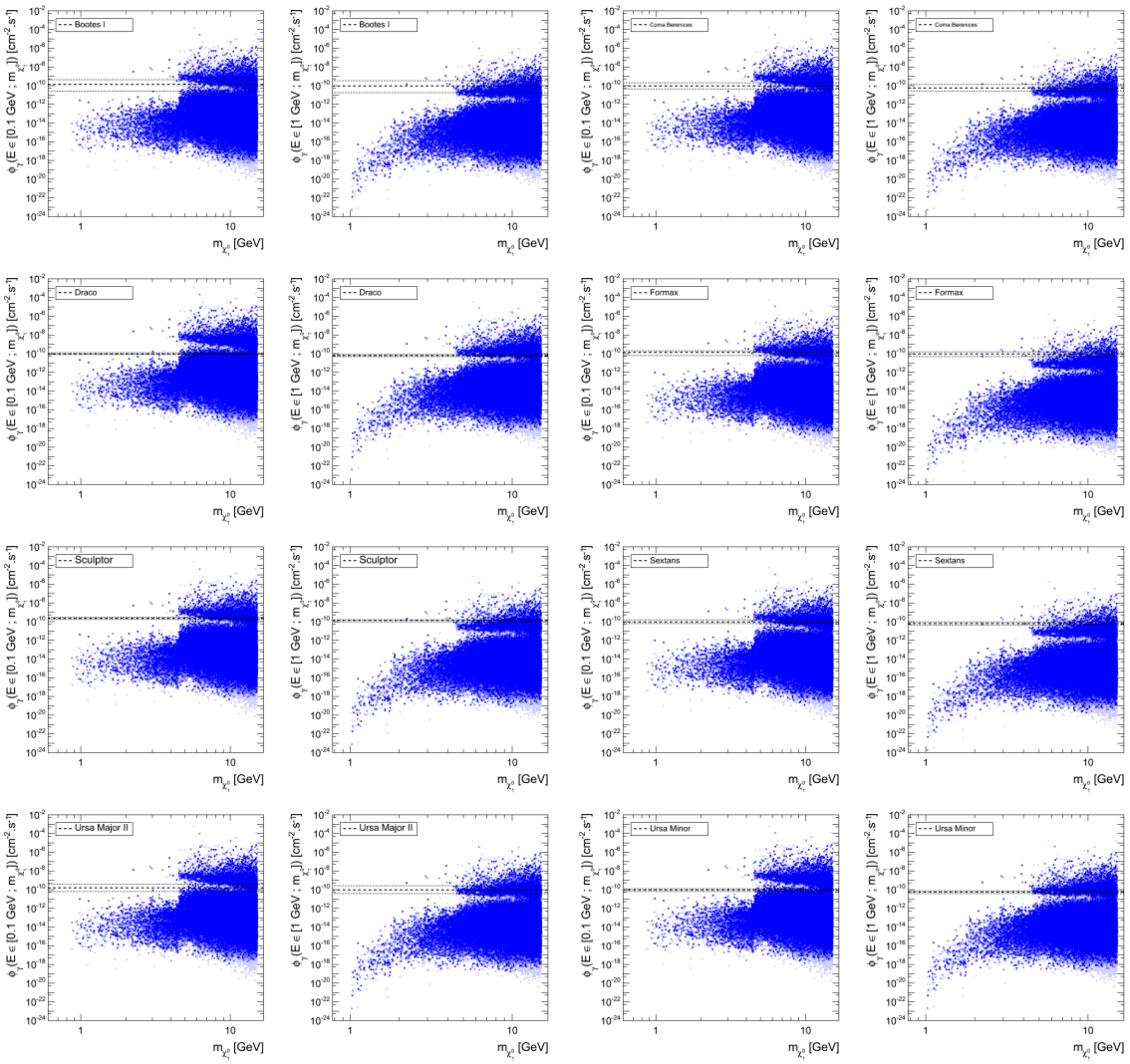

Fig. 9.41: Predicted γ-ray fluxes from the eight dSphs analyzed in [24] for which upper limits are drawn in the light neutralino NMSSM search. The color code is described in Sec. 8.4.2.

bulk of the resonance is not integrated over and thus the cross section is lower. If M_{A_1} is even a bit larger but still close enough to $E^{EU}_{\chi^0_1}$ then the resonance is only integrated in its lower tail at both EU and lower velocities, thus the cross section is less dependent upon the resonance. Large couplings can complete the picture to yield large enough cross sections at EU, but now with a similar cross section at low velocities, which is then enough to overproduce γ-rays again. On the contrary, if M_{A_1} is slightly smaller than the EU resonance, then at low velocities the full resonance is integrated in the cross section, thus getting a large boost and being therefore ruled out by Fermi-LAT. That is why we observe two different red lines in Fig. 9.31. Also in agreement is Fig. 9.32, in which the red dots are always corresponding to $M_{A_1} \leq 30\,GeV$.

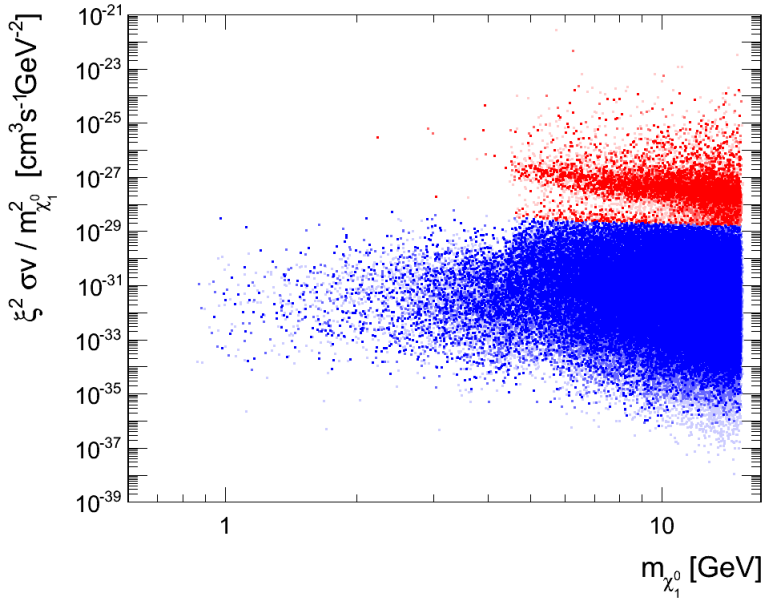

Fig. 9.42: $\left(\xi/m_{\chi^0_1}\right)^2 \times \sigma v$ as a function of the neutralino mass in the light neutralino NMSSM search. The color code is described in Sec. 8.4.2. Here, red dots correspond to points excluded by Fermi-LAT.

9.2.5 *Further indirect detection checks with benchmark points*

Once limits were established using γ-rays and the Fermi-LAT constraints, we aimed to further study the remaining points. However, as it has already been discussed, computing the fluxes of antiparticles and other photonic signals is less straightforward and should be done point by point. Thus we defined benchmark points which helped to give an idea of the other ID yields.

Choice of benchmark points

The dSphs limits was translated in terms of an upper bound for $\left(\xi/m_{\chi^0_1}\right)^2 \times \sigma v$. Thus we chose the benchmark points such as

$$\left(\xi/m_{\chi^0_1}\right)^2 \times \sigma v \lesssim (2-5)\ 10^{-29}\, cm^3 s^{-1} GeV^{-2},$$

but as close as possible to the limit. Also, they were asked to lie in the first group of weights, that is to say with $Q \leq 0.32 \times Q_{max}$. Graphically speaking, we looked for dark blue points right below the red cloud in Fig. 9.42. Furthermore, since the final states of neutralino annihilations at low velocities are set by the kinematic configuration of the interaction, namely, by the neutralino mass and those of the SM fermions, we looked for roughly one point per $1\,GeV$ bin from $15\,GeV$ down to $1\,GeV$. A summary of the fourteen benchmark points thus defined is given in Table 9.4.

$m_{\chi_1^0}$ [GeV]	ξ	$\sigma v\|_{v=10^{-4}c} \times 10^{27}$ [$cm^3 s^{-1}$]	$\tau\bar{\tau}$	$b\bar{b}$	$s\bar{s}$	R(radio)
0.976	0.373	0.209	0	0	0.997	0
2.409	1	0.297	0.964	0	0.026	0.040
3.342	0.935	0.345	0.972	0	0.018	0.044
4.885	0.465	3.298	0.0970	0.901	0.0016	0.041
5.626	0.376	5.389	0.0698	0.929	0.0011	0.040
6.551	0.528	3.547	0.0618	0.937	0	0.046
7.101	0.689	2.425	0.0586	0.940	0	0.050
8.513	0.829	2.161	0.0416	0.958	0	0.055
9.274	0.827	2.497	0.0533	0.946	0	0.060
10.27	0.906	2.323	0.0634	0.935	0	0.063
11.50	0.960	2.575	0.0611	0.937	0	0.074
12.74	0.955	3.224	0.102	0.897	0	0.088
13.51	0.558	9.571	0.0781	0.921	0	0.085
14.48	0.147	148.4	0.0748	0.924	0	0.088

Tab. 9.4: Benchmark points used to compute positron, antiproton and radio signals. Their main characteristics are displayed: neutralino mass, fraction of neutralino in the DM density distribution function, annihilation rate at low velocities, branching ratios of its $\tau\bar{\tau}$, $b\bar{b}$ and $s\bar{s}$ final states and the radio signal to background ratio from the galactic center of the Milky Way.

Antimatter signals: antiprotons and positrons

The positron and antiproton yields from the galactic center of the Milky Way for these 14 points is shown in Fig. 9.43, along with parametrizations for the backgrounds, from [78] and [79] respectively. In the case of antiprotons, the computation was done for two sets of diffusion parameters in agreement with the astrophysical data: the MED and MAX sets, as given in Table I in [77]. The MAX set defines the upper limit for these parameters regarding astrophysical uncertainties and yield the largest antiproton fluxes, whereas the MED set gives a more realistic treatment of the antiproton diffusion around the galaxy. Regarding the background, it represents a good fit to the data by itself, however, its estimation carries a theoretical error of around 10%. Therefore, the MED estimation for the benchmark points being always at least 1 order of magnitude below the background, and the MAX estimation only flirting with the background below $1\,GeV$, we cannot use the antiproton flux to rule out more points. Regarding positron fluxes, the MED set was used, which is the same as in [77] (see [80] for more details). The prediction is always 2 orders of magnitude below the background. This was to be expected, since even the τ dominated annihilation channels yield a large fraction of light mesons instead of muons, electrons and positrons. Anyhow, the

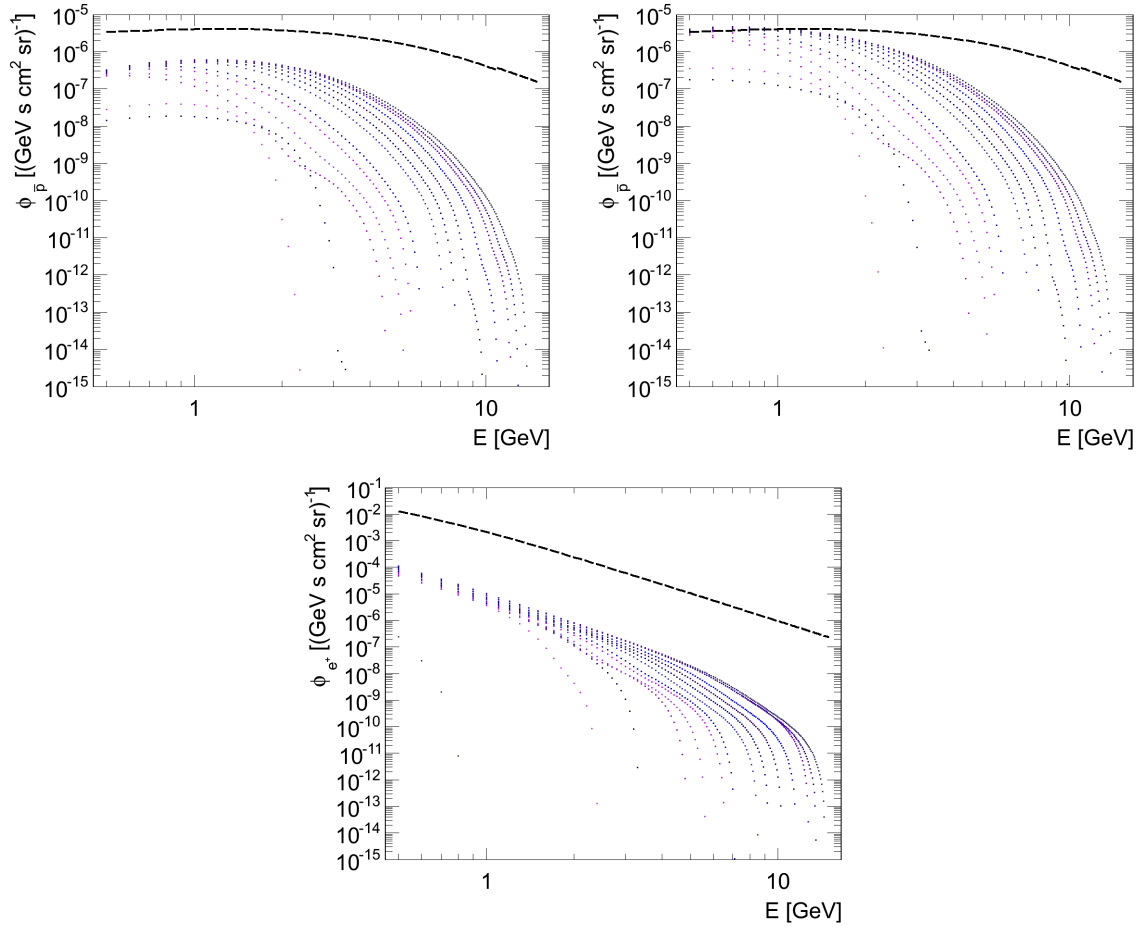

Fig. 9.43: Top: antiproton flux expected at Earth for the 14 benchmark points given in Table 9.4 for two different set of parameters. Left panel: MED. Right panel: MAX (see Table I in [77]). The dashed line represents the background parametrization as given in [78]. Bottom: positron flux expected at Earth for the 14 benchmark points given in Table 9.4. The dashed line represents the background parametrization as given in [79].

$\tau\bar{\tau}$ dominated channels are those contributing the most to the positron flux.

Radio flux from the galactic center and the Coma cluster

Finally, we checked the radio flux observed at earth. These signals depend on the production of electrons which is associated with the total annihilation rate at low velocities, together with the propagation conditions through the magnetized ISM, and particularly on the strength of the magnetic field B. These estimations were done for the benchmark points presented in Table 9.4. The dependence of such signals on the magnetic field is not obvious, since its value plays a role both in the generation of radio waves as well as in the propagation energy losses and in the diffusion in general (see Figure 3 in [82] and Sec. 4.3.3). The interplay

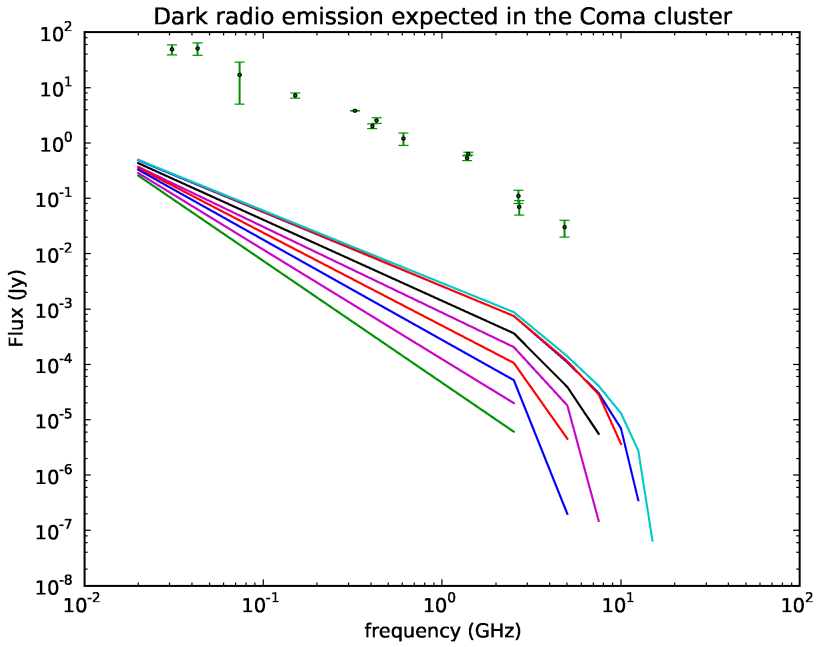

Fig. 9.44: Radio flux from the Coma cluster for the benchmark points from the lightest (left) to the heaviest (right) candidates. The dataset are taken from the references in [81].

in theoretical errors stemming from the diffusion parameters (namely the half-thickness of the diffusion zone, a normalization of the flux and a spectral index of the space diffusion coefficient, see [80] for a complete study on the matter), energy losses, magnetic field, DM density and velocity distributions are beyond the scope of our study. However, it is important to check whether the radio flux is overestimated for safe points.

Let us first focus in the potential signals from the GC of the MW. The method is that described in [83, 82]. In particular, the DM distribution is assumed to correspond to a NFW profile. We use the MED set of parameters for propagation as described in [80], and a value of $B = 20\mu G$ for the magnetic field. While it has been commonly assumed that the magnetic field should be fifty times larger, thorough studies have shown that a value of $\simeq 10\mu G$ is preferred [84]. Using the monochromatic approximation, i.e. associating the electron energy to the frequency of maximum emission, the radio flux at $\nu = 330 MHz$ was estimated for the benchmark points. It was compared to the measurements which set the observed flux to $360 Jy$ for a $7'$ angular resolution. Thus, the ratio R of radio flux predicted to the observed flux for each benchmark point is presented in the last column of Table 9.4. It is important to notice that none of the benchmark points predicts a larger flux than observed. What is more, the ratios are vry small. This suggests that even the points predicting the largest fluxes are at least an order of magnitude below the oberved flux. Hence, not more than 10% of the observed flux could be due to DM annihilations at the MW's center. Here, no strong

conclusions can be drawn, since the radio flux is used to constrain the magnetic field and to estimate the galactic center production of accelerated leptons. Thus there is no trustworthy estimation of the astrophysical background. Nevertheless, the contribution of these scenarios is not dominant, and if some development is achieved in the knowledge of the conventional sources, then only very loose limits could be drawn. Therefore, we can claim that radio fluxes from the galactic center are not in conflict with the scenarios we have presented.
Galaxy clusters are also magnetized media containing DM. Thus, radio photons are also expected, since neutralino annihilations would produce electron and positron that would propagate in such a medium. Previous studies have focused in the Coma cluster for which observations are available (see [81] and references therein). We started by testing the procedure described in [83, 82] with the results shown in [85], two independent studies. For a MSSM configuration with neutralino LSP at $40\,GeV$ annihilating into $b\bar{b}$ pairs with a cross section of $\sigma v = 4.7 \times 10^{-25}\,cm^3\,s^{-1}$, propagated for a magnetic field of $1.2\mu G$, we validated that the results were compatible. Thus used the same analysis that in [83, 82] to predict the radio flux from the Coma cluster for the benchmark points given in Table 9.4. In order to do so we assume a NFW profile with $r_0 = 4.4\,10^2 GeV\,cm^{-3}$, $r_s = 400\,kpc$, a detector angular resolution of 1°, a magnetic field of $4.7\,\mu G$ and a density of electrons of $3\,10^{-3} cm^{-3}$. The electron spectrum stemming from neutralino annihilations was computed for an annihilation cross section at $v = 0.01 \times c$, since the mean DM velocity is expected to be larger in such a system. We display the results in Fig. 9.44. The predicted fluxes lie at least two orders of magnitude below the observations. It would be difficult to make our configurations yield a large enough signal to account for the measured flux, or conversely, to further constrain our scenarios using these limits. However, it may be possible that points ruled out by Draco, with particularly large annihilation rates, may overproduce the radio flux from Coma as well. Regarding the astrophysical uncertainties, increasing the value of the magnetic field up to $12\,\mu G$ increases the radio flux at $4.58\,GHz$ by a factor ~ 4.5 for the last, heaviest benchmark point. It is still not enough to come close to the experimental points.
In conclusion, radio fluxes do not constrain the light neutralino parameter space in the NMSSM. Nonetheless, the flux from the GC could be sizeable, and thus suggests that it is important to further understand the real value of the magnetic field and the DM distribution towards that region. Indeed, if any other signal for light neutralinos is found, then this particular observable might turn out to be a good way to probe their presence in the galactic center of the MW.

9.2.6 Direct detection

Let us now focus on DD signals. Neutralinos can scatter on nucleons elastically by interacting with quarks through the exchange of a Z-boson, of a squark or of a Higgs boson. The former two yield SD processes while the latter two intervene in SI processes.

Spin independent interactions

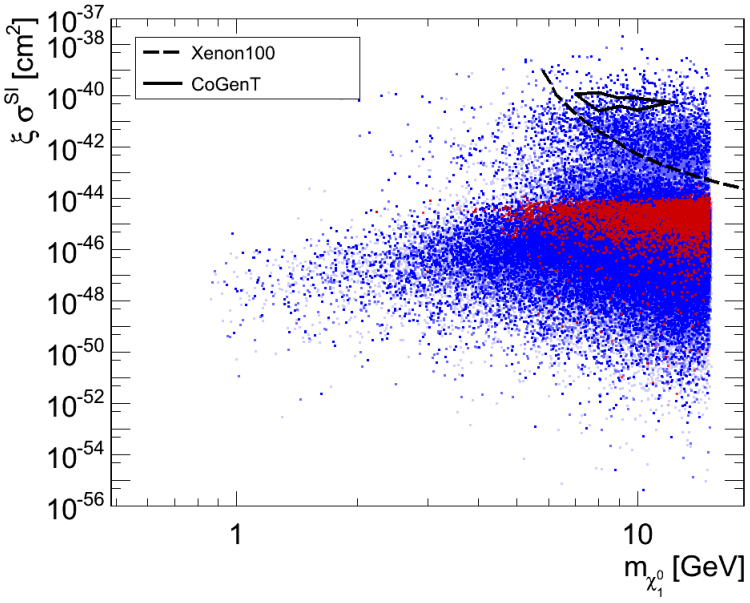

Fig. 9.45: Spin independent neutralino-nucleon interaction rates, normalized to the neutralino contribution to the local DM density, as a function of the neutralino mass. The color code is described in Sec. 8.4.2. Here, the red points are excluded by Fermi-LAT. Limits from CDMS-II and XENON100 are shown, as well as the preferred contour given by the CoGeNT experiment.

Let us start by addressing the SI interactions. These occur via a t-channel exchange of Higgs bosons or squarks. The former are much more favored. In Fig. 9.45 we show $\xi\sigma^{SI}$ vs. $m_{\chi_1^0}$. Points excluded by Draco are tagged in red. We see that the cross sections $\leq 10^{-41}\,cm^2$ are obtained for $m_{\chi_1^0} \gtrsim 5\,GeV$. Fig. 9.46 shows σ^{SI} vs. M_{H_1}. We observe that cross sections $\leq 10^{-41}\,cm^2$ correspond to $M_{H_1} \lesssim 5\,GeV$. This means that for these points, $M_{H_1} \lesssim m_{\chi_1^0}$. Furthermore, the correlation between SI interactions and the H_1 mass is striking. It is easily explained: the SI interactions occurs via a t-channel exchange of a Higgs, here H_1. The interaction cross section, which is proportional to the propagator, goes as

$$\sigma^{SI}_{\chi_1^0 q\to\chi_1^0 q} \propto \frac{1}{\left(t - M_{H_1}^2\right)^2}.$$

The effective treatment of the theory involves the interaction between the neutralino and a parton, namely a quark, of the nucleon. The effective mass that enters the cross section is neither that of the nucleon nor that of the quark itself, but its contribution to the nucleon total mass. In this interaction the 3-momentum of the neutralino and the nucleon are small compared to the mass energy, thus $t \simeq \left(m_{\chi_1^0} - Q\right)^2$, where Q is the exchanged momentum.

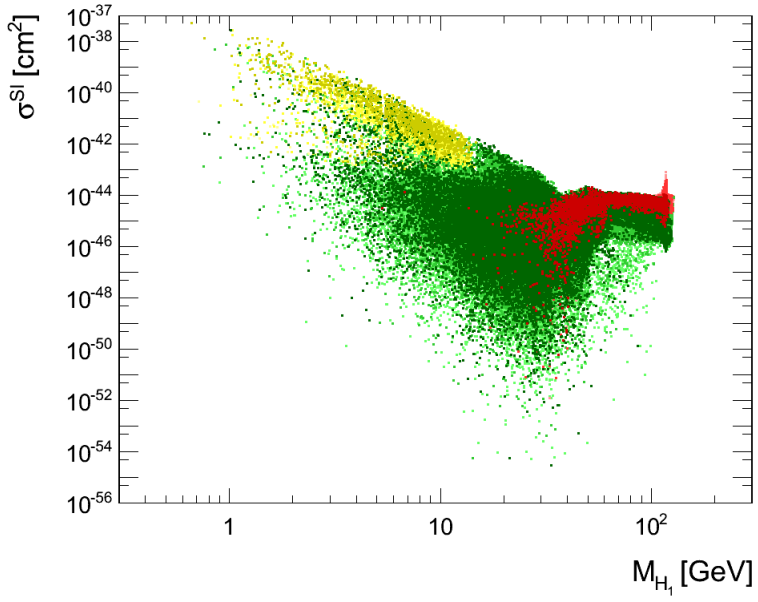

Fig. 9.46: Spin independent neutralino-nucleon interaction rates as a function of the lightest CP-even Higgs mass. The color code is described in Sec. 8.4.2. Here, the red points are excluded by Fermi-LAT and yellow points are above the XENON100 exclusion limit.

A good approximation gives,

$$\sigma^{SI}_{\chi_1^0 q\to\chi_1^0 q} \propto \frac{1}{\left(\left(m_{\chi_1^0}-Q\right)^2 - M_{H_1}^2\right)^2} \propto \frac{1}{M_{H_1}^4}\frac{1}{\left(\left(\frac{m_{\chi_1^0}-Q}{M_{H_1}}\right)^2 - 1\right)^2}.$$

A singularity appears for $M_{H_1} = m_{\chi_1^0} - Q$. This is not a physical singularity, though, it is artificial and arises because of the approximation we take. Also, before going into these narrowly tuned cases, the higher order corrections should be taken into account. Thus we ignore the possibility of this singularity. If one sets a relation between the neutralino and Higgs mass, namely $M_{H_1} = \alpha m_{\chi_1^0}$ with $\alpha \lesssim 1$ (which is the case of our points) and neglecting the effective mass, we get

$$\sigma^{SI}_{\chi_1^0 q\to\chi_1^0 q} \propto \frac{1}{M_{H_1}^4}\frac{1}{\left(\left(\frac{1}{\alpha}\right)^2 - 1\right)^2}.$$

This behaves as $\sigma^{SI} \propto M_{H_1}^{-4}$ down to very low mass values. Actually, at least in the upper limit of the cloud and for $M_{H_1} \leq 30\,GeV$, there is a power law of exponent -4, in agreement with our approximative analysis. As it was seen in Sec. 6.2.3, the same diagram exists for a pseudoscalar exchange, however the relevant terms vanish in the limit of zero momentum transfer since they depend upon the square of the exchanged momentum, and are thus irrel-

evant for DD interactions [86]. In particular, the smallness of M_{A_1} cannot help making large elastic scattering interactions.

XENON100 exclusion limit

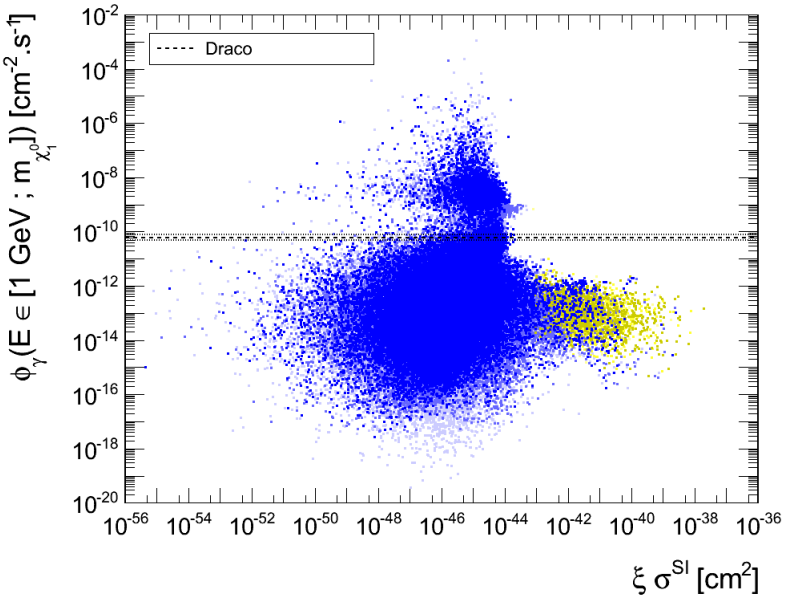

Fig. 9.47: Integrated γ-ray flux from the Draco dwarf spheroidal galaxy as a function of the spin independent neutralino-nucleon interaction rates normalized to the neutralino contribution to the local DM density. The color code is described in Sec. 8.4.2. Here, the yellow points are above the XENON100 exclusion limit.

At present, the most stringent limits have been set by the XENON100 collaboration [34]. We intend to use these limits to further constrain the parameter space. It is very interesting to see that in Fig. 9.45 there is no overlap between the red points and the cloud which is ruled out by the XENON100 results: the intersection is null. That is why the points above the XENON100 limit have been tagged in yellow, thus, they can be distinguished from those excluded by Draco in a same plane, and can be tracked down all the green-red-yellow plots. In Fig. 9.32 we see that the yellow points coincide with light H_1: $M_{H_1} \lesssim 15\,GeV$. That is to say, only light CP-even Higgs configurations can be seen or ruled out by SI interactions scanning experiments. Moreover, we observe in Fig. 9.31 that the yellow points correspond indeed to the $M_{H_1} \lesssim m_{\chi_1^0}$ case, whereas Fig. 9.35 shows that the yellow points correspond to dominant H_1H_1 annihilation channels in EU. We saw that those interactions happen through the exchange of a neutralino and that they imply a large enough $H_1\chi_1^0\chi_1^0$ coupling, which is entirely compatible with large SI cross sections since the very same coupling intervenes.
Not only the points excluded by γ-ray considerations are not the same that would be excluded by XENON100, but also the inverse is (obviously) true. But what is more important, these

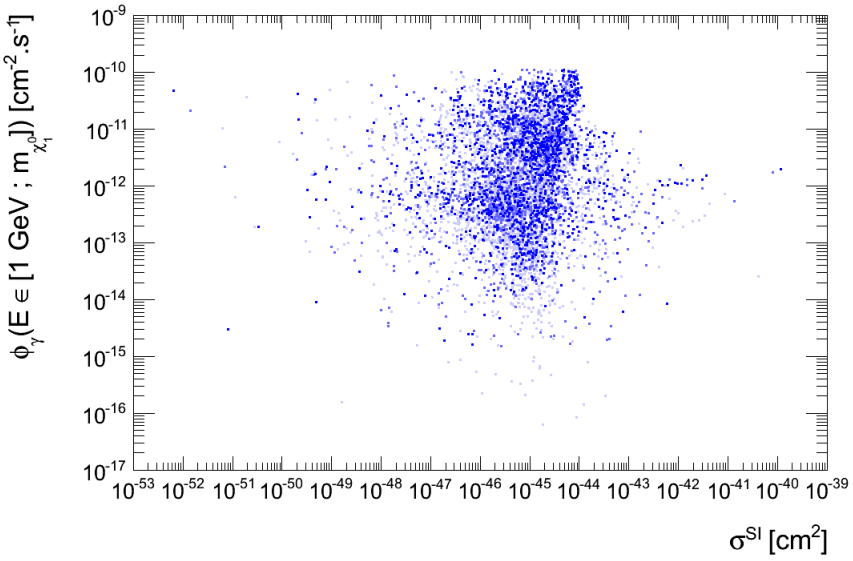

Fig. 9.48: Integrated γ-ray flux from the Draco dwarf spheroidal galaxy as a function of the spin independent neutralino-nucleon interaction rates normalized to the neutralino contribution to the local DM density. Only points safe with respect to XENON100 and Fermi-LAT, as well as having $\xi = 1$ (thus neutralinos representing the whole CDM of the universe) and a total weight $Q \leq 0.32 \times Q_{max}$. The color code is described in Sec. 8.4.2.

regions lie a few orders of magnitude away from each other, as can be seen in Fig. 9.47: points touched by XENON100 lie between 1 and 5 orders of magnitude below the Draco limits, wehreas we saw in Fig. 9.45 that points excluded by Draco are between a factor ~ 2 and 9 orders of magnitude below the XENON100 limits. This is a desperate claim for the need of various and different techniques of DM detection to work together in order to find the DM particles.

If we take the XENON100 limits seriously, the yellow points are excluded –up to the astrophysical uncertainties, which are far from being completely understood nor fully taken into account. If we restrain our results to those points with good weights, i.e. points for which $Q \geq 0.32 \times Q_{max}$, and whose FO yield is contained in the WMAP 5 year interval, and further ask the configurations to be safe with respect to dSphs and XENON100 limits, then we only get then the remaining parameter space represented in the $\phi_\gamma(E \in [0.1\,GeV; m_{\chi_1^0}])$ vs. σ^{SI} plane is given in Fig. 9.48. The extension is very large: there are many points escaping XENON100 and Fermi-LAT by several orders of magnitude at the same time. The light NMSSM parameter space needs to be further constrained by other complementary experimental techniques.

M_1	M_2	$M_{\tilde{l}}$	$M_{\tilde{q}}$	μ	$\tan\beta$	λ	κ	A_λ	A_κ	A_t
14.6	1257	166	1284	175	20.7	0.55	0.27	3529	-361	1005
22.3	157	528	1701	164	20.0	0.55	0.15	3281	-212	1591
16.8	605	192	1782	186	18.3	0.70	0.25	3464	-317	2437

Tab. 9.5: Three examples of NMSSM points falling in the CoGeNT contour in the $\xi\sigma^{SI}$ vs. $m_{\chi_1^0}$ plane. For all of them we have set $M_3 = 3 \times M_2$ and $A_b = A_\tau = 0$. All quantities are expressed in GeV units.

The CoGeNT preferred region

There has been controversy in the SI DD experimental scene. It is beyond the scope of this work to establish whether experimental results are to be trusted or not. That is why, we now address the possibility of the CoGeNT results to be actually right. It is important to notice that we found supersymmetric configurations falling in the CoGeNT preferred contour, as can be seen in Fig. 9.45. It is also worth noticing that all these points lie above the XENON100 limit, which means that they are represented in yellow throughout this section. Moreover, it means that these points correspond to the $M_{H_1} \lesssim m_{\chi_1^0}$ configuration: they achieve the relic density through neutralino exchange annihilations into light CP-even Higgs bosons. With respect to ID, their yields are suppressed, as it was previously discussed. When we check the values of $\left(\xi/m_{\chi_1^0}\right)^2 \times \sigma v$ for these points we find that they yield values $\leq 6 \times 10^{-31}\, cm^3\, s^{-1}\, GeV^{-2}$, that is to say, at least two orders of magnitude below the limits established by Draco.
In Table 9.5 we present three examples of points with weights in the first group and which fall in the CoGeNT preferred region.

Spin dependent interactions

SD interactions were also computed for all points of the run. These are not attaining the current limits that have been set by various experiments, and are thus not further constraining the parameter space. Results are presented in Fig. 9.49. SD elastic scattering interactions occur via the the exchange of a Z or a squark (see Fig. 6.1), while the main channel is that of the exchange of a Z-boson because of the mass differences: the Z is generally much lighter than the squarks. We recall that the $Z\chi_1^0\chi_1^0$ coupling is $\propto N_{13}^2 - N_{14}^2$. Looking at Fig. 9.30 we see that this coupling tends to be rather small. The other mechanism, namely the exchange of a $\tilde{q}$, is even more suppressed since $M_{\tilde{q}}$ is always heavier than $800\, GeV$ and most often above $1.7\, TeV$, as it can be seen in Fig.9.29. Thus, in any case, there is no large cross section configuration. Moreover, there is an upper limit of roughly $5 \times 10^{-40}\, cm^2$, which is more than an order of magnitude below the most stringent limits even for masses around $15\, GeV$. Points ruled out by γ-ray overproduction mask those falling above the XENON100 limits,

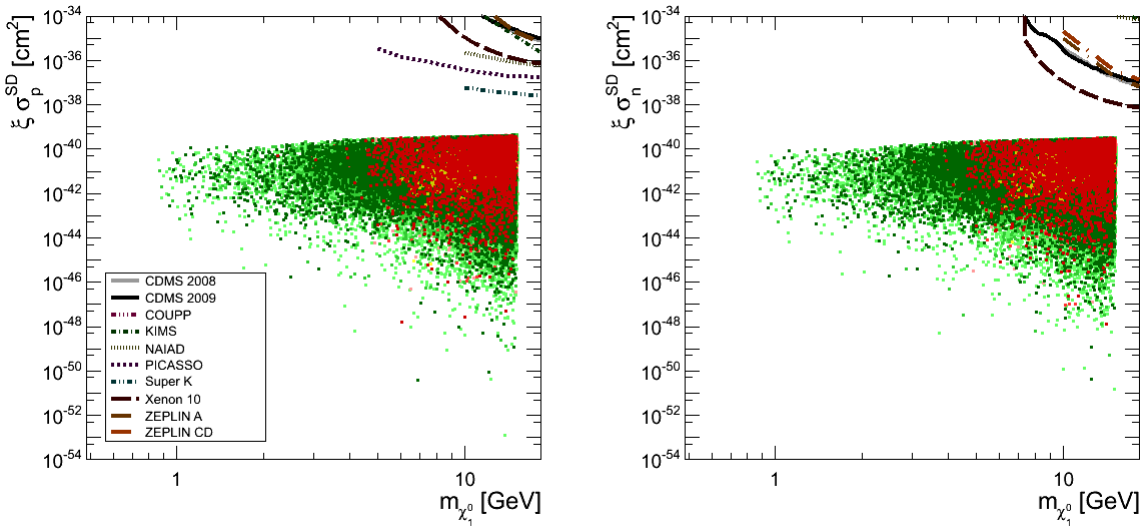

Fig. 9.49: Spin dependent interactions of light neutralinos off protons (left panel) and neutrons (right panel) in the NMSSM. Exclusion limits shown for reference: CDMS [51], COUPP [52], KIMS [53], NAIAD [54], PICASSO [55], SuperKamiokande [56], XENON10 [57] and ZEPLIN [58], whereas all data points were obtained at [59]. The color code is described in Sec. 8.4.2.

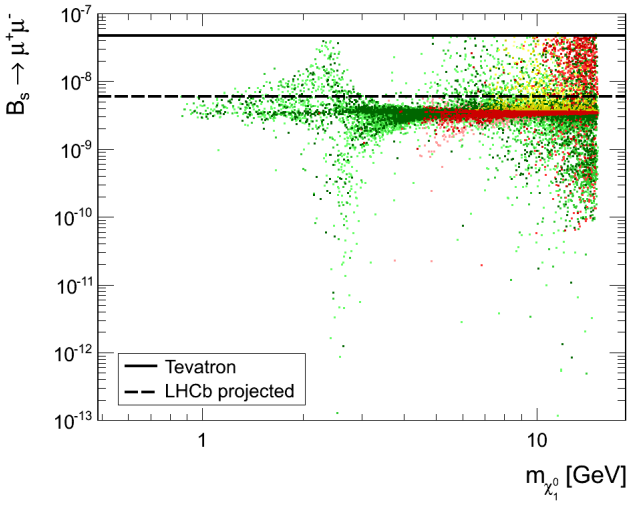

Fig. 9.50: Supersymmetric contribution to the $B_s \to \mu^+\mu^-$ branching ratio as a function of the neutralino mass for light neutralinos in the NMSSM. The color code is described in Sec. 8.4.2. We include the current best limit obtained at the Tevatron, and the projected LHCb results for 1 fb^{-1} analyzed data.

and are surrounded by a large cloud of points spanning more than 15 orders of magnitude in cross sections.

9.2.7 LHCb projections

In Fig. 9.50 we present the full $B_s \to \mu^+\mu^-$ branching ratio contribution calculated for all points in this run. We observe that most of the points have contributions of the order of $(3-4)\times 10^{-9}$. Knowing that the SM prediction is of $(3.6\pm 0.4)\times 10^{-9}$ [87], this means that the supersymmetric contribution in light NMSSM neutralino configurations is subdominant. Indeed, the expected contribution from SUSY is stemming from the Higgs sector. We have seen that the lighter bosons are highly dominated by the singlet field, which makes the contribution rather small. Furthermore, the LHCb projection will not be sensitive to most of our configurations, as their projected sensitivity is still not yet attaining the SM prediction.

10 Directional detection experiments and neutralinos

We already argued that it is necessary to probe DM models with as many different detection techniques as possible. That is why the possibility of adding new dimensions to the quest of finding the DM in the near future is exciting.

Future DD experiments will lower current sensitivities to elastic scattering interactions of nucleons and WIMPs. Of course, not everything can be controlled: new unexpected backgrounds may appear, which might be difficult to control, even to understand in their nature. However, current prospects show a very interesting progression in this sense, as we argued in Sec. 4.2.3.

In particular, there is a growing community of directional detection experimental efforts. As the Sun –hence the solar system and the Earth– flies through the MW's DM halo towards the Cygnus constellation, a fundamental asymmetry on the nucleus-WIMP relative velocity is expected to be imprinted in the direction of the nuclear recoil track. With the aim of detecting an asymmetric signal, various prototypes[1] are being conceived and tested, and routines for the analysis of the expected data is in rapid development. These detectors will be sensitive to the SD proton-WIMP interactions –since they will use mainly CF_4 as the interacting medium–, which has not been sufficiently explored yet to constrain the parameter space of neutralinos. This is why we now couple our searches for neutralino DM candidates to the results shown in [36] where the projected sensitivity to SD proton-DM interactions of a forthcoming fluorine detector are estimated. The characteristic of the simulated detector were set to be those of the MIMAC project, but are representative of the whole generation of detectors currently in development. Thus, data was generated and analyzed following these characteristics: $10\,kg$ of CF_4 operated at $50\,mbar$, assuming that recoil tracks can be resolved, including the head-tail determination of the event, an energy threshold at $5\,keV$, and an exposure of $30\,kg\,yr$.

The projection shows that if no background events are recorded, the detector would be able to exclude cross section down to $\simeq 4\times10^{-42}\,cm^2$ for a mass of $10\,GeV$. Furthermore, deter-

[1] Collaborations such as DRIFT, DM-TPC, D^3, Emulsions, NEWAGE and MIMAC are rapidly progressing in the development of their detectors, and also actively collaborating. See Sec. 4.2.3 for references.

mining the directionality increases the number of observables. Using a likelihood analysis, it is possible to determine the WIMP mass and interaction cross section. The needed statistics to solve these characteristics can be translated into a sensitivity curve, which is, of course, above the exclusion limit. In light of these sensitivity curves three regions are defined in the $\xi\sigma_p^{SD}$ vs. $m_{\chi_1^0}$ plane: above the discovery limit, between discovery and exclusion limits, and below the exclusion limits. In the first region, neutralinos are expected to be detected, their mass and cross section could be measured. Of course, if no event is measured, then the corresponding configuration would be ruled out. In the second region, neutralinos would produce some signal but not enough to be solved. If they do not, then scenarios lying in this region would be excluded. Finally the third region is populated by neutralinos that would not yield any effect in the forthcoming directional detection experiments.
In order to explore the impact of the projected sensitivity, we make use of the MCMC described in Chapter 8 for a wide exploration of the different possibilities for neutralinos in the range of detection for directional experiments. Namely, we open the door for random walks with larger masses, around and above 100 GeV, thus making an extension of the applications so far shown. Then, we explore the yield in terms of SD proton-neutralino cross sections and compare it to the projected sensitivity of forthcoming directional detectors. Thus, we are be able to show this reach in terms of supersymmetric parameters, which consequently sets the possibilities of predictions for collider physics. Finally, we show the very good complementarity of searches that are respectively sensitive to SI, SD and annihilation cross sections for the case of neutralino DM in the MSSM and NMSSM. Results presented here are preliminary, and a detailed study is in preparation.

10.1 General runs in the MSSM and the NMSSM: more similarities than differences

In order to study the potential of DM directional detectors on supersymmetric configurations with neutralino LSP, we have performed vast runs in both the MSSM and the NMSSM using the MCMC as described in Chapter 8. Since the general procedure is similar to that depicted in Chapter 9, we stress the main intrinsic characteristics of these runs. In particular, these runs did not include an upper limit for the neutralino mass. Hence, we successfully scanned configurations with LSP neutralinos of masses up to several hundred GeV.
In the MSSM we performed a run with multiple chains scanning the parameter space described in Table 9.2. Here we have used two different starting point techniques: forced initializations were performed in the light slepton and light Higgs regions in order to ensure their representation in the results, while random points were also used in order to ensure the larger masses to be explored. We found 1124360 successful points with a Q_{max} of 0.75. More than 25% of the points lie in the 1σ group, while 97.3% belong to either of the three

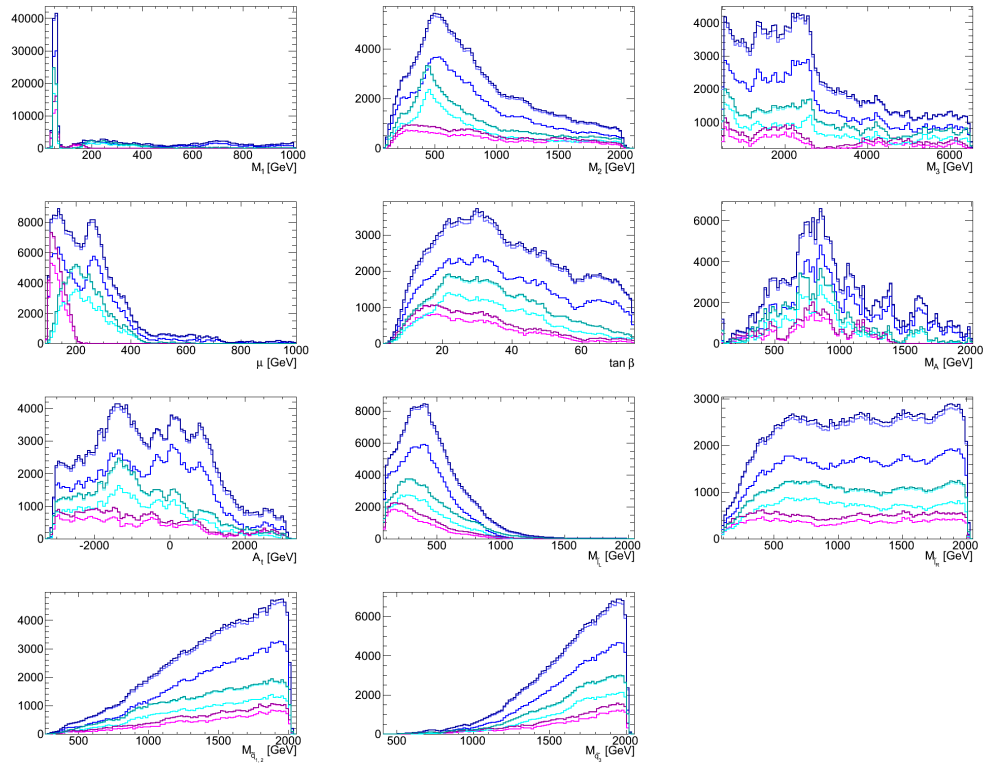

Fig. 10.1: Frequency distributions of the lightest neutralino components in the MSSM run for directional detection. The color code is described in Sec. 8.4.2. The magenta and cyan curves represent the distributions for those sets falling in the discovery and exclusion regions of the projected sensitivity of directional detectors respectively (see Sec. 10.2).

first groups. Neutralino masses span the $(11.1-693.7)\,GeV$ interval.

For neutralino masses below $50\,GeV$ we find the same configurations already discussed in Chapter 9. Actually, the only striking feature in the parameter configurations shown in Fig. 10.1 is the large peak in M_1 corresponding to the bino-like neutralinos annihilating via the Z-resonance. Above that limit we found neutralinos of two sorts: bino-dominated neutralinos around the SM-like Higgs resonance (corresponding thus to masses of $\sim (55-65)\,GeV$) and higgsino-like neutralinos for even larger masses. In the $(60-100)\,GeV$ range an interplay of both bino-like and higgsino-like neutralinos is found. The neutralino LSP components can be seen in Fig. 10.2. Higgsino-like neutralinos annihilate through various channels. Large higgsino fractions increase the neutralino coupling to the Z, sfermion masses tend to be closer to the neutralino mass and the coupling to the Higgs scalar and pseudoscalar can be large depending on the Higgs mixing parameters α and β. Finally, since the mass of the neutralino is mainly determined by μ, the chargino has a mass of the same order, allowing the coannihilation of the two in EU.

The run we present for the NMSSM included a few relaxations in the choice of parameters

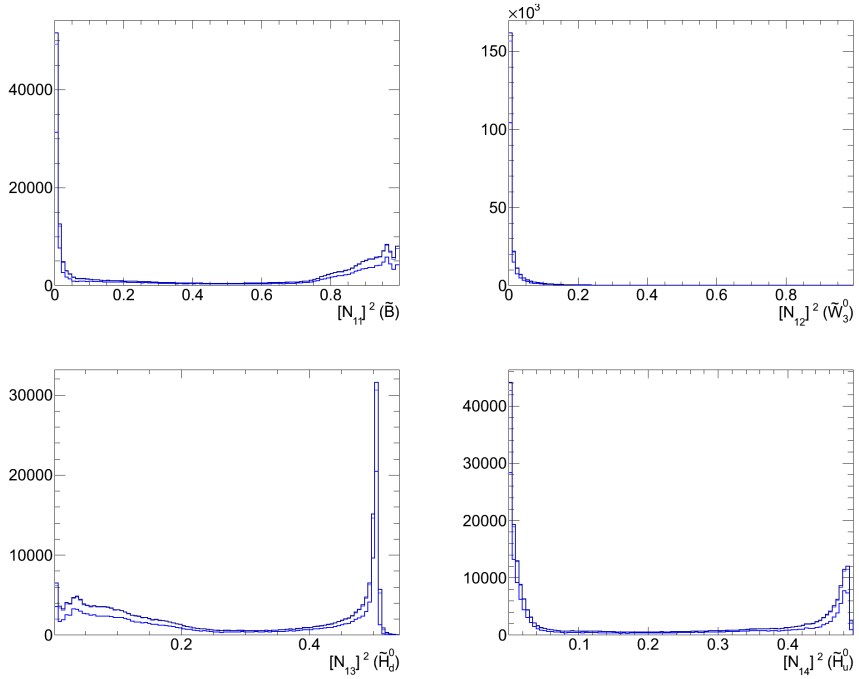

Fig. 10.2: Frequency distributions of the lightest neutralino components in the MSSM run for directional detection. The color code is described in Sec. 8.4.2.

and ranges with respect to the previous run (see Table 9.3). Indeed, the squark masses were split in two and we included M_3 as a free parameter as already discussed for the MSSM. Furthermore we symmetrized the A_λ and A_κ intervals, and we extended the M_1 and $\tan\beta$ upper limits. Hence the parameters scanned and their intervals are given in Table 10.1. Similarly to what was done for the MSSM, in some chains we used light neutralino points previously found as starting points in order to ensure the presence of the fine-tuned regions found for LSP masses below $15\,GeV$, while other chains were started randomly. This run yielded 818816 points with a maximum weight of 0.62. Among these points, 32.4% lie in the first group of points, while 95.4% are have weights $\geq 0.003 \times Q_{max}$. Neutralino LSP masses were found from $3.0\,GeV$ to $634.5\,GeV$.

As it can be seen in Fig. 10.1, the same conclusions can be drawn in the parameter distributions: the only feature is still the very pronounced Z-resonance region in the bino mass. Indeed, the NMSSM does not add much to such a general run. At larger neutralino mass, there is no need for a fine-tuned light Higgs spectrum, nor for light singlino-like neutralinos. Indeed, Fig. 10.2 shows that the neutralino LSP composition is here almost the same than in the MSSM, and that excepting insignificant exceptions, the singlino component is always null. We do observe a larger higgsino fraction in the MSSM, and more bino-like neutralinos in the MSSM. This might be only a statistical artifact in the interplay between M_1 and μ. We will discuss further the correlations between these two crucial parameters in what follows.

Parameter	Minimum	Maximum	Tolerance
M_1	1	1000	3
M_2	100	2000	30
M_3	500	6000	30
μ	0	1000	10
$\tan\beta$	0.1	75	3
λ	0	.75	0.1
κ	0	0.65	0.8
A_λ	-5000	5000	100
A_κ	-5000	5000	100
A_t	-3000	3000	100
$M_{\tilde{l}}$	100	2000	15
$M_{\tilde{q}_{1,2}}$	300	2000	14
$M_{\tilde{q}_3}$	300	2000	14

Tab. 10.1: NMSSM free parameter intervals for a directional detection run (GeV units).

Therefore we can treat both cases in a very similar way for most of the mass range explored. However, we do know that below $\sim 30\,GeV$, neutralino configurations are different in both cases. Notice that for the current NMSSM run the slepton masses have not been split, hence the light slepton configurations have not been thoroughly explored.

10.2 Projected sensitivity to neutralinos: discovery and exclusion

10.2.1 The discovery and exclusion regions in terms of the spin-dependent proton-neutralino interactions

Directional detectors based on fluorine are sensitive mostly to the SD interactions of DM with protons. Let us now analyze the yield of the runs previously described in light of such cross sections. We present the results for the MSSM and NMSSM in Fig. 10.5. First of all it is worth observing that many configurations lie above the projected exclusion limit in both the MSSM and the NMSSM. This already encourages the efforts for building fluorine directional detectors. Let us discuss the common features of the models first.

The points that can be detected around the Z-resonance are those not falling exactly in it, but rather those of masses $\lesssim 40\,GeV$ and $\gtrsim 50\,GeV$. This is easily understood in terms of the elastic scattering cross section. As it was shown in Fig. 6.1 and discussed in Sec. 6.2.3, the SD interactions occur mainly via the exchange of a Z-boson. While the Z-resonance is an

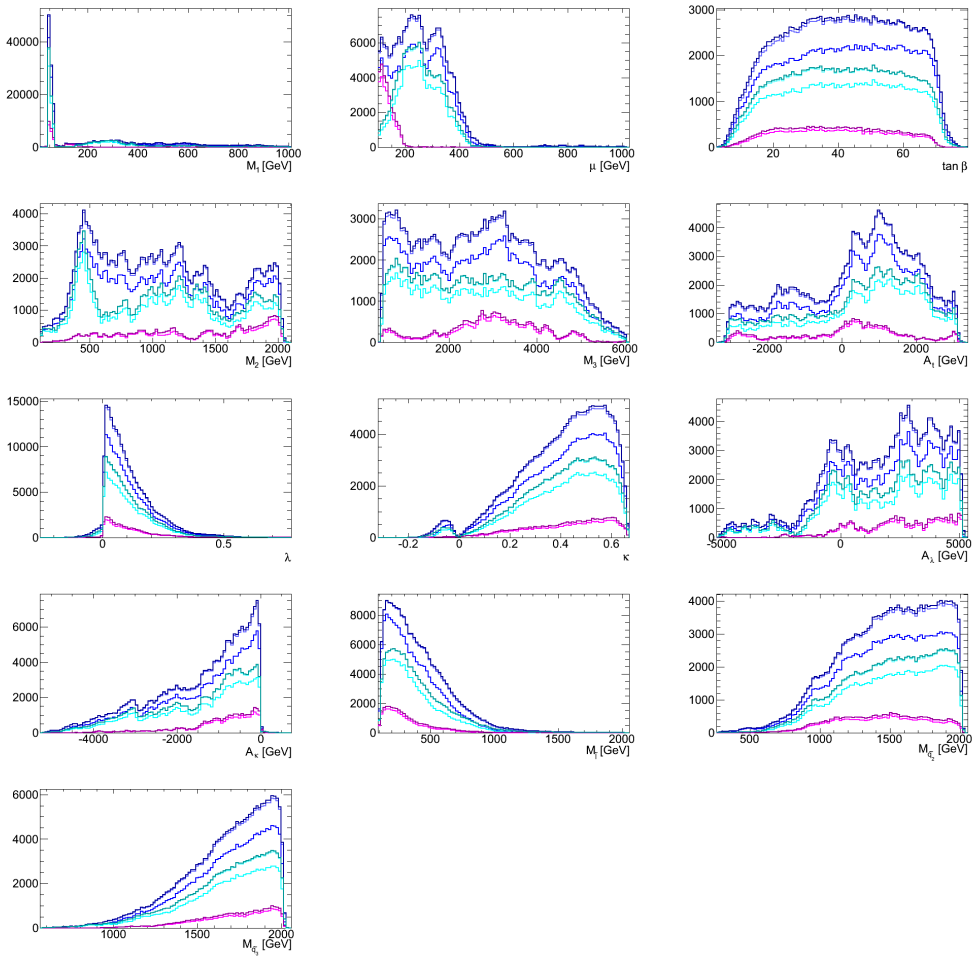

Fig. 10.3: Frequency distributions of the lightest neutralino components in the NMSSM run for directional detection. The color code is described in Sec. 8.4.2. The magenta and cyan curves represent the distributions for those sets falling in the discovery and exclusion regions of the projected sensitivity of directional detectors respectively (see Sec. 10.2).

attractive pole in order to achieve a plausible relic density, a too fine-tuned relation leads to a too small relic density unless the coupling to the Z is small. Thus, for points with $m_{\chi_1^0}$ sitting too close of $M_Z/2$, the $Z\chi_1^0\chi_1^0$ coupling is small, hence SD interactions are consequently small.

For the larger masses, hence higgsino dominated neutralinos, the $Z\chi_1^0\chi_1^0$ coupling is usually large, since it is proportional to $N_{13}^2 - N_{14}^2$. However, at larger masses the mass split between neutralinos and squarks narrows. Hence both Z and $\tilde{q}_{u,d}$ contribute to the interactions. It turns out that these two contributions are destructive. Therefore, for a generally dominating Z exchange with rather large couplings, those configurations having a large enough squark exchange can lower down the SD proton-neutralino cross section of a few orders of magnitude. This is why not all the higgsino points have large interactions. Thus, only a fraction of

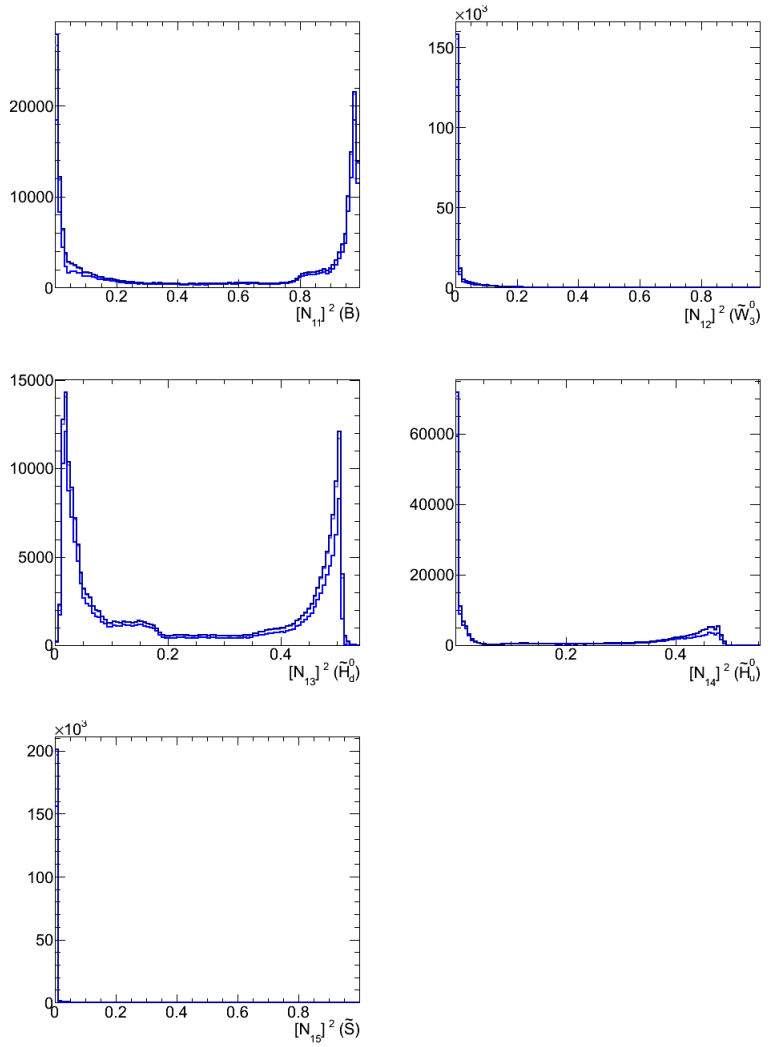

Fig. 10.4: Frequency distributions of the lightest neutralino components in the NMSSM run for directional detection. The color code is described in Sec. 8.4.2.

them falls in the discovery region. The general trend to have smaller cross sections towards larger neutralino masses is a consequence of the kinematic behavior of the cross section: when $m_{\chi_1^0} \gg m_p$, then the neutralino-proton cross section is proportional to $m_{\chi_1^0}^{-2}$. When the maximum $Z\chi_1^0\chi_1^0$ coupling is achieved –i.e., $N_{13}^2 - N_{14}^2 \simeq 0.5$–, the upper limit for the interaction cross section as a function of the neutralino mass is the -2 power law observed in both panels in Fig. 10.5.

Finally, the lighter neutralinos, as we already discussed in Chapter 9, present different features in both the MSSM and the NMSSM. In Sec. 9.1.2 we argued that in the MSSM there are two branches of points for neutralino masses below $30\,GeV$: the light Higgs configurations and the light slepton configurations. In the top panel of Fig. 10.5, however, we only see

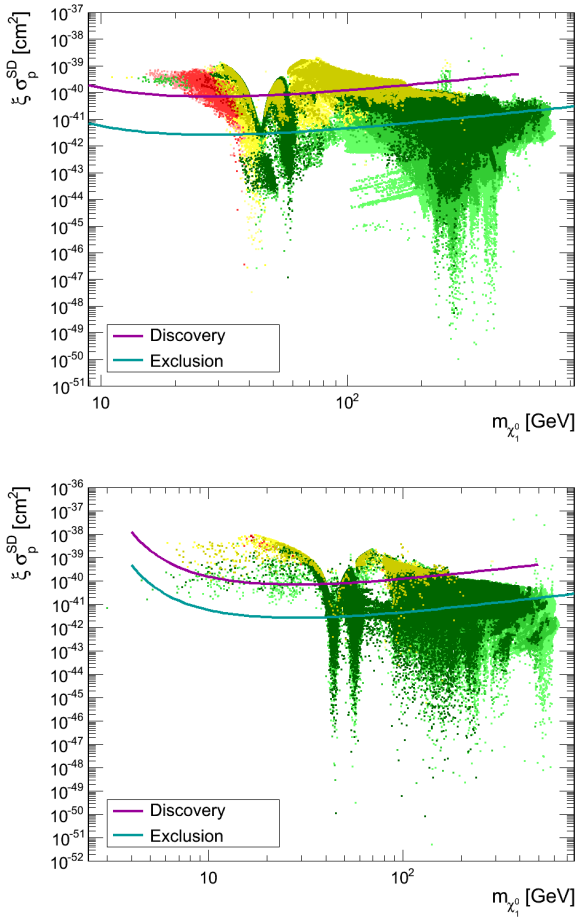

Fig. 10.5: Spin-dependent proton-neutralino interactions as a function of neutralino mass in the MSSM (top panel) and the NMSSM (bottom panel) runs for directional detection. The color code is described in Sec. 8.4.2. We have included the projected sensitivity of a typical directional detector as given in [36].

one bunch of points towards lighter neutralino masses. Nonetheless the color code helps us disentangling both cases. Indeed, we know that light Higgs configurations are excluded by both XENON100 and Fermi-LAT and are consequently tagged in red, while the light slepton points are safe regarding both of these experimental bounds, and are consequently tagged in green. Two remarkable features are to be commented. On one hand both configurations tend to roughly the same value of the cross section which, on the other hand, lies in the discovery region. It can be interpreted in the sense that both scenarios select bino-like neutralinos with a small but not null fraction of higgsino. The largest values of the red cloud are above the larger values of the green cloud due to the larger higgsino fraction of the Higgs exchanging red points. Kinematically, large interactions are expected since the neutralino approaches the proton mass, which implies we do not have a $m_{\chi_1^0}^{-2}$ suppression below $30\,GeV$. However, this

is not enough to meet the largest values obtained for the lightest higgsino dominated points at $m_{\chi_1^0} \sim 60\,GeV$, for which $N_{13}^2 - N_{14}^2 \simeq 0.5$, since here the higgsino fraction only reaches 10%, thus $N_{13}^2 - N_{14}^2 \lesssim 0.1$. Anyhow, both configurations could be resolved by a directional detector.

In Sec. 9.2 we presented the light neutralino phenomenology in the NMSSM. Here the regions of neutralino mass below $15\,GeV$ are not well represented. However, we know that, similarly to the MSSM, the higgsino fractions are of, at most, 10%. Hence the maximum value of the proton-neutralino cross section should tend to the same value as in the MSSM. However, we observe a larger spread of values, with, nevertheless, a central value around the same as in the MSSM, i.e., $\sigma_p^{SD} \simeq (10^{-40} - 10^{-39})\,cm^2$. Here however, cross sections reach $5 \times 10^{-39}\,cm^2$, which is a factor ~ 5 above the largest values encountered in the MSSM. This is probably the effect of the interplay between the $\tilde{H}_d$ and $\tilde{H}_u$ components. For a maximal splitting one needs a large $\tan\beta$. In the light neutralino MSSM configurations $\tan\beta \geq 40$ was found only for the light slepton points as it can be seen in Fig.9.17, which means higgsino fraction well below 10%. In the NMSSM, though, $\tan\beta$ as large as ~ 50 could be reached for the lighter points with a higgsino fraction around 10% (see Fig. 9.29). Conversely, in the NMSSM there are configurations for which the splitting is rather small since $\tan\beta$ can fall well below ~ 20. Hence, the coupling to the Z exhibits more variability in the NMSSM light neutralino scenarios, and so does the proton-neutralino SD cross section.

10.2.2 Implications of the discovery and exclusion regions in the supersymmetric parameter space

In Figs. 10.1 and 10.3 we have displayed the parameter distributions found for all points in blue together with those of the points falling in the discovery region in magenta and the exclusion region in cyan. As it was expected, the most important parameter regarding the directional detection regions is the μ mass term. Indeed, it has been discussed above that the crucial point is the neutralino coupling to the Z boson, in turn determined by the higgsino fraction of the neutralino. And we know that the smaller the μ term, the larger the higgsino fraction. Also, the lines that separate the three regions (of discovery, of exclusion and of no sensitivity) depend upon the neutralino mass. As we have seen in Figs. 10.2 and 10.4, the sizeable contributions to the neutralino are those of the higgsino whose mass is determined by μ, and the bino whose mass is M_1. In particular, no important singlino nor wino contributions are observed.

Hence a good plane to summarize the situation is the μ vs. M_1 plane, shown in Fig. 10.6 for both the MSSM and the NMSSM. In these plots, the points around the $y = x$ line are those for which the higgsino and bino fractions are similar, while points lying above it correspond to $M_1 \leq \mu$, hence to bino-like neutralino, and those lying above it correspond to $\mu \leq M_1$, hence to higgsino dominated neutralinos. We can readily see that for $\mu, M_1 \lesssim 200\,GeV$ there is a

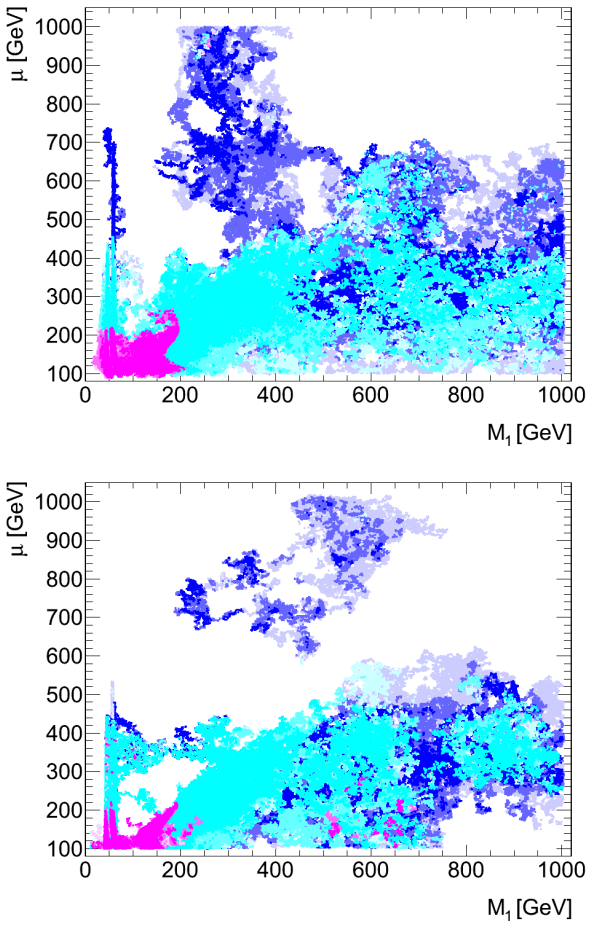

Fig. 10.6: Higgsino mass parameter μ as a function of the bino mass in the MSSM (top panel) and the NMSSM (bottom panel) runs for directional detection. The color code is described in Sec. 8.4.2. The magenta and cyan points represent the configurations for those sets falling in the discovery and exclusion regions of the projected sensitivity of directional detectors respectively.

very large probability of detection. Indeed, in Fig. 10.5 we saw that resolvable configurations have masses below $200\,GeV$. Those figures also show that –higgsino-like– neutralinos up to $\sim 600\,GeV$ could be excluded. Indeed, the bottom-right cyan cloud in the μ vs. M_1 plane correspond to exactly those neutralinos. Notice that some points tagged in cyan or magenta are found for very large μ in the bino-like half plane, in both MSSM and NMSSM. These marginal points can only be explained by a dominant squark exchange, hence we expect those points to correspond to the lightest squarks possible.

In the hypothesis of a discovery, in principle, the directional detectors will be able to resolve the mass and the cross section of the neutralino. Thus, in case of discovery the precious information about the mass can help disentangling the possible value of μ.

Indeed, if the detected mass is, say, $\lesssim 100\,GeV$ then we know the neutralino is bino domi-

nated, which fixes M_1 to be close to the measured mass, and μ should be $\lesssim 200\,GeV$. This, in turn, translates into a prediction for the existence of a rather light chargino of mass $\lesssim 200\,GeV$. A better precision of μ could be obtained from the measurement of the cross section, however, since the neutralino coupling to the Z depends not only on the higgsino mass but also on its mixing, $\tan\beta$ also enters the game and the degeneracy is larger.
If a discovery yields a neutralino mass $\gtrsim 100\,GeV$ the neutralino is most likely higgsino-like. In order to disentangle possible bino-like and higgsino-like configurations one should look at the squark masses needed to achieve a SD proton-neutralino cross section as measured, i.e. $\gtrsim 10^{-40}\,cm^2$, which should be known in the forthcoming months from LHC results. If such squark masses are ruled out, then the neutralino could only be higgsino, in which case M_1 has to be rather large. Again, one would predict a chargino of a mass close to the measured DM mass, hence lighter than $\sim 200\,GeV$.
In summary: directional detection can give precious information about μ through the neutralino mass, which in turn implies a certain range of values for M_1. This should be enough to predict signatures for collider experiments. In particular, it is very likely that a discoverable neutralino would push for the search of a rather light chargino.

10.3 Complementarity of detection techniques

It is interesting to confront the sensitivity to SD proton-neutralino interactions to other neutralino interactions searched for. We can start by comparing the SD interactions between themselves. Indeed, while the nuclei –by the nature of its unpaired nucleon, if it contains any– used in DD and directional detection experiments determine whether a given detector is mostly sensitive to nucleon-DM or proton-DM collisions, it is the model which determines whether one or the other cross section is favored. Thus we present the correlation between the $\xi\sigma_p^{SD}$ and the $\xi\sigma_n^{SD}$ observables in the MSSM and NMSSM in Fig. 10.7. Here we observe three different behaviors in both cases. Two proportional lines are drawn at two different values, while at lower cross sections there is a spread tending asymptotically towards constant σ_p^{SD} or σ_n^{SD}. The latter tendency as well as the upper line are much more explored in the MSSM run than in the NMSSM case. The lower line, which is the most prominent, indicates the dominant Z exchange interactions. Indeed, these happen through a t-channel, implying that the only difference between up and down quarks could come from their couplings to the neutral weak boson, which is determined by SM physics and not from any neutralino characteristic. Hence, the relation between the two is constant for any strength of the $Z\chi_1^0\chi_1^0$ coupling. Indeed, there is a constant ratio of $\sigma_p^{SD}/\sigma_n^{SD} \simeq 1.41$ for Z exchange dominated elastic scattering interactions. Deviations from this dominant behavior can only be due to a sizeable fraction of squark exchanges. If the latter remain small compared to Z exchanges, then only a small interference is obtained, which is quark –hence nucleon– dependent, im-

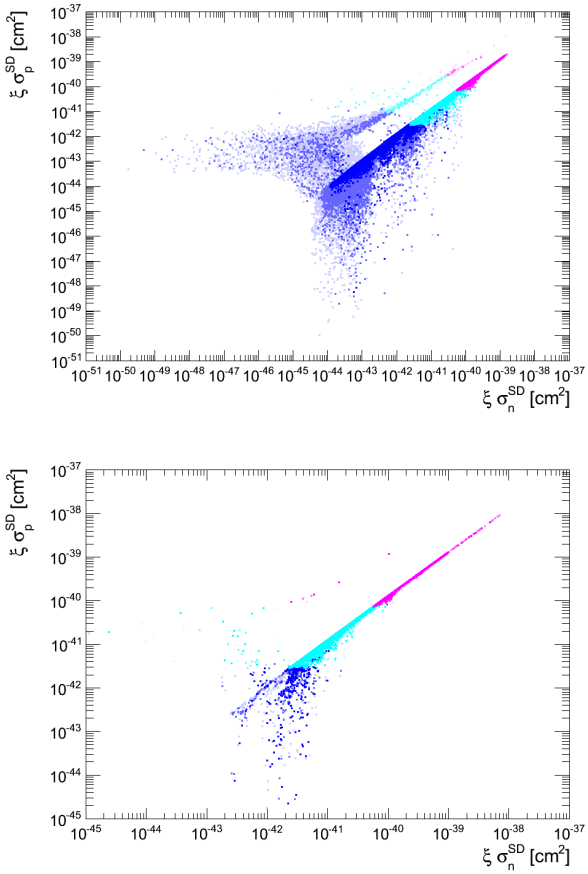

Fig. 10.7: Spin-dependent proton-neutralino cross sections as a function of spin-dependent neutron-neutralino cross sections in the MSSM (top panel) and the NMSSM (bottom panel) runs for directional detection. The color code is described in Sec. 8.4.2. The magenta and cyan points represent the configurations for those sets falling in the discovery and exclusion regions of the projected sensitivity of directional detectors respectively.

plying that points have a small deviation from the line. These small interferences would primarily affect the proton-neutralino interactions, yielding a deviation towards the bottom of the $\xi\sigma_p^{SD}$ vs. $\xi\sigma_n^{SD}$ plane. If both the Z and squark exchanges are of the same size, then the destructiveness is maximal. In order to have this situation we need light squarks. Here, a small difference in the split of up-type and down-type squarks couplings to the Higgs yield an important difference in the mass. The lighter squark will determine the most important channel, either up-type hence proton interactions, or down-type hence neutron interactions. Then, the process of the largest transition amplitude is the most suppressed. Finally, the upper line appears when squark exchanges dominate completely. This implies that the neutralino is either bino dominated or has $N_{13} \simeq N_{14}$ and the squarks are the lightest possible. In this run we allow values that are probably already ruled out by the LHC, hence we expect the

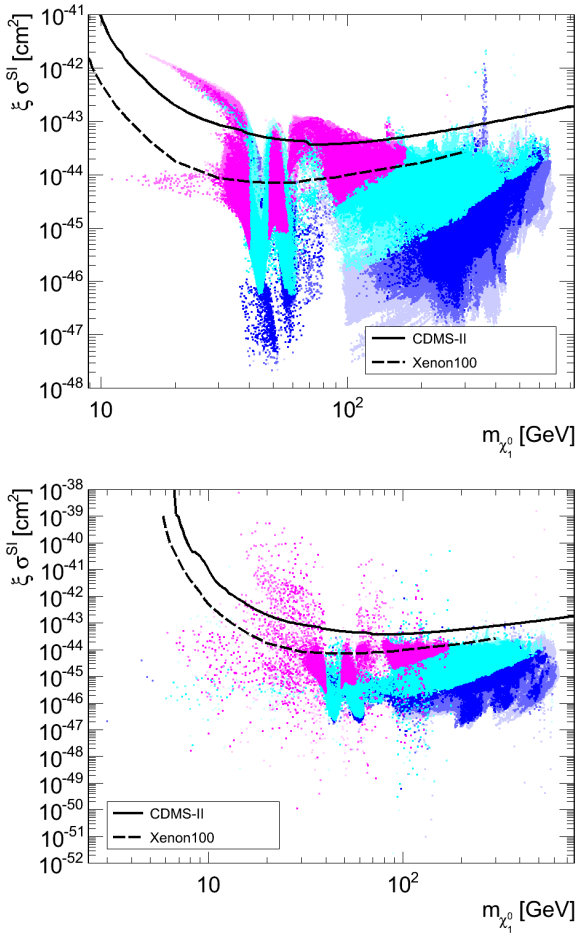

Fig. 10.8: Spin-independent nucleon-neutralino cross sections as a function of neutralino mass in the MSSM (top panel) and the NMSSM (bottom panel) runs for directional detection. The color code is described in Sec. 8.4.2. The magenta and cyan points represent the configurations for those sets falling in the discovery and exclusion regions of the projected sensitivity of directional detectors respectively.

upper line and most of the maximal interference points to disappear in the near future. Anyhow, a limit on one of the cross sections sets automatically a limit on the other, especially if we are confined to the $\sigma_p^{SD}/\sigma_n^{SD} \simeq 1.41$ case. For example, the σ_n^{SD} sensitive XENON10 and XENON100 experiments –that use ^{131}Xe which contains 54 protons, thus an odd number of neutrons– could lower the current limits on the $\xi\sigma_n^{SD}$ interactions, which, in the scope of the MSSM and the NMSSM, imply a limit on $\xi\sigma_p^{SD}$.

Let us now look at the SI interactions for these runs. In Figs. 10.8 we display the points in the $\xi\sigma^{SI}$ vs. $m_{\chi_1^0}$ plane, using the magenta and cyan tagging for those configurations that could be discovered and excluded by a nominal directional detector. As it has been already stressed before, the XENON100 exclusion limits rule out part of the parameter space. Here, however, we may stress that many magenta and cyan points lie below the XENON100 limits:

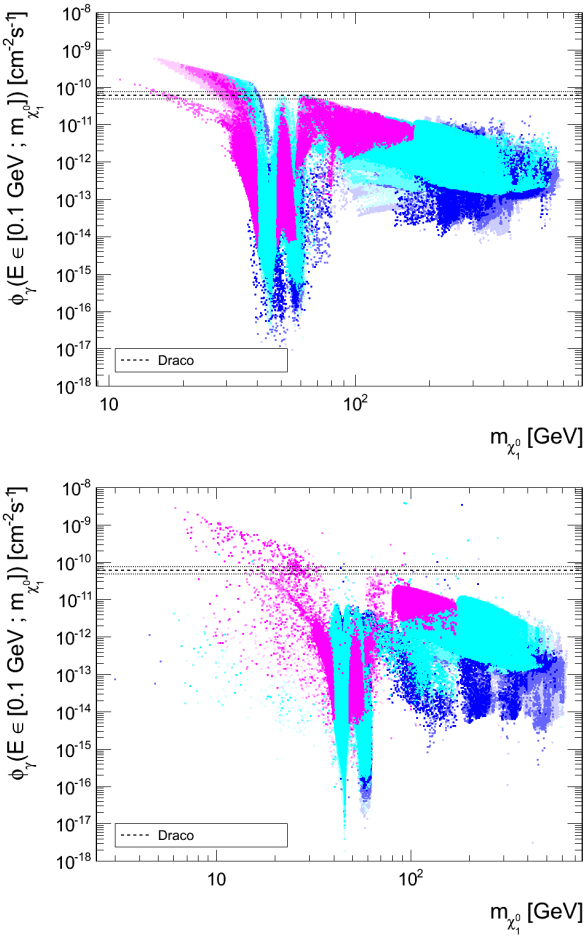

Fig. 10.9: Predicted γ-ray fluxes from the Draco dwarf galaxy as a function of neutralino mass in the MSSM (top panel) and the NMSSM (bottom panel) runs for directional detection. The color code is described in Sec. 8.4.2. The magenta and cyan points represent the configurations for those sets falling in the discovery and exclusion regions of the projected sensitivity of directional detectors respectively.

a fluorine based directional detector would scan configurations that are safe with respect to XENON100 limits on SI interactions. Furthermore, in the MSSM, the magenta point with the smallest SI interaction reads $\xi\sigma^{SI} \simeq 4 \times 10^{-46}\, cm^2$, which is unlikely to be within the sensitivity of the projected XENON-1ton or other SI-oriented projected direct detectors. In the NMSSM this is even more exaggerated: there is a point in magenta with $\xi\sigma^{SI} \simeq 10^{-50}\, cm^2$! We do the same exercise regarding the indirect γ-ray flux from the Draco dSph predicted for the neutralinos we found. We present the yield in that observable together with the Fermi-LAT limits in Fig. 10.9 together with the same tagging for the points as before. The conclusion is similar: we find discoverable configurations which lie up to four orders of magnitude below the Fermi-LAT limits in the MSSM, and even more in the NMSSM.

In Fig. 10.10 we present a summary of the interplay between the projected sensitivity of

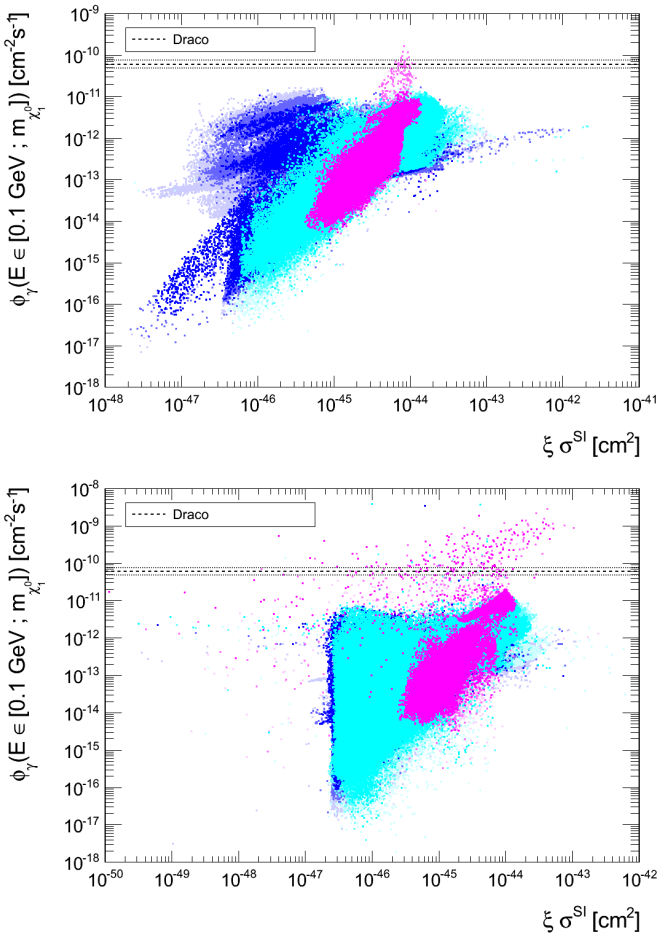

Fig. 10.10: Predicted γ-ray fluxes from the Draco dwarf galaxy as a function of $\xi\sigma^{SI}$ in the MSSM (top panel) and the NMSSM (bottom panel) runs for directional detection. Points excluded by XENON100 are not drawn. The color code is the same as in Fig. 10.9.

fluorine directional detectors, the SI interactions and the γ-ray fluxes expected for neutralinos in the MSSM and the NMSSM. In those plots the points excluded by XENON100 have been omitted. It is important for the prospect of directional experiments that we find large concentrations of points which are not excluded by any experiment yet, which are far away from detectability by other techniques such as ID and DD, and which could be discovered or excluded by such projected detectors.

11 Light scalar dark matter in hadron colliders

This chapter is devoted to study the production at hadron colliders of the new particles introduced in Chapter 7. Recall that we have introduced a scalar DM candidate coupled to SM fermions and their new mirror partners via Yukawa couplings. In particular, the possibility of these couplings being large in the quark sector, and the fact that the F_q's are coupled to gluons, imply that a large production rate could have happened at the Tevatron, and would certainly take place at the LHC. The results of this study were presented in [88].
Here we introduce the relevant processes and compute the cross sections at parton level both analytically and numerically. Then, we scan the parameters and show the production cross sections at Tevatron and LHC. Finally, for the case of the ATLAS detector, we compare the expected signal to the SM background, after studying numerically generated events.

11.1 Production processes

Hadron colliders result from parton collisions, where partons are the hadron (here, protons and antiprotons) constituents. While their main components are light quarks and antiquarks, at high energies gluons and heavier quarks and antiquarks –especially of the strange flavor– may play an important role. Therefore, when colliding protons against protons, or protons against antiprotons, all production processes derived from quark, antiquark and gluon interactions are expected, although with different cross sections.

11.1.1 Relevant diagrams for hadron collisions

The (7.1) and (7.2) vertices imply tree level production of F_q particles at hadron colliders. Large enough interactions are needed to produce a signal at the LHC –a collider made to scan the EW-scale physics–, or conversely, to constrain the parameter space of this phenomenological configuration. Processes where two quarks exchanging a rather light particle –the scalar– produce particles with $[100\,GeV - \text{few}\,TeV]$ mass –the quark mirror partners– seem to be favored. In the same train of thought, gluon fusion –therefore a purely strong interaction process– can give birth to two F_q particles with rather large rates. Of course, the q-quarks and F_q fermions correspond in flavor (flavor conservation is to be respected since

we assume no flavor mixing in the mirror side) and span all possibilities.
Hence, at parton level, relevant di-F_q production processes include (see Fig. 11.1):

1. $qq \to F_q F_q$ and $\bar{q}\bar{q} \to \bar{F}_q \bar{F}_q$ through t and u-channels scalar exchanges;
2. $q\bar{q} \to F_q \bar{F}_q$ with the same scalar exchange;
3. $q\bar{q} \to F_q \bar{F}_q$ with a gluon exchange in s-channel;
4. $gg \to F_q \bar{F}_q$ through t and u-channels F_q exchanges, and through an s-channel gluon fusion.

Notice that 1. and 2. imply only the (7.1) vertex, whereas 3. and 4. stem from the (7.2) vertex alone, and are therefore purely QCD processes.
We can also expect the production of just one F_q accompanied by a scalar through the following processes (see Fig. 11.2):

5. $qg \to F_q S$, and,
6. $\bar{q}g \to \bar{F}_q S$ through a t-channel F_q and $\bar{F}_q$, as well as a q and $\bar{q}$ exchange in an s-channel.

Both 5. and 6. rely on one (7.1) vertex and one (7.2) vertex.

11.1.2 $qq \to F_q F_q$ *partonic cross section form*

Let us focus on the production of two F_q particles through qq annihilation with the exchange of an S. It is indeed expected to happen at the LHC for $m_{F_q} \sim O(100\,GeV - 1TeV)$ for u-quark annihilation, for example. Furthermore, since the S is light compared to the F_q, for q energies $\gtrsim m_{F_q}$, the F_qs can be produced almost on-shell. Let us explore the behavior of such production channels at these energies. These processes are the most characteristic to this particular model, invoking twice the (7.1) vertex. Such a vertex will introduce the combined $c_l^q P_R + c_r^q P_L$ projected coupling, which we call, for simplicity, g_{lr}. The same way, we note $\bar{g}_{lr} \equiv c_r^q P_R + c_l^q P_L$. Notice that the c_l^q and c_r^q contributions are symmetric. To tag particles, let us introduce the subscripts $i \in \{1, ..., 4\}$ for the two entering quarks and the two resulting F_qs respectively, each carrying a 4-momentum p_i. With the usual Feynman rules and spinor notation (see for example [89]), and writing the results as functions of the Mandelstam variables, we have the t and u amplitudes for these processes expressed as follows

$$\mathcal{M}_t = \frac{i}{t - m_S^2} \left[\bar{u}_4 g_{lr} u_2\right] \left[\bar{u}_3 g_{lr} u_1\right],$$
$$\mathcal{M}_u = \frac{i}{u - m_S^2} \left[\bar{u}_4 g_{lr} u_1\right] \left[\bar{u}_3 g_{lr} u_2\right].$$

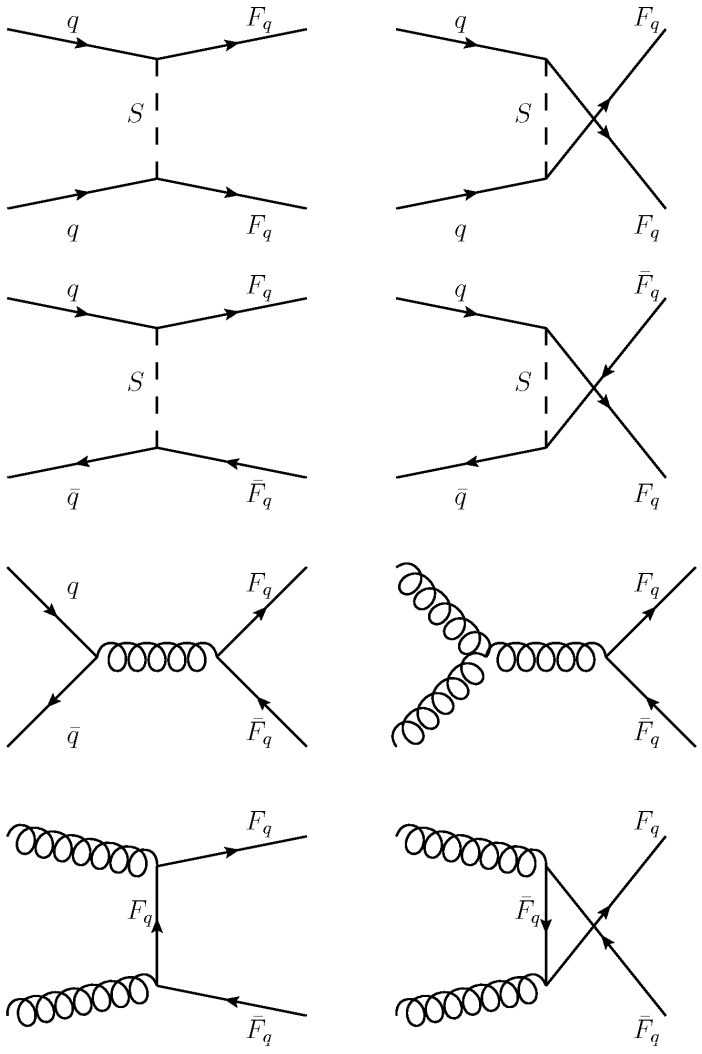

Fig. 11.1: Partonic production of di-F_q at tree level.

The squared amplitude is therefore

$$|\mathcal{M}|^2 = \frac{9}{2}\left(|\mathcal{M}_t|^2 + |\mathcal{M}_u|^2\right) - \frac{3}{2}|\mathcal{M}_{mix}|^2, \tag{11.1}$$

where $|\mathcal{M}_{mix}|^2$ stems from the interference between both exchange channels. The pre-factors shown are color factors. Indeed, each fermionic current must conserve color, since scalars do not carry any. Notice that t and u channels are indistinguishable if both fermionic currents are of the same color. This part contributes to both the single channel and the interference terms, and accounts for the three same-colored leg processes, to which we have to subtract the repeated half, which makes $3/2$. There are also two different colored leg diagrams, which do not interfere, making three combinations. Therefore, the non-interfering term gets a factor

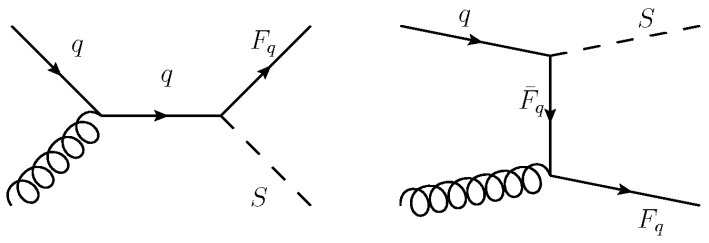

Fig. 11.2: Partonic production of $F_q + S$.

$3+3/2=9/2$, whereas the negatively interfering term just gets a factor $-3/2$. Noticing that

$$\begin{aligned}
g_{lr}^2 &= \bar{g}_{lr}^2 = c_l^{q\,2} P_L + c_r^{q\,2} P_R, \\
g_{lr}\bar{g}_{lr} &= \bar{g}_{lr} g_{lr} = c_l^q c_r^q, \\
p_3.p_1 &= p_4.p_2 = \frac{-t + m_{F_q}^2 + m_q^2}{2}, \\
p_3.p_2 &= p_4.p_1 = \frac{-u + m_{F_q}^2 + m_q^2}{2},
\end{aligned}$$

we come to

$$\begin{aligned}
|\mathcal{M}_t|^2 =& \frac{1}{\left(t - m_S^2\right)^2} \times Tr\left[\left(\not{p}_4 + m_{F_q}\right) g_{lr} \left(\not{p}_2 + m_q\right) \bar{g}_{lr}\right] \\
& \times Tr\left[\left(\not{p}_3 + m_{F_q}\right) g_{lr} \left(\not{p}_1 + m_q\right) \bar{g}_{lr}\right] \\
=& \frac{1}{\left(t - m_S^2\right)^2} \left[\left(c_l^{q\,2} + c_r^{q\,2}\right)\left(-t + m_{F_q}^2 + m_q^2\right) + 4 m_{F_q} m_q c_l^q c_r^q\right]^2, \qquad (11.2)
\end{aligned}$$

$$\begin{aligned}
|\mathcal{M}_u|^2 =& \frac{1}{\left(u - m_S^2\right)^2} \times Tr\left[\left(\not{p}_4 + m_{F_q}\right) g_{lr} \left(\not{p}_1 + m_q\right) \bar{g}_{lr}\right] \\
& \times Tr\left[\left(\not{p}_3 + m_{F_q}\right) g_{lr} \left(\not{p}_2 + m_q\right) \bar{g}_{lr}\right] \\
=& \frac{1}{\left(u - m_S^2\right)^2} \left[\left(c_l^{q\,2} + c_r^{q\,2}\right)\left(-u + m_{F_q}^2 + m_q^2\right) + 4 m_{F_q} m_q c_l^q c_r^q\right]^2, \qquad (11.3)
\end{aligned}$$

$$\begin{aligned}
|\mathcal{M}_{mix}|^2 =& \frac{1}{\left(t - m_S^2\right)\left(u - m_S^2\right)} \times \\
& Tr\left[\left(\not{p}_2 + m_q\right) \bar{g}_{lr} \left(\not{p}_3 + m_{F_q}\right) g_{lr} \left(\not{p}_1 + m_q\right) \bar{g}_{lr} \left(\not{p}_4 + m_{F_q}\right) g_{lr}\right] \\
=& \frac{1}{\left(t - m_S^2\right)\left(u - m_S^2\right)} \times \\
& \left[\frac{1}{2}\left(c_l^{q\,4} + c_r^{q\,4}\right)\left(s^2 + t^2 + u^2 + 2\left(m_{F_q}^2 + m_q^2\right)\left(2s - m_{F_q}^2 - m_q^2\right) - 4 m_{F_q}^2 m_q^2\right)\right. \\
& \left. + 2 c_l^q c_r^q \left(\left(c_l^{q\,4} + c_r^{q\,4}\right) s m_{F_q} m_q + c_l^q c_r^q s\left(m_{F_q}^2 + m_q^2\right) - 2 c_l^q c_r^q m_{F_q}^2 m_q^2\right)\right]. \qquad (11.4)
\end{aligned}$$

Now, if we express the Mandelstam variables in the CM frame,

$$
\begin{aligned}
s &\equiv (p_1+p_2)^2 = 4E^2, \\
t &\equiv (p_1-p_3)^2 = m_{F_q}^2 + m_q^2 - \frac{s}{2} + \frac{1}{2}\sqrt{s-4m_{F_q}^2}\sqrt{s-4m_q^2}\cos\theta, \\
u &\equiv (p_1-p_4)^2 = m_{F_q}^2 + m_q^2 - \frac{s}{2} - \frac{1}{2}\sqrt{s-4m_{F_q}^2}\sqrt{s-4m_q^2}\cos\theta,
\end{aligned}
$$

where $\theta \equiv (\vec{p}_1, \vec{p}_3)$ and E stands for the individual energy of the particles. We choose to express t and u as a function of s rather than E. Now, taking $m_{F_q} \gg m_q, m_S$, (11.2), (11.3) and (11.4) become,

$$
|\mathcal{M}_t|^2_{CM} \simeq \left[\frac{\left(c_l^{q\,2}+c_r^{q\,2}\right)\left(1-\sqrt{1-4\zeta}\cos\theta\right)}{1-2\zeta-\sqrt{1-4\zeta}\cos\theta}\right]^2, \tag{11.5}
$$

$$
|\mathcal{M}_u|^2_{CM} \simeq \left[\frac{\left(c_l^{q\,2}+c_r^{q\,2}\right)\left(1+\sqrt{1-4\zeta}\cos\theta\right)}{1-2\zeta+\sqrt{1-4\zeta}\cos\theta}\right]^2, \tag{11.6}
$$

$$
|\mathcal{M}_{mix}|^2_{CM} \simeq \frac{\left(c_l^{q\,4}+c_r^{q\,4}\right)(4\zeta-1)\left(\cos^2\theta-1\right)-8c_l^{q\,2}c_r^{q\,2}\zeta}{\left(\cos^2\theta-1\right)(4\zeta-1)+4\zeta^2}, \tag{11.7}
$$

where the dimensionless parameter ζ stands for $m_{F_q}^2/s$. Now, the on-shell limit is achieved for $E \to m_{F_q}$, which is equivalent to $s \to 4m_{F_q}^2$ and $\zeta \to 1/4$. Taking this limit into (11.5), (11.6) and (11.7), and replacing in (11.1) we get

$$
lim_{(\zeta\to 1/4)}|\mathcal{M}|^2_{CM} \simeq 36\left(c_l^{q\,2}+c_r^{q\,2}\right)^2 - 12c_l^{q\,2}c_r^{q\,2}. \tag{11.8}
$$

Regarding the cross section, if we take the usual expressions (see for example [89])

$$
\frac{d\sigma}{d\Omega_{CM}} = \frac{1}{64\pi^2 s}\frac{|\vec{p}_1|}{|\vec{p}_3|}|\mathcal{M}|^2_{CM},
$$

$$
\begin{aligned}
\sigma &= 2\pi\int_{-1}^{1}\frac{d\sigma}{d\Omega_{CM}}d\cos\theta = \frac{1}{32\pi s}\frac{|\vec{p}_1|}{|\vec{p}_3|}\int_{-1}^{1}|\mathcal{M}|^2_{CM}d\cos\theta \\
&= \frac{1}{32\pi s}\left(\frac{1-4\zeta}{1-4\frac{m_q^2}{s}}\right)^{\frac{1}{2}}\int_{-1}^{1}|\mathcal{M}|^2_{CM}d\cos\theta \\
&\simeq \frac{1}{32\pi s}\sqrt{1-4\zeta}\int_{-1}^{1}|\mathcal{M}|^2_{CM}d\cos\theta,
\end{aligned} \tag{11.9}
$$

which when applying the same limit in (11.8) vanishes as expected:

$$
lim_{(\zeta\to 1/4)}\sigma \simeq \frac{1}{32\pi s}\sqrt{1-4\zeta}\int_{-1}^{1}|\mathcal{M}|^2_{CM}d\cos\theta = 0.
$$

The same limit is found for $s \to \infty$. Let us look for the maximum value of the cross section σ_{max} between these two extreme cases. Intuitively, we expect this maximum to happen for $s \gtrsim m_{F_q}$. Therefore we introduce the ε parameter such that $s \equiv 4m_{F_q}^2(1+\varepsilon^2)$. We therefore look for ε_0 such as

$$\frac{\partial \sigma}{\partial \varepsilon}(\varepsilon = \varepsilon_0) = 0.$$

Now, we expect the general solution of ε to depend upon θ, or more accurately stated, on the integral over $\cos\theta$ of the squared amplitude. As a proof of concept, let us look ε_0 for $\cos\theta = 0$. Then, ε_0 is the solution of

$$\begin{aligned} &-4\,[7(c_l^{q\,4}+c_r^{q\,4})+12c_l^{q\,2}c_r^{q\,2}]\varepsilon^6 - 16\,[3\,(c_l^{q\,4}+c_r^{q\,4})+5\,c_l^{q\,2}c_r^{q\,2}]\varepsilon^4 \\ &-3\,[5\,(c_l^{q\,4}+c_r^{q\,4})+8c_l^{q\,2}c_r^{q\,2}]\varepsilon^2 + 2\,[3(c_l^{q\,4}+c_r^{q\,4})+5c_l^{q\,2}c_r^{q\,2}] = 0, \end{aligned}$$

which is $\varepsilon_0 \simeq 0.47$. A numerical resolution including the integral gives $\varepsilon_0 \simeq 0.64$. For $c_l^q = c_r^q = 1$ and $m_{F_q} = 300\,GeV$ one finds $\sigma \simeq 30\,pb$. This sets a order of magnitude of the cross sections we may expect for production of di-F_q events for typical values of the parameter space.

By analysing the different production processes expected (Fig. 11.1 and 11.2), the behavior described above is also expected to happen for $q\bar{q} \to F_q\bar{F}_q$ events, with however some interference with the s-channel gluon exchange process. Therefore, for quark and antiquark involving processes, at large couplings (c_l^q, $c_r^q \gtrsim 1$), we expect to be dominated by the Yukawa coupling vertex (7.1). At lower coupling values, the QCD-like vertex (7.2) becomes dominating. Again, single F_q production processes are a mix of both cases. They need non-vanishing c_l^q, c_r^q values though.

11.2 Parameter space scanning and tools

We may now address the scan and numerical evaluation of parameter space. We compute the cross sections at parton level and hadron level for both Tevatron and LHC. We do not include cuts in these calculations. The detector sensitive region is only taken into account for event generation. As one can see in (11.9), the relevant parameters at parton level are c_l^q, c_r^q and m_{F_q}. These, of course, hold for hadronic cross sections as well, the only difference being the convolution with the PDF. Numerical cross section calculations were achieved using different tools. At parton level, we compared our analytical results with the outcome of Comphep 4.5.1 [90], and mainly of Calchep 2.4.5 [91]. Indeed, this model was implemented by including the (7.1) and (7.2) vertices in addition to the SM. Once the model files were successfully modified, we tested the parton level cross sections using the Easy 2×2 integrator, and the more sophisticated VEGAS Monte-Carlo phase space integrator. Convergence was achieved

without problems and our results were validated. This also gave us an idea of the behavior of the other expected processes such as $\bar{d}\bar{d} \to \bar{F}_d\bar{F}_d$, since we could trust the outcome of these numerical tools. We have also implemented the model in micrOMEGAs 2.4 [2] to make use of its facilities to perform scans. Here, the cs22 function allows one to compute 2×2 cross sections, and results were in good agreement with the Calhep output.
At hadron level, the same tools were used. In Calchep, by specifying the PDF package one wants to use, the convolution is done. In micrOMEGAs there is a function called hCollider which computes a given production channel for proton-proton or proton-antiproton collisions, at a given CM hadron energy, making not only the convolution but also the sum over all processes contributing to the production channel asked. For all convolutions the CTEQ6L [92] package was used.

11.3 Parton level cross sections

If we take the u-quark as a representative example of the quark content of the proton, let us see the resulting behavior of some production cross sections. To do so, let us fix the value of $m_{F_q} = 300\,GeV$, and take $m_S = 2\,MeV$ although its value is highly irrelevant once it lies in the interval defined in Sec. 7.2.2.

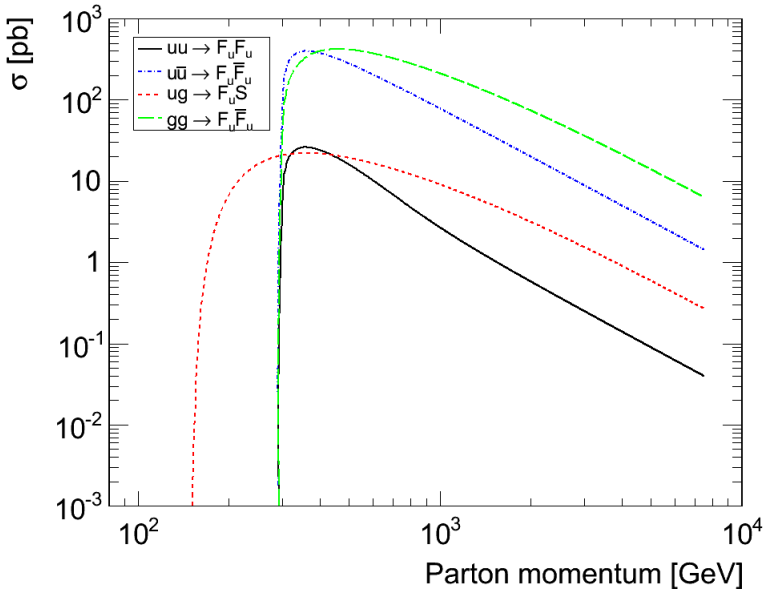

Fig. 11.3: Partonic cross sections for $m_{F_u} = 300\,GeV$ and $c_l^q = c_r^q = 1$.

The parton energy behavior is shown in Fig. 11.3 for $c_l^q = c_r^q = 1$. For this choice of parameters we see that the dominant channels are indeed those producing $F_u\bar{F}_u$, getting to the very large value of $\sim 500\,pb$. This implies that the dominant interaction is the gluon exchange

process, since it is the only difference between $uu \to F_u F_u$ and $u\bar{u} \to F_u \bar{F}_u$ (and potentially its interference with the t and u-channel S exchange). Besides, the $gg \to F_u \bar{F}_u$ process implies only QCD couplings and is of the same magnitude as $u\bar{u} \to F_u \bar{F}_u$. For lower values of c_l^q and c_r^q the domination of gluon exchange and QCD-like interactions emphasizes. It is worth to remark the general shape of these cross sections. Indeed, not only we encounter the predicted form for $uu \to F_u F_u$, but the other processes share this shape. It was to be expected: the exchanged particles allow the almost on-shell production of the F_u, assuming that the dominant diagrams are always those exchanging light particles. As it was shown in Sec. 11.1.2, the evolution of the cross section regarding energy is strongly coupled to the m_{F_q} mass. Namely, if we take larger masses we will get the same shape but kinematically shifted towards larger values of energy. Notice that the $uu \to F_u F_u$ process reaches $\sim 30\,pb$ at its maximum, as predicted by the analytical calculation.

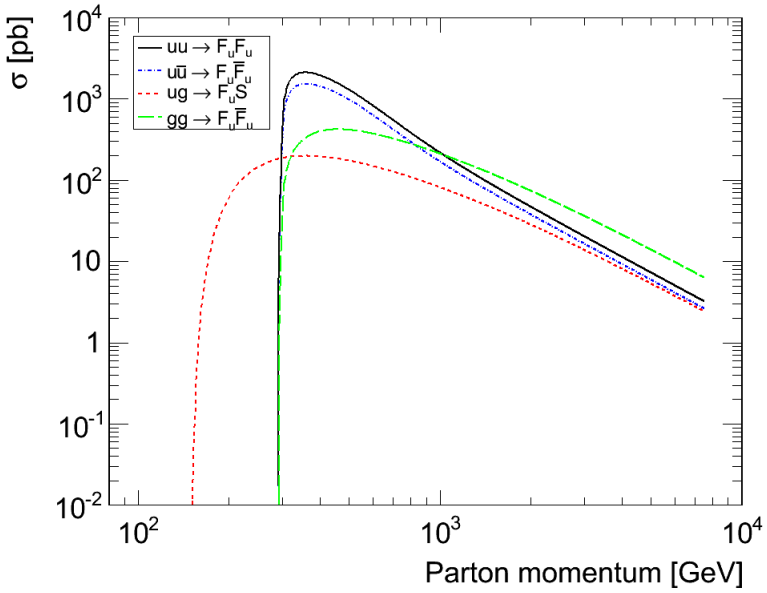

Fig. 11.4: Partonic cross sections for $m_{F_u} = 300\,GeV$ and $c_l^q = c_r^q = 3$.

In Fig. 11.4 we repeat the exercise but for $c_l^q = c_r^q = 3$. This is an extreme behavior, indeed $uu \to F_u F_u$ reaches the value of $2\,nb$, and would be easily ruled out. However, we can observe that for these values we are dominated by the Yukawa coupling of quarks to F_q and S with interaction rates larger than strong interactions.

11.4 Signals: F_q decay

Detection of the new particles introduced by this model could not be achieved only by their production, but also by their decay into observable SM particles. Actually, the F_q being

charged and colored, we expect it to interact in the detector. However, even more probable is its decay. This decay, namely the $F_q \to qS$ process, is represented in Fig. (7.1) and would be driven by the (7.1) vertex.
Using the same notations as previously but now using subscripts given by particle names, the transition matrix of such a decay is given by

$$\mathcal{M}_D = \left[\bar{u}_q \bar{g}_{lr} u_{F_q}\right],$$

which leads to

$$\begin{aligned} |\mathcal{M}_D|^2 &= Tr\left[\left(\not{p}_{F_q} + m_{F_q}\right) g_{lr} \left(\not{p}_q + m_q\right) g_{lr}\right] \\ &= 2\left(c_l^{q\,2} + c_r^{q\,2}\right) p_{F_q}.p_q + 4 c_l^q c_r^q m_q m_{F_q}. \end{aligned}$$

Notice that there is no particular color factor to the decay, since averaging over F_q colors and summing over q colors cancel out. In the CM frame which is the rest frame of F_q, we can express the decay rate as

$$\begin{aligned} \Gamma_{F_q} &= \frac{|\vec{p}_q|}{32\pi^2 m_{F_q} E_S} \int |\mathcal{M}_D|^2 d\Omega_q \\ &\simeq \frac{c_l^{q\,2} + c_r^{q\,2}}{8\pi} m_{F_q}, \end{aligned}$$

where we used the $m_{F_q} \gg m_q, m_S$ approximation. For $m_{F_q} = 300\,GeV$ and $c_l^q = c_r^q = 1$ this gives $\Gamma_{F_q} \simeq 24\,GeV$, or equivalently, the F_q mean lifetime is $\tau \simeq 3\,10^{-26}\,s$. Obviously, this is short enough for the decay to be considered as instantaneous.
Hence, the production of F_q particles would be followed by its decay into quarks and scalars, the former generating a jet, the latter escaping the detectors as missing energy. Thus, a di-F_q production with subsequent decay would produce $\{2\ jets + \not{E}_T\}$, whereas a single F_q production process would potentially show up as a $\{1\ jet + \not{E}_T\}$ event. These are the signals to be looked for at hadron colliders.

11.5 Production at Tevatron: a limit on m_{F_q}

In Sec. 11.1.2 and 11.3 we showed that the cross section of di-F_q production can reach very large values. Therefore it is crucial to address the question whether these particles would have been seen at (or constrained by, or ruled out by) the Tevatron. For low values of the c_l^q and c_r^q couplings, production of such particles may still be large because of new QCD couplings. Thus, regardless of the Yukawa coupling values, we expect to constrain m_{F_q} by comparing cross sections yielded by this model to those of similar Leptoquark signatures at the DØ detector at Tevatron where the analysis of $\{jets + \not{E}_T\}$ sets a limit to $\leq 1\,pb$ [93]. This translates into a more stringent bound for m_{F_q} than new quark generation searches.

Nevertheless, this comparison is not as accurate as what a proper study dedicated to this model would yield, thus it sets only an order of magnitude and represents a preview of the limits that could be found.
Furthermore, we show that this limit can be established regardless of the c_l^q and c_r^q couplings. Fig. 11.5 shows the F_u production cross sections for $p\bar{p}$ collisions at $1.96\,TeV$ CM energy for different channels, taking $c_l^q = c_r^q = 3$. We see that the dominant final state is $F_u\bar{F}_u$, which is to be linked with the quark-antiquark asymmetry intrinsic to $p\bar{p}$ collisions. Fig. 11.6 indicates that the production cross section does not vary much with the coupling values. Furthermore, it appears that for $c_l^q = c_r^q \sim (1-2)$ there is negative interference between the channels, getting lower cross sections than when $c_l^q = c_r^q = 0$ or 3. Hence, it is this channel that is used to constrain the F_u mass, since we know that it stays dominant even for small values of the Yukawa couplings. With this analysis we can conclude that m_{F_u} must be heavier than $\sim 450\,GeV$ if such particles exist, otherwise they would have been seen at DØ.

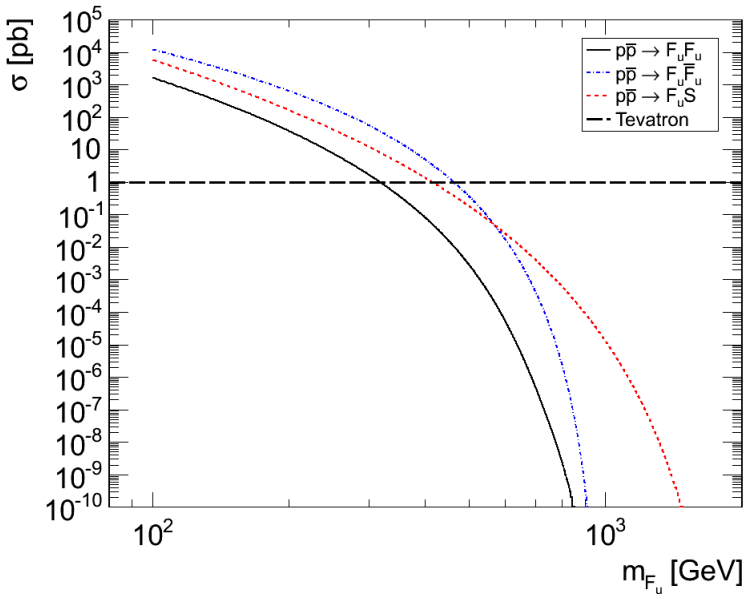

Fig. 11.5: F_u production cross sections at the Tevatron for $c_l^q = c_r^q = 3$. Also displayed is the $\sim 1\,pb$ limit established by the DØ collaboration for scalar leptoquarks [93], which may be adapted to this case.

11.6 Production at the LHC

11.6.1 Production cross sections at the LHC

Let us now address the possible signals at the LHC. When studying the parton level cross sections we established that the interaction rate is large for a parton energy which is just above the F_q mass. The parton energy is the outcome of a probabilistic convolution with

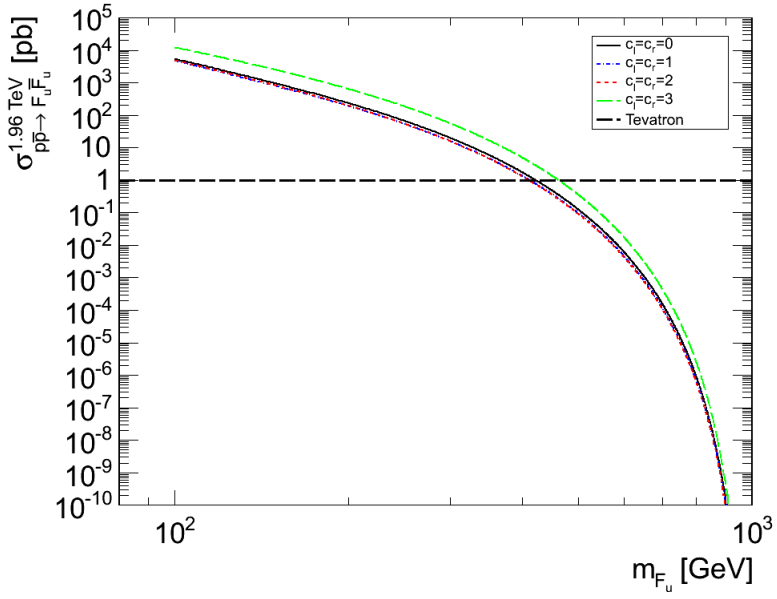

Fig. 11.6: $F_u\bar{F}_u$ production cross sections at the Tevatron for various c_l^q and c_r^q values. Also displayed is the $\sim 1\,pb$ limit established by the DØ collaboration for scalar leptoquarks [93], which may be adapted to this case.

the PDF. In general, partons will carry only a fraction of the incoming hadron momentum. However, up to some point, the larger the proton energy, the larger the probability of a large parton energy. Therefore, it is to be expected that the second run of the LHC at $10\,TeV$, and even more the ultimate run at $14\,TeV$, would produce many more events than the $7\,TeV$ ongoing run. Nevertheless, it is most interesting to use whatever data is available, understood and released by the detectors collaborations, and as soon as possible.

Hence, let us check the cross section values for F_u (we still focus on the u-flavor since u-quarks are the most likely to interact in proton-proton collisions) production at different CM energies. Fig. 11.7 represents such behavior for $m_{F_u} = 300\,GeV$ and $c_l^q = c_r^q = 1$. Fixing the proton momentum to $3.5\,TeV$ for a CM energy of $7\,TeV$ leads to a dominant $F_u\bar{F}_u$ channel. The F_uF_u and F_uS channels only can be dominant for $c_l^q, c_r^q \gtrsim 2$. In any case, the production cross sections for such a configuration go from hundreds of pb for the earlier LHC run to a few nb for the maximum energy expected.

We recall that $m_{F_u} = 300\,GeV$ is already excluded though, but even if cross sections lose a few of orders of magnitude for larger masses, they still are competitive and interesting to look for. Indeed, Fig. 11.8, in which the collision energy is set to $7\,TeV$, shows cross sections as a function of m_{F_u}. As expected, the lighter the F_u, the larger the production rate. This confirms the rather large cross section scenario: for $\sim TeV$ F_u, the $F_u\bar{F}_u$ and F_uS channels reach $1\,pb$. By the end of 2012 LHC will have provided $(5-10)\,fb^{-1}$, which means $(5000-10000)$ events for such cross sections, a large enough value to be seen by the ATLAS and CMS

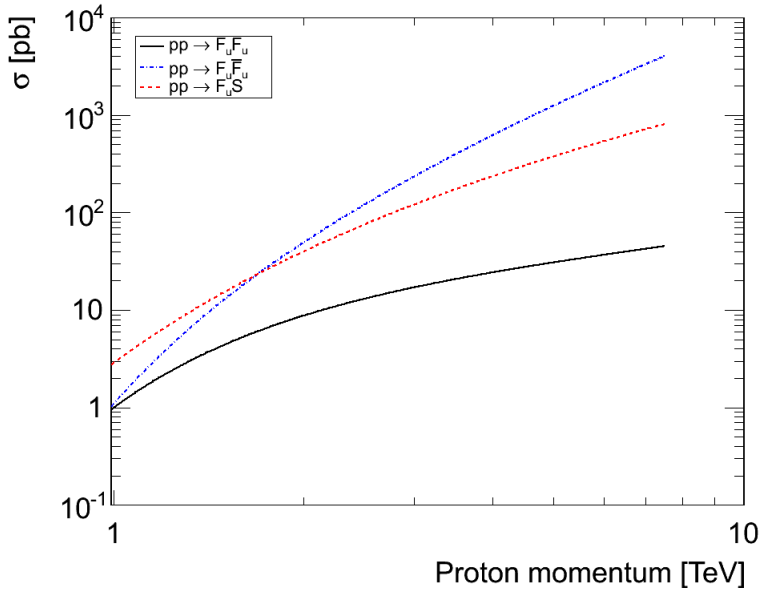

Fig. 11.7: F_u production cross sections in pp collisions for $m_{F_u} = 300\,GeV$ and $c_l^q = c_r^q = 1$.

detectors within their first run.

11.6.2 Relevant backgrounds

In order to detect or constrain this scenario we need to address its detectability at a given detector. This was explored in a collaboration with John Idárraga of the ATLAS collaboration for this purpose. Steps to follow are to identify the SM processes with the same signature as the signal, and compare kinematical behaviors at the detector to study the possibility of disentangling observed events systematically. The first physics run of ATLAS sets the CM energy to $7\,TeV$. Let us focus in di-F_u production. These events will produce $\{2\ jets + \not{E}_T\}$. That same signature is characteristic of several SM processes. The procedure for a complete study of the detectability of a given event includes the simulation of such SM events, which represent the unwanted background. The first step is to identify the relevant processes, then estimate their production cross section at the detector. It is crucial to be careful in the background processes selection, as there is a probability of mismatch or of losing part of the event at the detector. For example, an original $\{3\ jets + \not{E}_T\}$ background event has a certain probability to be observed as $\{2\ jets + \not{E}_T\}$ if a *jet* is lost by merging with its neighboring *jet*. For the selected background processes, the cross sections calculation was achieved using MadGraph [94], which generates events and takes into account the preselection cuts matching the ATLAS calorimetry and tracking devices as defined by the ATLAS collaboration [95]. We stay at production level and do not analyze the final state for background.
The first background process to address is the production of a Z boson along with *jets*. In-

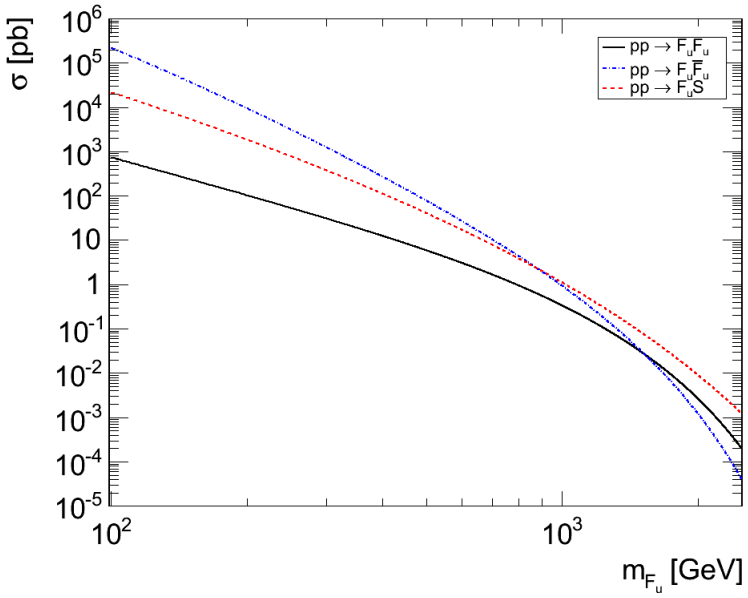

Fig. 11.8: F_u production cross sections at $7\,TeV$ pp collisions for $c_l^q = c_r^q = 1$.

deed, when the Z decays into neutrino pairs, the observed event is $\{jets + \not{E}_T\}$. For this process the estimated cross section is of $8\,nb$. Such a large cross section makes a further analysis of these processes mandatory. Actually, it has been shown that a cut based analysis can solve this background down to a few fb ([95], p. 1595). It is decisive, though, that the kinematic distributions of the signal and background do not share the same shape.

Another source of background is the fraction of the copious production of $t\bar{t}$ events that subsequently experiences the following decay chain $t\bar{t} \to W^+bW^-\bar{b} \to l^+\nu_l b l'^-\nu_{l'}\bar{b}$. If the leptons l and l' fall out the region of identification of the ATLAS detector, namely if their pseudorapidity η reaches ≥ 2.8 and thus escape detection by propagating close to the beam axis. The cross section for $t\bar{t}$ production reaches $\sim 1\,nb$. In spite of its very large cross section, it is possible to overcome such a background. Indeed, this channel has been studied in detail, and it has been shown that it is not a real threat for $\{2\ jets\ +\ \not{E}_T\}$ events ([95], p. 1595), nor other combination of leptons, hadrons and $\not{E}_T$ [96]. Indeed, the ATLAS detector is able to identify b-$jets$: b-tagging reduces the background with high efficiency.

Finally, another background is the production of a pair of vector bosons: WZ, ZZ or WW. The former two can experience the decay of a Z into neutrinos, making the $\not{E}_T$, while the other boson produces two $jets$. WW production would need a missed lepton, just like in the $t\bar{t}$ case, thus its contribution is expected to be smaller. WZ production has a cross section of $11\,pb$ and ZZ of $4\,pb$. The same analysis used for $Z + jets$ can be applied for these channels, and when the kinematic shapes can be disentangled, a signal produced with a few fb could be detected ([95], p. 1595).

These preliminary conclusions lead to a very optimistic scan of parameter space and suggest the possibility to constrain most m_{F_u} values up to a few TeV for almost any set of couplings. Indeed, in the pessimistic scenario of $c_l^q = c_r^q = 0.3$, the di-F_u production exceeds the fb for $m_{F_u} \leq 2\,TeV$ as one can see in Fig. 11.9.

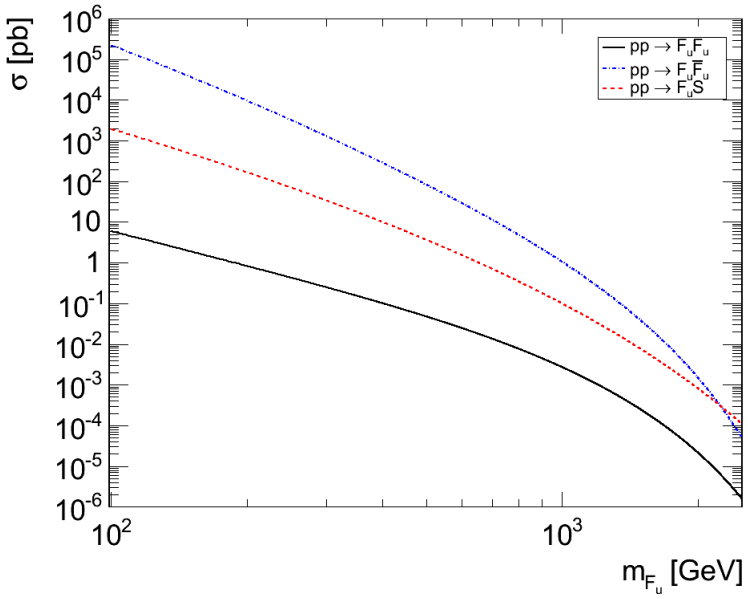

Fig. 11.9: F_u production cross sections at $7\,TeV$ pp collisions for $c_l^q = c_r^q = 0.3$.

11.6.3 The ATLAS potential to detect scalar dark matter

With these considerations, it is necessary to further analyze the background kinematic distributions, specially for Z and $jets$ production, and to compare them with the expected behavior of the F_u potentially produced at pp collisions. Therefore, we analyze the transverse momentum p_t and pseudorapidity η of $Z + jets$ (at parton level) of the outcome of the MadGraph simulation run. We compare these to the same variables obtained from Calchep event generation for one of the two F_u produced. These events were generated for a CM energy of $7\,TeV$, for $m_{F_u} = 300\,GeV$ and $c_l^q = c_r^q = 1$. Results are shown in Fig. 11.10.

The F_us are produced at rather low $|\eta|$, and rather large values of p_T, as compared to the background. This was expected, since we concluded that the F_u have a larger production probability if produced almost on-shell, therefore with not much energy and no preferred direction. This feature is crucial to allow a good kinematic separation of the signal and the most competitive background, as seen in Fig. 11.10. The background tends to produce particles much more forwardly and therefore could be reduced by a cut analysis. This suggests the scalar DM scenario has a large potential of detectability at ATLAS. This signal is not very unique in its shape. Indeed it resembles that of MSSM signatures [95]: one more rea-

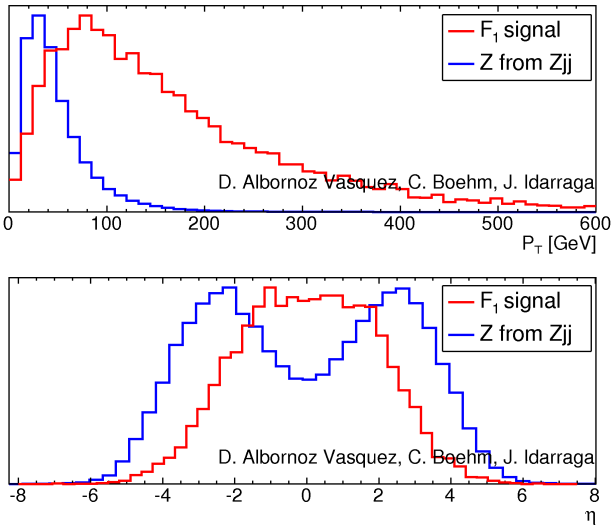

Fig. 11.10: Comparison of kinematic distributions of an F_u signal from di-F_u production and the $Z + 2\,jets$ background at the ATLAS detector for $\sqrt{s} = 7\,TeV$, $m_{F_u} = 300\,GeV$ and $c_r^q = c_r^q = 1$.

son to further study this scenario, since the potential discovery of such signals would imply a degeneracy in the possible theoretical explanations.

11.6.4 Perspectives for a complete study

Not only the ATLAS detector has the potential to detect this scenario, it is also crucial to apply more detailed and sophisticated analyses in order to find means to disentangle this model from other theoretical predictions. A full simulation of the final state has to be carried out, including all decays and the Geant-4 simulation of the ATLAS detector, tested and validated by the ATLAS collaboration.

11.7 Summary

We have showed that the possibility of dark matter being of scalar nature implies the possibility of a large amount of events at the LHC. It has been analytically shown that parton level cross sections producing the F_q almost on shell reach very large rates. After implementation in automatic codes, an exploration of m_{F_q}, interaction energies, and couplings, numerical calculations lead to the same conclusion. Furthermore, m_{F_q} is the most critical parameter, since QCD-like interactions always ensure F_q the production, the amount depending of its mass. Hence, the Tevatron can already constrain m_{F_q} to be lighter than $\sim 450\,GeV$ by a rough comparison with other searches performed for the Leptoquarks model. The LHC first run could explore F_q masses of the order of a few hundreds of GeV and up to a few TeV regardless of the couplings between the scalars, quarks and F_q. The kinematic distribution of the produced

particles is promising: it has a different shape from that of the largest background process. It has also a drawback: this shape is similar to that of other theoretical signature such as the MSSM. In any case it seems that it is worth to study this model in detail in light of the coming years of data accumulation and analysis at the ATLAS detector.

Bibliography

[1] Daniel Albornoz Vásquez, Geneviève Bélanger, Céline Boehm, Alexander Pukhov, and Joseph Silk. Can neutralinos in the MSSM and NMSSM scenarios still be light? *Phys.Rev.*, D82:115027, 2010.

[2] G. Bélanger, F. Boudjema, A. Pukhov, and A. Semenov. micrOMEGAs 2.0.7: A program to calculate the relic density of dark matter in a generic model. *Comput.Phys.Commun.*, 177:894–895, 2007.

[3] Abdelhak Djouadi, Jean-Loic Kneur, and Gilbert Moultaka. SuSpect: A Fortran code for the supersymmetric and Higgs particle spectrum in the MSSM. *Comput.Phys.Commun.*, 176:426–455, 2007.

[4] G. Bélanger, F. Boudjema, C. Hugonie, A. Pukhov, and A. Semenov. Relic density of dark matter in the NMSSM. *JCAP*, 0509:001, 2005.

[5] Ulrich Ellwanger and Cyril Hugonie. NMSPEC: A Fortran code for the sparticle and Higgs masses in the NMSSM with GUT scale boundary conditions. *Comput.Phys.Commun.*, 177:399–407, 2007.

[6] Ulrich Ellwanger, John F. Gunion, and Cyril Hugonie. NMHDECAY: A Fortran code for the Higgs masses, couplings and decay widths in the NMSSM. *JHEP*, 02:066, 2005.

[7] Ulrich Ellwanger and Cyril Hugonie. NMHDECAY 2.0: An Updated program for sparticle masses, Higgs masses, couplings and decay widths in the NMSSM. *Comput. Phys. Commun.*, 175:290–303, 2006.

[8] Daniel Albornoz Vásquez, Geneviève Bélanger, and Céline Boehm. Revisiting light neutralino scenarios in the MSSM. 2011. [arXiv:1108.1338]. Sent to Phys. Rev. D.

[9] Philip Bechtle, Oliver Brein, Sven Heinemeyer, Georg Weiglein, and Karina E. Williams. HiggsBounds: Confronting Arbitrary Higgs Sectors with Exclusion Bounds from LEP and the Tevatron. *Comput. Phys. Commun.*, 181:138–167, 2010.

[10] Philip Bechtle, Oliver Brein, Sven Heinemeyer, Georg Weiglein, and Karina E. Williams. HiggsBounds 2.0.0: Confronting Neutral and Charged Higgs Sector Predictions with Exclusion Bounds from LEP and the Tevatron. 2011.

[11] A. Djouadi, M.M. Muhlleitner, and M. Spira. Decays of supersymmetric particles: The Program SUSY-HIT (SUspect-SdecaY-Hdecay-InTerface). *Acta Phys.Polon.*, B38:635–644, 2007.

[12] R. Brun and F. Rademakers. ROOT: An object oriented data analysis framework. *Nucl.Instrum.Meth.*, A389:81–86, 1997.

[13] Nicholas Metropolis, Arianna W. Rosenbluth, Marshall N. Rosenbluth, Augusta H. Teller, and Edward Teller. Equation of State Calculations by Fast Computing Machines. *The Journal of Chemical Physics*, 21(6):1087–1092, 1953.

[14] E. Komatsu et al. Five-Year Wilkinson Microwave Anisotropy Probe (WMAP) Observations:Cosmological Interpretation. *Astrophys. J. Suppl.*, 180:330–376, 2009.

[15] D. Larson et al. Seven-Year Wilkinson Microwave Anisotropy Probe (WMAP) Observations: Power Spectra and WMAP-Derived Parameters. *Astrophys. J. Suppl.*, 192:16, 2011.

[16] K. Nakamura et al. Review of particle physics. *J.Phys.G*, G37:075021, 2010.

[17] M. Misiak et al. The first estimate of B(anti-B -¿ X/s gamma) at O(alpha(s)**2). *Phys. Rev. Lett.*, 98:022002, 2007.

[18] E. Barberio et al. Averages of $b-$hadron and $c-$hadron Properties at the End of 2007. 2008.

[19] Florian Domingo and Ulrich Ellwanger. Updated Constraints from B Physics on the MSSM and the NMSSM. *JHEP*, 12:090, 2007.

[20] R. Barate et al. Search for the standard model Higgs boson at LEP. *Phys.Lett.*, B565:61–75, 2003.

[21] G. Abbiendi et al. Search for chargino and neutralino production at s**(1/2) = 192-GeV to 209 GeV at LEP. *Eur.Phys.J.*, C35:1–20, 2004.

[22] G. Belanger, F. Boudjema, A. Pukhov, and A. Semenov. Dark matter direct detection rate in a generic model with micrOMEGAs 2.2. *Comput.Phys.Commun.*, 180:747–767, 2009.

[23] S. Durr, Z. Fodor, J. Frison, T. Hemmert, C. Hoelbling, et al. Sigma term and strangeness content of the nucleon. *PoS*, LATTICE2010:102, 2010.

[24] A. A. Abdo et al. Observations of Milky Way Dwarf Spheroidal galaxies with the Fermi-LAT detector and constraints on Dark Matter models. *Astrophys. J.*, 712:147–158, 2010.

[25] Doug Benjamin et al. Combined CDF and D0 upper limits on MSSM Higgs boson production in tau-tau final states with up to 2.2 fb-1. 2010.

[26] Marcela S. Carena, S. Heinemeyer, C.E.M. Wagner, and G. Weiglein. MSSM Higgs boson searches at the Tevatron and the LHC: Impact of different benchmark scenarios. *Eur.Phys.J.*, C45:797–814, 2006.

[27] Serguei Chatrchyan et al. Search for Neutral MSSM Higgs Bosons Decaying to Tau Pairs in pp Collisions at $\sqrt{s} = 7$ TeV. 2011.

[28] R Aaij et al. Search for the rare decays Bs $\rightarrow$ mumu and Bd $\rightarrow$ mumu. *Phys.Lett.*, B699:330–340, 2011.

[29] Z. Ahmed et al. Dark Matter Search Results from the CDMS II Experiment. *Science*, 327:1619–1621, 2010.

[30] Z. Ahmed et al. Results from a Low-Energy Analysis of the CDMS II Germanium Data. *Phys.Rev.Lett.*, 106:131302, 2011.

[31] E. Aprile et al. First Dark Matter Results from the XENON100 Experiment. *Phys.Rev.Lett.*, 105:131302, 2010.

[32] J.I. Collar and D.N. McKinsey. Comments on 'First Dark Matter Results from the XENON100 Experiment'. 2010.

[33] The XENON100 Collaboration. Reply to the Comments on the XENON100 First Dark Matter Results. 2010.

[34] E. Aprile et al. Dark Matter Results from 100 Live Days of XENON100 Data. *Phys.Rev.Lett.*, 2011. Long author list - awaiting processing.

[35] C.E. Aalseth et al. Results from a Search for Light-Mass Dark Matter with a P-type Point Contact Germanium Detector. *Phys.Rev.Lett.*, 106:131301, 2011.

[36] J. Billard, F. Mayet, C. Grignon, and D. Santos. Directional detection of Dark Matter with MIMAC: WIMP identification and track reconstruction. 2011.

[37] C. Farnier, E. Nuss, and J. Cohen-Tanugi. Dark matter annihilations search in dwarf spheroidal galaxies with fermi. *Nucl.Instrum.Meth.*, A630:143–146, 2011.

[38] R. Bernabei, P. Belli, F. Cappella, R. Cerulli, C.J. Dai, et al. New results from DAMA/LIBRA. *Eur.Phys.J.*, C67:39–49, 2010.

[39] E. Armengaud et al. Final results of the EDELWEISS-II WIMP search using a 4-kg array of cryogenic germanium detectors with interleaved electrodes. 2011.

[40] John Skilling. Nested Sampling. *AIP Conf. Proc.*, 735:395–405, 2004.

[41] Daniel Albornoz Vásquez, Geneviève Bélanger, and Céline Boehm. Astrophysical limits on light NMSSM neutralinos. 2011. [arXiv:1107.1614]. Sent to Phys. Rev. D.

[42] John R. Ellis, J.S. Hagelin, Dimitri V. Nanopoulos, Keith A. Olive, and M. Srednicki. Supersymmetric Relics from the Big Bang. *Nucl.Phys.*, B238:453–476, 1984.

[43] Leszek Roszkowski. Light neutralino as dark matter. *Phys.Lett.*, B262:59–67, 1991.

[44] John McDonald, Keith A. Olive, and Mark Srednicki. Relic densities of neutralinos. *Phys.Lett.*, B283:80–84, 1992.

[45] S.A. Abel, Subir Sarkar, and I.B. Whittingham. Neutralino dark matter in a class of unified theories. *Nucl.Phys.*, B392:83–110, 1993.

[46] A. Bottino, N. Fornengo, and S. Scopel. Light relic neutralinos. *Phys.Rev.*, D67:063519, 2003.

[47] A. Bottino, F. Donato, N. Fornengo, and S. Scopel. Lower bound on the neutralino mass from new data on CMB and implications for relic neutralinos. *Phys.Rev.*, D68:043506, 2003.

[48] Herbi K. Dreiner et al. Mass Bounds on a Very Light Neutralino. *Eur. Phys. J.*, C62:547–572, 2009.

[49] E. Aprile, L. Baudis, B. Choi, K.L. Giboni, K. Lim, et al. New Measurement of the Relative Scintillation Efficiency of Xenon Nuclear Recoils Below 10 keV. *Phys.Rev.*, C79:045807, 2009.

[50] John R. Ellis, John S. Hagelin, and Dimitri V. Nanopoulos. Spin 0 leptons and the anomalous magnetic moment of the muon. *Phys.Lett.*, B116:283, 1982.

[51] Z. Ahmed et al. Search for Weakly Interacting Massive Particles with the First Five-Tower Data from the Cryogenic Dark Matter Search at the Soudan Underground Laboratory. *Phys.Rev.Lett.*, 102:011301, 2009.

[52] E. Behnke et al. Improved Spin-Dependent WIMP Limits from a Bubble Chamber. *Science*, 319:933–936, 2008.

[53] H.S. Lee et al. Limits on WIMP-nucleon cross section with CsI(Tl) crystal detectors. *Phys.Rev.Lett.*, 99:091301, 2007.

[54] G.J. Alner et al. Limits on WIMP cross-sections from the NAIAD experiment at the Boulby Underground Laboratory. *Phys.Lett.*, B616:17–24, 2005.

[55] M. Barnabe-Heider et al. Improved spin dependent limits from the PICASSO dark matter search experiment. *Phys.Lett.*, B624:186–194, 2005.

[56] S. Desai et al. Search for dark matter WIMPs using upward through-going muons in Super-Kamiokande. *Phys.Rev.*, D70:083523, 2004.

[57] J. Angle, E. Aprile, F. Arneodo, L. Baudis, A. Bernstein, et al. Limits on spin-dependent WIMP-nucleon cross-sections from the XENON10 experiment. *Phys.Rev.Lett.*, 101:091301, 2008.

[58] V.N. Lebedenko et al. Limits on the spin-dependent WIMP-nucleon cross-sections from the first science run of the ZEPLIN-III experiment. *Phys.Rev.Lett.*, 103:151302, 2009.

[59] Jeff Filippini Dan Butler and Rick Gaitskell. Dmtools website, http://dmtools.brown.edu.

[60] Daniel T. Cumberbatch, Daniel E. Lopez-Fogliani, Leszek Roszkowski, Roberto Ruiz de Austri, and Yue-Lin S. Tsai. Is light neutralino as dark matter still viable? 2011.

[61] N. Fornengo, S. Scopel, and A. Bottino. Discussing direct search of dark matter particles in the Minimal Supersymmetric extension of the Standard Model with light neutralinos. *Phys.Rev.*, D83:015001, 2011.

[62] John R. Ellis, J.F. Gunion, Howard E. Haber, L. Roszkowski, and F. Zwirner. Higgs Bosons in a Nonminimal Supersymmetric Model. *Phys.Rev.*, D39:844, 1989.

[63] Ulrich Ellwanger, Cyril Hugonie, and Ana M. Teixeira. The Next-to-Minimal Supersymmetric Standard Model. *Phys.Rept.*, 496:1–77, 2010.

[64] Ulrich Ellwanger, Michel Rausch de Traubenberg, and Carlos A. Savoy. Particle spectrum in supersymmetric models with a gauge singlet. *Phys.Lett.*, B315:331–337, 1993.

[65] U. Ellwanger, Michel Rausch de Traubenberg, and Carlos A. Savoy. Phenomenology of supersymmetric models with a singlet. *Nucl.Phys.*, B492:21–50, 1997.

[66] Ulrich Ellwanger, Michel Rausch de Traubenberg, and Carlos A. Savoy. Higgs phenomenology of the supersymmetric model with a gauge singlet. *Z.Phys.*, C67:665–670, 1995.

[67] Debottam Das and Ulrich Ellwanger. Light dark matter in the NMSSM: upper bounds on direct detection cross sections. *JHEP*, 1009:085, 2010.

[68] Zhaofeng Kang, Tianjun Li, Tao Liu, Chunli Tong, and Jin Min Yang. Light Dark Matter from the $U(1)_X$ Sector in the NMSSM with Gauge Mediation. *JCAP*, 1101:028, 2011.

[69] John F. Gunion, Alexander V. Belikov, and Dan Hooper. CoGeNT, DAMA, and Neutralino Dark Matter in the Next-To-Minimal Supersymmetric Standard Model. 2010.

[70] Patrick Draper, Tao Liu, Carlos E.M. Wagner, Lian-Tao Wang, and Hao Zhang. Dark Light Higgs. *Phys.Rev.Lett.*, 106:121805, 2011.

[71] Rolf Kappl, Michael Ratz, and Martin Wolfgang Winkler. Light dark matter in the singlet-extended MSSM. *Phys.Lett.*, B695:169–173, 2011.

[72] Junjie Cao, Ken-ichi Hikasa, Wenyu Wang, and Jin Min Yang. Light dark matter in NMSSM and implication on Higgs phenomenology. 2011.

[73] Brian R. Greene and Paul J. Miron. Supersymmetric cosmology with a gauge singlet. *Phys.Lett.*, B168:226, 1986.

[74] Ricardo Flores, Keith A. Olive, and David Thomas. A new dark matter candidate in the minimal extension of the supersymmetric standard model. *Phys.Lett.*, B245:509–515, 1990.

[75] S.A. Abel, Subir Sarkar, and P.L. White. On the cosmological domain wall problem for the minimally extended supersymmetric standard model. *Nucl.Phys.*, B454:663–684, 1995.

[76] Kim Griest and David Seckel. Three exceptions in the calculation of relic abundances. *Phys.Rev.*, D43:3191–3203, 1991.

[77] F. Donato, Nicolao Fornengo, D. Maurin, and P. Salati. Antiprotons in cosmic rays from neutralino annihilation. *Phys.Rev.*, D69:063501, 2004.

[78] David Maurin, R. Taillet, and C. Combet. Approximate formulae for exotic GCR antiprotons and anti-deuterons: Fluxes and astrophysical uncertainties. *Phys.Rev.D*, 2006.

[79] Edward A. Baltz and Joakim Edsjo. Positron propagation and fluxes from neutralino annihilation in the halo. *Phys.Rev.*, D59:023511, 1998.

[80] T. Delahaye, R. Lineros, F. Donato, N. Fornengo, and P. Salati. Positrons from dark matter annihilation in the galactic halo: Theoretical uncertainties. *Phys.Rev.*, D77:063527, 2008.

[81] M. Thierbach, U. Klein, and R. Wielebinski. The diffuse radio emission from the coma cluster at 2.675 ghz and 4.85 ghz. *Astron.Astrophys.*, 397:53–62, 2003.

[82] Céline Boehm, Joseph Silk, and Torsten Ensslin. Radio observations of the Galactic Centre and the Coma cluster as a probe of light dark matter self-annihilations and decay. 2010.

[83] C. Boehm, T.A. Ensslin, and J. Silk. Can Annihilating dark matter be lighter than a few GeVs? *J.Phys.G*, G30:279–286, 2004.

[84] T.N. LaRosa, C.L. Brogan, S.N. Shore, T.J. Lazio, N.E. Kassim, et al. Evidence for a weak Galactic Center magnetic field from diffuse low frequency nonthermal radio emission. *Astrophys.J.*, 626:L23–L28, 2005.

[85] Sergio Colafrancesco, S. Profumo, and P. Ullio. Multi-frequency analysis of neutralino dark matter annihilations in the Coma cluster. *Astron.Astrophys.*, 455:21, 2006.

[86] Toby Falk, Andrew Ferstl, and Keith A. Olive. Variations of the neutralino elastic cross-section with CP violating phases. *Astropart.Phys.*, 13:301–316, 2000.

[87] Andrzej J. Buras. Flavour Theory: 2009. *PoS*, EPS-HEP2009:024, 2009.

[88] Daniel Albornoz Vásquez, Céline Boehm, and John Idárraga. Signature of Sub GeV Dark Matter particles at LHC and TEVATRON. *Phys.Rev.*, D83:115017, 2011.

[89] Francis. Halzen and Alan D. Martin. Quarks and leptons. Wiley, 1985.

[90] E. Boos et al. CompHEP 4.4: Automatic computations from Lagrangians to events. *Nucl. Instrum. Meth.*, A534:250–259, 2004.

[91] A. Pukhov. Calchep 2.3: MSSM, structure functions, event generation, 1, and generation of matrix elements for other packages. 2004.

[92] J. Pumplin et al. New generation of parton distributions with uncertainties from global QCD analysis. *JHEP*, 07:012, 2002.

[93] V.M. Abazov et al. Search for scalar leptoquarks and T-odd quarks in the acoplanar jet topology using 2.5 fb^{-1} of $p\bar{p}$ collision data at $\sqrt{s}$ = 1.96-TeV. *Phys.Lett.*, B668:357–363, 2008.

[94] Fabio Maltoni and Tim Stelzer. MadEvent: Automatic event generation with MadGraph. *JHEP*, 0302:027, 2003.

[95] G. Aad et al. Expected Performance of the ATLAS Experiment - Detector, Trigger and Physics. 2009.

[96] J. Idárraga. *Vector boson scattering at high energy at the LHC*. PhD thesis, Université de Montreal, 2009.

Conclusions

Light Dark Matter is an exciting, rapidly evolving subject. The possibility of interpreting all the gathered data of the past decade in terms of constraints, and drawing the possibilities of neutralino Dark Matter for masses below $\sim 15\ GeV$ is a difficult, yet enlightening exercise. The supersymmetric parameter space can be comprehensively scanned by combining the searches related to spin-independent and spin-dependent elastic scattering of neutralinos and nucleons, to the annihilation into Standard Model particles –in particular into γ-rays–, to the measurements at LHC, such as those of rare meson decays and oscillations as well as potential signals. In the MSSM it seems impossible to have neutralinos lighter than $\simeq 12.6\ GeV$ and still overcome all constraints, from Particle and Astroparticle Physics. However, in the NMSSM, the singlet sector of the model gives fruitful alternatives, in particular, Higgs bosons as light as $1\ GeV$. Finding these configurations, which predict a wide range of masses and cross sections for neutralinos, represents a major result in this hot topic. Moreover, the very light Higgs bosons in the NMSSM could yield specific signatures for the LHC: further phenomenological and experimental explorations are urgent to reveal or rule out these scenarios.

But not only Supersymmetry may be just around the corner. Another model, that of scalar Dark Matter particles at the MeV scale and their associated new charged and colored fermions, is within the reach of the LHC detectors. The signals predicted by this model could mimic some of the expected supersymmetric signatures. It is then crucial to make predictions as specific as possible for this model, for a trustworthy explanation of the observations to –hopefully– come from hadron collisions. A full simulation is yet to be done. Light scalars could also play an important role in the Early Universe, and maybe contribute to solve the primordial nucleosynthesis lithium problem –an interesting possibility to be explored. Furthermore, if these scalars are coupled to neutrinos and are as light as one MeV, they could be produced in supernova explosions, which could imply perturbations in the neutrino radiative transport theory of those magnificent events.

This work shows the congested cross road between experimental results and theoretical predictions around the Dark Matter problem. It becomes obvious that it is important to rely on all experimental techniques available in order to scan all the parameter space of Supersymmetry, of all the plausible models explaining Dark Matter, and of all the phenomenologies

predicted by the available theories. Indeed, the Dark Matter problem is still unsolved.
Thus far, the LHC has not yet reported the discovery of the long awaited Supersymmetry. The so-called new physics is not showing up in its most expected way, which should produce striking features above the SM background. The most conventional ideas for physics beyond the Standard Model and the star Dark Matter candidate, the neutralino, are still purely hypothetical considerations. With the parameter space rapidly closing down, we may have to go deeper in the comprehension of the Dark Matter related phenomena. The standard picture being –in my opinion– discredited, we need to start considering other scenarios. Is the freeze-out Nature's way to produce the Dark Matter observed? Could not the neutralino, or the scalars, acquire their relic density via the freeze-in mechanism?
Some DD experiments have shown unresolved events: DAMA/LIBRA, CoGeNT and more recently CRESST. They point towards a certain range of mass and cross sections for a Dark Matter particle. However, other direct detection experiments such as CDMS-II, XENON100 or KIMS rule out those regions. There is conflict between experiments that are designed to search for the same effect. This claims for a review of what is expected to happen in such experiments: maybe we are simply not observing what we expected. Are we interpreting the raw data in the best way? Are we losing valuable information by taking wrong hypotheses? Why should we assume the Dark Matter sector to be made only of one particle? There could be two stable relics –or many more. And what if the Dark Matter was a composite particle, would not it have much more complex interactions with ordinary matter? After all, we are made of a multitude of particles and molecules and so is all the known Universe.
New data is coming. The LHC is running better than expected. The Higgs boson could show up soon, or not. Cosmology is going one step further in its observation of the CMB with Planck. The finesse of the experiment is striking, reaching tiny effects which have enormous implications in the History of the Universe. While we may expect a refinement of the current parameter determination, it is yet to be seen whether high multipole and/or polarisation analyses can shed light on the nature of Dark Matter. New generations of direct detection experiments will go beyond the already remarkable achieved sensitivities, with larger and longer exposures, with better control of the experimental set up. If future directional detection experiments record events, they will be able to determine the Dark Matter mass and interaction rate, as well as the astrophysical parameters of the local Dark Matter distribution and velocity dispersions. Fermi-LAT, AMS, HESS and other detectors and observatories are scanning the skies in search of unexpected signals, and are ready to hunt for Dark Matter signatures.
However, it is not only by piling up experimental results –even if these are achieving excellence in the experimental point of view– that we will accomplish a broader understanding of the Universe and its constituents. Indeed, we are privileged to witness the most sophisticated observations and framework, with Cosmology and Particle Physics both being extremely

successful in telling the story of what we see at macroscopic and microscopic scales. But this privilege is not the only one, maybe not even the most exciting, for the challenges we are holding in our hands are bigger, deeper: we know a lot, but the unknown is even larger. We need to be ready for an inclusive synthesis of all the pieces of the puzzle we have been able to gather. We are trying to reconstruct a picture, and we have glimpse of the scenery it suggests. But we still do not know: is it a desert, is it a jungle, or is it *something else*...?